## INFORMATION TO USERS

This manuscript has been reproduced from the microfilm master. UMI films the text directly from the original or copy submitted. Thus, some thesis and dissertation copies are in typewriter face, while others may be from any type of computer printer.

**The quality of this reproduction is dependent upon the quality of the copy submitted.** Broken or indistinct print, colored or poor quality illustrations and photographs, print bleedthrough, substandard margins, and improper alignment can adversely affect reproduction.

In the unlikely event that the author did not send UMI a complete manuscript and there are missing pages, these will be noted. Also, if unauthorized copyright material had to be removed, a note will indicate the deletion.

Oversize materials (e.g., maps, drawings, charts) are reproduced by sectioning the original, beginning at the upper left-hand corner and continuing from left to right in equal sections with small overlaps. Each original is also photographed in one exposure and is included in reduced form at the back of the book.

Photographs included in the original manuscript have been reproduced xerographically in this copy. Higher quality 6" x 9" black and white photographic prints are available for any photographs or illustrations appearing in this copy for an additional charge. Contact UMI directly to order.

UMI®

Bell & Howell Information and Learning
300 North Zeeb Road, Ann Arbor, MI 48106-1346 USA
800-521-0600

Reproduced with permission of the copyright owner. Further reproduction prohibited without permission.

A

# The initiation and growth of extracellular lipid liposomes in arteries and valves

by

**Yongyi Yin**

A dissertation submitted to the Graduate Faculty in Engineering in partial
fulfillment of the requirements for the degree of Doctor Philosophy,
The City University of New York
1999

UMI Number: 9946233

---

---

UMI
300 North Zeeb Road
Ann Arbor, MI 48103

This manuscript has been read and accepted for the Graduate Faculty in Engineering in satisfaction of the dissertation requirement for the degree of Doctor of Philosophy.

16 September 1999
Date

David Rumschitzki
Professor David Rumschitzki, Mentor
Chair of Examining Committee

17 September 1999
Date

Mumtaz K. Kassir
Professor Mumtaz K. Kassir
Executive Officer

Professor Sheldon Weinbaum, Co-mentor

Professor Peter Ganatos

Professor Charles Maldarelli

Professor Kung-ming Jan

Supervisory Committee

The City University of New York

# Abstract

## The initiation and growth of extracellular lipid liposomes in arteries and valves

By

**Yongyi Yin**

Advisors: Professor David S. Rumschitzki, Mentor
Professor Sheldon Weinbaum, Co-mentor

Atherosclerosis is a well-known disease mainly of large arteries. It can also occur in valve leaflets, but usually does not affect function there. There is considerable suggestive evidence that lipoprotein cholesterol, after crossing the arterial endothelium and entering the intima from the vascular lumen, lodges in extracellular lipid packets (labeled "liposomes") bound to the extracellular matrix. In this thesis we shall model the transport of lipoprotein cholesterol and its intimal accumulation and show that the two are quantitatively linked. Moreover, we shall show that a single model for these accumulation processes, even one simple enough to contain only one adjustable parameter, can account for the liposome accumulation both in the arteries and in the valves of rabbits that suffered very different cholesterol histories. As such, it lends support to the hypotheses that the

transport and accumulation of lipid are ubiquitous, well defined processes that may indeed be the key molecular events that lie at the genesis of atherosclerotic plaques.

Liposomes appear to form by occasional attachment of a low-density lipoprotein (LDL) to the intimal matrix and to grow in place mainly by appending available free LDL. The liposome size distributions observed in chronically hypercholesteremic (WHHL) and in short-term cholesterol-fed rabbits are quite different. We propose a hierarchy of simple, well-stirred nucleation-polymerization models to describe the initiation and growth of extracellular lipid liposomes. Even the simplest of these (with only one adjustable parameter) agrees extremely well with the WHHL data. In contrast, even the most complicated well-stirred models fail to explain the cholesterol-fed rabbit data. The reason seems to be short-term feeding produces a local non-uniform intimal history of LDL supply, as a consequence of the focal nature of the transendothelial LDL flow through isolated transient leaky junctions. The same models used for the WHHL data, together with the fluid and macromolecular transport models provided by Huang *et al.* to describe this intimal non-uniformity, superimposed on a slow uniform transendothelial seepage also account very well for this cholesterol-fed rabbit data.

In contrast to the anatomy and placement of artery walls, heart valves consist mainly of extracellular matrix surrounded on two sides by an endothelial cell monolayer. Thus, the water flow pattern, and thus the cholesterol delivery, into heart valves differs greatly from that into the aortic wall. Therefore, the valve portion of this thesis begins with theoretical and experimental studies to describe water flow and macromolecular transport in valves.

We perform experiments using both ultrathin serial section and *en face* preparations with horseradish peroxidase (HRP) as a tracer for macromolecular transport in valves. The *en face* experiments show that macromolecular transport across the valves is localized around isolated endothelial cells. Since there is no internal elastic lamina (IEL) in valves, one might expect the serial sections about a localized leak for short HRP circulation times to show a gradual decrease in HRP concentration with tissue depth. In contrast, they show a very thin, subendothelial layer of intense staining comprising a relatively large spot and only diffuse staining below. This suggests a mismatch in extracellular matrix structure, and thus in the transport parameters, between the immediate subendothelial and deeper regions in valves. A new transport model based on these observations explains Tompkins' low density lipoprotein (LDL) concentration profiles with valve depth. Moreover, this new model, when coupled to the liposome formation and growth models from the artery, explains lipid accumulation in valves without the introduction of any new or changing any old adjustable parameters.

This thesis is organized as follows: The first part (Chapter I) provides background. The second part (Chapters II, III, IV, and V) presents the research on arteries. The third part (Chapters VI, VII, VIII, and IX) presents the research on valves. Finally, part four (Chapter X) summarizes and presents the outlook for future work.

To my wife: Wenqi

## Acknowledgements

I would like to express my sincere gratitude to my mentor, Professor David S. Rumschitzki and co-mentor, Professor Sheldon Weinbaum for their continuous great supervision during this research, which has been one of the most important parts of my life. During the course of this research, I benefited greatly from their constant support, guidance, encouragement, and superb understanding of biomedical phenomena.

I also wish to thank Dr. Shu Chien, University of California at San Diego, for his advice and support; Dr. Kung-ming Jan, Columbia University, for his guidance and assistance during my experimental studies; Professor Peter Ganatos for his suggestions on theoretical modeling; and Dean Mumtaz K. Kassir and Gerald G. Lowen for their handling of administrative details in such a warm and friendly manner. I would also like to thank NIH and NSF for the partial support under NIH grants CTS-9223089 and CTS-8658147 (to Professor David S. Rumschitzki) and NSF grant HL-19454.

Finally I would also like to thank Dr. Joy Frank, Department of Medicine and Physiology at the UCLA School of Medicine, for her kindly providing her unpublished experimental data on liposome formation in valve leaflets. I also thank Dr. Lemons, Department of biology in City College, for allowing me to use his experimental laboratory, and Peter Butler and Ji Song, for their fruitful discussion relating to my experimental study. My gratitude is also to my friends who shared my joys and pains throughout the course of this work: Jinnan Chen, Binmei Fu, Yulong Wu, Yaqi Huang, Dajun Zhang, Jianjun Feng, Xiaping Hu, Liyun Wang, Lidan You, Hsien-Hung Wei, Annie Yi-Xin Shou.

The thesis is dedicated to my father, mother, brother, father-and mother-in-law.

## Table of Contents

## Lists of Tables:

Part Three

**Lists of Figures:**

Part Two.

Part Three

# Part One. Introduction:

## I. Background

Low density lipoproteins (LDL) are commonly known as the "bad cholesterol" because they are generally associated with the arterial plaques common in arteriosclerosis and may, in fact, [49] initiate the intimal injury. Low density lipoprotein cholesterol consists of cholesterol, cholesterol ester, apoprotein B and a hydrophilic coat that makes this package blood soluble (see below for more details). Its principal function is to deliver cholesterol to body cells [3], which utilize cholesterol to build cell and organelle membranes and, in the case of hormonal secreting cells, as a chemical raw material for the production of hormones. Prolonged high plasma LDL levels, however, lead to lipid accumulation in the artery walls and, eventually, to atherosclerosis [22,29]. Below we describe the nature of the LDL particle, the origin of the LDL that circulates in the blood and what is known about the connection between lumen cholesterol and the onset of arterial plaques. We defer a discussion of the accumulation of lipid in the arterial and A/V valves to Chapter VI.

*What are low density lipoproteins (LDL)?* Figure 1 is a cartoon of an LDL particle. An LDL is a large spherical particle whose core is composed of about 2,000 molecules of the fatty alcohol cholesterol, about 1,500 of which are attached by an ester linkage to a long-chain fatty acid [33]. A layer of phospholipid and unesterified cholesterol molecules surrounds this core of cholesterol and cholesterol esters so that LDL will dissolve in blood. Embedded in the phospholipid is a molecule of apoprotein B-100, which the LDL receptor [47] specifically recognizes and binds with high affinity. That is, this receptor can pick out a single LDL particle from more than a billion molecules of water [33]. Some of the characteristics of an LDL particle are listed below [34]:

Low -Density Lipoproteins

Source: Plasma

Density: 1.006-1.063 g/ml

Size: 200-250 Å

Lipid content, % particle mass: 75

Lipid classes, % total lipids:

  Cholesterol ~60

  Phospholipids ~30

  Triglycerides ~10

Protein content, % particle mass: 25

  Major protein: apo B 100

  Minor proteins: apo Cs and apo E

*What is the origin of the circulating LDL?* The LDL transport system carries cholesterol and various triglycerides through the bloodstream and delivers it to cells that require it for membrane or hormone synthesis. This transport system consists of two pathways: 1) Exogenous: dietary cholesterol and triglycerides absorbed from the intestines enter the bloodstream and make their way to adipose tissue (for storage), muscle (for oxidation to supply energy) and the liver. 2) Endogenous: The liver packages cholesterol and triglycerides into lipoprotein packets which transport through the bloodstream to body cells for use in cell membranes and in hormone production. LDL transport belongs to this latter pathway. It comes from the liver, intestines and other non-intestinal tissues [33]. The liver first secretes a large very-low-density lipoprotein (VLDL) particle. The core of a VLDL has a larger amount of triglyceride but a smaller amount of cholesterol esters than LDL and its surface contains apoproteins B-100 and E. When a VLDL particle enters the capillaries of adipose tissue or of muscle, it becomes smaller and its store of cholesterol esters increases to yield a new particle called intermediate density lipoprotein (IDL). Almost half of the IDL particles are removed from the circulation by binding to liver cells, which make new VLDL and bile acids. The other half converts into low-density lipoprotein (LDL) when the apoprotein E leaves the particles. LDLs are longer lived than IDLs since apoprotein B-100 has a lower affinity for the LDL receptors.

*What are plaques and where in the artery wall do they occur?* Prolonged exposure to high concentrations of LDL leads to plaque formation. The core of these plaques tends to be cell-free. It is believed that these plaques begin from an accumulation of LDL cholesterol that infiltrates the artery wall. Before discussing the details of what is known about how these plaques form, let us first examine the architecture of the arterial wall. In large arteries such as the thoracic aorta, a monolayer of generally quiescent endothelial cells lies on the lumen side of the arterial wall. Beneath the endothelium lies the subendothelial intima, which in healthy animals is a thin, cell-free region comprised of proteoglycans and collagen, that ranges from 200-1000 nm in thickness. An internal elastic lamina (IEL) comprised of elastin separates the intima from the less ordered media. The IEL has the character of a continuous, cylindrical sheet (with fenestral holes) only in large arteries. The media contain smooth muscle cells, proteoglycans, partial sheathes of elastin and other constituents. A much more loosely packed adventitia lies beyond the media. Figure 5 summarizes this picture in a cartoon.

Guyton *et al.* [51] used light microscopy with oil Red O staining to show that early lipid-rich plaque cores appear in the deep intima, while their foam cell constituents are usually in the superficial intima. Studies on the ultrastructure and chemistry of core lipid deposits also show them to be largely extracellular. In large mature fibrous plaques in human aorta [10], approximately 90% of the core region is occupied by neutral (oily) lipid in the form of extracellular droplets with diameters $D < 0.4$ μm; very little is in foam cells, whose lipid droplet diameters are almost always larger than 0.4 (μm). This suggests that the cores of fibrous plaques develop directly from extracellular deposits of plasma lipoproteins.

*What are the first detectable prelesion events?* Schwenke and Carew [20] showed that one of the earliest events in the atherosclerotic process is an increase in the extracellular LDL concentration in the arterial intima that occurs within two weeks after rabbits begin a high cholesterol diet and prior to the entry of blood-borne monocytes into the arterial intima. They suggested that this increase was due to the binding of LDL to subendothelial intimal matrix to form lipid packets, dubbed liposomes, that contain the lipid from one or many LDL particles. As noted, the subendothelial matrix is comprised of collagen, elastin and proteoglycans. LDL and βVLDL interact with these matrix components both *in vitro* and in arterial plaques [4,13]. The binding is thought to occur through charged residues or by the columbic interaction between the carboxyl or sulfate groups of the polysaccharide with the positive side chains of apoprotein B [5,24]. Elastin also attracts $Ca^{++}$ (25), which facilitates lipoprotein association with polysaccharides.

Simionescu *et al.* [18, 23], using freeze fracture, discovered candidate liposomes, i.e., unesterified lipid packets, in lesion-prone but as yet lesion-free areas of the aortic arch of rabbits fed a high cholesterol diet for two weeks. They also showed that monocytes penetrate the endothelium and enter the intima in the same areas where the liposomes reside and then avidly devour the liposomes in the process of becoming foam cells. Stary and coworkers [27, 28] and Mitchison *et al.* [17] observed localized monocyte accumulation prior to lesion development in post-mortem studies of humans. They [27] detected macrophages both with and without extracellular lipid particles in arterial regions of infants less than 8 months old. These same regions developed into lesions in young adults [17, 27, 28]. Guyton and Klemp [10] observed extracellular lipid droplets in human intimal atherosclerotic lesions, and in particular in the 60-200 nm range for fibroatheroma lesions. This suggests that the formation of extracellular lipid liposomes plays a similar role in human aortic intima as it does in rabbit and that in either case, it is an important step in the chain of events leading to arterial plaque formation.

As liposomes mature, microfibrils and proteoglycans proliferate in the subendothelial matrix. Using ultra-rapid freezing without chemical fixation, followed by rotary shadow freeze-etching, Frank and Fogelman [8] obtained visual images of the liposomes clear enough to provide histograms of liposome sizes. The smallest liposomes are 22 nm in diameter, the size of an individual LDL particle, and range up to sizes corresponding to a few hundred times a single LDL volume. Since the large liposomes are much bigger than typical intimal matrix fiber spacings, their mobility in the intima would be near zero. This suggests that they form *in situ* after the entrainment of a single LDL particle.

Frank and Fogelman obtained histograms for WHHL rabbits that are receptor-deficient, and thus chronically hypercholesteremic (Fig. 9a), and for normal rabbits fed a high cholesterol diet for between 10 and 16 days (Fig. 9b). Interestingly, these histograms are dramatically different. Moreover, the images for the cholesterol fed rabbits show clusters of liposomes close to the endothelial side of the intima, surrounded by virtually liposome-free areas (Fig. 7).

*Where does the lipid found in liposomes come from and how does it get into the intima?* To demonstrate that the lipid in the liposomes derives from plasma LDL and βVLDL, Simionescu *et al.* [18,23] showed that apoprotein B, unesterified cholesterol and matrix proliferation were all concentrated in areas of liposome aggregation. Nievelstein *et al.* [17] used immunofluorescence microscopy with anti-apo-B antibodies and post-embedding immuno-gold-labelling to show the localization of apo B and LDL-associated gold accumulation in intimas of cardiac and A/V valves containing liposomes. Both particles were frequently found in the vicinity of collagen fibrils. Unfortunately, it has not yet been possible to simultaneously perform these tests and the rotary shadow images on the same specimen to provide definitive proof that liposomes derive from LDL. However the evidence is strongly suggestive of it.

The mechanism by which plasma LDL and other large molecules cross the endothelium at high lumen concentrations is the subject of much study. Since normal endothelial junctions typically screen out molecules larger than albumen (~8nm) [49], how does LDL cholesterol with a diameter of ~23nm pass through the arterial endothelium and enter the subendothelial intima? Palade [36] and Casley-Smith [37] began the early search for this large pore by which LDL and other large macromolecules can cross the endothelium. They suggested that the pathway of macromolecule transport across the endothelium is via vesicle translocation or fused, open-vesicle channels [36, 37]. Chien *et al.* [74, 76] and Bundgaard and coworkers [73, 75] used tannic acid preparations [73], double labeling methods [74], ultra-thin serial section reconstruction techniques [75] and cationized ferritin labeling methods [76] to find that the cytoplasmic vesicles, which were thought to be free, may be static structures attached to the plasmalemma through invaginating elements.

Weinbaum *et al.*[12, 31, 32] proposed a leaky junction-cell turnover hypothesis for the large pore in the arterial endothelium which had as its central tenet that the clefts around the rare cells in turn-over temporarily were leaky for macromolecules that ordinarily could not traverse the endothelium; that is, that the leaky clefts are the pathway for LDL permeability. They [31] proposed a new quantitative model to study if one could explain the observed permeability changes simply by allowing the intercellular clefts around widely-scattered endothelial cells to be leaky to the macromolecules during cell turnover. Their theoretical study shows that the local endothelial permeability can increase by 50%~100% because of the intercellular leaky junctions around the widely-scattered cells in turnover. Later, they [68, 70] developed time-dependent diffusion models for an experimental design to elucidate the origin of these leakage sites at the cellular level. Their theoretical studies led to experiments that we now discuss to study the permeability pathway at the cellular level and to confirm that cells in turn-over so indeed leak macromolecules.

Stemerman *et al.* [38] measured $^{125}$I-LDL permeability both in regions with and without leakage foci that leaked horseradish peroxidase (HRP) in order to estimate the relative LDL fluxes through the transcytotic and the leaky junctional pathway. They found that the permeability in the regions containing leakage foci is 20-50 times higher than that without the leakage foci. Lin *et al.* [14, 15] carried out *in vivo* experiments on rat aortas using hematoxylin as a marker for dividing cells and two different sized tracer molecules, EBA and lucifer yellow tagged to low density lipoprotein, called LY-LDL, to identify leakage sites. Figure 4a shows that fluorescent EBA surrounds a dividing endothelial cell in telophase three minutes after tracer injection. Almost 99% of the cells in the mitotic (M) phase were leaky to EBA. These experiments suggest that the endothelial cell junction gradually becomes larger during M phase and EBA can pass easily through an enlarged junction pore. Figure 4b shows a similar experiment ten minutes after the LY-LDL tracer injection. Almost 80% of the cells in the mitotic (M) phase were leaky to Lucifer yellow (LY) LDL. In addition, LY-LDL seems to be able to pass through the leaky cleft when the initial part of M phase is almost complete [14, 15]. Chuang *et al.* [7] found that the frequency of the leakage sites at the arterial intercostal branch areas of the rat was about two times of that at non-branch areas. Therefore, atherosclerotic lesion prone areas are associated with the regions of increased density of cellular level leakage sites with endothelial cell turnover for macromolecules (LDL).

In 1992, Truskey *et al.* [30] measured LDL permeability in the arterial wall with *en* *face* quantitative autoradiography (Häutchen preparation). They mapped [11] the LDL permeability in the intercostal, celiac, and iliac branches of the normal rabbit aorta. They found [30] that about 25% of the areas of elevated grain density had high densities of mitotic endothelial cells. These areas had higher permeabilities than others with fewer mitotic cells. Furthermore, these *en face* preparation pictures clearly showed the $^{125}$I-LDL concentration distribution in the arterial intima near a leakage site.

These experiments [31] show that significant transendothelial transport occurs via cellular level leakage sites associated with arterial endothelial cells of the thoracic aorta in turnover [2,7,11]. Such cells are indeed rare (less than one cell in 2000 in rat at any given time; less than half that in rabbit [2]). Since Evans blue binds to elastin in the IEL, it becomes a permanent marker of a leakage site even after leak has closed. If we assume that the rate of opening of new sites is the same as that of closure of old ones, the average duration time between consecutive leaks follows from the increase in the number of EBA leakage sites with time. From the data in [7] and [64], the average lifetime of a leaky cleft is about one hour in rat aorta.

What happens to the fluid and macromolecules that cross the endothelium via these leaky junctions? The experiments by Lin *et al.* noted above show that they very rapidly produce large spots that can be viewed *en face*. The fact that macromolecular leakage appeared to be localized meant that any model of these processes would have to consider the macromolecular transport both normal and parallel to the endothelium, i.e., had to be at least two-dimensional. The growth rate of these spots was much too rapid to be due solely to diffusion. In addition, the leakage spots grow initially after injection, but seem to reach a quasi-steady state quickly, as evinced by the fact that the HRP spots asymptotically approach their maximum size (200 μm dia) after only four minutes [7], rather than continuing to grow slowly with time. These facts suggested that a model utilizing convection as well as diffusion was necessary. However, such models, having either a single effective subendothelial medium [43] or two (intima and media) with identical properties and separated by an internal elastic laminar (which in arteries, is very likely an impermeable barrier except for these fenestrae) that would shunt the transendothelial flow parallel to the endothelium [12], could come within a factor of five of explaining the ultra-rapid spot size growth observed.

The key observation needed to explain these data was the recognition that the intima, although comprising less than one percent of the artery wall, could have a profound effect on the overall water and macromolecular transport there. Thus, when one notices that the intima has a surprisingly sparse matrix structure [8,12,19], in fact much sparser than that of the media, one could construct an *ab initio* model for its transport coefficients [12]. This model predicts that the intimal parameters calculated in this way are one to two orders of magnitude larger than those in the media. Thus, this parameter mismatch, together with the likely only slightly permeable, exiguously fenestrated IEL separating it from the media, would facilitate much faster intimal spread parallel to the endothelium than was possible with the earlier model parameters. This model proposed in [12] and sketched in Fig. 5 explains the HRP spot growth experiments extremely well. It thus presumes that the fluid that passes through the endothelial layer spreads parallel to the endothelium in the intima before seeping through the IEL's fenestrae and into the dense media [12,32]. The model [32] exhibits this behavior as well and also accounts for the very high local LDL concentrations and the concentration distribution in the intima close to a leak observed in the autoradiographic LDL spots by Truskey and coworkers in [30].

It is our hypothesis that some of the LDL supplied from these localized leaks becomes the LDL found in the liposomes and thus that the local accumulation of liposomes in the arterial intima is directly linked to the local endothelial leakage. Moreover, we propose that the kinetics of liposome formation and growth resemble those of classic nucleation /polymerization processes. Our recent models for the growth of LDL leakage spots in the intima [12,32] predict that the growth of the spots and their asymptotic quasi-steady size depend primarily on the relative permeability of the intimal matrix and the fenestral pores. The LDL concentration profiles that these models predict and that Truskey *et al.* have observed experimentally [30] (see Fig.6) show that there is a significant radial dilution of the high LDL concentration at the leak, and thus a sharp fall-off in the LDL concentration as a function of the distance from the leakage site, due to water entry into the arterial intima through normal inter-endothelial clefts. It is our hypothesis that the high LDL-concentration centers of individual leaks and the overlap regions of multiple leakage spots would seem to be the candidate spots for larger liposome formation, while the low LDL-concentration peripheries of the leakage spots would generate only smaller ones.

In the research described below, we shall construct a hierarchy of nucleation/ polymerization models and use them to provide a rational explanation for Frank and

Fogelman's histograms and the differences between them. In particular, we shall begin with the WHHL data, since these rabbits have been hypercholesteremic for most of their lives. As a consequence, each region of susceptible intima has experienced many leaks, centered both far from and near to the region in question. Therefore, spatial variation parallel to the endothelium is not an issue, and a spatially homogenous mathematical model can explain the data. This stands in contrast to the cholesterol fed rabbits, whose intimal regions have experienced relatively few high cholesterol leaks during the time of the 1-2 week feeding experiments and hence their intimal liposome number and local size distribution are highly heterogeneous. Thus we anticipate the need to incorporate spatial variation to explain the data from such rabbits.

Before proceeding to the detailed researches below, it is important to put the current work, extracellular lipid liposome formation, in the context of the overall picture of atherogenesis. At the commencement of high cholesterol feeding, elevated blood cholesterol levels lead to higher than normal fluxes of LDL from the blood into the artery wall and in particular into lesion-prone areas. If our hypothesis is correct, then a portion of this entering cholesterol bind to extracellular matrix and forms extracellular lipid liposomes, each with the lipid content of one to several hundred LDL particles, *in situ*. Simionescu *et al.* [23] also found that after two weeks of a high-cholesterol diet, monocytes adhere to and pass through the endothelium, enter the intima, devour the liposomes and turn into macrophages and then foam cells. Upon being overwhelmed with cholesterol, these foam cells can become necrotic. In the meantime smooth muscle cells which reside normally in the media migrate into the intima and also begin to take up cholesterol via their scavenger receptor [35]. These cells produce connective tissue matrix proteins and can also become necrotic foam cells. Consequently, debris accumulates in the intima. All these processes seem to contribute to early arterial plaque (lipid and connective tissue such as sulfated glycosaminoglycans, collagen and fibrin are the primary components of atherosclerotic plaques [47]) formation which may lead to endothelial injury [47]. Figure 3 summarizes these processes.

This thesis is divided into four parts. The first (present) part (Chapter I) provides a background for this work. The second part (Chapters II, III, IV and V) describes the work on artery walls. Chapters II and III introduce a hierarchy of spatially homogeneous (i.e., well stirred) models for the initiation and growth of extracellular lipid liposomes in the arterial intima. They begin by describing the simplest model (with only one adjustable parameter) and continue with various modified models that include the effects of liposome crowding, decay, merging, etc. Even the simplest of these models agrees extremely well with the Watanabe Heritable Hyperlipidemic (WHHL) data in [8], but none of the well-stirred models can explain the short-term feeding data. We examine in detail why this is the case. Chapter IV then develops a non-homogeneous model for liposome buildup in the 10-16 day cholesterol-fed rabbits. As we show, the cholesterol-fed rabbit data seem to result from the short-term, non-uniform intimal history of LDL supply which is a consequence of the focal nature of the transendothelial LDL flow through isolated, transient leaky junctions. Therefore, we employ the same models used for the WHHL data, together with this intimal nonuniformity, superimposed upon a slow, uniform transendothelial seepage. The resulting model can then account for the short-term feeding data very well, where the only new parameter introduced is the uniform seepage parameter. The end of part two, Chapter V, summarizes the artery wall work and draws conclusions.

Part three (Chapters VI, VII, VIII, and IX) presents the work on heart valves. Since heart valves consist mainly of extracellular matrix surrounded on both sides by an endothelial cell monolayer, the water flow pattern, and thus the cholesterol delivery, into heart valves is greatly differs from that of the aortic arteries (Part Two). In order to make Part Three self-contained, Chapter VI repeats an abbreviated literature review on lipoprotein transport and on liposome formation and growth in the arterial intima and valves. It stresses the recent liposome freeze fracture work on rabbit heart valves that the UCLA group [40] has performed. They have kindly provided us with unpublished freeze etching data for liposome formation in valves for which we are very thankful (Chapters VII and IX). Chapter VIIB describes the experimental methods used by Frank and coworkers to perform the ultra-rapid freezing/ rotary shadow etching technique for liposome and for the liposome size visualization just described.

As already mentioned, in order to study liposome formation and growth in valves, one needs to first quantitatively characterize the water and macromolecular transport in the valve. Since the valve architecture is significantly different from the artery wall's, one must do a series of transport-relevant experiments to guide the model development. Chapter VIIB describes these new experiments in valves. We carry out animals experiments on rats. This work, in collaboration with Dr. Kung-ming Jan of Columbia University and Dr. Anli Huang of Institute of Biomedical Sciences, Academia Sinica, Taipei, is the subject of Chapters VIIB and VIIC. Chapter VIIC discusses the experimental results. The first set of results show that trans-endothelial transport of large molecules again appears to be localized to the interendothelial clefts surrounding a small number of cells, typically 0-2 cells per valve leaflet face. Thus a two-dimensional transport model is indeed necessary and Chapter VIII develops it, albeit for a uniform subendothelial medium. This chapter also provides the *ab initio* theory for calculating the transport parameters, based on the matrix structure observed in the freeze fracture pictures. This theory was originally developed by Curry [79] and applied to the artery problem in Huang *et al.* [12].

The predicted short time HRP tracer results do not, however, agree with experiment. These experiments in fact suggest that there is a mismatch in the matrix structure, and thus in the transport parameters, between the immediate subendothelial region and the deeper portions of the aortic valves. The main goal of Chapter VIII is to develop a new picture of the water and macromolecular transport into cardiac valves and to determine the macromolecular (LDL) distribution in the valve (sections VIIIC and D). Section VIIID develops the new model to describe the filtration and macromolecular transport in valves, in which the filtration model admits an analytic solution. The results of our model are consistent with and thus provide a potential explanation for Tompkins *et al.*'s [43] experimentally observed LDL concentration profiles as a function of depth in aortic valves (Chapter VIIIE). They found substantial variation of these profiles between subject, between valve leaflets of the same subject and even between regions of the same leaflet. Since our experiments suggest that each face of each valve leaflet may have 0-2 leaky cells at any instant, there are a number of possible combinations for the numbers of leaks on the two faces. Model calculations show that the combinations for 0-1 leak per face yield LDL profiles in agreement with those that Tompkins *et al.* measured.

We then couple this model to our liposome initiation/growth models in Part Two (with the parameters unchanged) to explain the liposomes size distribution found in the valves of cholesterol-fed animals (Chapter IX). Finally, we provide the discussion for this research and an outlook for future work in Part four (Chapter X).

## Part Two

### II. The homogeneous models for the initiation and growth of extracellular lipid liposomes in arterial intima.

IIA. *LDL supply:* As just noted, in the WHHL rabbits, spatial variation in the intima, and hence consideration of the focal nature of transendothelial leaks, is unimportant. As a result, we simply consider a representative position within the intima, i.e., we use the so-called well-mixed models and allow the LDL supply L(t) to be prescribed. Typically, L(t) will be a series of pulses, separated by latent periods. As noted, typically one cell in ~ 4000 is leaky at any instant in rabbit, and this leak lasts about an hour (latter data available only for rat). From Huang *et al.* [12] and Truskey *et al.* [30] (see Figure 6), a single leak produces a subendothelial spot of very high LDL concentration of steady size that covers ~20 endothelial cells and a lower, gradually tapering, yet nevertheless elevated, concentration that covers >10 times this area. Thus, at a fixed point in the intima, the expected waiting time for the overlap of high concentration spots of two successive leaks is of the order of 200 hours.

For specific numerical calculations, we shall simply take the LDL supply to be pulses that are squares and of uniform duration [pulse width (w) is ~1 hour [7,32]], concentration (h), and waiting time [time between the (T-w); one entire cycle from the beginning of one LDL pulse to the beginning of the next one (T) is ~8 days [2]]. We shall, however, first derive analytic results in terms of an arbitrary, prescribed L(t), thereby allowing for arbitrary pulse shapes and varying heights.

The value for h requires some discussions, since Figure 6 shows the LDL concentration, even within the ~20 cells core of a leak, to be non-uniform. The LDL concentration in Figure 6 is normalized so that a value of one corresponds to the blood cholesterol level. To arrive at a value for h, we integrate the LDL-vs-time curve in Figure 6 (say, the lower two), divide by the area occupied by 20 cells and multiply by the blood cholesterol value. That is, we choose an average of h that uniformly distributes the total cholesterol in the intima during a leak uniformly over 20 cells. This turns out to be 0.54 × blood LDL concentration.

For WHHL rabbits we take the blood value to be 500 mg/dL (h=270 mg/dL) [the average of the 400~600 mg/dL for WHHL rabbits (J. S. Frank, personal communication) and close to 445 mg/dL [6]], an order of magnitude above the normal values [45~50 mg/dL (J. S. Frank, personal communication), 29 mg/dL (6) or 41.3 ± 6.6 mg/dL [1]]. For cholesterol fed rabbits, we infer values based on those in the literature. Atkinson *et al.* [1] give cholesterol values as a function of time of feeding for New Zealand White rabbits on a slightly different high cholesterol diet (1% cholesterol, rather than 2%) from that of Frank and Fogelman [8]. Interpolating these data to two weeks, one finds a value of about 1070 mg/dL. The rise time of blood LDL after the start of feeding decreases sharply and the peak increases moderately as the percent cholesterol in the feed increases (18 vs 8 weeks and 2100 vs 2700 mg/dL as the feed LDL goes from 0.5% to 1%). Thus, for 2 weeks at 2% feeding it seems reasonable to assume an average value of 700~1000 mg/dL.

IIB. *Simple nucleation-polymerization:* The vast majority of LDL entering the arterial intima via the leaky junctions sweeps through the artery wall and is picked up by the lymph system; that is, only a small fraction of it ends up in liposomes [15].

Furthermore, before rabbits are fed a high cholesterol diet, normal rabbit intimas do not evince the presence of lipid liposomes [8]. Thus binding to intima matrix must be a rare event that only occurs appreciably at a sustained high LDL concentration. The simplest way to model initiation is as a process that occurs only when the local concentration exceeds a certain threshold or as a first order process. The former model would require much more data than are available to pinpoint this threshold. Moreover, it is hard to picture a simple reaction mechanism that could account for such threshold behavior. Finally, Nievelstein *et al.* [17] note the presence of small isolated liposomes throughout the intima after a 2 hour bolus LDL infusion, presumably in regions of the intima in which the LDL concentration was not extremely high. This argues against a threshold process and thus we choose the first order model. If L represents free LDL, $M_1$ represents a liposome (i.e., bound to the matrix) composed of the lipid from a single LDL particle, and if the concentration of matrix is in excess, the nucleation "reaction" is represented by $L \rightarrow M_1$ with a small rate constant ($k^0$).

From the freeze etchings of Frank and Fogelman [8], one can observe the growth of the liposomes that have already formed by merging with fresh "monomers" supplied by a non-zero LDL concentration and with neighboring liposomes. Frank and Fogelman also note that the larger liposomes must have formed *in vivo* because, taking into account the surrounding matrix structure, their mobility is vanishingly small. We assume that the rate constant for the growth of liposomes ($k^1$) is sufficiently slow that the chance nucleation of a liposome in a normocholesteremic rabbit is unlikely to grow. Moreover, for lack of data and to minimize the number of parameters, we take $k^1$ to be size-independent. If this is indeed the case, it would correspond to liposomes of all sizes being equally reactive. One way of rationalizing this would be if each liposome, independent of size, had a preferred site on its surface for appending free LDL. However, no evidence for this exists. The rate of growth from a liposome composed of j monomers ($M_j$) to one of j+1 monomers ($M_{j+1}$) will be $k^1$ times the product of the concentration of sporadically abundant L(t) with the much smaller concentration of $M_j$, whereas that of the merging between a liposome of size j with one of size k will be proportional to the product of two small quantities: the concentrations of $M_j$ and $M_k$. Thus liposome growth in hypercholesteremic rabbits will proceed predominantly via the merging of existing liposomes with the L(t) and our first simple model consists simply of nucleation and of growth, viz.

$$L \xrightarrow{k^0} M_1 \tag{1a}$$

$$M_j + L \xrightarrow{k^1} M_{j+1} (j = 1,2,3,4,\ldots) \tag{1b}$$

Because only a very small fraction of the LDL in any leak ends up in liposomes, one may presume that these processes do not significantly affect L(t) and that one may still prescribe L(t). As such, if one uses the same symbol to represent both a species and its concentration, the corresponding kinetic equations are:

$$\frac{dM_1}{dt} = (k^0 - k^1 M_1)L \tag{2a}$$

$$\frac{dM_j}{dt} = k^1 L(M_{j-1} - M_j); (j \geq 2) \tag{2b}$$

Sometimes, it is cumbersome to retain the discrete nature of Equations 1 and 2, where liposomes have integral sizes, particularly when one progresses to more complex models.

Moreover, since j>>1 for a mature liposome, one would expect this discrete nature not to be important. Thus, we also consider a continuous-size (x) liposome model which obtains by replacing the difference in liposome concentrations in Equations 2b by a derivative. This yields a one-dimensional traveling front equation

$$\frac{\partial M(x,t)}{\partial t} + k^1 L \frac{\partial M(x,t)}{\partial x} = 0 (1 \le x \le \infty); M(1,t) = M_1(t) \qquad (3)$$

The discrete-size model in Equation 2 leads to a simple solution for the intimal liposome number distribution in terms of a single integral of an arbitrary L(t). For an initially liposome-free system, the solution is

$$M_j(t) = \frac{k^o}{k^1}[1 - e^{-a(t)} \sum_{n=0}^{j-1} (\frac{a^n(t)}{n!})] \qquad (4)$$

where a(t) is the time integral of the coefficient of $M_1$ in Equation 2a: $\int_0^t k^1 L(s)ds$ and s is a dummy variable. For the square pulse L(t) described above, $a(t)=a^0= k^1 h\tau$ where $\tau$ is a time variable that openly advances when the LDL supply is on and remains fixed when the supply is off { $\tau=iw+(t-iT)$ during the i$^{th}$ pulse ( $iT \le t \le iT+w$ ) and $\tau=(i+1)w$ during the i$^{th}$ waiting period [$iT+w < t < (i+1)T$]}. The total number and mass of liposomes, the latter in units of LDL masses, satisfy the simple equations

$$\frac{d}{dt}\sum_{j=1}^{\infty} M_j = k^0 L; \qquad \frac{d}{dt}\sum_{j=1}^{\infty} jM_j = k^0 L + k^1 L \sum_{j=1}^{\infty} M_j \qquad (5a,b)$$

the solutions of which, either directly, or via summation of Equation 4, are

$$\sum_{j=1}^{\infty} jM_j = \frac{k^o}{k^1} a(t) \qquad (6a)$$

$$\sum_{j=1}^{\infty} jM_j = \int_0^t k^0 L(s)[1 + a(s)]ds = \frac{k^0}{k^1}[a^0 + \frac{1}{2}(a^0)^2] \qquad (6b)$$

The solution for the continuous-sized liposome model proceeds by the method of characteristics for boundary and/or initial conditions of M(x,0)=0 and M(1,t) given by Equation 2a; it is

$$M(x,t) = 0, (t < t'); \qquad M(x,t) = M(1, t - t') = \frac{k^o}{k^1}[1 - e^{-a(t-t')}], (t \geq t') \qquad (7a,b)$$

where t' satisfies x-1 = $\int_0^{t'} k^1 L(s)ds$. For L(t) as described above

$$M(x,t) = \frac{k^0}{k^1}[1 - e^{-x-a^0-1}], (t \geq t') \qquad (7c)$$

The total number of liposomes in the continuous-liposome case is just the integral of M(x,t) over all x from 1 to $\infty$ plus M(1,t) because there is a non-zero contribution from the x=1 limit of integration. Its time evolution derives from integrating Equation 3 over x and adding Equation 2a; this procedure simply gives $k^0L$, the same as the right side of Equation 5a. The total liposome mass, M(1,t) + $\int_1^\infty xM(x,t)dx$, changes by virtue of the increase in the mass of existing liposomes plus the creation of new liposomes. One calculates the former by multiplying Equation 3 by x and integrating from 1 to $\infty$ so that, after integration by parts, it gives $k^1L$ times the total number of liposomes. The latter is the rate of creation of new liposomes at x=1, just determined to be $k^0L$. Note that the $-k^1M_1(t)L$ in Equation 2a, which expresses the growth of existing liposomes is already included in the former integral. Thus, the right side is the same as Equation 5b and therefore the solutions Equations 6a and 6b hold for the continuous case as well. Note that

Equations 6a and 6b also follows from direct integration of the solution for the M(x,t) in Equation 7.

IIC. *Comparison with experimental histogram:* Even the simple models *in Simple nucleation-polymerization* can explain the observed WHHL histogram extremely well, despite having essentially only one adjustable parameter. That is, the solutions Equation 4 or Equation 7 depend on the ratio of $k^0/k^1$ and $a(t)=k^1 \int_1^t L(s)ds$ for t, the fixed time corresponding to the age of the rabbit at the time of the measurement (experimental time). However, because $k^0/k^1$ multiplies the concentrations of all liposomes, it controls only the total number and mass of liposomes and is irrelevant to their size distribution. Thus, it is only the value of a(t) that one may adjust [via, equivalently, adjusting either $k^1$ or the various parameters in L(t) , e.g., h, w, T or i] to fit the data.

Figure 10 is a plot of the number of liposomes of a given size versus j for both the discrete and the continuous models of L(t) corresponding to different numbers of square pulses. w and T have the values in *LDL supply*, and we choose $k^1h$ to be the value 5.8 $hr^{-1}$ ($k^1 = 0.043$ $dLmg^{-1}h^{-1}$) that best matches the WHHL histogram at 5 months (19 leaks), the average age of the WHHL rabbits in Ref. 8. Note that the continuous model yields curves that resemble a step function moving to the right with increasing a(t) [in this case by increasing the number of pulses (i) while holding $k^1$ and pulse shape fixed] while the discrete solution is similar but drops off somewhat less sharply. Apparently, for any given value of a(t) the populations of the small liposome sizes reach steady state very quickly, the large liposomes are not yet populated and the transition region of j, which corresponds to liposomes that are populated but not yet steady, is very thin.

Conversion to a bar graph plotting number vs. diameter (d) to conform to the way Frank and Fogelman [8] present their histograms introduces a geometric factor. Because j is proportional to the liposome volume, if the liposomes are, say, spherical, then the number with diameters $d_1 \leq d \leq d_2$ is the total number of liposomes comprised of j monomers, where $4/3\times\pi\times(d_1/2)^3 \leq j\times4/3\times\pi\times(23/2)^3 \leq 4/3\times\pi\times(d_2/2)^3$, where a single LDL particle has a diameter of 23 nm. Figure 11, which labels the abscissa with both d and j, is a comparison of the Frank and Fogelman data with the best fit (by varying the value a(t), i.e., $k^1$, for the fixed time t at which the rabbit was killed) discrete and continuous model solutions. This curve corresponds to the 19 leak curve in Figure 10. Note that the ratio of the sizes of the first two blocks is essentially not adjustable since the populations of all of the liposomes of those sizes are steady. The height of the third block is determined by the position of the curve in Figure 10 at which the step occurs, and one chooses this by varying a(t) to fit the data. This optimum value of a(t) corresponding to 19 leaks is 220.5, or $k^1$=0.043 $\mathrm{dLmg^{-1}h^{-1}}$. Note that these models, particularly the continuous version, yield a probably artificially sharp size cutoff as a result of the exponential character of the solutions that follow from including only first order processes. Finally, Figure 12 shows another shortcoming of these models: each successive LDL pulse leads to a larger increase in total liposome mass than the previous one and will, in fact, alter the distribution. We shall discuss models that can remedy this situation in MODIFIED MODELS.

Before moving on to model modifications, a word about $k^0$ is in order. From the very clear freeze etching pictures of Frank and Fogelman (Figure 3 in Ref. 8), it is possible to count the number of liposomes present and to estimate their number density in their

Figure 3 as $3.5\times10^{13}/\mathrm{cm}^3$. If this etching from the WHHL rabbit were representative of the entire intima in that region of the rabbit's aorta, one could estimate $k^0$ from Equation 6a and the parameters in *LDL supply and Comparison with experimental histogram* as 0.4 $h^{-1}$. This value is almost definitely quite high, i.e., an upper bound, since the etching shown was probably picked because it was particularly dense with liposomes compared with its surroundings. A value a few times smaller than this, and much smaller than $k^1h$ in Figure 10 is consistent with binding being a rare event, even in the absence of the modifications described in MODIFIED MODELS.

## III. Modified models:

IIIA. *Size-dependent growth:* One way to correct for the sharp size-cutoff that the simple models display might be to allow the growth constant $k^1$ of the liposomes to be size dependent. Since the data are insufficient to justify most choices, the natural presumption is that $k^1$ is proportional to the liposome's surface area, which goes as $j^{2/3}$, i.e., $k^1(j)= k^{10} j^{2/3}$. Although one can solve the model with the above modification explicitly, it is easy to see that the result cannot fit the WHHL data. The reason is that, as before, at any given value of a(t), there will be a narrow transition between liposomes whose concentrations are steady and those that are unpopulated. The number vs j curve, instead of resembling a step function, will follow the steady curve $(k^0/k^{10})j^{-2/3}$ until the transition region, where it will quickly decay to zero. Plotting the result as a number vs d bar graph involves essentially integrating this function over j between limits that are the cubes of the diameters $d_1$ and $d_2$ corresponding to the edges of the bars. Since the integration of $j^{-2/3}$ from $d_1^3$ to $d_2^3$ is equal to $3(d_2-d_1)$, the result is proportional to the difference between the diameters at the opposite edges of the bar; it follows that the first two bars will be of approximately equal size since they are of equal width. Thus, such a model will give a worse fit to the WHHL data than do the section II models. This will be true irrespective of a(t), as long as a(t) is large enough to place the transition region beyond d=120 nm, a necessary condition to guarantee the existence of any large liposomes.

IIIB. *Crowding:* As noted in *Sized-dependent growth*, the simple models allow an unbounded growth in the total liposome mass, which is certainly not physically correct. On the contrary, one would presume that the WHHL rabbits' intima had reached some sort of steady state before monocyte entry. To correct for this, one can augment the simple model with a standard crowding term. The model equations for the discrete case are just those in Equations 2, with the right side of each multiplied by the factor [1-S(t)/K], where S{t) is the total liposome mass and K is the total holding capacity. This factor slows the rates of all of the reactions as S(t) approaches the K that, presumably, the WHHL rabbits have essentially reached. As such, crowding should not affect the liposome size distribution for a given S(t) at all, but because it slows the evolution of the latter, it also slows the evolution of the former. One can see this mathematically by noting that if one can come up with an explicit expression for the S(t) as a function of time, then the effect of crowding is just to rescale time by dt --> (1-S(t)/K)dt; thus the analytic solutions $M_j(t)$ or M(x,t) from the simple models above remain valid, with only the definition of a(t) altered to $a_c(t)$ by this rescaling, where $a_c(t) := k^1 \int_0^t L(s)\,[1-S(s)/K]\,ds$.

In fact, one can solve for S(t) explicitly. If N is the total number of liposomes, then appropriately summing (as in Equation 5) the model Equations gives:

$$\frac{dN(t)}{dt} = k^0 L[1 - \frac{S(t)}{K}]; \qquad \frac{dS(t)}{dt} = L[k^0 + k^1 N(t)][1 - \frac{S(t)}{K}] \qquad \text{(8a,b)}$$

Let $\alpha=(1+2Kk^1/k^0)^{1/2}$, $\beta=\alpha k^0/(k^1K)$; and $\gamma=(\alpha+1)/(\alpha-1)$. The solutions for N(t) and S(t) are

$$S(t) = N(t) + \frac{1}{2}\frac{k^0}{k^1} N^2(t) \qquad (9)$$

$$N(t) = \frac{k^0}{k^1} a_c(t) = \frac{k^0}{k^1} \frac{1 - e^{-\beta a(t)}}{\gamma + e^{-\beta a(t)}} (1 + \alpha) \qquad (10)$$

Note that both S(t) and N(t) now are bounded as t → ∞, with the total mass approaching K and the number approaching $(\alpha-1)k^0/k^1$. Figures 12 & 13 show the total liposome mass and the liposome size distribution, respectively, as functions of the number of pulses for the discrete model and the square pulse example discussed in *LDL supply*. They both display the slow-down in growth as the system approaches its local capacity. Note that because K itself controls the extent to which the step-like number-vs-size distribution progresses to the right in the number-vs-j plot (Figure 13), one can fit the WHHL rabbit's liposome size distribution to the same degree of accuracy as in the simple model just by choosing K appropriately. As long as $a_c(t)$ is large enough to ensure that the K is almost reached, the fit will be almost completely insensitive to $k^1$ and L(t) which go into $a_c(t)$; one may choose them so as to satisfy any other constraints. K = 24,531 (also in units of $k^0/k^1$); the value that gives the correct total mass for the WHHL rabbits is the value in Figures 12 & 13, and the value $k^1=0.148$ dLmg$^{-1}$h$^{-1}$ used in Figures 12 and 13, or any larger number, will ensure that the WHHL rabbits have reached steady state.

IIIC. *Phagocytosis by macrophages: Liposome decay.* Up to this point our models do not consider any element of recovery of the intima when lumen LDL concentration is reduced, i.e., total liposome mass is, thus far, non-decreasing with time, regardless of L(t). Such a situation is unrealistic for a number of reasons. First, it is well known [26] that infants can develop early plaques while on mother's milk and that these plaques quickly disappear after the infants are weaned. Second, with the passage of time, the integrals defining a(t), and $a_c(t)$ will increase monotonically ($a_c(t)$ in a bounded and a(t) in an unbounded manner), even for normocholesteremic individuals. Because the models in *Simple nucleation-polymerization* and *Crowding* provide a total liposome buildup solely on the value of a(t), they would predict that normocholesteremic individuals would develop the same liposome accumulation as hypercholesteremic individuals, albeit at the later time required by the normocholesteremic individual to attain the required a(t) value; conversely, at a fixed age, the normocholesteremic individual would have an existing distribution of liposomes equivalent to a younger hypercholesteremic individual. This certainly does not conform to experimental observation: Frank and Fogelman [8], for example, found no visible liposomes in control rabbits. Thus, the models need a means for cleaning up liposomes when LDL concentrations are reduced or when a chance small liposome forms in a normocholesteremic individual. Such a depletion mechanism would also have the effect of limiting the total growth of liposome mass without need for the explicit crowding terms.

In fact, such a mechanism exists, Simionescu *et al.* [22] showed that blood borne monocytes adhere to endothelial cells above intimal regions with a high LDL accumulation. The monocytes enter the intima there, transform into macrophages [9] and consume LDL by phagocytosis [22]. Because phagocytosis is a process in which an entire liposome is ingested the decay rate will not depend on the size of the liposome.

We now choose the simplest type of recovery mechanism, a first order decay of liposomes of each size, with a single rate constant $k_d$ for all liposome sizes, as a phagocytotic process would dictate. The resulting model for, say, the continuous liposome case becomes

$$\frac{dM_1}{dt} = (k^0 - k^1 M_1)L - k_d M_1; \qquad \frac{\partial M(x,t)}{\partial t} + k^1 L \frac{\partial M(x,t)}{\partial x} = -k_d M(x,t), (1 \le x \le \infty) \quad (11)$$

Again, the method of characteristics provides an analytic solution; the solution, however, is no longer a function of a(t), the time integral of the coefficient of $M_1$ in Equation 2a, but rather of $M_1$ in Equation 11, namely, $b(t) = \int_0^t (k^1 L(s) + k_d) ds$, viz.

$$M(1,t) = \frac{k^0}{k^1} e^{-b(t)} [\int_0^{b(t)} \bullet\, db - k_d \int_0^t \bullet\, ds] e^{b(s)} = \frac{k^0}{k^1} e^{-b(t)} [e^{b(t)} - 1 - k_d \int_0^t e^{b(t)} ds] \quad (12a)$$

$$M(x,t) = M(1, t-t') e^{-k_d t'}, (t \ge t'); \qquad M(x,t) = 0, (t < t'); (continuous) \quad (12b)$$

$$\begin{aligned} M_n(t) &= \frac{k^0}{k^1} e^{-b(t)} [\int_0^{b(t)} \bullet\, db - k_d \int_0^t \bullet\, ds]^n e^{b(s)} \\ &= \frac{k^0}{k^1} e^{-b(t)} \sum_{i=0}^{n} \binom{n}{i} (-k_d)^i \int_0^t \int_0^{s_i} \ldots \int_0^{s_2} [e^{b(s_1)} - \sum_{j=0}^{n-i-1} \frac{b^j(s_1)}{j!}] ds_1 \ldots ds_i, (discrete) \end{aligned} \quad (12c)$$

where, as earlier, t' satisfies the equation x-1=a(t'). For L(t) a sequence of square pulses, one can, as usual, carry out these integrations explicitly. If one divides the solution into two parts, the "on" phase during a pulse and the "off" phase between pulses, it gives

$M(1,t-t')=M'(1,t-t')$ and $b(t)=ik^1hw+k^1h\ (t-iT)+k_dt$, $iT \le t \le iT+w$ for "on" and $M(1,t-t')$ $=M'(1,iT+w-t')\ e^{-kd(t-iT-w)}$ and $b(t)=(i+1)k^1hw+k_dt$, $iT+w < t < (i+1)T$ for off. Here $M'(1,t)$ is

$$
\begin{aligned}
M'(1,t) = \frac{k^0}{k^1} e^{-b(t)} \{ e^{b(t)} - 1 - k_d \frac{1}{k^1 h + k_d} \\
[e^{b(t)} - 1 + \frac{k^1 h}{k_d} e^{k^1 h\omega} (e^{k_d T} - e^{k_d \omega}) \frac{1 - e^{i(k^1 h\omega + k_d T)}}{1 - e^{k^1 h\omega + k_d T}}]\}
\end{aligned}
\qquad (13)
$$

We omit the explicit discrete liposome size solution for the square-pulse series L(t), because it is cumbersome. Because the continuous- and discrete-liposome solutions are quite similar, the discussion applies to both.

The novelty in the present model is that phagocytosis removes liposomes and this leads to a dynamic variation in liposome numbers even during periods between LDL pulses (see Figure 12). Thus, none of the liposome sizes maintains a strictly steady concentration in response to a stream of LDL pulses. Rather, the smaller liposomes achieve a steady concentration *cycle* forced by the repetitive, assumed identical pulses. The full-cycle, time-average total liposome number and mass for this L(t) are $(w/T)hk^0/k_d$ and $(w/T)hk^0/k_d[1+hk^1/k_d]$, respectively. In particular, they are bounded. Also, a cessation of high LDL pulses will result in a first order decay of liposome number (see Figure 12 between pulses).

Another manifestation of phagocytosis appears in the number vs. j plot after 5 months or 19 leaks (Figure 14) that, to the left of the transition region, follows a steady curve that decreases in a step-wise fashion as one moves to the right. This behavior derives from the alternate step supply of LDL followed by a pure phagocytosis decay phase. As in Figure 6, an initial pulse creates a step distribution which here slants downward due to phagocytosis; it then decays (lowers slightly) almost uniformly during the LDL off phase. The next LDL pulse and the traveling response nature of the solution basically displace this slightly reduced step to the right while creating a new step identical to the original one in its place. Subsequent pulses maintain this pattern.

Unfortunately, we do not know of data that would allow us to evaluate $k_d$ accurately as yet. Phagocytosis should be slow enough to account for the WHHL rabbits' liposome accumulation and be fast enough so as to more than balance the formation and growth terms for normocholesteremic rabbits, basically decaying with high probability the chance-formed liposome before the next overlapping leak occurs. However, this latter restriction is hardly constraining. From the data of Huang *et al.* [12], one sees that the blood LDL concentration of a normocholesteremic rabbit is less than 1/10 that of the WHHL rabbits. Our simplest models in THE SIMPLEST MATHEMATICAL MODELS (Equation 6b) that the total liposome mass after 1 or 2 leaks of the normocholesteremic rabbit is on the order of 1% of that of the WHHL. Thus, even a modest decay between leaks is sufficient to prevent the growth of the chance-formed liposomes in the normocholesteremic rabbit. On the other hand, one also requires that the absence of LDL supply during the off phases would not eliminate or degrade most of the liposomes in hypercholesteremic rabbits. Thus, to get a rough upper bound for $k_d$, suppose that, say, 40% or more of the liposomes present after a pulse survive until next pulse, then, because the ratio of the liposome numbers at the end and the beginning of an LDL-free waiting period of length 200 hrs is $e^{-kd200} > 0.4$, one has $k_d < .005\ hr^{-1}$. A better estimate of $k_d$

follows by noting that phagocytosis could be the mechanism that limits the growth of the liposome distribution and thereby could be responsible for the Floquet (i.e., average over one input cycle)-steady limit of the liposome accumulation in the WHHL rabbits. From Equations 12 and Figure 14, one can see that, for the step-pulse LDL supply and for the Floquet-steady $M_1$ value ($M_1^{ss}$), the steady part of the liposome number vs. j curve, i.e., the part that lies to the left of the transition region, decreases and satisfies $M_1^{ss}e^{-k_d(x-1)T/(k_1hw)}<M(x,t)<M_1^{ss}e^{-k_d(x-1)T/(k_1hw)}\,e^{k_d(T-w)}$. At either bound, one can, by integration, calculate the theoretical ratio of the first two bars in Frank and Fogelman's [8] WHHL rabbit data (Figure 11) in terms of $k_d$ and set it equal to their experimental value of 2.35; one finds $k_d = 0.01\ k^1hw/T$. One may then choose $k^1$ to adjust the position of the step in Figure 8a so as to match the experimental result of the third bar. The corresponding floquet limit of the ratio of the WHHL second to third data bars at infinite time is then 1.94, which compares with Frank and Fogelman's value of 1.42. Figure 14 chooses its parameters ($k_d$=.00097 $h^{-1}$, $k^1$=.078 $dLmg^{-1}h^{-1}$) in this way and Figure 11 shows the comparison with the experiment.

IIID. *Merging of liposomes:* Whereas any of the above well-stirred models is capable of accounting for the WHHL rabbit data, none (in their homogeneous intima incarnation) can account for the cholesterol-fed normal rabbit data. The technical reason for this is that, to keep the ratio of small-to-medium sized liposomes as high as in Figure 9b, or even simply greater than one, these models produce essentially zero large liposomes, contrary to the data (see Figure 15, dash-dot curve and corresponding number vs. j plot in Figure 10). Conversely, equating the number of medium and large liposomes requires the ratio of the number of small to medium liposomes to be significantly <1.

Whereas slight adjustments in the parameter values may slightly perturb the resulting liposome distributions, these generic features derive from the model, irrespective of the precise parameter values. [1] Naively, one might seek to append steps to the mechanism that alter the liposome size distribution without abandoning the homogeneous intima framework. As noted earlier, the freeze etchings of Frank and Fogelman [8] seem to suggest one possibility, the merging of liposomes of different sizes. This merging of any pair of existing liposomes ($M_j + M_k \rightarrow M_{j+k}$; j, k≥1) leaves the equation for the total liposome mass unchanged (Equation 5b) while skewing the distribution towards larger liposomes.

For merging rate constant $k_m$, the equations for this model are:

$$\frac{dM_1}{dt} = (k^o - k^1 M_1)L - k_m M_1 (M_1 + \sum_{j=1}^{\infty} M_j) \tag{14a}$$

$$\frac{dM_j}{dt} = k_1 L(M_{j-1} - M_j) - k_m M_j (M_j + \sum_{n=1}^{\infty} M_n) + k_m \sum_{n=1}^{\text{largest integer} \leq \frac{j}{2}} M_n M_{j-n};\ j \geq 2 \tag{14b}$$

---

[1] One might suggest that the liposome distribution in Figure 9b is the result of pooling the data from two rabbits that were fed for 16 days and one for 10 days. A simple calculation in terms of the continuous model belies this conjecture. It is reasonable to presume that 16 days is short enough so that crowding and other effects are negligible and the simple model (2)-(3) suffices. Let us approximate the solution in Figure 6 by a step function $1-\Theta(j-k^1Lt)$ where $\Theta$ is the Heaviside function ($\Theta(x)=1$ if $x > 0$, $\Theta(x) = 0$ if $x < 0$) and assume that the pooling contains 1/3 data from the one 10 day fed rabbit and 2/3 from the two 16 day fed rabbits. The resulting histogram, plotted as in Figure 10, would be 1 from 0 to some value $(k^1L)10$, 2/3 from $10(k^1L)$ to $16(k^1L)$ and 0 beyond. In order to fit Figure 9b, there must exist some large liposomes, i.e., $16(k^1L) > 142$, or $10k^1L > 89 > 28$. The ratio of the first to second box is then $28 / [\ (10k^1L-28) + (142-10k^1L) \times 2/3\ ]$ for $10k^1L<142$ and 14/57 for $10k^1L>142$. Neither can match the experimental value of 6 for this ratio in Fig. 9b for any positive value of $k^1L$.

The equation for the total number of liposomes involves the sum of $M_j^2$. The equation for the evaluation of $M_j^2$ leads to an infinite hierarchy of equations. Although one can simplify these equations greatly with Z-transforms, we choose to show (Figure 14) the numerical solution of the model equations for the first few hundred j values for parameters chosen to favor a large ratio of small- to medium-size liposomes, in accordance with the short-time feeding data. The lower curves in Figure 14 show that merging depletes the small liposomes and gives the liposome distribution a large liposome tail. The magnitude of $k_m$ controls this effect. To mimic the cholesterol-fed rabbit data, i.e., to adjust the ratio of small- to medium-size liposomes to the experimental ratio of 6, one would need a low a(t), and to obtain large liposomes, a large $k_m$. The dotted curve in Figure 14 [2] and the corresponding dashed curves in 15 show that the number of large liposomes is still too small. Increasing the $k_m$ further raises the number of large liposomes at the expense of lowering the number of small liposomes; it also introduces significant populations of liposomes that are much larger than those observed in experiment. When these large $k_m$ values are run for 5 month old WHHL rabbits, the numbers of liposomes that are much larger than those found by Frank and Fogelman [8] become very large, contrary to experiment.

---

[2] That this curve should have a maximum is not immediately clear. At the conclusion of a pulse, the distribution is indeed monotonically decreasing, resembling a step function that is slightly sloping downward and having a tail. During the waiting period before the next pulse, the merging terms serve only to deplete the smallest liposomes and, due to their low concentration, only to increase the values along the tail. On the other hand, liposome sizes initially near the right edge of the step are both produced by the merging of smaller liposomes and destroyed by their merging with other liposomes. So, even though their absolute numbers decrease during the waiting period, they decrease slower than the numbers of smaller liposomes. This accounts for the maximum.

## IV. The 10-16 day cholesterol-fed rabbit: the non-homogeneous intima:

At this point, recall that the short feeding time in the experiments on normal rabbit strongly suggests that one must account for the nonhomogeneity of the intima. In particular, Frank and Fogelman [8] note that the intimas of these rabbits display localized clusters of liposomes of varying sizes and, in addition, small individual liposomes outside of these clusters. Moreover, the larger clusters appeared just beneath the endothelium. From Huang *et al.* [12], the LDL concentration distribution about a leaky junction achieves a steady state in the order of five minutes, and the experiments by Chuang *et al.* [7] show that the leakage lasts on the order of an hour. Moreover, this steady spatial LDL distribution is relatively flat under the leaky cell and then, due to a dilution flow of water through normal inter-endothelial clefts, decays fairly rapidly with distance from the leaky cell's perimeter (Figure 6). That is, there is a small region of high LDL that is close to the lumen concentration and a relatively larger region of lower LDL concentration. It is the former, together with overlap regions from different leaks, that may account for the large and medium-size liposomes, and it is the latter that may generate the abundant smaller ones. In addition, there is suggestive evidence [11,21] (based on a total LDL balance) for an additional slow uniform transendothelial LDL seepage that is superimposed on the leak-based LDL supply. This seepage would tend mostly to increase the number of small liposomes. On this point, Nievelstein *et al.* [19] note the presence of small liposomes of the same size (23nm) as a single LDL particle (which they distinguish from free LDL by virtue of their extensive connections to matrix and collagen fibers) "dispersed throughout the matrix" in addition to the larger liposome clusters.

The generic feasibility of such an idea to account for the data should be clear: one could crudely model the high concentration regions as a variable-area fraction with uniform a(t) values chosen to give equal numbers of medium and large liposomes; the low concentration regions would simply have an a(t) value chosen to produce only small liposomes; variation of the area fraction would yield an arbitrarily good fit of the data. Below, however, we perform a computer simulation that is somewhat more realistic. We choose a square corresponding to an area of intima (say 50 × 50 cells) that is large compared with the extent of a single leak. Then we subject this area to leaks that occur as a Poisson process (in time of occurrence and in duration) at random locations in the square with periodic boundary conditions. The spatial and temporal frequencies of the leaks (the means of the distributions) conform to experimental observation.

We started with a liposome-free intima and allowed the leaks to temporally generate liposomes and a local liposome size distribution at each site on the 50×50 grid. For each leak, we need a precise steady LDL concentration profile as a function of the distance r from the center of the leak. Figure 6 shows one of the predicted profiles of Huang *et al.* [12] (with r normalized by the radius R of an endothelial cell) for the LDL distribution around a cellular level leakage site. Because the present results show that the liposome size distribution is sensitive to the precise nature of the concentration profile used, we preferred here to use the enlargements of the autoradiographs kindly provided by G. Truskey's group. These autoradiographs provide a detail distribution of radioactive

LDL particles near a leakage site obtained from Häutchen preparation (Figure 5D in Ref. 30 and Figure 9B in Ref. 16). A manual counting of the dots as a function of distance r in photographically enlarged reproductions of these two autoradiograms yields the other two curves in Figure 6 (Truskey's group has sent us a number of such photos and the profiles in Figure 3 are representative of them.) At each grid point within the square, we calculated the distance from the leak and from its periodic images in the neighbouring 50×50 cell squares and thus the L(t) there. From the L(t), one then updates the $a(t)/k^1$ values at that grid point due to the present leak. Using the liposome models developed above, we calculated how this leak changes the local distribution of the different-size liposomes at each grid point at each time step. To keep the calculation tractable and because the feeding experiments being modeled are short-term, we employ the basic model in *Simple nucleation-polymerization* with the same parameters and neglect any crowding, merging, or decay. Moreover, we approximated the solution in Fig. 4 by a step function (in number vs. j plots) which travels to the right with speed $k^1L(t)$; thus, each leak simply moves the local histogram to the right by an amount $[\Delta a(t)]$ for the L(t) at that location due to that leak. Finally, at the end of the number of leaks corresponding to 10-16 days, we sum up the local distributions to get an overall histogram to compare with the cholesterol fed rabbit data. Figure 9 shows the results both with and without a superimposed uniform seepage. As one can see, the spatial dependence even without the uniform seepage is a major improvement over the uniform intimal models. It gives a population of large liposomes comparable to the population of medium-size ones while allowing the population of small liposomes to be larger than either of these, and it does not generate exceedingly large liposomes. The fit becomes much better simply by superimposing an adjustable slow, uniform leakage [the rate of seepage is the product of a seepage constant ($k_s$) times the lumens LDL concentration] onto the model, with $k_s$=0.003 (see Figure 16). Both of these fits are closest to the data for a blood LDL concentration of 730 mgdL$^{-1}$, which is in the range given in *LDL supply.* Perhaps a more clever choice of parameters could lead to an even better fit without reliance on seepage, but we chose to retain the $k^1$ value from the WHHL fit. Finally, at long times (~5 months) and WHHL blood cholesterol concentrations, this model, with the same parameters, reduces to the WHHL histogram (see dotted curve in Figure 11).

## V. Summary and Conclusions:

Frank and Fogelman [8] observed an accumulation of extracellular lipid liposomes in the arterial intimas of both WHHL and normal, 10- to 16-day cholesterol-fed rabbits. The liposome size distributions in these two types of rabbits differ significantly, with the liposomes in the former being mostly medium and large in size. In contrast, the normocholesteremic rabbits have an overwhelming majority of small liposomes and almost equal numbers of medium and large liposomes. It is worth noting here that these data derive from a small area of aorta from a small number of specimens (2 WHHL rabbits and 3 cholesterol-fed rabbits). Frank and Fogelman constructed these histograms based on measurements of 130 and 100 liposomes for the WHHL and cholesterol fed rabbits, respectively. These came from examining ten different micrographs from ten different areas of intima per animal. Their implication (J. S. Frank and A. M. Fogelman, personal communication) is that the WHHL distribution is representative of these animals because the cell-free, liposome-rich regions were plentiful and similar to each other. Of course, the small number of animals suggests that the absolute magnitude of the populations in the two histograms may not be accurate for a larger sample. However, the difference in the shapes of the profiles is so striking and the numbers of intimal areas examined and liposomes counted are sufficiently large that the trends appear general and compelling. We construct a hierarchy of nucleation-polymerization type models, almost all of which admit exact analytical solutions; even the simplest of these explains the WHHL data extremely well with only a single adjustable parameter. In addition to the nucleation and polymerization of liposomes, these models can include liposome decay, crowding and merging as well as a polymerization rate constant that depends on liposome size.

None of these models alone, however, can adequately account for the cholesterol-fed normal rabbit data. We argue that the reason lies in the difference between the cholesterol histories of the intimas of the two types of rabbits. In the WHHL rabbits which have long been hypercholesteremic, the intima is homogeneous because each region has witnessed numerous leaks. In contrast, after short periods of cholesterol feeding, the normal rabbits' intimas are highly heterogeneous, with regions that happened to have been near the center of a leakage spot having large- and medium-size liposomes and regions on the periphery of a spot exhibiting only small liposomes. With this view and the leakage spot's LDL concentration as a function of position taken from measured data [16, 30], one can account for the normal rabbit data quite well while employing the same intrinsic model parameter ($k^1$) as in the WHHL rabbit case. As a result, the sharp difference between the liposome histograms for the two populations of rabbits argues for localized intimal cholesterol leaks as being the mechanism for the formation of the large and medium size liposomes in cholesterol-fed rabbits.

## Figure legends:

**Figure 1.** Low density lipoprotein cholesterol (LDL) consists of cholesterol, cholesterol ester, apoprotein B and a hydrophilic coat that makes this package blood soluble. It is a major cholesterol carrier in the bloodstream. Its principal function is to deliver cholesterol to body cells, which utilizes cholesterol to build cell and organelle membranes and, in the case of hormonal secreting cells, as a chemical raw material for the production of hormones [33,34].

**Figure 2.** The inner convex region of the aortic arch of a hyperlipidemic rabbit after 2 weeks of high cholesterol diet. The intima contains extracellular liposome-like vesicles(el) associated especially with microfibrils(mf), elastic bundles(eb), and internal elastica(ie). The extracelluar liposomes(el) are found beneath the endothelium(e). l and m represent lumen and smooth muscle cell of the media; c represents collagen.(×28,000)

**Figure 3.** Summation of the processes of plasma low density lipoprotein (LDL) entering the subendothelial space and being oxidized, and the consequent formation of foam cell. These processes seem to contribute to early arterial plaque (lipid and connective tissue such as sulfated glycosaminoglycans, collagen and fibrin are the primary components of atherosclerotic plaques [47]) formation which may lead to endothelial injury [47].

**Figure 4.** The association of an EBA leaky spot with a dividing endothelial cell (arrow) in the telophase. Fluorescence photomicrograph of an *en face* preparation of aortic

endothelium stained with hematoxylin. Bar=20 μm [14,15].

**Figure 5.** A convective-diffusive model of transendothelial transport flow of water and large molecules such as LDL by Huang *et al.*[12]. The model assumes that the inter-cell junctions around the rare endothelial cell that is in mitosis or that is during allow a solute-bearing convective flow from the lumen into the intima. The convection spreads mainly parallel to the internal elastic lamina and is diluted by a water flow that is free of large solutes across the normal inter-cell junctions into the intima. This model accounts for the experimentally observed [5] tracer spot size growth very well and provides the concentration as a function of distance from the leaky cell in the intimal region.

**Figure 6.** LDL concentration in the intima as a function of distance from the center of a cell whose perimeter leaks. Curves obtained from Truskey *et al.* 's [30] experimental data by counting the dots in concentric annular shells and from Huang *et al.* 's [12] theoretical prediction data. This non-uniform concentration is normalized by the plasma LDL concentration.

**Figure 7.** The fracture images for the cholesterol fed rabbits show clusters of liposomes close to the endothelial side of the intima, surrounded by virtually liposome-free areas (From Frank & Fogelman [8]).

**Figure 8.** After 21 days cholesterol feeding, there are numerous packets of aggregated lipid

particles in the A-V valves. These lipid particles with different sizes were enmeshed in the extracellular matrix microfibrils.

**Figure 9 a,b.** Bar Graph shows liposome size distribution in WHHL and cholesterol-fed rabbits. (From Frank & Fogelman [8] ).

**Figure 10.** Section II's model predictions for the liposome size distribution after different number of leaks. Both liposome monomer number j and the corresponding diameter are shown on the absissa. Solid and dashed curves represent continuous and discrete models for WHHL rabbits, respectively, with the parameters: T=8 days, w=1hr, $k^1$=.043 ($dLmg^{-1}hr^{-1}$), and uniform LDL concentration h= 270 ($mgdL^{-1}$). Dot-dashed curve represents 16 days of feeding for NZW rabbits the same $k^1$ as above. Matching to the given liposomes number distribution [8], one can obtain h=394 ($mgdL^{-1}$), or a lumen LDL concentration of 730 mg/dL.

**Figure 11.** A comparison of the Frank and Fogelman's [8] data (solid curve) with the best fit solutions of the Section II's model. Long dashed curve is for both the discrete and continuous models with $k^1$=.043 ($dLmg^{-1}hr^{-1}$), h=270 ($mgdL^{-1}$), T=8 days, w=1 hr, t=5 months, which gives a(t)=220.5. Short dashed curve is for the simple models above with phagocytosis: $k_d$=.00097 $hr^{-1}$, $k^1$=.078 ($dL\ mg^{-1}\ hr^{-1}$). Dotted curve is for non-homogeneous model with 5 months of cholesterol feeding; all parameters are the same as in the long dashed curve except that the blood cholesterol level 500 mg $dL^{-1}$, corresponding to h=270 $mgdL^{-1}$.

**Figure 12.** The time evolution of the total liposome mass in response to five identical square impulses. The comparison is between the initial model and models modified that include phagocytosis and crowding effects. The solid, dotted, and dashed curves represent the initial model, the initial model with phagocytosis, and the initial model with crowding, respectively. In the initial model, $k^1$=.043 ($dLmg^{-1}hr^{-1}$), h=270 ($mgdL^{-1}$), w=1 hr-1, T=8 days, t=5 months. When the model includes phagocytosis, $k^1$=.078($dLmg^{-1}hr^{-1}$) and $k_d$=.00097 $hr^{-1}$. When it includes crowding, $k^1$=.148 ($dLmg^{-1}hr^{-1}$) and K=24,531.

**Figure 13.** Liposome size distribution for different numbers of pulses for the discrete model modified with crowding. The holding capacity K for crowding is K=24,531, which is the total liposome mass divided by ($k^0/k^1$); thus K turns out to be dimensionless. $k^1$=.148 ($dLmg^{-1}hr^{-1}$). All the cholesterol supply parameters are the same as in Fig. 10 and correspond to the WHHL rabbits.

**Figure 14.** Liposome size distribution for models that include phagocytosis (5 months at WHHL rabbit's cholesterol levels, $k_d$=.00097 $hr^{-1}$) or merging (10 days cholesterol-feeding and 5 months at WHHL rabbit's cholesterol levels for values of $k_m$ listed on the graph. All merging curves use $k^1$=.03 $dLmg^{-1}hr^{-1}$ and the same LDL supply parameters as previous curves).

**Figure 15.** A comparison of the simple and modified models with Frank & Fogelman's experimental liposome size distribution for cholesterol-fed NZW rabbits. The initial models

with $k^1$=.043 ($dLmg^{-1}hr^{-1}$) and h=394 ($mgdL^{-1}$) produce no large liposomes with diameters d > 120nm. In the model modified with merging with $k^1$=.03 ($dLmg^{-1}hr^{-1}$), $k_m$=.005 $hr^{-1}$ produce larger liposomes with diameters d > 397nm, contrary to experimental observation.

**Figure 16.** Histogram shows liposome size distribution for the cholesterol-fed rabbit data and the computer simulation of liposome formation and growth, both with and without seepage. All model parameters are the same as in the initial models except that we take the time t=10 days and h=453 $mgdL^{-1}$ correspond to the short time cholesterol feeding experiments.

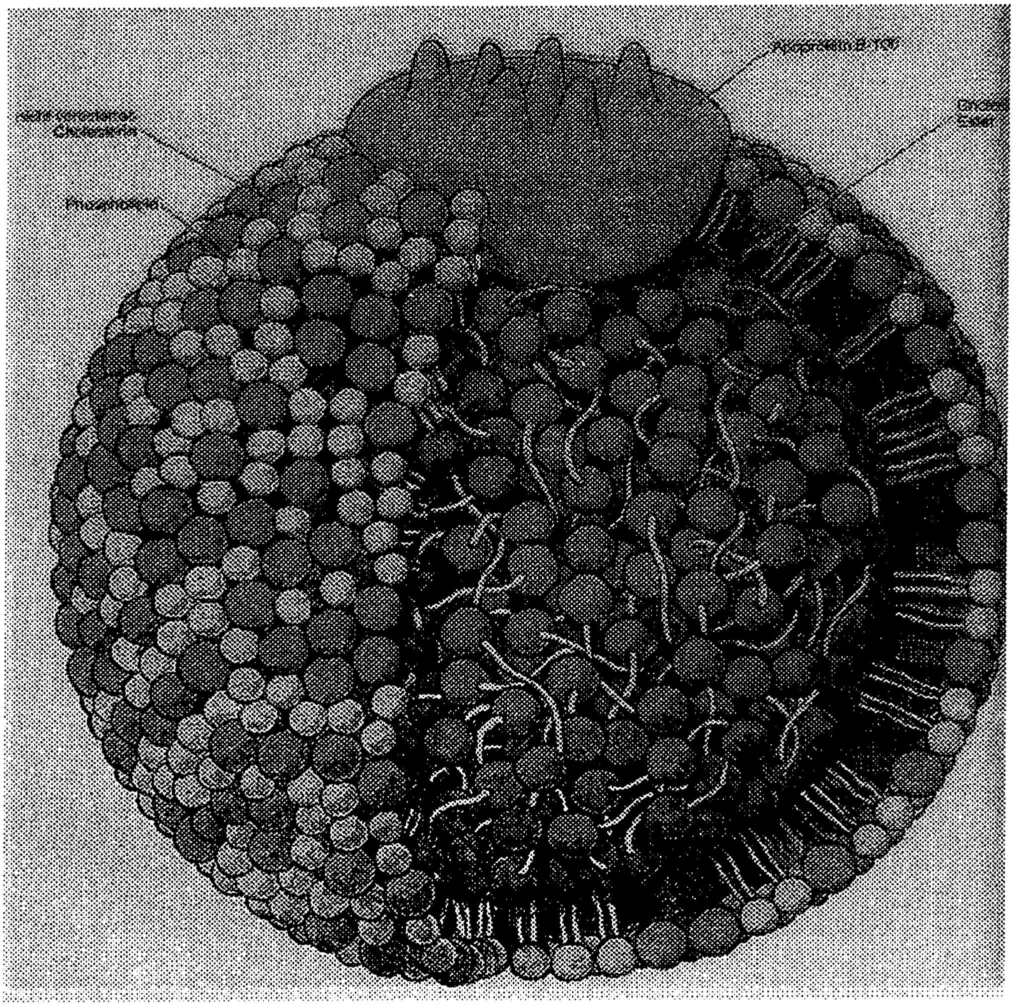
Apoprotein B-100
Unesterified Cholesterol
Phospholipid
Ester

Fig. 1

Fig. 2

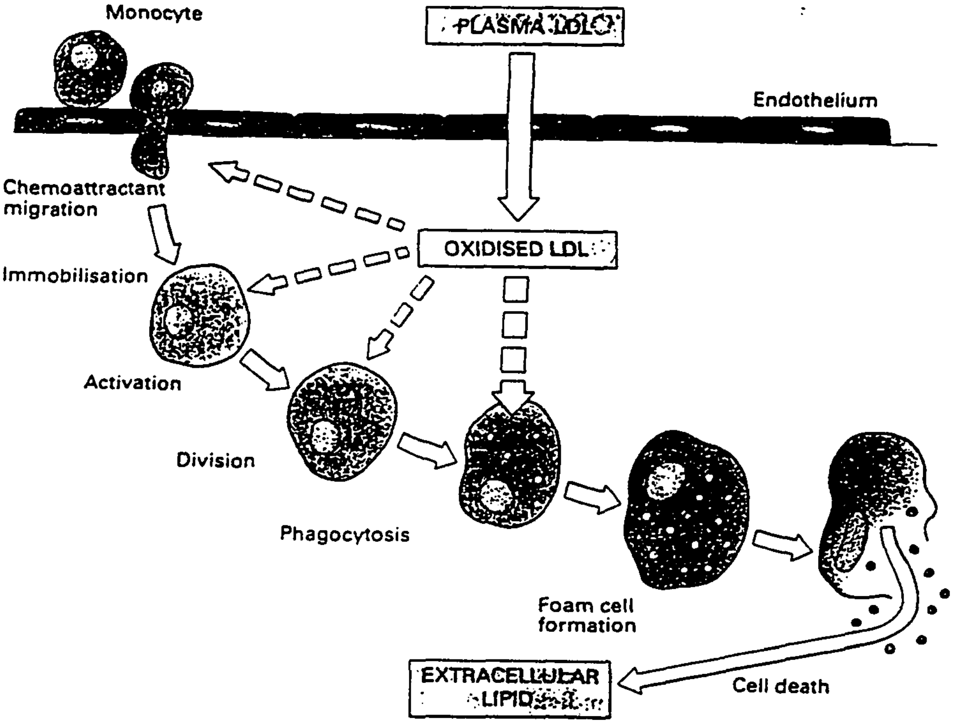

*Diagram to show plasma low density lipoprotein (LDL) entering the subendothelial space and being oxidised, and the consequent formation of a foam cell.*

Fig. 3

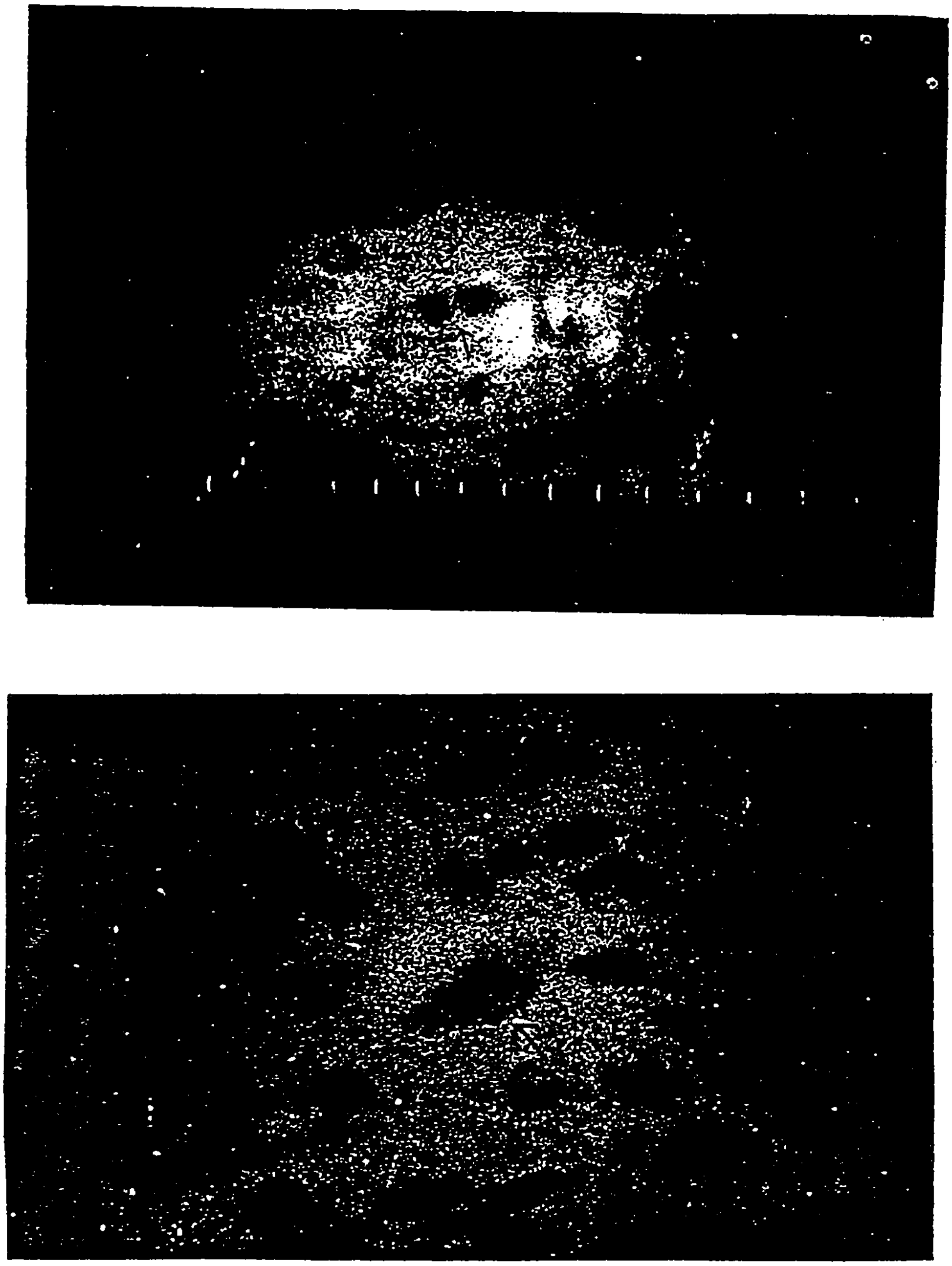

Fig. 4

TRANSPORT MODEL
Convection/Diffusion Darcy Flow

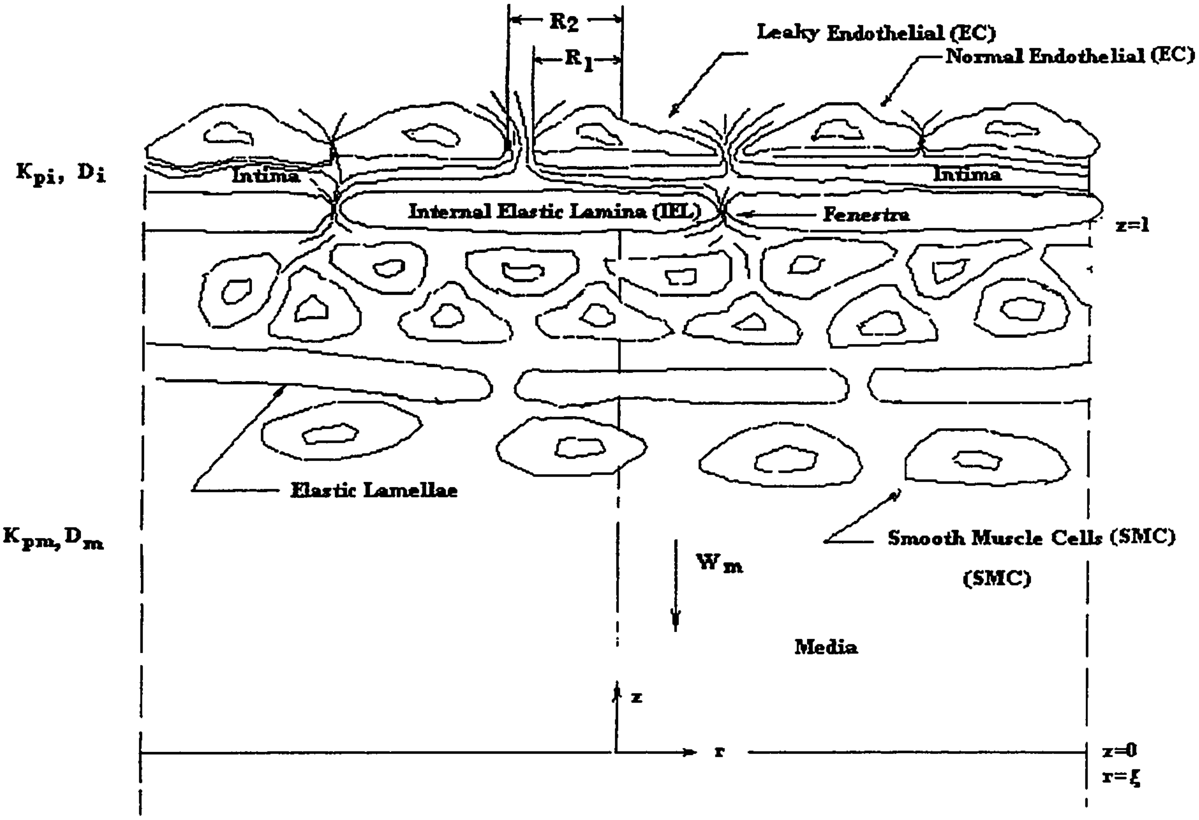

Fig. 5

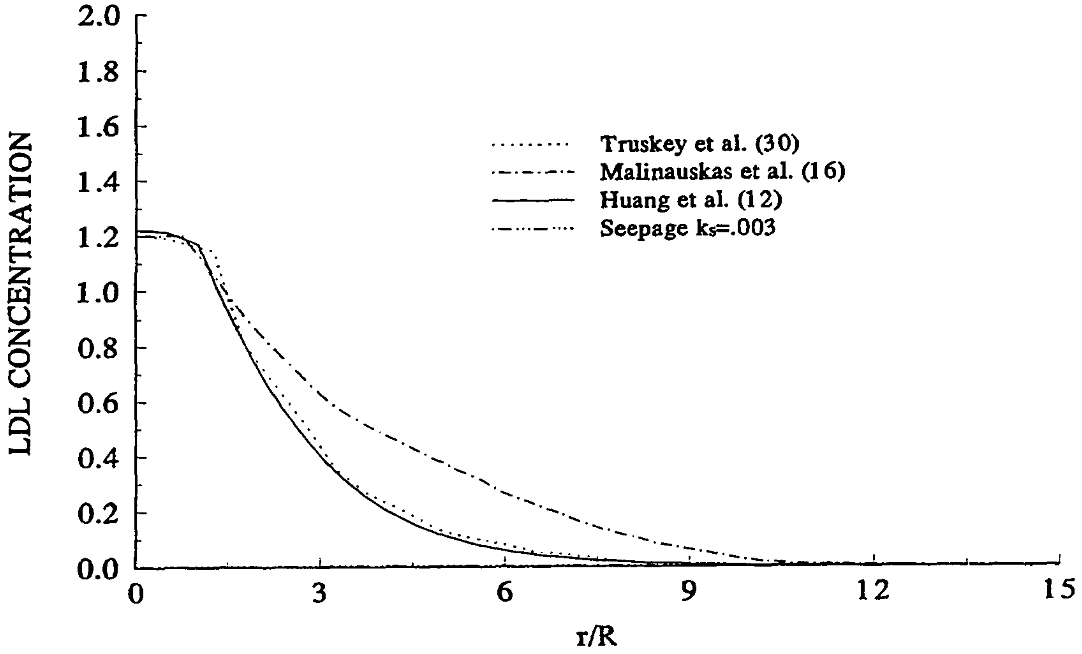
2.0
1.8
1.6
1.4
1.2
1.0
0.8
0.6
0.4
0.2
0.0
LDL CONCENTRATION
Truskey et al. (30)
Malinauskas et al. (16)
Huang et al. (12)
Seepage ks=.003
0
3
6
9
12
15
r/R

Fig. 6

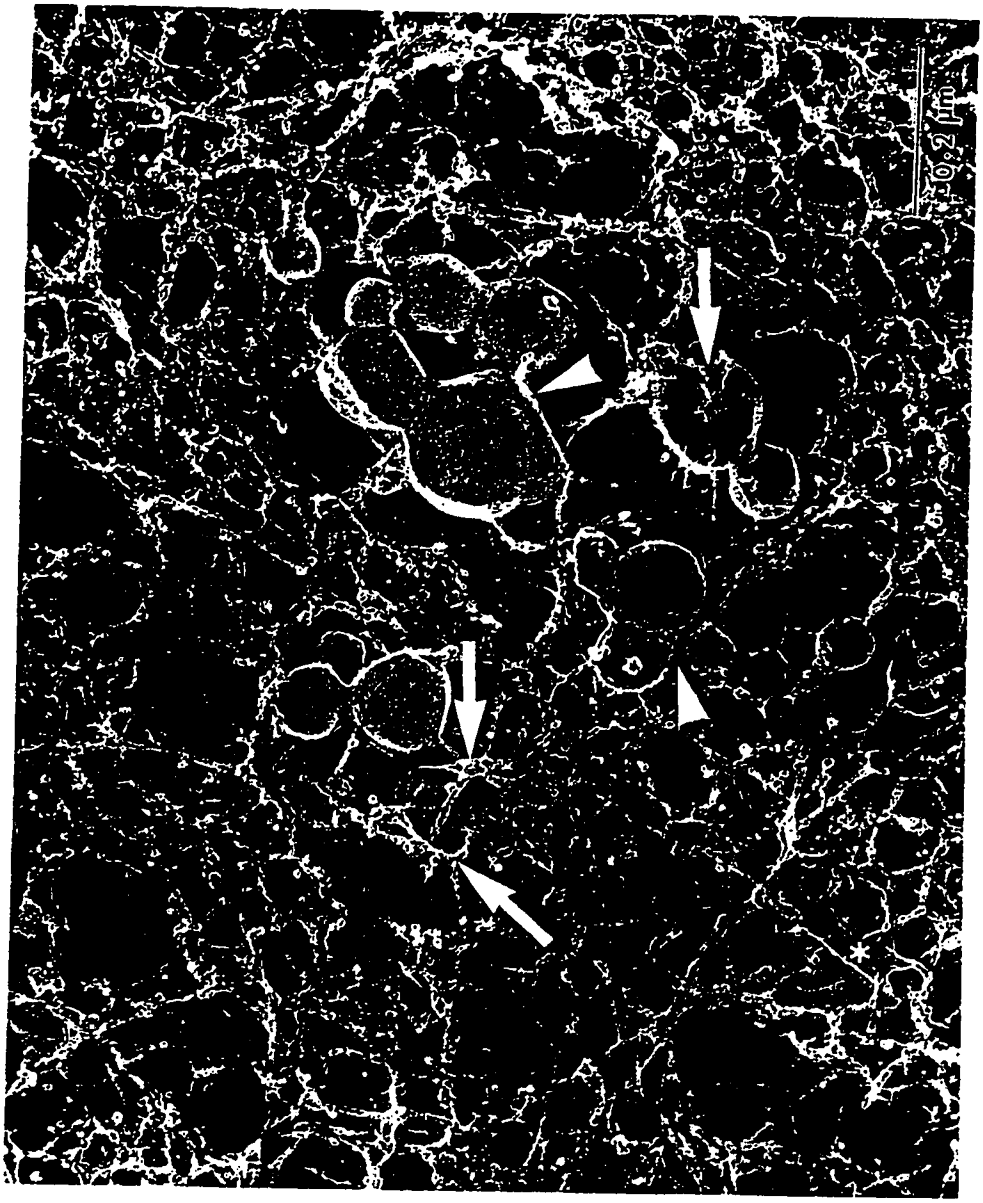

Fig. 7

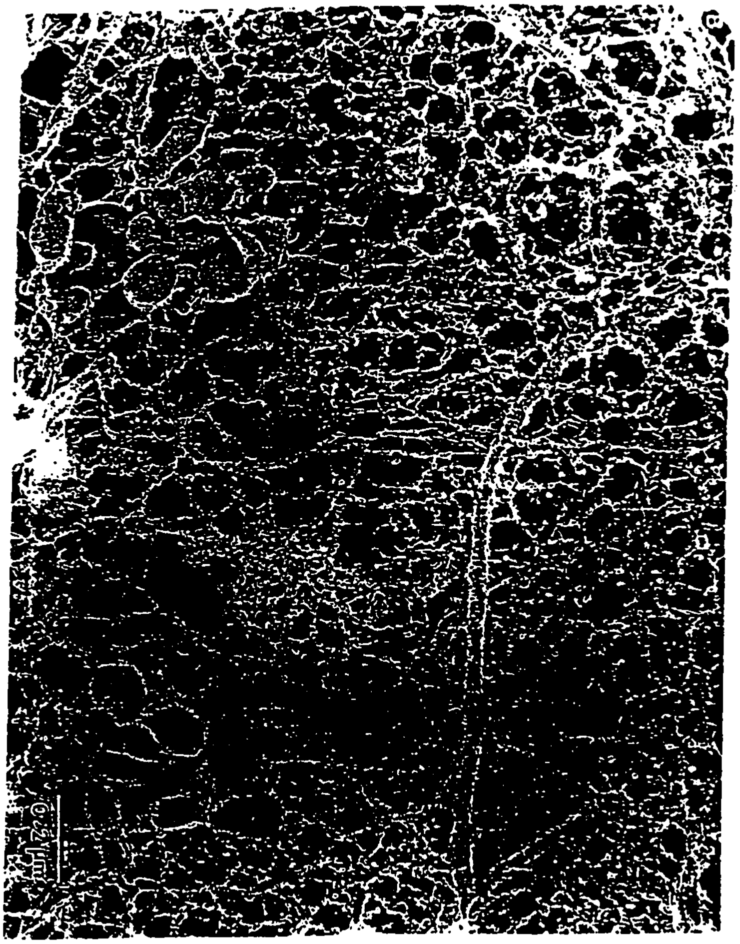

Fig. 8

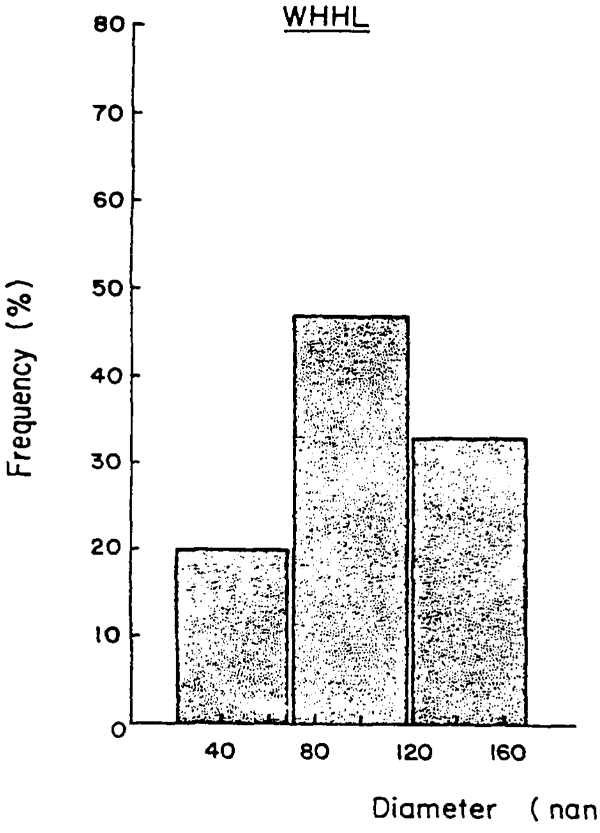
WHHL
Frequency (%)
80
70
60
50
40
30
20
10
0
40
80
120
160
Diameter

Fig. 9a

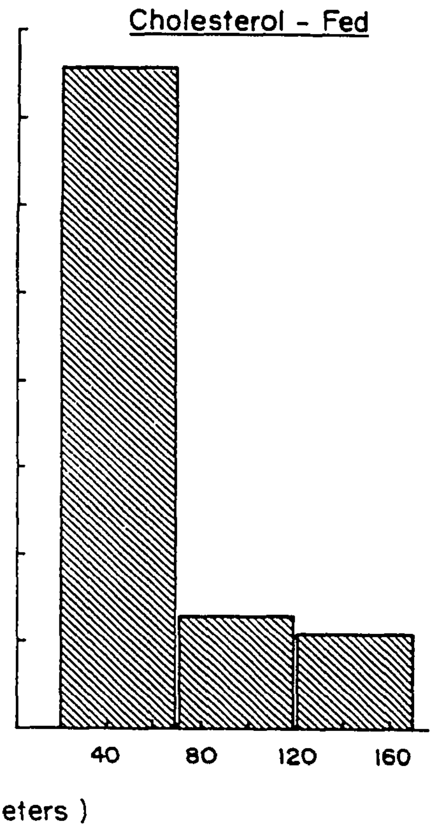
Cholesterol - Fed
40
80
120
160
( nanometers )

Fig. 9b

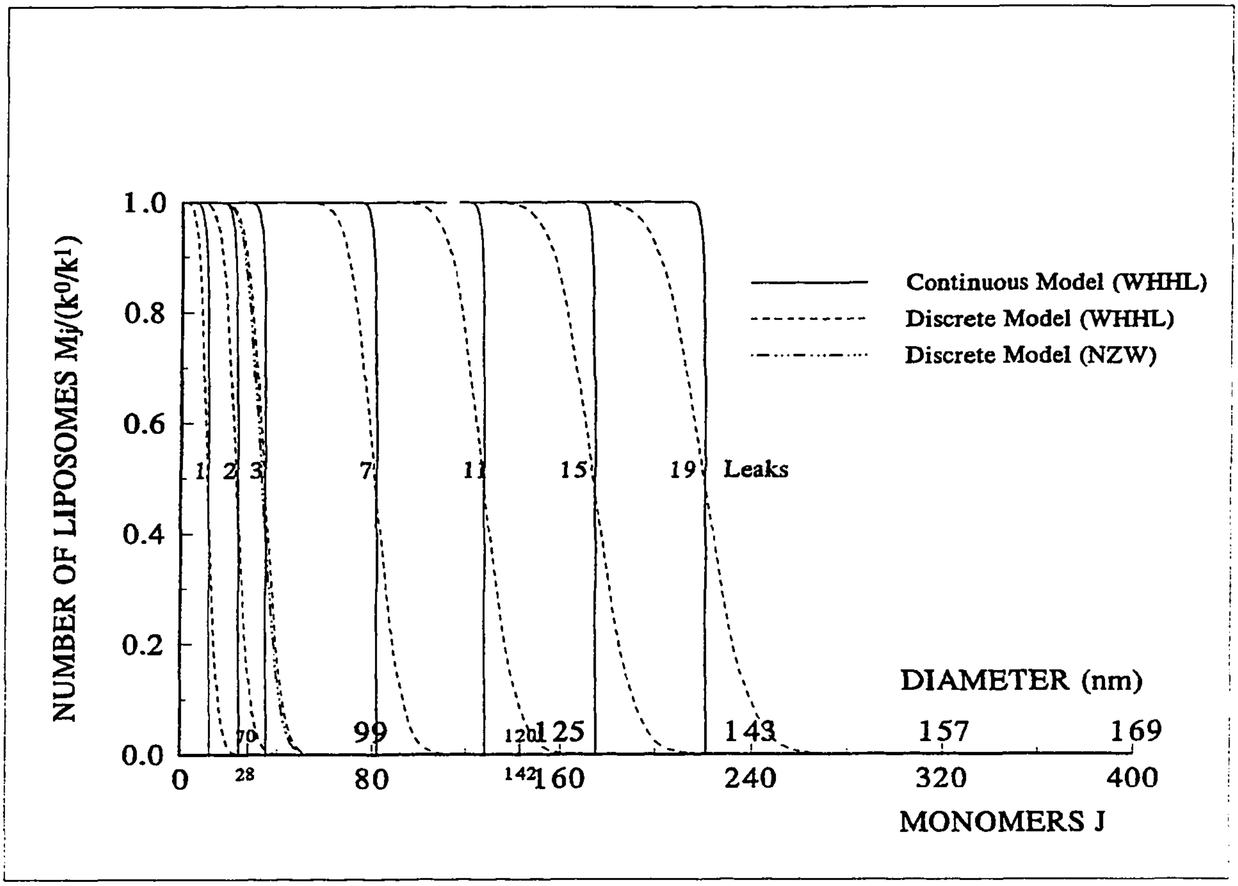
NUMBER OF LIPOSOMES $M_j/(k^0/k^1)$
1.0
0.8
0.6
0.4
0.2
0.0
1
2
3
7
11
15
19
Leaks
Continuous Model (WHHL)
Discrete Model (WHHL)
Discrete Model (NZW)
DIAMETER (nm)
70
99
120
125
143
157
169
0
28
80
142
160
240
320
400
MONOMERS J

Fig. 10

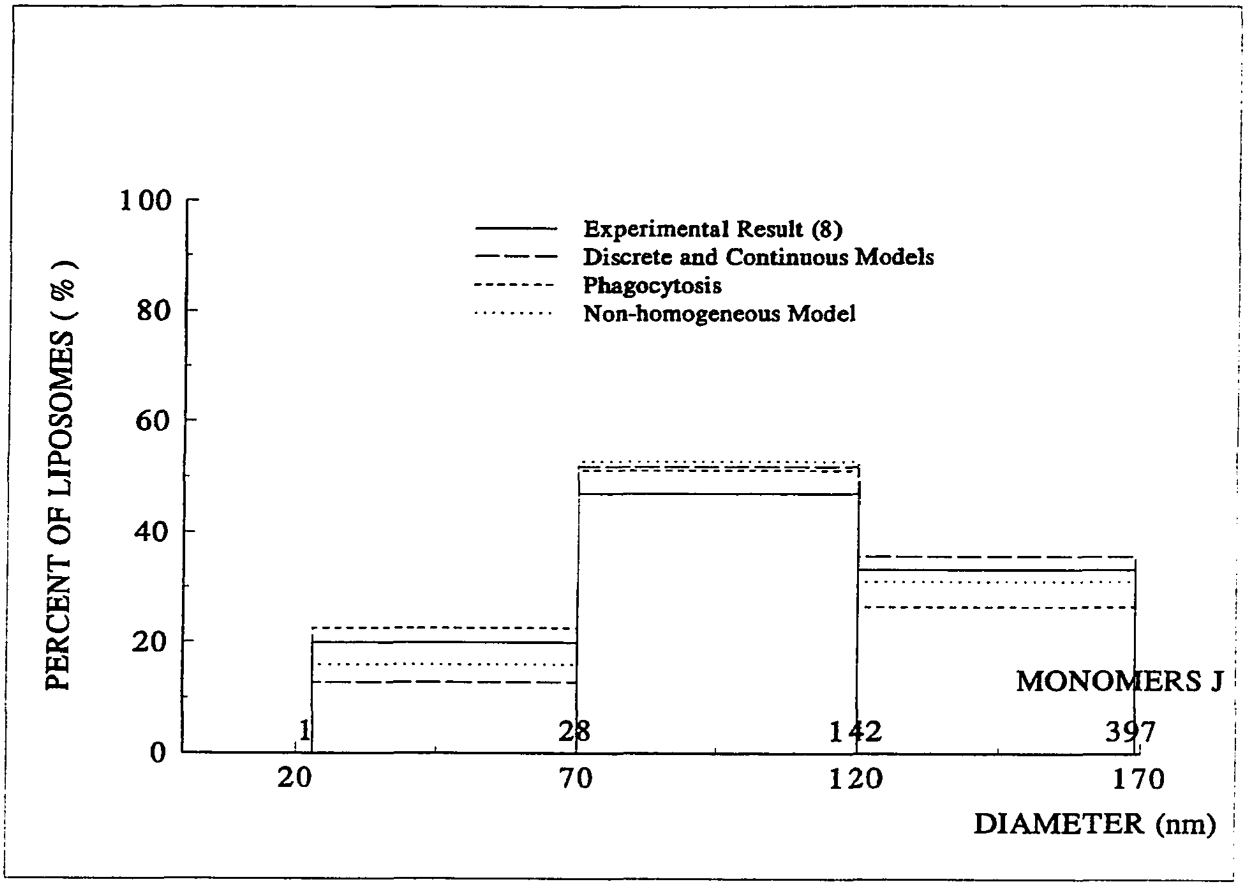
PERCENT OF LIPOSOMES ( % )
100
80
60
40
20
0
Experimental Result (8)
Discrete and Continuous Models
Phagocytosis
Non-homogeneous Model
MONOMERS J
1
28
142
397
20
70
120
170
DIAMETER (nm)

Fig. 11

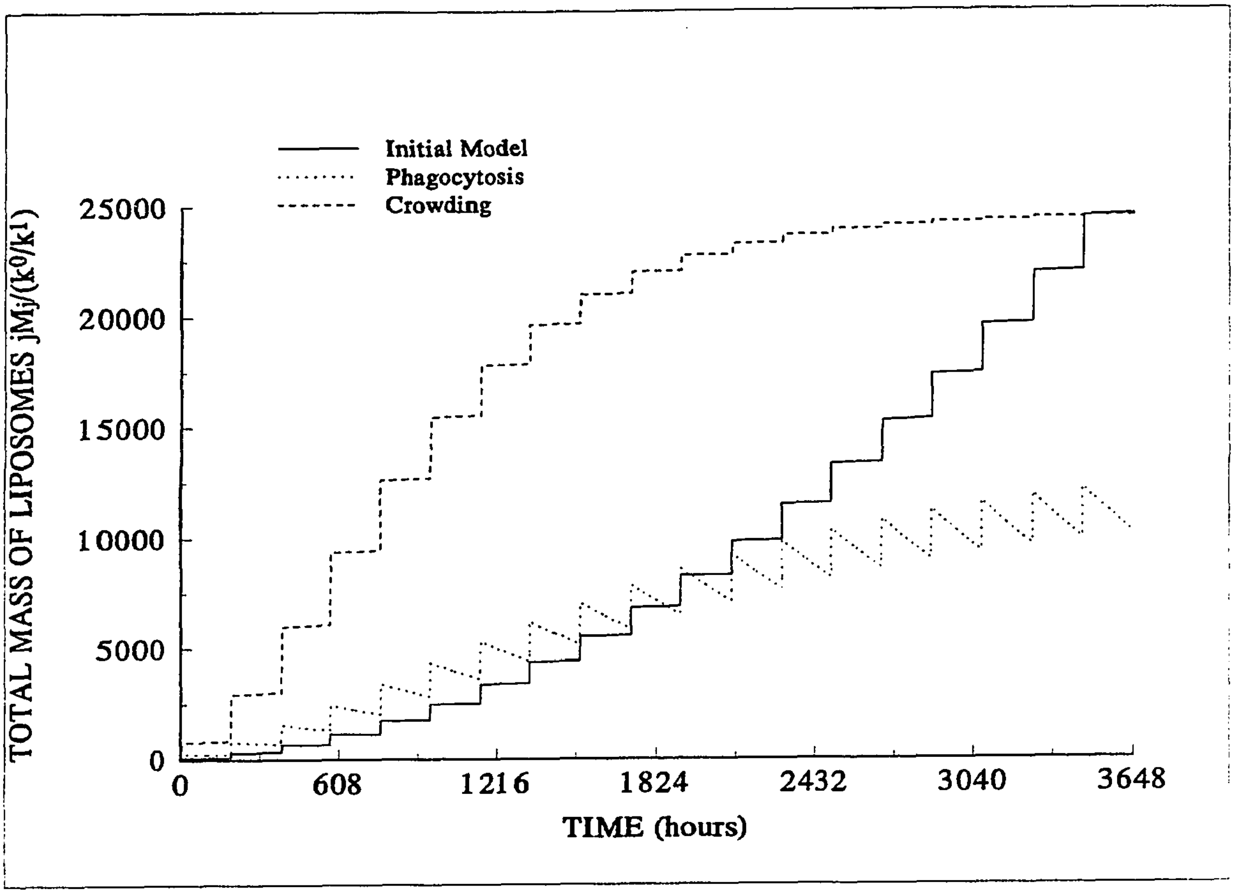
Initial Model
Phagocytosis
Crowding
TOTAL MASS OF LIPOSOMES jMj/(k0/k1)
25000
20000
15000
10000
5000
0
0
608
1216
1824
2432
3040
3648
TIME (hours)

Fig. 12

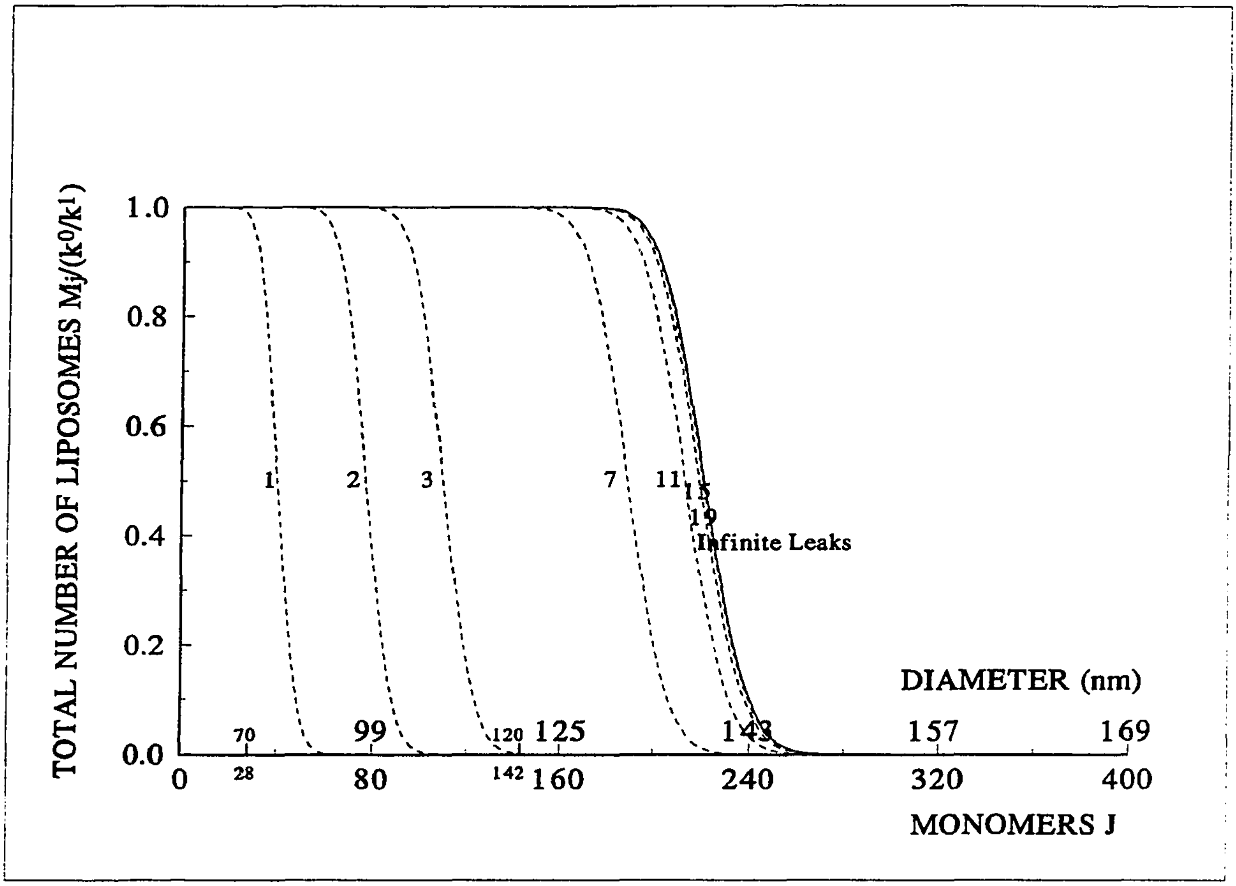
TOTAL NUMBER OF LIPOSOMES Mj/(k0/k1)
1.0
0.8
0.6
0.4
0.2
0.0
1
2
3
7
11
15
19
Infinite Leaks
DIAMETER (nm)
70
99
120
125
143
157
169
0
28
80
142
160
240
320
400
MONOMERS J

Fig. 13

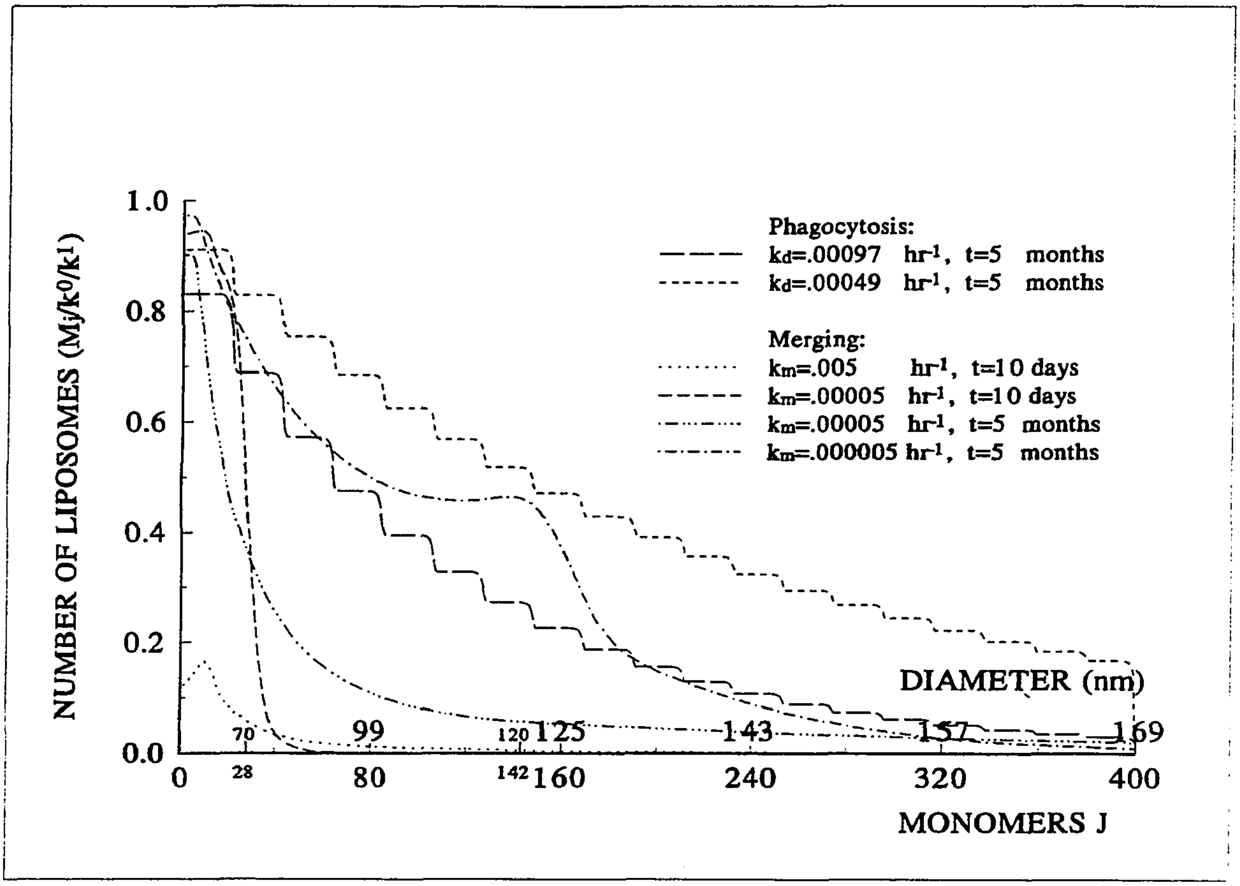
NUMBER OF LIPOSOMES (Mj/k0/k1)
1.0
0.8
0.6
0.4
0.2
0.0
Phagocytosis:
kd=.00097 hr-1, t=5 months
kd=.00049 hr-1, t=5 months
Merging:
km=.005 hr-1, t=10 days
km=.00005 hr-1, t=10 days
km=.00005 hr-1, t=5 months
km=.000005 hr-1, t=5 months
DIAMETER (nm)
70
99
120
125
143
157
169
0
28
80
142
160
240
320
400
MONOMERS J

Fig. 14

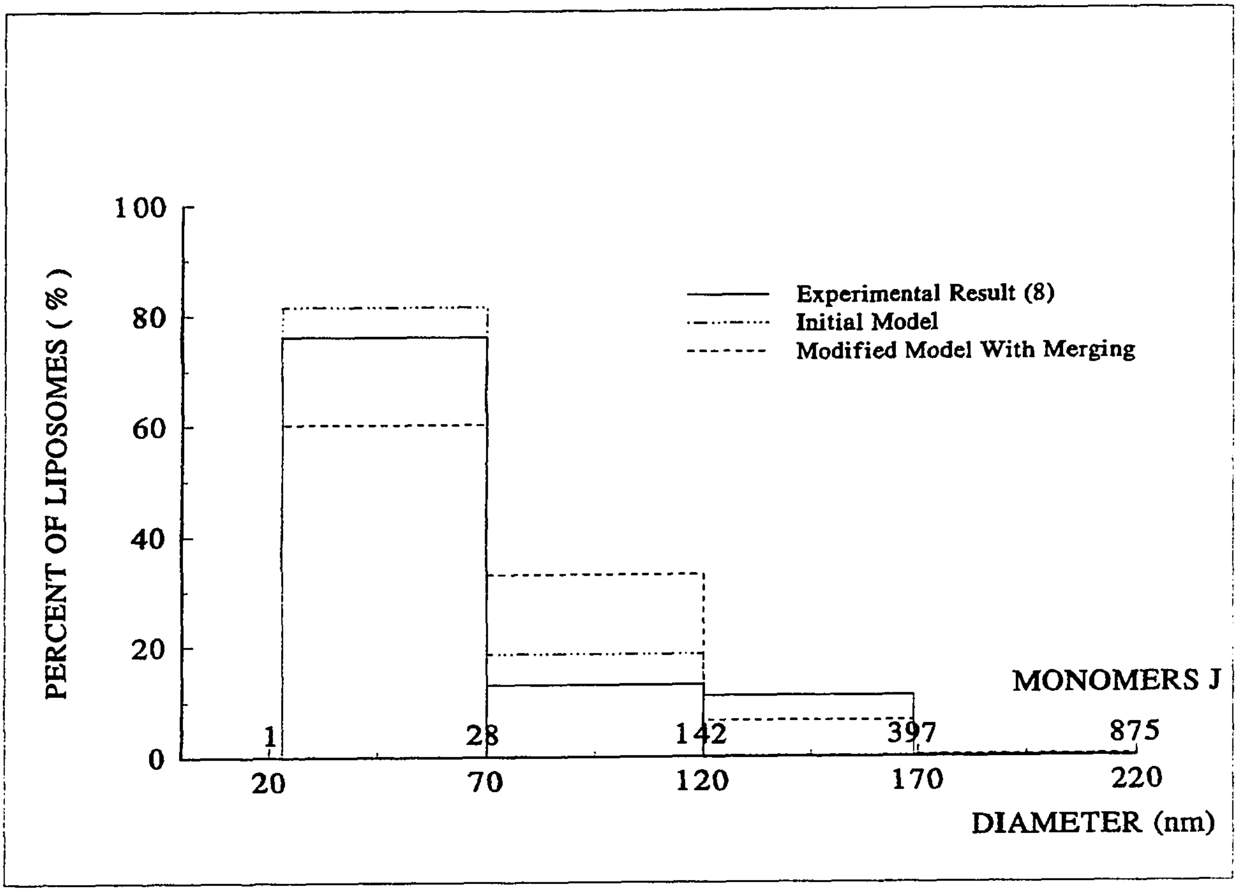
100
80
60
40
20
0
PERCENT OF LIPOSOMES ( % )
Experimental Result (8)
Initial Model
Modified Model With Merging
MONOMERS J
1
28
142
397
875
20
70
120
170
220
DIAMETER (nm)

Fig. 15

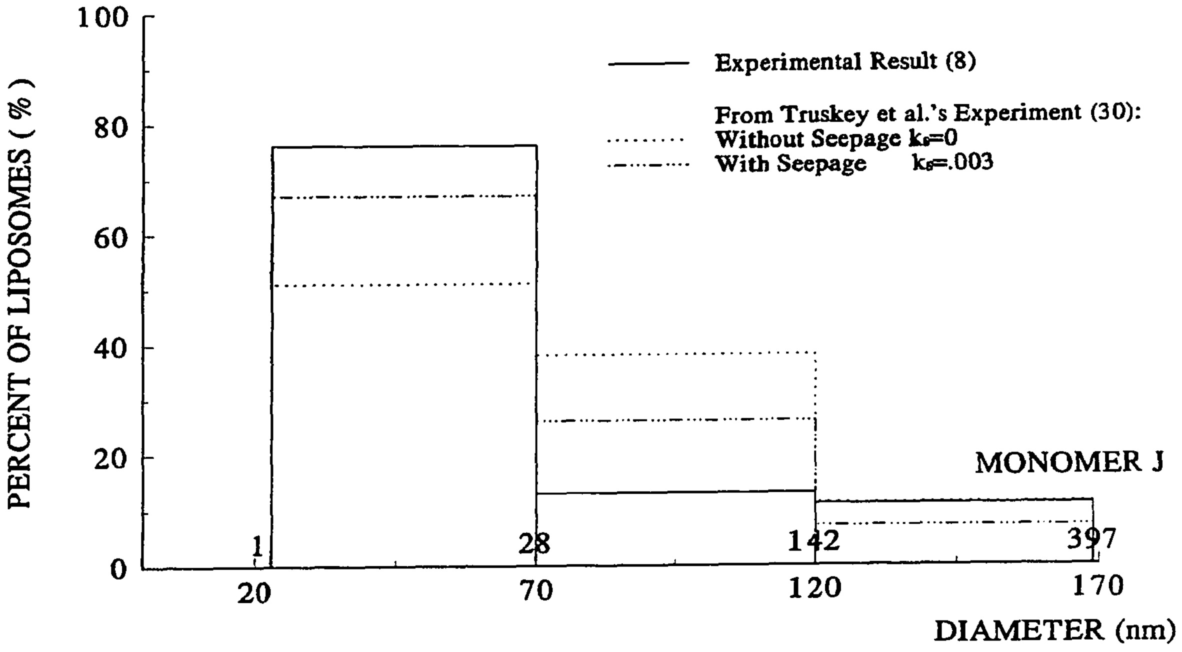

100
80
60
40
20
0
PERCENT OF LIPOSOMES ( % )
Experimental Result (8)
From Truskey et al.'s Experiment (30):
Without Seepage ks=0
With Seepage ks=.003
MONOMER J
1
28
142
397
20
70
120
170
DIAMETER (nm)

Fig. 16

# Part three Liposome formation and growth in heart valves

## VI. Introduction

*Background:* As noted in Chapter I, atherosclerosis is a disease mainly of the large arteries. The prelesion events of atherosclerosis include the lipid transport across the endothelium and accumulation in the arterial intima, followed by monocyte migration from the blood into the arterial intima, their transformation into macrophages, smooth muscle cell proliferation and progression of these two cell types to foam cells [48, 55, 56].

Does atherosclerosis occur in other vessels? The pulmonary artery only is susceptible to atherosclerosis in hypertensive patients [91]. Walton *et al.* [44] has found that cardiac and A/V valve leaflets also showed the evidence of lipid accumulation and lesion formation similar to that commonly associated with atherosclerosis. Under normal conditions, atherosclerosis does not occur in veins. On the other hand, lipid accumulation also appears in veins grafted into arteries as in coronary artery bypass procedures [85,86,87]. Boerboom *et al.* [85] has studied the cholesterol and apolipoprotein-B accumulation by grafts from animal models of graft atherogenesis. They found that distention pressure, i.e., chronic exposure of a venous graft to arterial pressure (which is much higher than native venous pressure), is a primary factor for vein bypass graft degeneration.

Van Beusekom *et al.* [86] studied the vascular wall of saphenous vein aortocoronary bypass grafts after the implantation of a wall stent. They examined the grafts by light microscopy, immunocytochemistry and both scanning and transmission electron microscopy. They found that a large amount of platelets and leukocytes began surrounding the stent wires several days after the implantation. After 3 months, the wires were layered by a new intima, which contained smooth muscle cells in a collagenous matrix. After 6 months, extracellular lipids and cholesterol crystals appeared in the stent wires. In order to confirm lipid concentration is a factor of the atherosclerosis disease in coronary disease. Gotto [87] performed clinical trials by reducing the lipid concentration, and the result showed that lowering lipid reduces coronary disease's risk.

Clearly, lipid can accumulate in locations other than in the large arteries, and the vessel type and the conditions to which it is exposed seem to play important roles in determining the vessel's susceptibility to atherosclerosis. We would like to understand why lipid accumulates in some areas but not in others. Our working hypothesis is: If one can understand how vessel wall structure and pressure conditions affect the mechanical processes by which water and lipoprotein cholesterol are delivered to the interior of vessel walls and by which they accumulate there, then the resulting accumulation differences might shed light on the different observed susceptibilities.

Here we focus on such differences between arteries and valves. We leave the study of other vessels such as veins and vein grafts to future work. At this point we simply concern ourselves with the more restricted question, are the mechanisms of transport and accumulation in the valve and the artery the same, modulo the differences in geometry? The most recent theoretical studies on water and lipid transport in arteries and in valves, each with experimental underpinnings, are Huang *et al.* [12], and Tompkins *et al.* [43], respectively. Huang *et al.* [12] demonstrated that lipid transport in arteries is convection dominated. Tompkins *et al.* [43] only considered one-dimensional diffusional transport without convection in their theoretical model. But, as we shall see, their model cannot account for all of their experimental observations. Therefore, we need to see if the postulated mechanism/principles in arteries, which are in fact convection-dominated, are also consistent with the valve data. These data include Tompkins *et al.*'s [43] trans-leaflet macromolecular concentration profiles. In addition, Frank has generously provided us with numerous freeze-etchings of valves taken from cholesterol-fed rabbits. Below we measure the liposomes in these freeze-etchings and compile a histogram of liposome sizes to compare with predictions of the new two-dimensional, convective-diffusive/ liposome formation and growth theory that we develop below.

*Literature Review:* Valves such as the aortic and the A/V valves are comprised of three leaflets that can close to obstruct or open to allow flow. During the ventricular systolic period when the pressure in ventricularis is higher than that in arteries, the aortic valve is open and blood is pumped from the ventricularis through it to arteries. During the ventricular diastolic period, the pressure in ventricularis is lower than that in arteries, and the aortic valve is closed to avoid blood back flow.

In 1931, Gross *et al.* [62] mapped out the topographic anatomy and histology of valves. They found that the aortic valve is attached to the aortic wall at the annulus fibrosis. The leaflet of the aortic valve consists of two opposing layers of endothelium and an interposed collagen matrix. The surface that is close to ventricularis is called the downstream aspect of the leaflet, and the other, which is close to arteries, is called the upstream aspect. The downstream ventricular face sees a relatively low average pressure while the upstream aortic face is exposed to a relatively high average pressure. The interposed collagen matrix is a backbone of connective tissue with a dense collagenous layer (fibrosa) on the (aortic) face that is exposed to high pressure, and a loose layer (spongiosa) on the (ventricular) face that is exposed to low pressure, with no IEL layer between them. Elastic elements are rare. See figure 20.

In contrast, the subendothelial arterial intima, which abuts only one endothelium, has a sparse matrix structure [8,12,18] that consists of collagen fibers, elastin, microfibrils, proteoglycans that is separated form the media by an internal elastic lamina. Although it shares constituents with the valve, the normal aortic intima is significantly thinner (0.5~1.0μm rabbit, 0.1~0.5μm rat [12]) than valve leaflets (~100μm [43]). Obviously then, both the geometry and the structure of the arterial intima and the valve leaflets are different; consequently, one expects the flow and molecular transport patterns to differ as well.

In 1972, Rasche *et al.* [63] performed *in vivo* transport studies and showed that heart valvular endothelium is more permeable to macromolecules, i.e., albumin and HRP, etc., compared with the arteries. In 1989, Tompkins *et al.* [43] measured LDL and albumin concentrations profiles across the valves using quantitative autoradiography. They theoretically analyzed the macromolecular transport across the valves using a one-dimensional diffusion model without convection and with permeabilities for each endothelium that were fit by comparing the model with the data. The model assumed uniform properties across the valve. Tompkins *et al.* [43] also calculated that endothelial permeability to LDL is much higher in valves than in the aorta in rabbits but that lesions in valves appear slightly later than those in the arteries [40]. Their three parameter model fit the data well in each region they examined, but showed significant parameter variation, and indeed significant transport variation, both between different leaflets and even between different regions of an individual valve leaflet. Clearly a one dimensional model cannot account for this variation in the direction normal to the overall transport, and one must study the detailed trans-endothelial transport mechanism across the endothelia to describe it. We shall experimentally investigate if endothelial leakage in valves is uniform or, as appears to be the case in the artery, is localized to isolated, leaky cells. We shall then look to see if the transport through the interposed region is purely diffusive or convective / diffusive in character; and if the interposed region behaves like a uniform medium due to the absence of an internal elastic laminar or if it shows evidence of having layers with significantly different properties.

*Liposome formation and growth in valves*: Since valve leaflets are essentially all intima, they are much easier to study than arteries. It is easy to isolate an intact valve for *in vitro* preparations following lipid feeding and there is therefore much more data on lipid deposition and liposome size distribution in valves than in arteries (see figures 18 and 19). In early 1970, Walton *et al.* [44], using an immuno-fluorescence technique, found there are lipid packets in the pre-stage of valvular lesion. In 1977, Zahor and Czabanova [42] showed that heart valves in rat frequently accumulate lipids within proliferated extracellular matrix. The topography of the valves shows that early in a 6 month cholesterol diet, most of the rat's lipid streaks and lipid spots occur on the ventricular surface of the mitral valve and on the aortic surface near the region of attachment of the aortic valves. Later the lesions grow thicker.

In 1987, Simionescu and coworkers found [41] that atherosclerotic lesions can form in heart valve leaflets and alter their normal functions. They studied the initiation and development of valvular ultrastructural changes in cholesterol-fed rabbits and found that extracellular lipid deposition in heart valves is a very early event in atherogenesis. It can occur even during the pre-lesional period, with extracellular liposomes appearing within two weeks after the rabbit begins a high cholesterol diet. The numerous extracellular lipid liposomes of various sizes that form in the hyperplastic basal lamina of the valves are similar to those found in early atherosclerotic lesions in the aortic intima. After the second week of the high cholesterol diet, monocytes begin to adhere to and migrate through the endothelium covering the fibrosa region of the valve (see Figure 17). They then migrate through the fibrosa which contains numerous interstitial cells. At about eight weeks into the new diet, interstitial cells progressively accumulate lipid deposits. Consequently, after a long period of this diet, most of the interstitial cells become foam cells and become part of an advanced lesion (24 weeks in hamsters and 12 weeks in rabbits). At this point the marked deformations of the valvular leaflet begins to affect normal valve function. Finally, Frank [40] found that lipid accumulation in extracellular lipid liposomes is much faster in valves than in arteries and that these liposomes are associated with collagen strands within the extracellular matrix (see figure 8).

The first attempt to model the formation of extracellular lipid liposomes in the arterial intima was presented in the first half of this thesis. It consisted of a hierarchy of locally well-stirred kinetic models of the nucleation/polymerization type which easily explained the observed liposome size distribution in genetically hypercholesteremic (WHHL) rabbits. With coupling to either Truskey *et al.*'s experimental or Huang *et al.*'s theoretical curves for the intimal LDL inhomogeneity, it also explained the histograms deriving from the short term feeding experiments.

*What's to come?:* Our goals here are to explore the differences in water and macromolecular transport as well as in extracellular lipid accumulation between valves and arteries. Below, as in the paper [61], we focus exclusively on the first stages of the atherosclerotic process, those of lipid transport and accumulation in the form of extracellular liposomes in cardiac valves. We begin by presenting experiments that characterize the qualitative aspects of this transport, which serve as prerequisites for constructing a sensible model. We show that HRP molecular transport across the valve endothelium is localized to isolated leakage sites associated with individual endothelial cells and that the transport in valves shows a surprising transport pattern in the interposed region. The size of valvular endothelial cell and leakage frequency have been measured by our experiments. Based on these experiments and observations, we shall propose a new water and macromolecular transport model to study LDL convective and diffusive transport in valves. This new model will confirm that convection is dominant near cell leakage sites, as in large arteries. We then combine the new transport model with our liposome model [61] to explain liposome formation and growth in the valves and compare with Frank's experimental results.

## VII. Experiments on transport in valve leaflets

### A. Questions and objectives

As we discussed earlier, the geometry and thus the convective/diffusive pattern in heart valves is completely different from that in arteries. Thus it is necessary to develop a new permeability/filtration model for the valve and to measure the corresponding parameters. The resulting theory, combined with the liposome formation and growth models of Chapters II will yield a theory for the liposome distribution in the valves of rabbits exposed to high serum cholesterol for short and for long times, in analogy with the artery wall theory.

Before we start our theoretical modeling, we need to know answers to the following questions:

1). Do macromolecules such as HRP or LDL cross the valve endothelia uniformly or are there isolated leaks? In the former case, a one-dimensional model, with variation of the dependent variables in the direction normal to the endothelia, would be an appropriate model. In the latter case, even assuming azymuthal symmetry, one would need at least a two-dimensional model, including one independent variable parallel to the endothelium.

2). Is macromolecular transport diffusion or convection dominated? In the former case, one would only need a diffusion equation for the tracer motion, whereas in the latter, a convective-diffusion equation would be necessary. Moreover, if trans-endothelial transport is localized, then the former would result in a spot that would grow continuously in time, whereas in the latter case, one would expect the existence of a limiting size, and this limit would be achieved rather rapidly.

3). Is the assumption that the interposed region between the two endothelial layers is a uniform medium with uniform, isotropic properties a good one? Whether or not this assumption is reasonable will greatly influence the transport pattern. If yes, then transport will mainly be in the direction normal to the endothelia (the "vertical" direction). If trans-endothelial transport turns out to be localized, one would expect a horizontal spread of a short-time macromolecular tracer away from its point of entry that was comparable to its vertical spread. In addition, one would expect a gradual variation in tracer concentration with distance from the endothelium. These features are quite different from the situation in the artery wall. On the other hand, if the answer is no, and if there are layers with different properties, then one might find a very different spot size spread and depth profile.

4). Are the endothelia on both sides of the valve permeable to macromolecules? If so, are they equal? The permeabilities of these layers control the entrance and exit of macromolecules such as LDL into and out of the valve leaflet. As such, if macromolecules can enter, they must also have the possibility to leave. It stands to reason that either both or neither surface will be permeable. These permeabilities will determine the macromolecular diffusion and convection across the endothelial cell layers, which appear in the boundary of our theoretical models. In the preliminary work that we present in this thesis, we shall assume, after showing experimental evidence that the trans-endothelial transport is localized, that the two sides are permeable and that their characteristics, i.e., leakage duration, resemble those of the artery wall.

5). Is this true that macromolecular transport across the endothelial cells is co-localized with leakage sites? This is critical to our modeling. It links the transport supply of LDL to the formation and growth of liposomes. If the answer is yes, after LDL enters the intima, the majority of it transports out of the valve leaflet, but a small fraction binds to extracellular matrix and forms liposomes. We shall work under the assumption that this is true. We shall then test it by seeing if the combined transport and reaction model, using the liposome formation and growth models from the artery wall *with the same parameter values*, can predict the liposome size distributions which we shall extract from the unpublished data provided us by J. Frank.

In order to explore the questions above, we performed the following experiments: Chuang *et al.* [7] and Stemmerman *et al.* [38] used HRP as a tracer to identify leakage sites in the study of the macromolecular transport across arterial endothelia in rats. Therefore, we performed the experiments in valves using the same technique. The reason for using HRP tracer is that it is much easier to obtain, to work with and is much cheaper than labeled LDL. If HRP transport is localized, then LDL transport is most likely localized as well since macromolecule LDL is larger (a factor of three in diameter) than HRP. On the other hand, if it is not localized, then we can conclude nothing about the larger molecule's transport. Thus, to address question 1, we injected HRP into a rat for a very short circulation time (one minute) and looked at the valve leaflets *en face* with light microscopy to see if the HRP infiltration into the wall was uniform or localized in isolated spots. In addition, we looked to see if the infiltration occurred on one or both sides of the valve leaflet (question 4). Should the results show localized leakage, we would then repeat this experiment for various lengths of time to get an idea of the spot spread with time.

To address question 2, A. Huang, our collaborator from the Institute of Biomedical Science of the Academia Sinica in Taipei, injected a rat with HRP tracer for a circulation time of four minutes. She then examined transverse sections under the electronic microscope and observed the transendothelial HRP profile. Finally, Frank and coworkers did rapid freezing/rotary shadow etching studies of rabbit valve leaflets for rabbits on a high cholesterol diet for various lengths of time. Below we shall review in detail the experimental procedures used in each of these experiments.

## B. Experimental Methods

B.1 *Huang's experimental methods.* Huang [67], from the Institute for Biomedical Science of the Academia Sinica in Taiwan, used Sprague-Dawley rats (about 300 gm) for her experiments. She anaesthetized the rats with pentobarbital (30 mg/kg intraperitoneally). She dissected and cannulated the right femoral artery and the left femoral vein with needle catheters. Then HRP (Sigma Type II dissolved in 0.5 ml of saline and at a dosage level of 10 mg/100gm body weight) was injected into the femoral vein of the rat. After 4 minutes, the rat was sacrificed by an overdose of pentobarbital and circulation was terminated. In order to prevent blood coagulation, ten seconds before the termination of each circulation period, 0.2 ml of heparin (5000 USP units/ml; China Chemical & Pharmaceutical, Taipei, Republic of China) was injected through the femoral vein. A catheter was placed in the carotid artery and connected to a pressure reservoir in order to keep a physiologic pressure of 100 mm Hg during the perfusion. The perfusion with a heparinized saline solution continued until clear fluid flowed from the egress site. The perfusion took about 10 seconds. Then the perfusate was switched to 60 ml of 2% glutaraldehyde for preliminary fixation. The valves were then cut from the heart. She pinned the cone-shaped valve onto a dental wax plate with the endothelial cell layers parallel to the wax plate and then incubated them for 1 hour at $37^0$ C in 30 ml of the reaction solution (0.05M Tris-HCL buffer, pH 7.4, containing 45 mg of 3.3' - diaminobenzidine tetrahydrochloride and 20 µl of 30% $H_2O_2$).

The valvular specimens were then processed for electron microscopic examination. Huang dissected them into small pieces, further fixed them in a 2% glutaraldehyde solution (in 0.1M sodium caco-dylate buffer, pH 7.4) for 30 minutes, and then used Karnovsky's method (66) for contrast enhancement with a mixture of 15 tannic acid and 1.5% potassium ferrocyanate (in 0.1 M sodium cacodylate buffer, pH 7.4) for 1 hour. Next, after rinsing the specimens, she postfixed them in 1 % osmium tetroxide (in 0.1 M sodium cacodylate buffer, pH 7.4) for 90 minutes. Then, the specimens were washed with distilled water, stained with 2% aqueous solution of uranyl acetate at 60° C for 15 hours, dehydrated in a graded series of ethanol, infiltrated by propylene oxide and embedded in Epon 812. Finally, the specimens were properly oriented during embedding so as to be cut perpendicularly to the long axis of the vessel. Ribbons of such ultra-thin sections with the reflection color of silver or pale gold were cut with a diamond knife on an ultramicrotome (Reichert-Jung, Vienna , Austria) and collected on Formvar-coated single-slot grids without post-staining. As a result, more than one specimen blocks was examined in the JEM 1200EX electron microscope (JEOL, Tokyo, Japan) for each set of injections. The concentration distribution of HRP was observed in the inter-endothelial cleft with a densitometer (IRIS video-digitizer, Boulder, Colorado).

B.2 *Yin's experimental methods.* We used Sprague-Dawley rats for our experiments. We weighed the rats (about 300mg) and then anesthetized them according to their weight using 5% chloral hydrate (3~5 ml / per rat 300 ~ 500 g weight). We then removed the hair near the region of the right femoral vein.

After the rat was ready, we prepared a 3,3'-diaminobenzidine (DAB) (from Sigma Chemical Company) solution as follows: We began by making a 0.3M Tris [hydroxymethyl] aminomethane (from Sigma Chemical Company) solution and adding 5 ml of this Tris solution to a 50 ml container with 25 ml $H_2O$. Next, we gently added 0.045gm of DAB to the previous solution and stirred until completely dissolved. Finally, we added 20 micro-liter of 30% Hydrogen peroxide ($H_2O_2$) and adjusted the pH of the solution to 7.0 with a 1.0 ml/L HCL solution.

The next step was the valve dissection. We cannulated the right femoral vein and injected 0.2 ml of heparin prior to a slow injection of 4 ml of HRP into the right femoral vein. After circulation times of either 20 seconds, 1 minute, 2 minutes or 4 minutes, we sacrificed the rats with an overdose of pentobarbital intravenously and opened the heart immediately. The heart was perfused first at room temperature with a heparinized saline solution (PBS), then the perfusate was switched to 10% formaldehyde and allowed to flow over night. Finally, we carefully dissected out the aortic valves under a micro-dissection apparatus and washed completely with PBS solution.

The final steps were the staining and subsequent microscopic examination. We first tested the staining time and found that the optimal time for staining for valve endothelial cells with Harris' Hematoxylin (from Sigma Chemical Company) was about 45 seconds. We then stained these valve samples accordingly, immediately flushed them with PBS solution for three times (10 minutes each time) and mounted them onto a glass slide and cover-slipped for microscopic examination. The pictures were taken under the microscope and printed out.

B.3 *Frank et al.*'s *experimental methods*. Frank *et al.* [40] performed an ultra-rapid freezing and rotary shadow freeze-etching technique that provided a clear picture of liposomes of various sizes in rabbit aortic valves. It was from these pictures that we measure the detailed valve matrix structure for the transport theory and the liposome size distribution to test the combined transport/liposome accumulation model below. For the sake of completeness, we reproduce their experimental methods section below.

*Freeze Fracture Experiments:* New Zealand White rabbits were maintained on a high cholesterol chow diet for a certain number of days (i.e., 29 days). The rabbit was killed by an overdose of pentobarbital. The heart was removed immediately and put into a dissection dish with oxygenated physiological Hanks' Trizma maleate buffer (mmol/L: NaCl 133, KCL 3.6 $CaCl_2{\cdot}2H_2O$ 1.0, Trizma maleate 5.0, dextrose 16, pH 7.25, 27°C). The aortic valves were dissected from the left ventricle. The valves were incubated either with 25μm/mL LDL-gold conjugated in PBS/$NaHCO_3$ buffer supplemented with 4.5mg/mL freshly thawed human lipoprotein-deficient serum for 4 hours or with 300μg/mL LDL for 2 hours in a 5% $CO_2$ incubator. Then, oxygenated buffer was used to rinse the valves. Tissue pieces were cut from the valves for ultra-rapidly freeze etching.

Each frozen piece of valve was fractured very superficially (about 10μm) to insure that the fracture plane was within the area of good freezing. Fracturing was performed at -150°C and a vacuum of $1x10^{-7}$ mm Hg. During the deep etching period, the specimens were maintained at -110°C for 3 minutes, followed by 3 minutes at -100°C and 2 minutes at -95°C. The fractured and etched surface of the specimen was rotary replicated. It was then digested from the replica with household bleach, rinsed in distilled water, and put onto Formvar-coated grids.

## C. Experimental Results

This section presents experimental results found by A. Huang and Y. Yin together with the questions that motivated them. These results will be the foundation of our new theoretical models that will adequately explain macromolecular transport and liposome formation and growth in valves.

*C.1. Yin's Experiment.* Let us begin with the measurement of the average endothelial cell radius, the length scale by which we will be non-dimensionalizing our models. Figure 23 shows an *en face* view of the rat valve endothelium for a rat that was sacrificed after 30 seconds of HRP circulation. The black spots are Harris' Hematoxylin staining products for endothelial cells, which represent the nuclei of the endothelial cells. The brown areas are the HRP tracer's DAB reaction products. Since the endothelial cell mono-layer tiles the surface of the valve (approximately 1 mm $^2$), one can estimate the average area per endothelial cell area from this picture as the total area of the picture divided by the total number of nucleus spots. If one assumes that each endothelial cell is roughly circular (even though circles do not tile the plane), the effective radius ($R_1$) of the endothelial cell in our experiments becomes about 11.71μm, which is similar in size to that (15μm) in arteries.

Recall that our first question that requires experimental investigation were whether macromolecular leakage across the valve endothelium is uniform or localized to the inter-endothelial cell junctions around isolated endothelial cells. In the case that the transport turns out to be localized in this way, it would be useful to see how the spot generated by a tracer traversing such an isolated leak grows with time. Such a measurement would shed light on potential faults in our assumptions as to the detailed structure of the valve and, at the same time, provide a valuable quantitative test for our transport models to reproduce.

Again we appeal to the *en face* view of a rat endothelium from an animal that had been sacrificed 30 seconds after HRP injection. We chose 30 seconds because HRP is significantly smaller than LDL and, in fact, leaks through even normal junctions in rat aorta that are impermeable to LDL after about 5 minutes. However, at short times, the HRP only penetrates the larger junctions. The experiments show that the brown areas only appear in very few, localized parts of the valve endothelium and not uniformly everywhere. This indicates that HRP transports across the endothelial cell layer appears to be localized. This suggests us that, as in the aorta, we should use localized leakage model instead of uniform leak model to study the macromolecular transport in valves. This distinction is significant, because the resulting model must have at least two independent spatial variables, the distances z into the valve and r radially from the center of the localized leak, rather than simply z, with no variation in r. This additional dimension complicates the model substantially, but appears to be indicated by experiment.

Having established the locality of macromolecular leakage, we now estimate the endothelial cell leakage frequency. First we measured the total number of the leakage sites in an entire valve face and the total area of the face. The average area per leak is the total area of the valve divided by the total number of leaks it contains. As in the artery work, we again assume that the endothelial cells are effectively circular. Then the radius of the periodic unit ($\xi$) is 624 μm. If we denote leakage frequency as $\Phi$, the relationship $\Phi=R_1^2/\xi^2$ gives the leakage frequency $\Phi=.00035$.

We next repeat the above-mentioned experiment for different HRP circulation times in order to observe the average growth rate of the HRP spot. We located the leakage areas in *en face* examination of rat endothelia taken from rats sacrificed after different circulation times (0.5, 1, 2, 4 minutes) and measured the area of the brown spot for each of them. Figure 31 plots the results with solid circular symbols. The abscissa represents the HRP circulation time and the ordinate represents the HRP spot size. Since the valve does not appear to have an internal elastic laminar (IEL) and a matrix that appears to be essentially isotropic in a region of many microns beneath the endothelium, one would expect a more-or-less comparable rate of spreading in the r and z directions inside the valve. That is, one would expect the growth rate of the spot in the radial direction, i.e., as observed form *en face* examination, to be significantly slower than that in the aorta, which has an IEL that apparently acts as a barrier to transport in the z direction and has a thin sub-endothelial intima that has a much sparser structure than the deeper and much thicker medial layer. Together with the convection-dominance of the transendothelial macro-molecular transport, this line of argument leads to the conclusion that transport in the aorta encounters vastly less resistance in the r direction than in the z direction. It follows that one expects extremely fast spot growth in the aorta, and much more lethargic growth in the valve.

In contrast to these expectations, however, Fig. 23 shows that the HRP spots in the valve grow only about 23% slower than in the aorta. This entirely unexpected result was repeated in 10 rats, and seems to be a trustworthy result. Since the growth rates of the spots in the valve and in the artery only differ quantitatively and not qualitatively as one would have expected, it is tempting to suspect that the transport mechanisms in the valve and in the aorta are similar. But, other than postulating that they are both convection-dominated, how can they be similar, since, as noted, the valve apparently lacks a sparse sub-endothelial intima and an IEL? In our initial model (Section VIIIC) we shall quantitatively test if simply assuming convection dominance can account for the measured spot size growth. If not, then this puzzle might seem to suggest that despite the absence of an IEL, a thin, sparse, low resistance layer may indeed exist in the sub-endothelial domain. As such, we have a motivation for the experiment of Huang described below.

*C.2. Huang's experiment.* The goal of this experiment is to examine directly if the HRP spread into the interior of the valve proceeds at isotropically. To do this, we examine a rat valve under the more discerning EM in cross section. This allows us to assess both the r and the z spread simultaneously and to compare them. If the rate of spread in both of these directions is comparable, then one would expect to see a gradual decrease of tracer intensity as a function of distance from the leak of comparable magnitude in both the radial and depthwise directions. Figure 21 are the electron micrographs of the transverse sections of the valves of rats sacrificed after 4 minutes of HRP circulation. In the figure. the lumen is on the top and the endothelial cells are aligned horizontally. Under the endothelial cells, there are areas labeled by HRP tracer (the dark areas), collagen fibers and interstitial cells. The dark areas appear directly under the endothelial cells and in the junctions between the endothelial cells. This latter fact indicates that the HRP tracer transports across the endothelial cell layer through the said junctions.

Furthermore, it is interesting that the tracer is evident in these dark areas primarily located in right underneath of the endothelium of the valve. One only observes a very thin layer of such dark areas, followed by an abrupt change in color to a much lower tracer concentration. That is, one finds these dark areas directly beneath, i.e., within a few hundred nanometers of the endothelium, and there seems to be a sharp boundary beneath which the tracer is no longer evident. There are at least two possible explanations for this observation. First, there is always a level of detectability in the DAB reaction which is dependent on the exact conditions used in conducting the DAB reaction. As such, the darkness would need to be internally calibrated in order to translate darkness into concentration. In addition, the development can lead to a rather narrow concentration range, over which the tracer product changes intensity from almost black to almost white (67). That is, there may be a detection threshold that is rather sharp, and thus would explain the thin dark layer as simply being the region having concentration above this threshold; the white area close to the abrupt transition might have concentration that is only slightly lower, and thus the true concentration profile might indeed be continuous rather than abrupt. Arguing against this interpretation is the fact that the darkness does seem to persist in the r direction for a rather long distance. Thus if the falloff in concentration were comparable in the two directions, one would expect a dipping below this threshold in the r direction close to the leak as well.

A second interpretation is one that would be consistent with the suggestion at the end of the discussion of Yin's experiments above. It would propose that, after the HRP transports across the endothelium, it indeed spreads primarily in the direction parallel to the endothelial layer in the tiny area which is closest to the endothelial cell layer. The reason for this might be the presence of a thin, sparse, immediately sub-endothelial layer with very little resistance to flow. The reason why it has not been observed previously might be because of the absence of an IEL demarcating it and because it is many orders of magnitude thinner than the adjacent denser layers. One might call this tiny area the "thin layer of the valve" and the other region farther away from this tiny area the "middle layer of the valve."

If there is indeed such a thin layer, Huang's EM pictures would allow one to estimate its size by measuring the depth of the dark layer in the EM. We say estimate because of the problem with the threshold of detectability of the DAB reaction discussed above. With this in mind, the thin layer of the valve is about 200nm thick. This dimension is in the same order as the thickness of the arterial intima in the normal aorta (100~500nm rats [12]). Again, despite the absence of an IEL in valves, it appears that HRP still transports primarily in the thin layer of valves in a manner similar to that in the sub-endothelial intima of arteries. This suggests that the matrixes for the thin layer and the middle layer may be very different and that this mismatch in both matrix structures and thicknesses of adjacent layers may in fact be much more significant in dictating the overall flow pattern than the presence or absence of an IEL.

Below we shall first investigate if a single-layer model for the interposed layer can account for the spot size growth with HRP circulation time. If it cannot, we shall then construct a thin-thick layer model similar in spirit, but different in geometry, to the one in the aorta work. We shall then test the feasibility of such a model by seeing if it can explain all of the above data. If that turns out to indeed be the case, we shall calculate the change in transport parameters that would result from the use of LDL rather than HRP as the tracer (LDL is significantly larger). Using these values, we shall solve the flow model and the subsequent convective-diffusion equations for both LDL and HRP tracers. We will compare the HRP results with the spot size data above. We shall then combine the LDL convection-diffusion results with the liposome formation and growth models of the first half of this thesis (with the same rate parameter values) to predict liposome size distributions in valves for given feeding times. These results can then be compared with the data garnered from Frank's measurements, reported on in Section VIIC3. If all of these comparisons turn out to be successful, we shall then propose, but not carry out, future experiments to directly test whether such a sparse layer actually exists and to observe it.

C.3. *Experimental Liposome Histogram.* J. Frank has generously provided us with her unpublished experimental freeze fracture pictures. Figures 18 and 19 are examples of such visualizations. Based on her experimental data, we manually counted the number of liposomes for each of the range of liposome sizes, i.e., diameters between 23nm and 70nm, 70nm and 120nm, 120nm and 170nm, 170nm and 220nm, etc. These measurements determine the liposome histogram shown by the solid curve in Fig. 35. This figure is similar to the one given by Frank and Fogelman [8] from the arteries of rabbits that have been on a high cholesterol diet for short feeding times, but the current histogram contains liposomes that are larger (about 0.30% with diameters larger than 170nm) than any of those observed in the artery work. We shall develop a new theoretical model for valvular filtration and macromolecular transport and combine the new model with the liposome model used in the arteries (Chapter VIIID) to explain the valvular liposome histogram.

## VIII. Theoretical modeling of water and macromolecular transport in the valve leaflet.

### A. Basic geometry.

Let us now construct a theory for the filtration flow through the valve. We model the valve as two parallel endothelia separated by an interposed media of one or more layers, each of which is a uniform, isotropic, homogeneous medium. Fluid and macromolecules enter from the upstream (aortic valve: aortic) side, progress through the media and exist through the downstream (aortic valve: ventricular) endothelium. There are two issues that we need to clarify before proceeding to write down the model. The first is whether the macromolecules such as HRP or LDL cross the valve endothelium uniformly or, as appears to be the case in the aorta, via localized cellular leaks. Our short time HRP experiments that showed localized brown spots in *en face* light observation strongly suggest that the latter is indeed the case. We presume this and thus postulate a two-dimensional model. The second issue is how to describe the interposed layer as an effective medium with effective transport parameters.

Consider a valve leaflet, which is approximately 1mm$^2$ in area. In the Experimental Results Section, we noted that each valve face has approximately 2300 cells and appears to have 0-2 or, on average, one leaky cell at any given time. Thus, let the face in question has a single leaky cell which, for purposes of axisymmetry, we place exactly at its center. Should the model be successful, we can then examine the effects of having this leak at an off-center position. We again simplify the geometry by assuming that the face is now axisymmetric about the central leaky cell, as shown in Figure 24b. We shall detail below the Darcy and continuity equations for the water flow and the convective-diffusion equation for the solute flow, along with the appropriate boundary conditions on the two endothelial surfaces in the next section. However, before doing so, we develop the *ab initio* theory described in [12] that Huang *et al.* use to construct transport parameters, such as the Darcy permeability of the interposed media and the solute diffusivities, based on the fiber matrix structure of this region, as determined from the freeze etchings. The exposition below follows theirs very closely, since it is essentially the same theory.

### B. Fiber matrix model for the thin layer

As in the arterial subendothelial intima, the layer interposed between the two endothelia in the valve is largely comprised of proteoglycan and collagen fibers (see figure 22). Frank provided us clear freeze fracture pictures of the ultra-structure of this layer, and this allows us to measure the dimensions of the proteoglycan and collagen fiber constituents. We then estimate the permeability $K_p$ and solute diffusivisity $D_f$ by using these measurements in a random matrix theory for these parameters [78-81]. We assume that the resistance comes from the proteoglycan and collagen fibers.

From Frank's photos, we find that the proteoglycan matrix has a typical spacing of 35~45 nm. The proteoglycan core protein diameter is 3.5~5 nm, as is its central filament (3.5~5 nm). Compared with any of these proteoglycan components, the collagen is much thicker, and therefore, its length per unit volume is much smaller. So we consider the proteoglycans and collagen separately in this matrix model. and assume that their effects add like capacitors in series, i.e.,

$$\frac{1}{K_{p(total)}}=\frac{1}{K_{p(PG)}}+\frac{1}{K_{p(CG)}} \tag{15}$$

Levick [78] calculated $K_{p(PG)}$ previously as the permeability of the proteoglycan matrix with the collagen included simply via an excluded volume factor, and $K_{p(cG)}$ similarly for the collagen. In order to avoid *ad hoc* geometric corrections such as excluded volume, we follow Huang *et al.* [12] so that our $K_{p(PG)}$ is the permeability of a pure proteoglycan matrix without excluded volume correction.

First we calculate $K_{p(PG)}$ , which we simply denote as $K_p$. Frank's pictures (Figures 18,19) show that there are many more proteoglycan than collagen fibers, and proteoglycan fibers appear randomly arranged. Therefore, $K_p$ should follow the Carman-Kozeny expression [79-81] with a random matrix comprised of fibers of a single radius a with a void volume ε and the Kozeny constant G.

$$K_p = \frac{a^2\varepsilon^3}{4G(1-\varepsilon)^2} \tag{16}$$

The Kozeny constant G is a rapidly increasing function of the void volume ε when the void volume is high (ε>0.9). Happel and Brenner [82] found the following relation between G and ε for the beds of electrically neutral and uniform cylindrical fibers:

If the flow is parallel to the cylinders, $G_p$ becomes

$$G_p = \frac{2\varepsilon^3}{(1-\varepsilon)[2\ln(\frac{1}{1-\varepsilon}) - 3 + 4(1-\varepsilon) - (1-\varepsilon)^2} \tag{17a}$$

If the flow is perpendicular to the cylinders, $G_r$ becomes

$$G_r = \frac{2\varepsilon^3}{(1-\varepsilon)[\ln(\frac{1}{1-\varepsilon}) - \frac{1-(1-\varepsilon)^2}{1+(1-\varepsilon)^2}]} \tag{17b}$$

If the cylinders are oriented randomly in three dimensions, the Kozeny constant G is

$$G = \frac{2}{3}G_r + \frac{1}{3}G_p \tag{17c}$$

We consider a proteoglycan core protein PCP with an average fiber spacing δ aligned in a hexagonal array, cylinders (radius ξ) of which we take to be periodic in space, as in Figure 22. It can be shown that the total fiber number N in the areas $\pi\xi^2$ for this geometry is

$$N = 1 + 3n(n+1) \tag{18}$$

where n=[ξ/δ]. Since ξ is much larger than δ, N is close to $3n^3$. One can estimate the volume fraction of proteoglycans if one assumes that the core proteins extend across the entire layer thickness and adds an additional length for the central filaments themselves. Before doing this, one needs to define an effective radius $r^*$, since the proteoglycan constituents have non-uniform thicknesses. Comparison of the fiber spacing (35~45nm) measured from Frank's pictures and the dimensions of the fibers in the freeze etching with data from cartilage condroitan sulfate proteoglycan (CSPG) [82] suggests that the interposed layer in the valves appear to have proteoglycan aggregates arranged along a central filament. Aggregates generally consist of proteoglycan monomers (comprised of a proteoglycan core protein (PCP, radius $r_{cp}$ about 2.0nm) with CSPG rich glycosaminoglycans (GAG) (radius ($r_G$) about 0.6nm) attached to it along a central filament of hyaluronic acid. As our group did in the artery treatment [12], we assume that the radius $r_{CF}$ of the central filament is about 2.0nm, which is same as that of the core protein. In order to calculate the effective radius $r^*$, we introduce the ratio $\beta$ of the total GAG to total protein core lengths and the ratio $\alpha$ of the total protein core to central filament length in the thin layer. Figure 22 shows the geometric meaning of these symbols.

Curiously, the freeze etching pictures for some reasons do not show the GAG fibers, probably because the preparation environment has caused them to collapse onto the PCP, or because they are beyond the resolution of this technique. In any case, we treat the GAGs as if they are aggregated along the core protein of the proteoglycan monomer. As such, the sizes that go into our model are just the ones read from the freeze-fracture picture.

Let us now begin the volume fraction estimate. Define an effective monomer radius $r_M$ for a hypothetical fiber of uniform size that would have the same total volume as the combination of GAG and PCP and the same length as the PCP. Then $r_M$ satisfies

$$r_M = [\beta r^2{}_G + r^2{}_{CP}]^{1/2} \tag{19a}$$

Recall that $r^*$ is to be defined for the whole proteoglycan matrix or aggregate. The effective radius is supposed to include a fiber with both the same total volume and total length as the combination of the monomers and the central filament, i.e.,

$$r^{\cdot} = (\frac{\alpha r_M^2 + r_{CF}^2}{\alpha + 1})^{1/2} \tag{19b}$$

This leads to a PG volume fraction estimate of

$$1 - \varepsilon = (\frac{r^*}{\xi})^2 (\frac{\alpha + 1}{\alpha}) N \tag{19c}$$

Monoclonal antibody studies [88] have identified CSPG as the predominant proteoglycan in the arterial intima. Unfortunately, we are not aware of any such studies on valve matrix. As such, based simply on the similarity of the freeze fracture photos of the arterial intima and the valve, we guess that they have similar matrix constituents, in which case $\alpha$ is about 3~10 and $\beta$ is about 5~10. One can obtain $K_{p(PG)}$ by combining the expressions for $r^*$ and $\varepsilon$ with the equation [16].

One also needs to consider the contribution to the hydraulic resistance from the collagen. Sangani and Acrivos [83] calculated the hydraulic resistance from the exact solution for Stokes flow perpendicular to a parallel, periodic array of infinitely long circular cylinders. Tsay and Weinbaum [84] have found a simplified approximation for $K_p$

$$K_p = 0.0527 a^2 (\frac{\Delta}{a})^{2.377} \tag{20}$$

where a is the fiber radius and Δ is the open spacing between fibers. Therefore, the ratio of the resistance of the composite proteoglycan fiber of radius $r^*$ and collagen fibrils of radius $r_{CG}$ is well approximated by

$$\frac{K_{p(PG)}}{K_{p(CG)}} = (\frac{r_{CG}}{r^*})^{0.377} (\frac{\Delta_{PG}}{\Delta_{CG}})^{2.377} \tag{21}$$

In arteries, Huang *et al.* [12] estimated that the fractional volume of collagen is about 5% from measurements of Frank's [8] rotary shadow freeze etching. This value of collagen of about 5% gives Δ approximately 120nm. Since the freeze etchings of the interposed layer in valves and of the arterial intima look similar and since we are not aware of monoclonal antibody studies to identify the types of proteoglycans in valves, we use this value of Δ for arterial intima for valves as well. Therefore, combination of expressions (21) and (15) gives the total resistance of $K_p$.

One can estimate the effective diffusivities in a manner exactly analogous to that used in arteries. Ogston *et al.* [65] derived an expression for the diffusion coefficient for a solute of radius $r_s$ in a fiber matrix as

$$D_i = D_f \exp[-(1-\varepsilon)^{1/2} (1 + \frac{r_s}{r_*})] \tag{22a}$$

To compensate for the presence of the collagen, we replace the $D_f$ by $D_{feff}$.

$$D_{feff} = D_f \zeta \exp[-(\frac{V_{CG}}{V})^{1/2} (1 - \frac{r_s}{r_{*CG}})] \tag{22b}$$

where $\zeta = 1 - (V_{CG} + V_{PG})/V$ is a tortuosity factor. $D_f$ is available for LDL and albumin, but not for HRP. Since our experiments have been conducted with HRP, we need to model HRP transport in valves and thus we need to know the parameters for HRP, i.e., $D_f$. The following is an indirect method to get $D_f$ for HRP. $D_f$ satisfies the Stokes-Einstein equation [80]:

$$D_f = \frac{kT}{6\pi\mu r_s} \tag{23}$$

where T is the absolute temperature and k is the Boltzman constant and μ is the fluid viscosity. Equation (23) implies a relationship between the $D_f$ for albumin and for HRP:

$$\frac{D_{f(HRP)}}{D_{f(albu\min)}} = \frac{r_{albumin}}{r_{HRP}} \tag{24}$$

Since $D_f$ for albumin is known, an estimate $D_f$ for HRP follows from equation (24).

## C. Preliminary model

Recall, we consider the aortic valves as a uniform, homogeneous, isotropic medium, bordered by upper and lower endothelial layers. There are two lumen regions, one above the aortic face at a higher pressure and the other below the ventricular face at a lower pressure (see Fig. 20). Water transports from the aortic face to the ventricular face. Tompkins' one dimensional model [43], which does not consider isolated endothelial leakage, suggests that the hydraulic conductivity of the aortic face is larger than that of the ventricular face [43]. For a preliminary calculation, we presume that the conductivity of the ventricular face is uniform; the conductivity of the arterial face is uniform as well, except for a local increase due to the presence of a leaky cell at the center of the face.

Addition or removal of leaks to or from either face is certainly possible within the context of this model. If a face only contains one leak at its center, then let $\xi$ be the face's radius. If the face has more than one leak, then assume that the leaks are far enough apart so that the face can be divided up into roughly axisymmetric regions (of radius $\xi$) having no fluid or macromolecular flux between them, i. e., forming a periodic tiling of the face. Let $A=\pi\xi^2$ be the area of a unit cell (see Figure 20). This abuse of geometry greatly simplifies the analysis and is common [12, 32].

*C.1. Equations for the velocity field in the valve.* Figure 24b is the filtration model for the aortic valve, in which U and W represent the velocities in the directions parallel and normal to the endothelium, with r and z representing the corresponding coordinates. These velocities can be denoted as $\underline{V}$ =(U, W). The origin is at the center of leakage site on the aortic face. The edge of periodic unit is $r=\xi$; the aortic face is $z=0$, and the ventricular face is $z=1$. $R_1$ is the radius of the endothelial cell. Assume that the leaky cleft is circular and stretches from $r=R_1$ to $r=R_2$. The subscripts $e_j$ and e stand for the leaky endothelial junction and normal endothelial junction, respectively, and L is the valve thickness. Subscripts 1 and 2 represent arterial and ventricular surfaces. $(L_p)_{ej}$ is the hydraulic conductivity in the leaky junction on the aortic face, and $(L_p)_{e1}$ and $(L_p)_{e2}$ are the hydraulic conductivities in the normal junctions on the aortic and ventricular faces, respectively. $K_p$ is the medium's Darcy permeability and $\mu^*$ is viscosity of the fluid. Let $(L_p{*})_v = K^*_p/\mu^* L^*$ be the hydraulic conductivity of the valve's interior media. P is the pressure in the valve, $P_{10}{*}$ and $P_{20}{*}$ are the average pressures in the lumens above the aortic face and below the ventricular face, respectively. $\Delta P^*$ is the difference between these two pressures ($\Delta P^* = P_{10}^* - P_{20}^*$ ).

We use non-dimensional variables throughout. The superscript * represents a dimensional variable. The non-dimensional coordinates and velocities are

$$r = \frac{r^*}{L}, \quad z = \frac{z^*}{L} \tag{25}$$

$$U = \frac{U^*}{(L_p^*)_v \, \Delta P^*}, \quad W = \frac{W^*}{(L_p^*)_v \, \Delta P^*} \tag{26}$$

The non-dimensional pressure and hydraulic conductivities in the intima are

$$P = \frac{P^* - P_{20}^*}{\Delta P^*}, \quad (L_p)_{ci} = \frac{(L_p^*)_{ci}}{(L_p^*)_v}, \quad (L_p)_{cj} = \frac{(L_p^*)_{cj}}{(L_p^*)_v} \; ; \; i = 1,2 \tag{27}$$

In the interposed region, assume that the water velocity and pressure obey Darcy's law, whose dimensional form is $U^* = -(K_p^*/\mu^*)\, \partial P^*/\partial r^*$ and $W^* = -(K_p^*/\mu^*)\, \partial P^*/\partial z^*$. The non-dimensional form of Darcy's law is

$$\underline{V} = -\underline{\nabla} P \text{ or } U = -\frac{\partial P}{\partial r}; \quad W = -\frac{\partial P}{\partial z} \tag{28}$$

The velocities in the interposed region satisfy the continuity equation

$$\underline{\nabla} \bullet \underline{V} = 0 \text{ or } \frac{\partial U}{\partial r} + \frac{U}{r} + \frac{\partial W}{\partial z} = 0 \tag{29}$$

To obtain a boundary value problem for the pressure, substitute equation (28) into (29):

$$\nabla^2 P = 0 \text{ or } \frac{\partial^2 P}{\partial r^2} + \frac{1}{r}\frac{\partial P}{\partial r} + \frac{\partial^2 P}{\partial z^2} = 0 \tag{30}$$

Symmetry at r=0 and no flux at r=ξ, either by periodicity or because r=ξ is the edge of the valve, yield the boundary conditions

$$U = -\frac{\partial P}{\partial r} = 0 \quad at\ r = 0, r = \xi \tag{31}$$

The hydraulic conductivity of a layer is the constant of proportionality of the assumed linear relationship between the fluid velocity and the local pressure difference between the two sides, i.e., the local driving force. On the (aortic) face (z=0) outside of the leaky cleft (at $0<r<R_1$, $R_2<r<\xi$) and on the entire ventricular face, the hydraulic conductivities $(L_p^*)_{e1}$ and $(L_p)_{e2}$ characterize the normal junctions. The water velocity across the leaky cleft (at $R_1<r<R_2$) is related to the separate hydraulic conductivity $(L_p^*)_{ej}$ of the leaky junction. On the (ventricular) face of the valve, there is negligible pressure (near zero when the valve is closed) compared with the pressure (over 100 mm Hg) on the (aortic) face. We use the dimensionless variables to describe the boundary conditions. The dimensionless pressure $P_1$ near the aortic face (lumen in ascending aorta) is equal to 1 and $P_2$ near ventricular face (lumen in the ventricle) is equal to 0. Therefore, The corresponding boundary conditions on both faces of the valve (at z=0 and z=1), which completes the specification of the boundary value problem, are

$$W = -\frac{\partial P}{\partial z} = (L_p)_{e1}[1-P]\ at (0 < r < R_1), (R_1 < r < \xi); z = 0 \tag{32}$$

$$W = -\frac{\partial P}{\partial z} = (L_p)_{ej}[1-P] \quad at\ (R_1 < r < R_2), z = 0 \tag{33}$$

$$W = -\frac{\partial P}{\partial z} = (L_p)_{e2}P \quad at\ 0 < r < \xi, z = 1 \tag{34}$$

*C.2. Solution method for water flow in the valve.* In order to solve this problem for P, we write the solution as a superposition of a contribution $P_1$, representing the solution for an endothelium without any leaks, and $P_2$ representing the difference induced by the leak, i.e.,

$$P = P_1 + P_2 \tag{35}$$

All of the boundary conditions for $P_1$ are the same as for P except for (33), in which one replaces the hydraulic conductivity of leaky cleft by that $(L_p)_{e1}$ of the normal cleft. The problem for $P_1$ becomes one dimensional (in z) and its solution is simply

$$P_1 = c_1 z + c_2 \tag{36}$$

where $c_1$ and $c_2$ are

$$c_1 = -\frac{(L_p)_{e1}(L_p)_{e2}}{(L_p)_{e1} + (L_p)_{e2} + (L_p)_{e1}(L_p)_{e2}} \tag{37}$$

$$c_2 = \frac{(L_p)_{e1} + (L_p)_{e1}(L_p)_{e2}}{(L_p)_{e1} + (L_p)_{e2} + (L_p)_{e1}(L_p)_{e2}} \tag{38}$$

The boundary conditions (32 and 33) for $P_2$ become

$$-\frac{\partial P_2}{\partial z} + (L_p)_{e1} P_2 = f(r) = [(L_p)_{ej} - (L_p)_{e1}][1 - P_1 - P_2] \quad at\ R_1 \cdot\cdot r \cdot\ R_2, z = 0 \tag{39}$$

$$-\frac{\partial P_2}{\partial z} + (L_p)_{e1} P_2 = 0 \quad at\ (0 \cdot\cdot r \cdot\ R_1), (R_2 \cdot\ r \cdot\ \xi); z = 0 \tag{40}$$

Using the method of separation of variables and boundary conditions (34 for $P_2$, 39 and 40), one easily finds

$$P_2 = a_0(z + l_p) + \sum_{j=1}^{\infty} a_j[\sinh(\lambda_j z) + \mu_j \cosh(\lambda_j z)] J_0(\lambda_j r) \tag{41}$$

where $J_0$ is a Bessel function of the first kind of order zero, $\lambda_j$ is the $j_{th}$ zero of $J1(\lambda_j \xi)=0$. $l_p$ and $\mu_j$ are

$$l_p = -\frac{1+(L_p)_{e2}}{(L_p)_{e2}}; \ \mu_j = -\frac{\lambda_j + (L_p)_{e2}\tanh(\lambda_j)}{\lambda_j \tanh(\lambda_j) + (L_p)_{e2}} \tag{42}$$

and

$$a_0 = \frac{1}{[(L_p)_{e1} l_p - 1]\xi^2} \int_{R_1}^{R_2} r' f(r') dr' \tag{43}$$

$$a_j = \frac{2}{\mu_j [(L_p)_{e1} l_p - \lambda_j] \xi^2 J_0^2(\lambda_j \xi)} \int_{R_1}^{R_2} r' f(r') J_0(\lambda_j r') dr' \tag{44}$$

The expressions (41-44) for $P_2$ are in terms of an as yet unknown function f(r). Then, after substituting equations (36) and (41) into (39), one can obtain that function f(r) needs to satisfy

$$\sum_{j=1}^{\infty} \beta_j J_0(\lambda_j r) \int_{R_1}^{R_2} r' f(r') J_0(\lambda_j r') dr' = [l_q - l_r \int_{R_1}^{R_2} r' f(r') dr'] \tag{45}$$

where

$$\beta_j = \frac{2}{\xi^2 J_0^2(\lambda_j \xi)} [1 + \frac{\mu_j \cosh(\lambda_j)((L_p)_{ej} - (L_p)_{e1})}{\mu_j (L_p)_{e1} - \lambda_j}] \tag{46}$$

$$l_q = [(L_p)_{ej} - (L_p)_{e1}](1 - c_2) \tag{47}$$

$$l_r = \frac{1}{\xi^2} \frac{[(L_p)_{ej} l_p - 1]}{[(L_p)_{e1} l_p - 1]} \tag{48}$$

Due to the boundary condition equation (39), f(r) also needs to satisfy f(r) = $[(L_p)_{ej} - (L_p)_{e1}][1 - P_1 - P_2]$ in the cleft, i.e., for $R_1<r<R_2$ and z=0. Because this region is very thin ($10^{-4}$~$10^{-5}$ times) compared with the domain of r, its resolution would require an astronomically large number of terms in a standard Fourier-Bessel series. Weinbaum *et al.* [31] illustrated one solution technique to obtain the unknown function f(r) that arises in

the problem of finding the Greens function for Laplace's equation on a region having homogeneous boundary conditions except on such an extremely thin, but not infinitely thin, ring. The basic idea is as follows: they essentially impose two artificial homogeneous Neumann boundary conditions at $r = R_1$ and $R_2$. This allows the construction of an orthonormal basis (relative to the standard inner product for cylinder functions with weight function r) for the subspace of $C^1[R_1,R_2]$ having zero endpoint derivatives as the eigenfunctions of the resulting eigenvalue problem. They then expand f(r) in this basis, substitute into (45) and take the components of this equation in terms of this basis. Completeness of the basis implies linear independence of the resulting equations for the unknown coefficients $\{D_m\}$ in the f(r) expansion, and so truncation will lead to a solvable (non-singular) matrix equation. The integrals in (45) involving f(r) can then be done analytically and one can solve for the $\{\beta_j\}$.

What troubled these authors, though, was the restriction of imposing the Neumann conditions at $R_1$ and $R_2$. They attempted to alleviate it by expanding the interval at each end by an amount $\Delta r$ much smaller than the endothelial cell leakage width $(R_2-R_1)$. (The user would later numerically vary $\Delta r$ in an attempt to find a situation where the solution was insensitive to its exact value.) The Neumann conditions, and thus the resulting eigenvalue problem, would then be applied at the endpoints of the expanded interval, rather than at $R_1$ and $R_2$, but the integral that formerly represented the inner product would remain unchanged. It would, simply loose its significance as an inner product and require calculation of integrals of what used to be the inner products of orthogonal functions, and the values of these integrals now would clearly be linear in $\Delta r$ rather than zero. As such, the solutions become insensitive to $\Delta r$ only when the distinction between the original and the expanded intervals is irrelevant. The lack of completeness of the eigenfunctions on $(R_1,R_2)$ (they no longer allow representation of functions that are not well-behaved at $R_1$ and $R_2$) no longer guarantees non-singularity of the resulting matrix, although the user can numerically try to invert it anyway. However, the thinness of the region $(R_1,R_2)$, whether or not it is expanded by a small $\Delta r$, together with the Neumann endpoint conditions and the absence of high derivatives in the governing equations, do not allow the function to bend over this interval. Thus, despite the numerical acrobatics, the solution, with or without the added complication of $\Delta r$, is essentially a constant over the leak.

Since (i) we originally did the calculation via the method described above, and realized these shortcomings only after having done the calculations; (ii) the solutions agrees with simply assuming that the solution is constant over the interval $(R_1,R_2)$, with the value of this constant determined via the simpler method not invoking $\Delta r$; and (iii) since this model's results, as shown below, do not agree even qualitatively with experiment, we did not repeat the calculation using the simpler method. As such, we present the equations that make up the method of Weinbaum *et al.*

First, let $R_+ := R_2 + \Delta r$ and $R_- := R_1 - \Delta r$ with $\Delta r << |R_2 - R_1|$, and suppose

$$\frac{df(r)}{dr} = 0,\ r = R^- = R_1 - \Delta r; \quad \frac{df(r)}{dr} = 0,\ r = R^+ = R_2 - \Delta r \qquad (49a,b)$$

We plug the eigenfunction solutions

$$\{K_m(r):=J_0(\alpha_m r)-T_m Y_0(\alpha_m r),\ m=1,2,..;\ K_0(r):=1,\ m=0\} \tag{50}$$

(where $Y_0$ is the Bessel function of the second kind with order zero) into the Bessel's equation that results from the separation of variables in (30) into (49) to arrive at the eigenvalue problem for $\{\alpha_m, T_m\}$:

$$J_1(\alpha_m R^-) - T_m Y_1(\alpha_m R^-) = 0 \tag{51a}$$

$$J_1(\alpha_m R^+) - T_m Y_1(\alpha_m R^+) = 0 \qquad \text{for } m=1,2,\ldots \text{ and } \alpha_0=0 \tag{51b}$$

With $\{\alpha_m, T_m\}$ and thus the eigenfunctions known, we assume we can expand f(r) in terms of the unknown coefficients $\{D_m{:}m=0,1,2,\ldots\}$ as

$$f(r) = D_0 + \sum_{m=1}^{\infty} D_m [J_0(\alpha_m r) - T_m Y_0(\alpha_m r)] \tag{52}$$

To obtain the $D_m$, we multiply (45) sequentially by the product of each of the pseudo-basis functions with the weight function r, and integrate from $R_1$ to $R_2$ ( rather than from $R_-$to $R_+$ which would have been the true inner product). The result is:

$$\sum_{j=1}^{\infty} \beta_j \int_{R_1}^{R_2} r'f(r')J_0(\lambda_j r')dr' \int_{R_1}^{R_2} K_n(r'')J_0(\lambda_j r'')dr'' = [l_q - l_r \int_{R_1}^{R_2} r'f(r')dr'] \int_{R_1}^{R_2} K_n(r'')dr'',\ n \geq 0 \tag{53}$$

This generates a set of linear equations for the unknown $D_m$, m=0,1,2,3,... in equation (53). After substituting series representation, equation (51), for f(r) and the pseudo-basis functions $K_n(r)$ (n>0) (51), one can obtain

$$\sum_{j=1}^{\infty} \beta_j \int_{R_1}^{R_2} r'\{D_0 + \sum_{m=1}^{\infty} D_m [J_0(\alpha_m r') - \frac{J_1(\alpha_m R^-)}{Y_1(\alpha_m R^-)} Y_0(\alpha_m r')]\} J_0(\lambda_j r')dr'$$

$$\int_{R_1}^{R_2} r'[J_0(\alpha_n r') - \frac{J_1(\alpha_n R^-)}{Y_1(\alpha_n R^-)} Y_0(\alpha_n r')] J_0(\alpha_m r')dr'$$

$$= \{l_q - l_r \int_{R_1}^{R_2} r'[D_0 + \sum_{m=1}^{\infty} D_m(J_0(\alpha_m r') - \frac{J_1(\alpha_m \bar{R})}{Y_1(\alpha_m \bar{R})} Y_0(\alpha_m r'))]dr' \}$$

$$\int_{R_1}^{R_2} r'[J_0(\alpha_n r') - \frac{J_1(\alpha_n \bar{R})}{Y_1(\alpha_n \bar{R})} Y_0(\alpha_n r')]dr' \qquad for\ n > 0, \tag{54a}$$

$$\sum_{j=1}^{\infty} \beta_j \int_{R_1}^{R_2} r'\{D_0 + \sum_{m=1}^{\infty} D_m[J_0(\alpha_m r') - \frac{J_1(\alpha_m \bar{R})}{Y_1(\alpha_m \bar{R})} Y_0(\alpha_m r')]\} J_0(\lambda_j r')dr' \int_{R_1}^{R_2} r' J_0(\lambda_j r')dr'$$

$$= \{l_q - l_r \int_{R_1}^{R_2} r'[D_0 + \sum_{m=1}^{\infty} D_m(J_0(\alpha_m r') - \frac{J_1(\alpha_m \bar{R})}{Y_1(\alpha_m \bar{R})} Y_0(\alpha_m r'))]dr' \} \int_{R_1}^{R_2} r'dr' \quad \text{(n=0)} \tag{54b}$$

Then, we define the following parameters to simplify the above equations (54)

$$\bar{R} = (R_2^2 - R_1^2)/2 \tag{55a}$$

$$\gamma_j = \int_{R_1}^{R_2} r' J_0(\lambda_j r')dr' = [\frac{r'}{\lambda_j} J_1(\lambda_j r')]\Big|_{R_1}^{R_2} \tag{55b}$$

$$f_1(m) = \int_{R_1}^{R_2} [J_0(\alpha_m r') - T_m Y_0(\alpha_m r')]r'dr' = [r' \frac{J_1(\alpha_m r')}{\alpha_m} - T_m r' \frac{Y_1(\alpha_m r')}{\alpha_m}]\Big|_{R_1}^{R_2} \tag{55c}$$

$$f_3(m,j) = \int_{R_1}^{R_2} r' J_0(\alpha_m r') J_0(\lambda_j r')dr' = [-r' \frac{\lambda_j J_0(\alpha_m r') J_1(\lambda_j r') - \alpha_m J_1(\lambda_m r') J_0(\lambda_j r')}{\alpha_m^2 - \lambda_j^2}]\Big|_{R_1}^{R_2}$$

(55d)

$$f_4(m,j) = T_m \int_{R_1}^{R_2} r' Y_0(\alpha_m r') J_0(\lambda_j r')dr' = T_m[-r' \frac{\lambda_j Y_0(\alpha_m r') J_1(\lambda_j r') - \alpha_m Y_1(\lambda_m r') J_0(\lambda_j r')}{\alpha_m^2 - \lambda_j^2}]_{R_1}^{R_2}$$

(55e)

$f_1=f_1(m)$, $f_2=f_1(n)$, $f_3=f_3(m,j)$, $f_4=f_4(m,j)$, $f_5=f_3(n,j)$ and $f_6=f_4(n,j)$. Substituting equations (55) into (54), one obtains

$$Do[l_r R^2+\sum_{j=1}^{\infty}\beta_j r_j^{\,2}]+\sum_{m=1}^{\infty} D_m[l_r R f_1+\sum_{j=1}^{\infty}\beta_j r_j(f_3-f_4)]=l_q R\ ,\quad n=0; \tag{56a}$$

$$Do[l_r f_2 R+\sum_{j=1}^{\infty}\beta_j r_j(f_2-f_6)]+\sum_{m=1}^{\infty} D_m[l_r f_1 f_2+\sum_{j=1}^{\infty}\beta_j (f_3-f_4)(f_5-f_6)]=l_q f_2\ ,$$

$$n > 0 \tag{56b}$$

If we truncate the hierarchy in n in equation (56b) at some value N, the j sum at J and the m sum at N as well, equations (56) constitute N+1 linear equations in N+1 unknowns $D_m$, m=0,1,…,N.

$$Do[l_r R^2+\sum_{j=1}^{J}\beta_j r_j^{\,2}]+\sum_{m=1}^{N} D_m[l_r R f_1+\sum_{j=1}^{J}\beta_j r_j(f_3-f_4)]=l_q R\ ,\quad n=0; \tag{57a}$$

$$Do[l_r f_2 R+\sum_{j=1}^{J}\beta_j r_j(f_2-f_6)]+\sum_{m=1}^{N} D_m[l_r f_1 f_2+\sum_{j=1}^{J}\beta_j (f_3-f_4)(f_5-f_6)]=l_q f_2\ ,$$

$$n=1,\ldots,N+1 \tag{57b}$$

The solution provides $D_m$ and thus the function f(r) has been solved. The complete solution for the pressure and water filtration results can be obtained through these equations (28, 35, 36, 41, 51, 57). By using this filtration solution, one can analyze the macromolecular , i.e., LDL, distribution in the valves.

*C.3. Boundary value problem for the concentration profile in the valve.* Let the variables $C^*$ and $C_L$ denote the dimensional LDL concentration in the valve and in the plasma, respectively. The variable $C := C^*/C_L$ represents the dimensionless LDL concentration in the valve. The axisymmetric convective-diffusion equation for C is

$$\frac{\partial C}{\partial t}=[\frac{\partial^2 C}{\partial r^2}+\frac{\partial C}{r\partial r}+\frac{\partial^2 C}{\partial z^2}]-[P_{er}\frac{\partial C}{\partial r}+P_{er}\frac{C}{r}+P_{ez}\frac{\partial^2 C}{\partial z}] \tag{58}$$

where $P_{er}$ (= $fLU^*/\gamma D$) and $P_{ez}$ (= $fLW^*/\gamma D$) are the non-dimensional water velocities in the form of Peclet-numbers in r and z directions. D and f are the diffusion and retardation coefficients. $U^*$ and $W^*$ are the r and z components of the dimensional water velocity profile described above. $\gamma$ is the volume partition coefficient.

The filtration model yields the pressure distribution P(r,z,t). $U^*$ and $W^*$ follow consequently from equations (26) and (28) and enter the Peclet-numbers $P_{er}$ and $P_{ez}$. The initial condition for equations(58) is C=0 at t=0, which corresponds to an animal that is initially tracer-free; the experiment introduces a pulse of tracer. The boundary conditions are: (a). $\partial C(r,z,t)/\partial r=0$, at r=0, $r=\xi$; $0<z<1$. That is, there is no tracer flux either at r=0 due to axisymmetry or at $r=\xi$ due to periodicity; (b). $q_j(t)= -\gamma D\partial C^*(R_1,0,t)/\partial z +fW^*(R_1,0)C^*(R_1,0,t)$, at $R_1 <r< R_2$, z=0, where $q_j(t)= (e^{P_{ej}}-C_j(t))/(e^{P_{ej}}-1)$ and $P_{ej}=fWh/\gamma D$ [70]. This prescribes the mass transport across the leaky cleft of the aortic face as the sum of diffusive and convective contributions; (c). $fC^*(r,0,t)W^*(r,0,t)-\gamma D\partial C^*(r,0,t)/\partial z = k_1(C_L-C^*(r,0,t))$, at $0 < r < R_1$, $R_2 < r < \xi$; z=0. This corresponds to the mass transport across the normal cleft of the aortic face; (d). $fC^*(r,1,t)W^*(r,1,t)-\gamma D\partial C^*(r,1,t)/\partial z = k_2(C^*(r,1,t)-C_L)$, at $0 < r < \xi$, z=1, which corresponds to the mass transfer on the (ventricular) face. Here $k_1$ and $k_2$ are the permeabilities to LDL of the normal endothelial surfaces. Note that these boundary conditions can be phrased non-dimensionally in terms of $Bi_1$ ($Bi_1=k_1L/D$) and $Bi_2$ ($Bi_2=k_2L/D$), the Biot numbers for the normal clefts on the aortic face and the ventricular face, respectively.

*C.4. Solution of the water flow problem and comparison with experiment.* The dashed curve in figure 24c shows the pressure distribution in valves right underneath the endothelial cell layer (at z=0) for this preliminary model. It represents the pressure as a function of radial distance r from the center of the leaking cell. The figure shows that the pressure drop for the preliminary model is very quick and levels off within about two cell radii. This means that the horizontal velocity quickly drops to near zero within a couple of cell radii. Thus convective solute transport in this direction must also be small. Therefore, this model can only predict a small leakage spot. In contrast, our experiments (see Section VIIC) have showed that the leakage spot in valves, even after 2-4 minutes of tracer circulation, is indeed large and in fact similar in size to that in arteries. Thus, we find that this preliminary model cannot account for the experimental data. We need to appeal to these data and the other data that we have thus far gathered in order to formulate a new theoretical model.

*C.5. Suggestive evidence for the possible existence of an intima-like layer in the valve sub-endothelia.* As just noted and as learned from our group's artery wall transport models [12], to generate a large HRP spot from a single endothelial cell's leaking junction requires a significant subendothelial convection in the "plane" parallel to the endothelium. The preliminary model above was based on a uniform, isotropic interposed layer between the two endothelial layers and was unable to generate such convection. In the artery wall this so-called lateral convection was due to two factors: the presence of a continuous internal elastic laminar (IEL) which did not appear to allow straight forward fluid progression from the endothelium through the intima and into the media. Rather, it apparently forced the advancing fluid to shunt perpendicular to the prevailing flow direction and spread out in the intima until it found enough IEL fenestrae to handle the entire flow. This brought the calculated spot size to within a factor of five of Lin *et al*'s spot size measurements. However, in order to easily match the observed spot size, it was necessary for us to look at the matrix structure in the intima and to compare it to that in the media. To our surprise, we found that the intimal matrix structure was significantly less dense than the media's. In fact, the intimal albumen space was close to 90%, whereas that in the media was circa 1%. As a result, an *ab initio* theory for the intima's Darcy permeability showed it to be one to two orders of magnitude higher than the media's. Inclusion of this calculated (not fit) permeability value resulted in the observed spot sizes.

The valve endothelia do not seem to have continuous, directly subendothelial elastin layers. In addition, to the best of our knowledge, no one has yet suggested that the immediate subendothelial matrix in valve is any different from the matrix that characterizes the deeper regions of the valve. It is worth noting, however, that until we examined the ultra-rapid freezing/rotary shadow etchings of Frank and Fogelman, no one had made a similar suggestion for the artery wall either.

Let us then reexamine what might lead us to such a conjecture. In addition to the spot size data, if the valve matrix is homogeneous, uniform and isotropic, then one would expect water, and thus a convected or simply a diffusing tracer, to spread in the subendothelial space at more-or-less comparable rates both normally and tangentially to the endothelium. Recall that in the experiments reported above, our collaborator Anli Huang did a 4 minutes HRP circulation experiment, after which she sacrificed the rat and examined transverse EM sections of the valve. Rather than finding a gradual variation in

HRP reaction product intensity with distance from the endothelium, or from a focal leak, she found (see Figure 21) a very dark, immediately subendothelial staining 100-200 nm in thickness, and only very faint staining below. It is hard to see how any model assuming a uniform, homogeneous, isotropic media could possibly account for this observation. On the contrary, comparison with the artery wall work certainly suggests the possibility of there being a thin subendothelial layer of much higher voidage, and thus much higher Darcy permeability, in valve as well. That is, this mismatch in transport parameters in the valve might perform more or less the function with regard to water and macromolecular flow that the IEL plus a similar mismatch perform in arteries. Since this explanation seems to be qualitatively consistent with both the *en face* spot size measurements and with the transverse EM sectioning results, we shall now develop a new model that incorporates this *Ansatz.* Our goal is to see if the agreement is quantitative as well, and thus if this model is indeed a plausible explanation of the observations.

Below we incorporate this mismatch in transport parameters (high permeability through a loose matrix just below the endothelium and low permeability through a dense matrix in the interior) into a new model of water filtration and macromolecular transport across valves. We model the interposed region of the valves with three different layers, a relatively dense matrix layer (called area II) in the middle of the valves, and two relatively loose matrix layers that cover area II in the upper and lower surfaces (called areas I and III, respectively). Each thin layer is covered by an endothelial cell layer. Because of our inability to make direct hydraulic conductivity measurements on such thin layers and due to the fact that the direct observations [40] of the matrix structure there did not specify near which valve face the crack plane lay, we take the hydraulic conductivities in areas I and III as to be the same, and a value that is significantly smaller than area II's as calculated in section D.4.4. We anticipate that this will result in flow patterns that differ significantly from those calculated assuming a uniform matrix as above. Moreover, the void spaces for large tracers are significantly different in these areas (I, II, and III) because area II is much denser than areas I and III. Consequently, HRP and LDL should spread out more in the directions parallel to endothelial cell layers after entering the intimas than in the preliminary model. Therefore, the expected LDL concentration profiles, and thus the spot sizes derived from them, should be qualitatively different from those resulting from the uniform matrix assumption. The new model is described in detail in the next subsection.

## D. New theoretical model

In this section, we use the ideas just discussed to develop a new model for filtration and macromolecular transport in valves. The filtration model again allows an analytical solution. However, the convective and diffusive macromolecular transport model again requires numerical solution.

*D.1. The geometry of the model.* In this model, as noted above, the interposed layer in the aortic valves is considered as a three-layer porous medium, surrounded by upper and lower endothelial mono-layers. There are two lumens; one is above the aortic (upstream) face at high pressure and the other is below the ventricular (downstream) face at a lower pressure (see Figure 20). Therefore, water convects from the aortic face to the ventricular face. As noted, the interposed region is divided into three layers (see Figures 25a and b), in which the relatively dense matrix (middle) layer is surrounded by thin upper and lower relatively loose matrix (surface) layers. We assume these two thin layers have similar matrix structures and thus the same permeability and conductivity properties. The permeability $(K_p^*)_m$ in the middle layer is smaller than that $(K_p^*)_i$ in the surface layers because of its assumed much denser matrix structure. In order to introduce a desired level of symmetry into the problem that significantly simplifies its solution, we assume that there is in a given valve leaflet face either: no leaks; one endothelial cell located at its center that is leaking; or that there is more than one leak per valve face, but that the leaks are far enough from one another that one can partition the face into roughly periodic regions, each having precisely one leaking cell at its center. The most unrealistic assumption here is that if both leaflets have leaks, the above implies that they are aligned. We call either an entire leaflet face in the leak-free or single leak case, or one of these regions in the latter case, a "periodic unit." In the latter case, we again abuse the geometry of the plane by taking these periodic regions to be axisymmetric, i.e., cylindrical; in the other cases this assumption is far less objectionable. The area A of each periodic unit is equal to the inverse of the average density of leakage sites. Similarly, we draw a circle (with radius $\xi = (A/\pi)^{1/2}$ and centered at the leaky cell) to obtain the periodic cylindrical unit for the aortic valve.

The dimension of the two thin layers can be measured from Figure 21, where, as discussed, HRP has presumably penetrated through the loose matrix with high permeability, but not yet into the more dense, lower permeability region. The depth measured from Figure 21 is about 150nm. Tompkins' experiments show that the whole trans-valvular thickness varies from 30μm to 160μm. Therefore, in our model we will use an average value of 100μm for the trans-valvular thickness. Since these thin layers only account for circa 0.3% of the total thickness, the thickness of the middle layer (having the dense matrix of low permeability) comprises over 99% of the valvular thickness, as was the case for the intima in the aorta.

### *D.2, Boundary value problem for the velocity profile in the valve*

D.2.1. *Geometry and variables.* Below we present the equations for the filtration flow in the valve leaflet. Figures 25 show one "periodic unit." Figure 25a is the filtration model for the aortic valve, in which $P_i^*$, $U_i^*$ and $W_i^*$ (i =1,2,3) represent the dimensional (denoted by $^*$; the non-dimensional quantities – see below – do not have the $^*$) pressure and velocities in the directions parallel and normal to the endothelium in three layers i =1,2,3, with r and z representing the corresponding cylindrical coordinates, respectively. The origin of the coordinates is at the center of the leaky cell, here chosen to be on the aortic face. Coordinate z increases from the aortic face z=0 to the ventricular face z=1. The leaky cleft is assumed circular and stretches from $r=R_1$ to $r=R_2$. The edge of the periodic unit is $r=\xi$ and the centerline r=0 (see figures 25a and b). The subscripts j and e stand for the leaky endothelial junction and the normal endothelial junction, and L is the valve thickness, here taken (unrealistically) to be uniform. When necessary, subscripts a and v represent arterial and ventricular surfaces.

$p_{10}^*$ and $p_{20}^*$ are the average dimensional pressures in the lumens above the aortic face and below the ventricular face, respectively and $\Delta p^*$ is their difference ($\Delta p^* = p_{10}^* - p_{20}^*$). $(K^*_p)_i$ and $(L^*_p)_i$ (i=1,2(=m),3) are the permeabilities and hydraulic conductivities in the three regions of the interposed layer. The hydraulic conductivities $(L_p)_{ea}^*$ and $(L_p)_{ev}^*$ refer to normal junctions on the aortic and ventricular faces. As noted, localized leakage can occur on either the aortic face and/or the ventricular face. We assume that the hydraulic conductivities $(L_p)_j^*$ in the leaky junction are same on the both faces when there are leaks on both faces. In addition, we take $(L^*_p)_1 = (L^*_p)_3$ since we assume that the two thin layers have the similar structures. We shall assume that $(L^*_p)_m$ is similar to that of the media of arteries [57].

We use non-dimensional variables throughout. Distances are non-dimensionalized by L, the pressure by the pressure $p^*_L$ in the lumen above the aortic face, and the velocities by the product $(K_p)_i(L^*_p)_m\Delta p^*$, where $(K_p)_i$ are the Darcy permeabilities (i= 1,3) dimensionalized by the Darcy's permeability in the middle layer. The product $(K_p)_i\ (L^*_p)_m$ is the hydraulic conductivities in the thin layer (i=1,3). The non-dimensional hydraulic conductivities of the endothelia and the leaky junctions are

$$(L_p)_{ei} = \frac{(L_p^*)_{ei}}{(L_p^*)_v},\ i = 1,2;\ (L_p)_j = \frac{(L_p^*)_j}{(L_p)^*_v} \tag{59}$$

D.2.2. *Governing equations and boundary conditions for the fluid flow problem.* In each of the three regions of the interposed layer, we assume that the water velocity and pressure obey Darcy's law; the dimensional equations are $U^*_i = -((K^*_p)_i/\mu^*)\ \partial p^*_i/\partial r^*$ and $W^*_i = -((K^*_p)_i/\mu^*)\ \partial p^*_i/\partial z^*$, where $\mu^*$ is viscosity of the fluid. If one defines $(L_p{*})_m=$

$(K^*_p)_m/\mu^* L^*$ and uses the dimensionless velocities, the dimensionless form for Darcy's law becomes

$$U_i = -\frac{\partial P_i}{\partial r}; \quad W_i = -\frac{\partial P_i}{\partial z}; \qquad i = 1,2,3 \tag{60}$$

The velocities in each of the regions of the interposed layer satisfy continuity:

$$\frac{\partial U_i}{\partial r} + \frac{U_i}{r} + \frac{\partial W_i}{\partial z} = 0 \tag{61}$$

Substituting equation (60) into (61) gives an equation for the pressure in each region of the interposed layer:

$$\frac{\partial^2 P_i}{\partial r^2} + \frac{1}{r}\frac{\partial P_i}{\partial r} + \frac{\partial^2 P_i}{\partial z^2} = 0, \qquad (i = 1,2,3) \tag{62}$$

The edge r = $\xi$ of the periodic unit allows no flux of liquid or of solute, either because of symmetry (if there is more than one leak per face) or because $r=\xi$ is the edge of the leaflet (if there is either 0 or 1 leak per face). Along the centerline ($r=0$) symmetry, i.e., no flux, also prevails. Thus:

$$U = -\frac{\partial P_i}{\partial r} = 0 \quad at\ r = 0, r = \xi \qquad (i=1,2,3) \tag{63}$$

On the (aortic) face of the valve ($z=0$), the water velocity across the normal intact endothelial layer excluding the leaky cleft, i.e., at $0<r<R_1$, $R_2<r<\xi$, is the product of the hydraulic conductivity $(L_p^*)_{c1}$ in the normal junctions and the local pressure drop across the aortic face. Similarly, the water velocity across the leaky cleft (at $R_1<r<R_2$) is the product of the hydraulic conductivity $(L_p^*)_{cj}$ in the leaky junction and the local pressure drop. Thus for the case of a single leak on the aortic face and none on the ventricular face,

the hydraulic conductivity $(L_p)_{e2}$ of the latter face is uniform. When the valve is closed, the pressure on the (ventricular) face of the valve is low (close to zero) compared to the pressure (over 100 mmHg) on the (aortic) face [71,95,96]. When the valve is open, the pressures on both faces are essentially equal to each other and to the systolic value; during this period, there is no driving force for flow. We employ the time average pressure values [97] in our model. The dimensionless pressures $P_1$ near the aortic face (the lumen in the ascending aorta) is equal to 1 and $P_2$ near the ventricular face (the lumen in the ventricle) is equal to 0. The boundary condition on aortic face of the valve (z=0) becomes

$$W_1 = -\frac{\partial P_1}{\partial z} = (L_p)_{ej}[1-P_1] \quad at\ (R_1 < r < R_2), z = 0 \tag{64}$$

$$W_1 = -\frac{\partial P_1}{\partial z} = (L_p)_{e1}[1-P_1]\ at (0 < r < R_1), (R_1 < r < \xi); z = 0 \tag{65}$$

and for the ventricular face,

$$W_3 = -\frac{\partial P_3}{\partial z} = (L_p)_{e2} P_3; \qquad at\ 0 < r < \xi, \qquad z = 1 \tag{66}$$

Let $z_{12}$ and $z_{23}$ be the z-positions of the interfaces between the layers denoted by their subscripts, the interfaces where the matrix mismatches occur. Here the pressures and velocities are continuous: $P_1=P_2$, $(K_p)_1\partial P_1/\partial z = \partial P_2/\partial z$ at $z = z_{12}$; $P_3=P_2$, $(K_p)_3\partial P_3/\partial z = \partial P_2/\partial z$ at $z = z_{23}$.

D.3. *Governing equations and boundary conditions for the tracer concentration problem.* Let the variables $C^*_i$ (i=1,2,3) and $C_L^*$ denote the dimensional LDL concentrations in valve and in the plasma, respectively. $D_m$ is the diffusivisity in the middle layer of the valves. $C_i$ (= $C_i^*/C_L$) and t (=$D_m t^*/L$) represent the non-dimensional LDL or other tracer concentration in the valve and the non-dimensional circulation time (see figure 25b). The convective-diffusive equation for $C_i$ is

$$\frac{\partial C_i}{\partial t} = [\frac{\partial^2 C_i}{\partial r^2} + \frac{\partial\ C_i}{r\partial r} + \frac{\partial^2 C_i}{\partial z^2}] - [P_{er}\frac{\partial\ C_i}{\partial r} + P_{er}\frac{C_i}{r} + P_{ez}\frac{\partial^2 C_i}{\partial z}] \tag{67}$$

where $P_{eri}$ (= $f_i L U^*_i/\gamma_i D_i$) and $P_{ezi}$ (= $f_i L W^*_i/\gamma_i D_i$) (i=1,2,3) are the non-dimensional velocity represented as Peclet-numbers in the r and z directions. $D_i$ and $f_i$ are the diffusion and retardation coefficients in the different layers i of the matrix discussed in the previous section (VIIIB) and $\gamma_i$ is the volume partition coefficient for the tracer in layer i relative to the lumen. The velocity profiles $U^*_i$ and $W^*_i$, and thus the Peclet-numbers $P_{eri}$ and $P_{ezi}$, are the solutions of the filtration model.

We turn now to the boundary and initial conditions. Before proceeding, we use the results of a local model that describes the macromolecular transport in the leaky cleft (subscript j). We assume that the leaky cleft in this model is a circular ring-source. Recall that the lumen concentration is equal to 1. The tracer concentration $C_j(t)$ in the leaky cleft is different from that in the lumen due to tracer convection and diffusion. Wen *et al.* [70], used a 1-D quasi-steady convection-diffusion equation to get the relationship between the macromolecular flux $q_j(t)$ and the possibly time-varying tracer concentration $C_j(t)$ in the leaky cleft concentration and found

$$q_j(t) = \frac{e^{Pej} - C_j(t)}{e^{Pej} - 1} \tag{68}$$

Here $P_{ej} = f_j W_j^* h/\gamma_j D_j$. $f_j$, $D_j$ and $\gamma_j$ are the retardation and diffusion coefficients and the volume partition coefficients in the leaky cleft and h is the endothelial cell layer thickness.

Figure 25b illustrates the boundary conditions for macromolecular transport. The initial condition is $C_i(r,z,t)=0$ $(i=1,2,3)$ at $t=0$, which corresponds to an animal that is initially tracer-free; the experiment introduces a pulse of tracer at $t=0$. The boundary conditions are: (a). $\partial C_i(r,z,t)/\partial r=0$, at $r=0$, $r=\xi$; $0<z<1$. No tracer mass transfer at the boundaries $r=0$ and $r=\xi$, which correspond to the axisymmetric condition at $r=0$ and the periodic condition (or the edge of the valve leaflet, as discussed above) at $r=\xi$; (b). $q_j(t)= -\gamma_1 D_1 \partial C_i^*(R_1,0,t)/\partial z + f_1 W^*_1(R_1,0) C_j^*(R_1,0,t)$, at $R_1 < r < R_2$, $z=0$, with $q_j(t)$ given by (68). This corresponds to the mass transport across the leaky cleft on the aortic face; (c). $f_1 C_1^*(r,0,t) W^*_1(r,0,t) - \gamma_1 D_1 \partial C_1^*(r,0,t)/\partial z = k_1(C_L - C_1^*(r,0,t))$, at $0 < r < R_1$, $R_2 < r < \xi$ and $z=0$, which corresponds to the mass transport across the normal clefts of the aortic face; (d). $f_3 C_3^*(r,1,t) W^*_3(r,1,t) - \gamma_3 D_3 \partial C_3^*(r,1,t)/\partial z = k_2(C_3^*(r,1,t) - C_L)$, at $0 < r < \xi$, $z=1$, which corresponds to the mass transfer across the (ventricular) face. Here $k_1$ and $k_2$ are the tracer permeabilities of the corresponding endothelial surfaces; (e). $C_1^*(r,z_{12},t)=C_2^*(r,z_{12},t)$, $f_1 C_1^*(r,z_{12},t) W^*_1(r,z_{12},t) - \gamma_1 D_1 \partial C_1^*(r,z_{12},t)/\partial z = f_2 C_2^*(r,z_{12},t) W^*_2(r,z_{12},t) - \gamma_2 D_2 \partial C_2^*(r,z_{12},t)/\partial z$, and $C_3^*(r,z_{23},t)=C_2^*(r,z_{23},t)$, $f_3 C_3^*(r,z_{23},t) W^*_3(r,z_{23},t) - \gamma_3 D_3 \partial C_3^*(r,z_{23},t)/\partial z = f_2 C_2^*(r,z_{23},t) W^*_2(r,z_{23},t) - \gamma_2 D_2 \partial C_2^*(r,z_{23},t)/\partial z$, which corresponds to the concentration and flux are continuous at the interfaces $z = z_{12}$ and $z = z_{23}$.

## D.4. Solution Method

D.4.1 *Filtration model.* Since the boundary value problem for filtration is independent of that for macromolecular transport, one can solve the former separately from the latter.

The boundary conditions for $P_i$ on the aortic face are

$$-\frac{\partial P_1}{\partial z} = (L_p)_{e1}[1-P_1]; \qquad 0 < r < R_1, R_2 < r < \xi, z = 0 \tag{69}$$

$$-\frac{\partial P_1}{\partial z} = (L_p)_{e1}[1-P_1] + [(L_p)_{ej} - (L_p)_{e1}][1-P_1]; \qquad R_1 < r < R_2, z = 0 \tag{70}$$

In principle, this yields a boundary value problem where the thickness $R_2$-$R_1$ of the cleft, the characteristic length over which the pressure varies dramatically from its average value in the cleft to its values far from the cleft, is much smaller than the characteristic distance $\xi$ in the radial direction. In principle, this would require one to retain an extremely large number of terms of the general solution of (62), a number comparable to the ratio $\xi/(R_2-R_1)$, here equal to 31,200. Experience with such problems garnered from [31,89,90] suggests that an accurate solution of (62) subject to these boundary conditions yields a functional dependence of P on r which is essentially uniform across the cleft. Near the cleft, the value then decays to background over an intermediate length scale. The reason for this is that the solutions cannot bend much over such a short distance $R_2$-$R_1$ without extremely large second derivatives when linked by continuity to much larger ($\xi, R_1 >> R_2-R_1$) adjacent regions over which the curvature is significantly smaller. As such, we simplify the problem by setting the pressure $P_1(r,0)$, $R_1 \le r \le R_2$ on the upstream (aortic) surface within the leak equal to an unknown constant $P_R$. Let $C_0=[(L_p)_{cj}-(L_p)_{c1}][1-P_1]$ and $\beta=(R_2^2-R_1^2)/\xi^2$. Using the method of separation of variables, one can easily obtain

$$P_i = [a_{2i-1}{}^{(0)}z + a_{2i}{}^{(0)}] + \sum_{j=1}^{\infty} [a_{2i-1}{}^{(j)}\sinh(\lambda_j z) + a_{2i}{}^{(j)}\cosh(\lambda_j z)]J_0(\lambda_j r) \tag{71a}$$

or, in matrix form,

$$\begin{pmatrix} P_1 \\ P_2 \\ P_3 \end{pmatrix} = \begin{pmatrix} a_1{}^{(0)} & a_2{}^{(0)} \\ a_3{}^{(0)} & a_4{}^{(0)} \\ a_5{}^{(0)} & a_6{}^{(0)} \end{pmatrix} \begin{pmatrix} z \\ 1 \end{pmatrix} + \sum_{j=1}^{\infty} \begin{pmatrix} a_1{}^{(j)} & a_2{}^{(j)} \\ a_3{}^{(j)} & a_4{}^{(j)} \\ a_5{}^{(j)} & a_6{}^{(j)} \end{pmatrix} \begin{pmatrix} \sinh(\lambda_j z) \\ \cosh(\lambda_j z) \end{pmatrix} J_0(\lambda_j r) \tag{71b}$$

The boundary conditions for $P_i$ at $r=\xi$ determine the eigenvalues $\lambda_j$: $J_1(\lambda_j\xi)=0$, $j=1,2,3,\ldots$ The values of the constant coefficients in the matrices on the right side of (71b) depend on these eigenvalues $\lambda_j$. These coefficients can be solved from the boundary conditions on z at the surfaces $z=0$, $z_{12}$, $z_{23}$, 1. Let us begin with those at the aortic surface $z=0$, equations (69) and (70). The procedure at the other surfaces will be similar. We begin by substituting (71b) and the definition of $C_0$ into equations (69) and (70):

$$[a_1{}^{(0)} - (L_p)_{e1}a_2{}^{(0)} + (L_p)_{e1})] + \sum_{k=1}^{\infty} [\lambda_k a_1{}^{(k)} - (L_p)_{e1}a_2{}^{(k)}]J_0(\lambda_k r)$$

$$= \begin{cases} -C_0, & R_1 < r < R_2 \\ 0 & 0 < r < R_1\,, R_2 < r < \xi \end{cases} \tag{72}$$

To solve for the unknown a coefficients in (72), we take the components of this equation with respect to an orthonormal set of basis functions for $C[0,\xi]$. These basis functions are the appropriate collection of Bessel functions (together with the constant function) for the homogeneous Neumann boundary conditions at $r=0$ and $r=\xi$ and the corresponding inner product uses the weight function r. To find these components, we take the inner product of this equation with each of the basis functions; in doing so, we make use of the orthogonality relations for the Bessel functions:

$$\int_0^{\xi} rJ_o(\lambda_j r)J_o(\lambda_k r)dr = \frac{1}{2}\xi^2 J_1^2(\lambda_j \xi)\delta(j,k) \tag{73}$$

where δ is the Kronecker delta. To find the component along the constant function direction, multiply equation (72) by $rJ_0(0r)=r$ and integrate dr from 0 to ξ using the boundary conditions $J_1(0)=J_1(\lambda_k\xi)=0$ to get the relation

$$[a_1^{(0)} - (L_p)_{e1} a_2^{(0)}] = 1 \tag{74a}$$

To get the remaining components of (72), multiply (72) by $rJ_0(\lambda_j r)$ and integrate dr from 0 to ξ, using the orthogonality relation (73) for the Bessel functions $J_0(\lambda_j r)$ to get

$$\lambda_j a_1^{(j)} - (L_p)_{e1} a_2^{(j)} = -\gamma C_0 \tag{74b}$$

where $\gamma = [\frac{2}{\xi^2 J_0^2(\lambda_j \xi)}]\int_{R_1}^{R_2} rJ_o(\lambda_j r)dr$. Next we invoke the same procedure to exploit the continuity of pressures and velocities at the interface $z=z_{12}$. Substituting equations (71) into the boundary condition $P_1=P_2$ at $z=z_{12}$ and rearranging the equation, one finds, in analogy to (72), for $0<r<\xi$:

$$[(a_1^{(0)} - a_3^{(0)})z_{12} + (a_2^{(0)} - a_4^{(0)})]$$

$$+ \sum_{k=1}^{\infty} [(a_1^{(k)} - a_3^{(k)})\sinh(\lambda_k z_{12}) + (a_2^{(k)} - a_4^{(k)})\cosh(\lambda_k z_{12})]J_0(\lambda_k r) = 0 \tag{75}$$

One again multiplies equation (75) by $rJ_0(\lambda_j r)$ ($j=0,1,2,3,\ldots$; $\lambda_0=0$), integrates dr from 0 to ξ, uses the orthogonality relations (73) for the Bessel functions $J_0(\lambda_j r)$ to get

$$(a_1^{(0)} - a_3^{(0)})z_{12} + (a_2^{(0)} - a_4^{(0)}) = 0 \tag{76a}$$

$$(a_1^{(j)} - a_3^{(j)})\sinh(\lambda_j z_{12}) + (a_2^{(j)} - a_4^{(j)})\cosh(\lambda_j z_{12}) = 0 \tag{76b}$$

Treating the condition of continuity of velocity at z=z$_{12}$ in exactly the same manner gives:

$$(K_p)_1 a_1^{(0)} - a_3^{(0)} = 0 \tag{77a}$$

$$[(K_p)_1 a_1^{(j)} - a_3^{(j)}]\cosh(\lambda_j z_{12}) + [(K_p)_1 a_2^{(j)} - a_4^{(j)}]\sinh(\lambda_j z_{12}) = 0 \tag{77b}$$

An identical treatment of the corresponding conditions at the interfaces z=z$_{23}$ gives for the continuity of pressures and velocities there:

$$(a_3^{(0)} - a_5^{(0)})z_{23} + (a_4^{(0)} - a_6^{(0)}) = 0 \tag{78a}$$

$$(a_3^{(j)} - a_5^{(j)})\sinh(\lambda_j z_{23}) + (a_4^{(j)} - a_6^{(j)})\cosh(\lambda_j z_{23}) = 0 \tag{78b}$$

$$(K_p)_3 a_5^{(0)} - a_3^{(0)} = 0 \tag{79a}$$

$$[(K_p)_3 a_5^{(j)} - a_3^{(j)}]\cosh(\lambda_j z_{23}) + [(K_p)_3 a_6^{(j)} - a_4^{(j)}]\sinh(\lambda_j z_{23}) = 0 \tag{79b}$$

Finally, the boundary condition equation (66) at z=1 yields the following relations:

$$[1 + (L_p)_2]a_5^{(0)} + (L_p)_2 a_6^{(0)} = 0 \tag{80a}$$

$$[(\lambda_j \cosh(\lambda_j) + (L_p)_2 \sinh(\lambda_j)]a_5^{(j)} + [(\lambda_j \sinh(\lambda_j) + (L_p)_2 \cosh(\lambda_j)]a_6^{(j)} = 0 \tag{80b}$$

Combining equations (74a)-(80a), one can obtain the matrix relation:

$$F^{(0)} \bullet \begin{pmatrix} a_1^{(0)} \\ a_2^{(0)} \\ a_3^{(0)} \\ a_4^{(0)} \\ a_5^{(0)} \\ a_6^{(0)} \end{pmatrix} = \begin{pmatrix} -[(L_p)_{c1} + \beta C_0)] \\ 0 \\ 0 \\ 0 \\ 0 \\ 0 \end{pmatrix} \tag{81a}$$

where $$F^{(0)} = \begin{pmatrix} 1 & -(L_p)_{e1} & & & & \\ z_{12} & 1 & -z_{12} & -1 & & \\ (K_p)_1 & & -1 & & & \\ & & z_{23} & 1 & -z_{23} & -1 \\ & & 1 & 0 & -(K_p)_3 & 0 \\ & & & & 1+(L_p)_{e2} & (L_p)_{e2} \end{pmatrix}$$

and the missing matrix elements are all zero.

Similarly, for each j=1,2,3,…, by combining equations (74b)-(80b), one obtains the matrix relations:

$$F^{(j)} * \begin{pmatrix} a_1^{(j)} \\ a_2^{(j)} \\ a_3^{(j)} \\ a_4^{(j)} \\ a_5^{(j)} \\ a_6^{(j)} \end{pmatrix} = -\gamma C_0 \begin{pmatrix} 1 \\ 0 \\ 0 \\ 0 \\ 0 \\ 0 \end{pmatrix} \tag{81b}$$

where

$$F^{(j)} = \begin{pmatrix} \lambda_j & -(L_p)_{e1} & & & & \\ \sinh(\lambda_j z_{12}) & \cosh(\lambda_j z_{12}) & -\sinh(\lambda_j z_{12}) & -\cosh(\lambda_j z_{12}) & & \\ (K_p)_1 \cosh(\lambda_j z_{12}) & (K_p)_1 \sinh(\lambda_j z_{12}) & -\cosh(\lambda_j z_{12}) & -\sinh(\lambda_j z_{12}) & & \\ & & \sinh(\lambda_j z_{23}) & \cosh(\lambda_j z_{23}) & -\sinh(\lambda_j z_{23}) & -\cosh(\lambda_j z_{23}) \\ & & \cosh(\lambda_j z_{23}) & \sinh(\lambda_j z_{23}) & -(K_p)_3 \cosh(\lambda_j z_{23}) & -(K_p)_3 \sinh(\lambda_j z_{23}) \\ & & & & \lambda_j \cosh(\lambda_j)+(L_p)_2 \sinh(\lambda_j) & \lambda_j \sinh(\lambda_j)+(L_p)_2 \cosh(\lambda_j) \end{pmatrix}$$

and the missing matrix elements are all zero.

For each j=0,1,2,3,…, inverting the (presumably non-singular) matrix in equation (81) determines the coefficients $a_i^{(j)}$ (i=1,2,3,4,5,6, j=0,1,2,3,…).

This procedure can be carried out analytically using computer algebra packages such as Mathematica or Maple. Here we used Maple package and obtained the solution for the inverse $G^{(j)}$ ($G^{(j)}=(g^{(j)})_{6x6}=[F^{(j)}]^{-T}$). Since the solutions are quite long for $G^{(j)}$ ($j>0$), we only show solution $G^{(0)}$ as follows:

$$
\begin{array}{l}
G^{(0)}[1..6,1]= \\
\{[-(K_p)_3\,(L_p)_{e2}], \\
[\;((K_p)_1(L_p)_{e2}(1 - z_{23} - (K_p)_3\,(z_{12}-z_{23})) + (K_p)1 \; + (L_p)_{e2}\,(K_p)_3\,z_{12})\;], \\
[-(K_p)_1(K_p)_3(L_p)_{e2}], \\
[\;(K_p)_1\,[(L_p)_{e2}(1 + ((K_p)_3-1)z_{23}) + 1]\;], \\
[-(K_p)_1(L_p)_{e2}], \\
[(1 + (L_p)_{e2})(K_p)_1]\}\ /\mathrm{mod1}
\end{array}
\tag{82a}
$$

$$
\begin{array}{l}
G^{(0)}[1..6,2]= \\
\{[-(K_p)_3\,(L_p)_{e2}\,(L_p)_{e1}], \\
[-(K_p)_3\,(L_p)_{e2}], \\
[-(K_p)_1\,(K_p)_3\,(L_p)_{e1}\,(L_p)_{e2}], \\
[\;(K_p)_1\,(L_p)_{e1}\,((L_p)_{e2}(\,1 + ((K_p)_3-1)\,z_{23}\,) + 1)\;], \\
[-(K_p)_1\,(L_p)_{e1}\,(L_p)_{e2}], \\
[(K_p)_1\,(L_p)_{e1}\,(1 + (L_p)_{e2})]\}\ /\mathrm{mod1}
\end{array}
\tag{82b}
$$

$$
\begin{array}{l}
G^{(0)}[1..6,3]= \\
\{[\;(L_p)_{e1}\,((L_p)_{e2}\,(\,z_{23} -1 + (K_p)_3\,(z_{12} - z_{23}))\,-1)\;], \\
[\;(L_p)_{e2}\,(\,z_{23} -1 + (K_p)_3\,(z_{12} - z_{23})\,)\;-1\;], \\
[\;(K_p)_3\,(L_p)_{e2}\,(1 + (L_p)_{e1}\,z_{12}\,)\;], \\
[\,-(L_p)_{e1}\,(L_p)_{e2}\,(\,((K_p)_3\;-1)\,z_{23}\,+1\,)\,z_{12}\;-(L_p)_{e2}\;(1+((K_p)_3-1)\,z_{23}\,) - 1 - (L_p)_{e1}z_{12}\,], \\
[\,(L_p)_{e2}\,(1 + (L_p)_{e1}\,z_{12})], \\
[\,-(1+(L_p)_{e1}\,z_{12}\,)(1+(L_p)_{e2}\,)\,]\}\ /\mathrm{mod1}
\end{array}
\tag{82c}
$$

$$
\begin{array}{l}
G^{(0)}[1..6,4]= \\
\{[\,-(L_p)_{e1}\,(L_p)_{e2}\,(K_p)_3\;], \\
[\,-(L_p)_{e2}\,(K_p)_3], \\
[\;-(L_p)_{e1}\,(L_p)_{e2}\,(K_p)_1\,(K_p)_3\,], \\
[\;(K_p)_3\,(L_p)_{e2}\,(\,((K_p)_1\,-1)(L_p)_{e1}\,z_{12}\;-1)\;], \\
[\;-(L_p)_{e1}\,(L_p)_{e2}\,(K_p)_1\,],
\end{array}
$$

$[\,(L_p)_{e1}\,(1 + (L_p)_{e2})\,(K_p)_1\,]\}\ \text{mod1}$ (82d)

$G^{(0)}[1..6,\,5]=$

$\{\,[\,(L_p)_{e1}\,(\,(L_p)_{e2}\,(z_{23}-1)\,-1)\,],$

$[\,(L_p)_{e2}\,(z_{23}-1) - 1\,],$

$[\,(L_p)_{e1}\,(K_p)1\,(\,(L_p)_{e2}\,(z_{23}-1)\,-1)\,],$

$[\,-(\,(L_p)_{e2}\,(1-z_{23}) + 1)((L_p)_{e1}\,(\,1-(K_p)_1\,)\,z_{12}+1)],$

$-[((K_p)_1\,(L_p)_{e1}\,(z_{12}-z_{23})-(L_p)_{e1}\,z_{12}-1)(L_p)_{e2}\,],$

$[(L_p)_{e1}\,(1 + (L_p)_{e2})((K_p)_1\,(z_{12}-z_{23}) - z_{12}\,)\,-(1+(L_p)_{e2}\,)\,]\}\ /\text{mod1}$ (82e)

$G^{(0)}[1..6,6]=$

$\{[\,-(K_p)_3\,(L_p)_{e1}\,],$

$[\,-(K_p)_3\,],$

$[\,-(K_p)_1\,(L_p)_{e1}\,(K_p)_3\,],$

$[\,(K_p)_3\,(\,(L_p)_{e1}\,(\,(K_p)_1-1\,)\,z_{12}\,-1)\,],$

$[\,-(K_p)_1\,(L_p)_{e1}\,],$

$[\,(L_p)_{e1}(\,(K_p)_1\,(\,(K_p)_3\,(z_{12}-z_{23})+\,z_{23}\,)\,-\,(K_p)_3\,z_{12})\,-(K_p)_3\,]\}\ /\text{mod1}$ (82f)

where mod1= $(L_p)_{e1}\,(L_p)_{e2}\,[(K_p)_1\,(\,(z_{23}-1) + (K_p)_3\,(z_{12}-z_{23})\,)\,-(K_p)_3\,z_{12}]\,-(K_p)_1\,(L_p)_{e1}\,-(K_p)_3\,(L_p)_{e2}$. Collecting the solutions for all of the unknown coefficients that we have determined, and plugging into equations (71), one can obtain $P_i$ in terms of the unknown constant $C_0$ as

$$\begin{pmatrix} P_1 \\ P_2 \\ P_3 \end{pmatrix} = \begin{pmatrix} P_1^{(1)} \\ P_2^{(1)} \\ P_3^{(1)} \end{pmatrix} + \begin{pmatrix} P_1^{(2)} \\ P_2^{(2)} \\ P_3^{(2)} \end{pmatrix} = -[(L_p)_{el} + \beta C_0]B^{(0)}\begin{pmatrix} z \\ 1 \end{pmatrix} - \gamma C_0 \sum_{j=1}^{\infty} B^{(j)}\begin{pmatrix} \sinh(\lambda_j z) \\ \cosh(\lambda_j z) \end{pmatrix} J_0(\lambda_j r)\,, \quad (83)$$

where $B^{(0)} = \begin{pmatrix} g_{11}^{(0)} & g_{21}^{(0)} \\ g_{31}^{(0)} & g_{41}^{(0)} \\ g_{51}^{(0)} & g_{61}^{(0)} \end{pmatrix}$; $B^{(j)} = \begin{pmatrix} g_{11}^{(j)} & g_{21}^{(j)} \\ g_{31}^{(j)} & a_{41}^{(j)} \\ g_{51}^{(j)} & g_{61}^{(j)} \end{pmatrix}$ are known analytically and $J_1(\lambda_j\xi)= 0$.

Finally, we now calculate the unknown constant $C_0$, which is equivalent to determining the unknown, assumed-constant pressure $P_R$ in the cleft. From equation (83),

$$P_R = P_1(R_1,0) = -[(L_p)_{e1} + \beta C_0]g_{21}{}^{(0)} - \gamma C_0 \sum_{j=1}^{\infty} g_{21}{}^{(j)} J_o(\lambda_j R_1) \tag{84}$$

Substituting the definition $C_0 = [(L_p)_{ej} - (L_p)_{e1}][1-P_R]$ gives

$$C_0 = \frac{1+(L_p)_{e1} g_{21}{}^{(0)}}{[(L_p)_{ej} - (L_p)_{e1}]^{-1} - [\beta g_{21}^{(0)} + \gamma \sum_{j=1}^{\infty} g_{21}{}^{(j)} J_o(\lambda_j R_1)]} \tag{85}$$

Equations (83) represent the complete solution for the pressure; combination with (60) yields the water velocity distribution in the valves as well. This solution will act as an input into the convection-diffusion equation for the space-time evolution of the tracer concentration.

D.4.2 *The macromolecular transport model:* With the complicated velocity profile (equations (60) and (83)) derived in the last section, it is unlikely that one can find an analytic solution of the corresponding convection-diffusion equation (67). Consequently, we shall numerically solve this convection-diffusion equation for the macromolecular (tracer) concentration $C_i(r,z,t)$ profiles.

We have implemented an implicit Euler method to solve this problem. The method is an efficient and stable for solving general transport equations of the form

$$\frac{\partial C(\mathbf{r},t)}{\partial t} = F[C(\mathbf{r},t)] \tag{86}$$

where $C(\mathbf{r},t)$ is the concentration, **r** is the position vector, t is time and F is a general convection-diffusion differential operator. With backward time differences, the above equation can be calculated by the implicit Euler steps, vis.,

$$C_{nm}^{k+1} = C_{nm}^{k} + \Delta t F_h[C_{nm}^{k+1}] \tag{87}$$

Here Δt is the time step, $F_h$ is the finite difference form of the convection-diffusion differential operator. $C^k_{nm}$ is the concentration at time $t_k = k\Delta t$, and position $r=n\Delta r$, $z_m = m\Delta z$; k, n, and m are natural numbers.

Since the cell leaky junction ($R_2$-$R_1$) and the thin layer depth ($L_1$or $L_3$) are much less than the radius of the periodic unit (ξ) and the depth of the middle layer ($L_2$), we transformed coordinate system (r,z) to (x,y) coordinate system in order to increase the resolution.

$$r = a_x x^3 + b_x x^2 + c_x x, \tag{88a}$$

$$z = a_y[e^{b_y y} - 1], 0 <= y <= 0.5; \qquad -z+1 = a_y[e^{b_y(-y+1)} - 1], 0.5 < y <= 1 \tag{88b}$$

where the constants $a_x$, $b_x$, $c_x$, $a_y$ and $b_y$ are determined by the following conditions: r=ξ/L at x=1; $r=R_1/L$ at x=0.1; $r=5R_1/L$ at x=0.5 and z=0.0015 at y=0.05; z=0.5 at y=0.5. We used 100 grids in each r and z direction in our calculation. Based on this transformation, there are 4 grids in the thin layer of the valve and one grid for cell leakage. Equation (87) is implicit and thereby in need of an iterative solution. The calculation is easily convergent and stable with a reasonable time step compared with a simple explicit iteration method such as $\{\Delta t<0.5/[(\Delta r)^{-2}+(\Delta z)^{-2}]\}$, which is about $10^{-8}\}$. To check convergence, we halved the time step and recalculated the solution until we found the relative error $\{[C^{k+1}-C^k]/C^k\}$ to have varied by less than $10^{-4}$. This led to a value of $\Delta t=5.2\text{x}10^{-5}$ in our calculations.

D4.3 *Note on the calculation method used in the discussion section below.* Recall that the analytic solution of the filtration problem presented in Section D4.1 for the three-section interposed layer model is, in principle, exact except for the assumption that the pressure is uniform across the thin cleft. Nevertheless, one must still numerically experiment so as to determine where it is safe to truncate the infinite sum on j so as to retain sufficient detail to resolve the relaxation of the pressure field close to the cleft. Once this has been done, one then takes the resulting velocity field, obtained by differentiation of the pressure field, inserts it into the convection-diffusion equations and solves them via the finite difference procedure. Here one must again experiment with grid size so as to guarantee sufficient resolution in the near-cleft region. Rather than implement these two procedures and go through two independent numerical procedures each with the same goal, we have chosen at this stage to solve both the filtration and the convection-diffusion problem by the same finite difference procedure. The goal here is to assess the feasibility of the said three-layer interposed region model and to do some basic calculations for comparison without limited data set. Our ultimate goal is to take much more extensive data and, provided that the current comparison proves fruitful for the data at hand, to then implement numerical calculations based on the analytic solution of the filtration problem. This is in fact the plan before publication. In order to substantiate this approach we note that in Fig. 24c, based on the single layer interposed region model, we present a comparison of both approaches and note how well they agree with one another.

D.4.4 *Constants and parameters used in the model:* Most of the constants and parameters in the models are summarized in table 1, which includes the related references. Several important parameters are illustrated below. As we discussed in the motivation for the three-layer interposed region, the experiments described above strongly suggest that there are thin subendothelial layers sandwiching the main layer of the interposed region and that these thin layers have much higher void fractions than this main layer. That is, there appears to be a mismatch transport parameters at $z_{12}$ and at $z_{23}$ in the valves. The permeability and diffusivity in the thin layers that result from our *ab initio* calculations based on Frank and coworkers' ultra-rapid freezing rotary shadow etchings are much larger than those of the middle layer. These calculations used the images of the proteoglycan monomers, collagen and central filament in these etchings in a fiber matrix model similar to Huang *et al.* [12] for the arterial subendothelial intima. Not surprisingly, many parameters, including the permeability and diffusivity in the thin layers of valves, turn out to be similar to those in sub-endothelial intima of arteries. Since we do not have direct measurements of the transport parameters in the middle section of the interposed layer, we use the same values of the permeability as in the media of the arteries. We use values for the permeability to LDL of the intact endothelial cell layer and for the solute diffusivity in the middle section of the interposed layer from Tompkins' experimental measurements in the valves of squirrel monkey. We discuss the calculated values described above in the beginning of the next section entitled Results and Discussion.

## E. Results and Discussion

### E.1 *Permeability and tracer diffusion coefficient in the thin layers of the valve.*

The Darcy permeability $K_p$ in the subendothelial thin layers, as we have described above, is a function of the fiber spacing $\delta$, the ratio $\beta$ of GAG to protein core length, and the proteoglycan's effective radius $r^*$. The permeability $K_p$ as a function of the core protein spacing $\delta$ is shown in figure 26. As one can see, $K_p$ varies between 0.6 and $1.6x10^{-12}$ $cm^2$ for $\beta$=5~15. Furthermore, these permeability values for HRP and LDL are only about 25% less than those found in the arterial intima [12]. This suggests that the permeability values in the thin layer of valves are similar to those in the arterial intima.

Similarly, figure 27 shows the tracer diffusion coefficient $D_i$ in this tissue as a function of the physiological fiber spacing $\delta$, in which the solute radii $r_s$=3.0 and 11nm represent HRP and LDL, respectively. The value for the molecular diffusivity $D_f$ used for LDL is the value in [30], and that for HRP is the value for albumin, a molecule of similar size, since we don't know the $D_f$ value for HRP directly. This latter value was then modified by using its the effective radius as described in section VIIIB. The results show that the diffusion coefficient for large molecules (LDL) is almost one fourth that for the smaller molecule (HRP) in the thin layer of the valve. We shall also need diffusivities for the thick layer of the interposed region. Since we do not have direct measurements for this region, we note that, neglecting inter-species differences, the values determined by Tompkins *et al.* [43] in squirrel monkey valves for LDL can serve as upper bounds. The reason for this is that Tompkins *et al.* attributed all solute transport to diffusion. In contrast, in our model convection accounts for part of this transport and thus a lower diffusivity can account for the difference. Moreover, although Tompkins *et al* had only a single layer interposed region, the middle layer of our model's interposed region in rat valves comprises over 99% of the total valve thickness. We shall discuss the precise determination of this value in Section E.4 below. Comparison of the resulting D values with those for the thin and thick layers of the interposed region substantiates the mismatch assumed in the postulation of the three-layer interposed region. That is, water permeation as well as macromolecular diffusion should be much faster in the thin layer than in the middle layer of the valve due to the much higher void there.

E.2 *Pressure distribution and velocity profiles in the thin layer.* Figure 28 is the pressure distribution result of the new model for the case of a single leak occurring on the top surface (aortic face, $z=0$) and no leak occurring on the bottom surface (ventricular face, $z=1$). The coordinate $z=0.5$ represents the position in the middle of the valve. The figure shows the pressure distributions as a function of the horizontal direction (parallel to the endothelial cell surface) from the leak at three different depths (perpendicular to the endothelial cell surface) into the valves. Each of these three depths is located in one of the three layers of the interposed region, with $z=.5$ in the middle of the thick layer. Unlike the situation in the artery wall, our new theoretical filtration model shows that about 30% of the total transmural pressure drop occurs across each of the two endothelial cell layers. In Fig. 28, solid and long dashed curves show the position $z=0$ and $z=z_{12}$ respectively. These two curves are very close. Similarly, the dotted curve (for $z=z_{23}$) and the dashed curve (for $z=1$) are also very close. This suggests that there is nearly no pressure drop across these two thin layers of the valve (the thin layer right underneath the top endothelial cell layer and right above the bottom endothelial cell layer), as a simple scaling analysis would predict. The radial gradient in pressure is by far the steepest in the cleft region. Notice how it is significantly damped away from the endothelium. It is this radial derivative of the pressure profile that determines the radial velocity in the thin subendothelial layers and thus the *en face* observed spot size from our experiments. As such, we have reproduced this curve on Fig. 24d for comparison with the result of the preliminary model. The radial gradient of the solid curve has a much longer range of non-zero slope than does the dotted curve.

Figure 29a shows this lateral velocity $U_1$ and $U_3$ in the thin layers at the $z$=0 (aortic) and z=1 (ventricular) faces, respectively. Here again, the velocities U are non-dimensionalized as local Peclet numbers in order to weigh the contribution of the convection relative to diffusion. Similar to figure 28, in figures 29 curves for z=0 and $z_{12}$ are very close, and curves for z=1 and $z$=$z_{23}$ are very close. Figure 29a clearly shows a large lateral velocity (convection dominance in the r direction) in the thin layer near the aortic surface close to the leak and radial convection remains important there even far from the leak. These characteristics decay to almost zero in the subsequent layers in the case of a single leak on the aortic surface and no leaks on the ventricular surface. Figure 29b and Figs. 29c and d, the dimensional versions of 29a and b, show that the velocity in the normal direction (perpendicular to the endothelial cells) is much smaller than that in the lateral direction in the thin layer just below the aortic face. (Note that the z=0 curve exhibits anomalous behavior at the edge of the cleft at r=1 due to the discontinuity in the value of $L_p$ there. There is a relatively high pressure at z=0 very close to r=1 which locally produces a reduced normal driving force across the endothelium. As the distance from the leak increases, the intimal pressure decreases and thus the normal velocity increases. This consequence of the imposed discontinuity disappears at z values far from this endothelium.) By comparing figure 29c and 29d, one can find that radial velocity is about 2 orders of magnitude larger than the normal velocity within about 7-8 cell radii in this thin layer. Therefore, the radial velocity is dominant there in the vicinity of the leakage. This large lateral velocity appears to have the potential to create large spot sizes, clearly extending to at least 7-8 cell radii, where the lateral velocity has decayed to a small value. As we shall see in the next section, this trend will indeed be borne out. Thus it does seem that the mismatch in matrix structure between the thin layer (loose matrix with high permeability) and the middle layer (dense matrix with low permeability) accounts for most of the role that we had attributed both to matrix mismatch and the presence of an internal elastic laminar in the artery wall. That is, it causes a large radial pressure non-uniformity, and thus radial velocity, near the leaky endothelial cell. Since, as we have seen, the vertical velocity is significantly smaller than the lateral velocity in the neighborhood of the leak, the HRP spot will grow mainly in the lateral direction in valves, as it does in arteries.

Figures 30 and 31 show dependencies similar to those in figures 28 and 29 for the case of no leak on the aortic side and one on the ventricular side (figures 30) and one leak on each of the two faces (figures 31). Similarly, curves for $z$=0 and $z_{12}$ are very close, and curves for $z$=1 and $z$=$z_{23}$ are very close. In the former case, note that the dimensional velocity in the thin layer beneath the upstream, i.e., aortic, face is now predominantly vertical, whereas that near the downstream, i.e., ventricular, face is now predominantly horizontal. This illustrates the barrier function of the lower endothelium coupled to the high permeability of the lower thin layer. Fluid entering almost uniformly through the leak-free aortic face traverses the thick layer and then flows inward through the downstream thin layer towards the ventricular face's leak. When we couple this flow to the convection-diffusion equation, we can formulate certain expectations. First, if diffusion is not negligible relative to convection, we can expect some tracer to diffuse in the direction opposite to the prevailing flow, from the lumen through the leak in the ventricular face and into the valve's lower thin layer. Moreover, since diffusion within this layer is much easier than through the thick layer, a large diffusivity could actually lead to a large spot on the ventricular face as well. Convection dominance in these regions, on the other hand, could keep such spots from forming in this way; it could, though, sweep whatever tracer crosses the aortic face into the ventricular face's thin layer to be swept out mainly through its leak. It was Tedgui and Lever [92] who noticed these possibilities long ago. As we shall see, this concept, as well as the case below, will be very useful in explaining the tracer concentration profiles across the leaflets of Tompkins *et al*'s squirrel monkeys [43].

As for the case of leaks on both faces (figures 31), there are large lateral velocities in each of the two thin layers as fluid spreads from the upstream leak and then converges towards the downstream leak. The prevailing flow in the thick layer is still vertical. The large lateral velocities near the ventricular face clearly corresponds to the fluid looking for the easier way out of the leaflet through the large leak that offers less resistance to flow than the normal clefts.

E.3 *HRP concentration profiles.* After one has found the velocity profiles, one can analyze the time-dependent macromolecular concentration profiles in the thin layer of the valve. In order to compare this theory with our experiments, we focus on macromolecular (HRP) transport. Due to a lack of direct observation, we take the value of the HRP diffusivity in the thick layer to be the average value $11\times10^{-9}$ $cm^2/s$ determined by Tompkins *et al.*[43].This calculation is very insensitive to the tracer permeability of the two endothelia . In fact, this insensitivity is the basis of this spot size measurement. We take a value $5.2\times10^{-7}$ cm/s which is about three times LDL's value, simply because a value is needed. The values in Tompkins ignored isolated leaks and had very high standard deviations. Thus they were not reliable for our study. With these values, Figure 32 plots the radial HRP concentration profiles after different circulation times in the thin layer of the valve leaflet. As usual, we normalize the HRP concentration by the lumen concentration. The abscissa again represents the position in the thin layer normalized by the endothelial cell radius. Note that since fiber matrices fill the valves, the available volume for HRP is everywhere less than 1. Furthermore, since there are matrix mismatches at the boundaries $z_{12}$ and $z_{23}$ between layers of the interposed region, there is the possibility of macromolecular (HRP) sieving in the thin layer of valve leading to local concentrations ($C>1$) above the lumen value.

Figure 32 shows that the lateral convection of the macromolecules in the thin layer ($0\leq z\leq 150$nm) is indeed very large for the HRP transport close to the cleft. Thus even over the shortest times of circulation of the corresponding experiments, the HRP spot generated in this region will be large. The concentration in the leading edge of the convective front is much lower than the lumen HRP concentration. Since the HRP concentration is not yet zero in the thin layer even for very large values of r/$R_1$., the exact spot size will depend upon the level of delectability of the HRP reaction product in the particular experiments in question. Since there is uniform seepage on the surface of the valves ($k_1$,$k_2$), the concentration in figure 32 does not go to zero as r gets large; it slowly decays to a non-zero background. The figure does show a non-trivial slope even at 7-8 radii, and thus the spot size will most certainly fall within this domain, in agreement with our experimental observations. It is noteworthy that such HRP spot size values are again similar to those found in the artery wall. As we did in the artery study, we choose a threshold value $C^+$ of C to define the edge of the spot in order to fit the experimental data at a single circulation time and maintain this value for all other times. The threshold value for our model, when the 60 seconds circulation time is used as the point of reference, is $C^+$=0.127. Figures 33 show the corresponding early time growth of the leakage spots. The filled circles symbol shows the short time *en face* HRP spot growth after 30 seconds, 1 minutes, 2 minutes and 4 minutes circulation from both the above theory (figure 33a for 30 sec. and figure 33b for 60 sec. as the reference curves) and our experimental measurements. The figures show that the theory (solid curves) is consistent with the experiment data.

E.4 *LDL concentration profiles in the valve leaflets.* In a manner exactly analogous to the way in which we obtained the HRP concentration profiles in the last section, Figure 36a calculates and plots the corresponding LDL concentration profiles for a similar experiment that substitutes LDL for HRP as the tracer molecule. To generate such a figure, one must decide on values for the permeabilities $k_1$ and $k_2$ of the two-endothelial layers to LDL and / or the diffusivity D of LDL in the thick layer. To this end we appeal to figure 2 of Tompkins *et al.* Curves 2-5 and 9. Let us focus on curve 9, which we reproduced in figures 34 and 35. We begin by using this curve to check our numerical code. We turn off convection and set the void fractions of both the thick and thin layer equal to Tompkins *et al.*'s value of 0.17. Using Tompkins et al.'s values for $k_1$, $k_2$ and D, we recover his fit, as shown in figure 34. In 35, we introduce the convection from the last section. $k_1$ and $k_2$ control the total amount of LDL entering the value during the experiment. However, convection will tend to skew the distribution in the downstream, i.e., ventricular direction, whereas D will tend to smooth it out. Thus, upon resting convection and the large $\varepsilon$ in the thin layers, we anticipate needing to readjust $k_1$ upwards and $k_2$ downwards with $k_1$+$k_2$ fixed so as to obtain a good fit to curve 9. Fig. 35 shows that the fit for, $k_1 = 14.\times 10^{-9}$ cm/s, $k_2 = 4.\times 10^{-9}$ cm/s, $D = 7.8\times 10^{-9}$ cm$^2$/s. we shall keep these values fixed for all further calculations. Note that in the absence of leaks, the problem is still one-dimensional, Thus there is full symmetry in the x and y directions, where z is the direction normal to the endothelial surfaces.

Let us return now to Fig. 36a. This figure contains the concentration of LDL as a function of radial distance from the center of the single leaking cell on the aortic face at different LDL circulation times. If we take a level of detectability as 0.127, then Fig. 36b shows the spot size growth as a function of time. Notice that as in the artery wall, the

LDL spot growth is substantially slower than that of HRP. Note that since LDL is much larger and thus diffuses much more slowly, the circulation times vary from 1 minute to 30 minutes, including the steady state, as in Tompkins *et al.* ' s experiments [43]. As in the HRP experiments discussed in the last section, the mismatch in matrix structures in between the three layers of the interposed region in the valves generates mismatches in volume availability for LDL, and thus in LDL diffusivity, between these layers as well. In fact, a conservative upper bound for the LDL space in the artery wall's media is that for the much smaller molecule albumin, which is well known to be 0.08 [92]. This is much smaller than the value 0.5 that we calculated [12] for LDL in the arterial intima. By comparison, the LDL space that we calculate for the thin layer in the valve is 0.602; for the thick layer, we take the Tompkins *et al*'s experiment value 0.0925 [43] which, as noted, is also a very conservative upper bound. Below we shall use Tompkins *et al.*'s data in a bit more clever way to extract a better value.

As a result of the noted mismatches, one can again expect LDL concentration sieving in the thin layer of valve. Figure 36a indeed shows this elevated LDL concentration close to the leak that then decays away from the leak. Note that this sieving actually increases the local LDL concentration near the leak with time until a steady state is reached. Again, as one would expect for a convection-dominated process, the spot size reaches a steady value, here after about 10 minutes, although the concentration profile still varies very slightly for approximately another half-hour. This time of about 10 minutes is longer than the 4-5 minutes in the artery wall. It must be noted though, that the aorta contains what appears to be a much more effective barrier, the fenestrated IEL, to fluid and macromolecular transport, in addition to the matrix mismatch between layers. Indeed, it is remarkable that the absence of an IEL in valve only has a minor qualitative effect on the flow patterns and the dominant effect is the result rather of the matrix mismatch alone. Note the spot sizes are significantly lower for the larger tracer.

Let us now turn again to Tompkins *et al'* experiments on squirrel monkey and rabbit valve leaflets. Recall that his data (see Figures 37) show profiles of various magnitudes and shapes, including high maxima only on the aortic face, only on the ventricular face, on both faces, or only small maxima on both faces. We note again that the variation in Tompkins *et al*'s curves does not result from a difference in experimental procedure, yet has been until now unexplained. Here we compare individual measurements from their paper with the four possible calculations described earlier, and thus attempt to provide just such a rational explanation.

As we have already discussed, it is the profiles that have uniformly low concentrations with only small maxima near both endothelia (note the scale of the ordinate, which is about a factor four smaller than those of the other figures) that we surmise come from valve leaflets that during the course of the experiment had no leaks on either the aortic or the ventricular faces. In that case, the transport is simply one-dimensional (in the z-direction), accounted for by convection and diffusion and the pressure and concentration fields are uniform in the horizontal direction. Consequently the lateral velocities are zero, and one would only observe a faint uniform staining on the ventricular face, rather than a localized spot. Since both the filtration and the convective-diffusion problems are by far the simplest here, we have used their solution and these data to find values for the permeabilities $k_1$ and $k_2$ of the two endothelia to tracer and the diffusivity of LDL in the middle layer as outlined above. We then retain these values for the solutions having one or more leaks on each valve face, which we compare with Tompkins *et al.*'s other experimental profiles.

(Alternatively, another rough method for estimating $k_1$ and $k_2$ is to appeal to our artery wall work that has been given in great detail in the first part of this thesis. In Section IV, we calculated the liposome size distribution that should form in a normal rabbit that had been on a high cholesterol diet for 10-16 days. The intimas of these rabbits were spatially highly heterogeneous, with certain areas having been subject to close-by leaks and others mainly only far-away leaks. However, in order to obtain the magnitude of small liposomes found in experiment, we found it necessary to superimpose on this cellular-leakage-derived LDL a uniform seepage from the lumen across the endothelium and into the intima. We set the magnitude of this uniform (in the lateral direction) leakage equal to the value that produced the best agreement with the measured size distribution. It seems reasonable to take this same value as a given here and to calculate the resulting LDL dependence on z. That value would be $1.4\times10^{-8}$cm/s, which compares well ($9.3\times10^{-9}$ cm/s) with the values determined from Tompkins *et al.* Clearly the values from the last paragraph are more reliable.)

Figures 38 show the LDL concentration across the valve depth (z), including both sample Tompkins *et al*'s measurements and our theoretical calculations that we discuss presently. It is critical to mention that these curves are not fits, but rather theoretical predictions based on parameters that have been or will be (see below) determined and/or calculated by the methods already discussed, methods unconnected with the present experiments. We choose a configuration of leaks on each face, calculate the result using the model and then compare it with a data set from Tompkins *et al.* that looks most similar.

As we have mentioned several times above, each valve face may have zero, one or more leaks. As throughout, the abscissas of these figures represent the normalized depth (z) into the valve leaflets from the top face inward. That is, position z=0 is at the aortic surface; position z=1 is at the ventricular face. The ordinates are the normalized local (in z) LDL concentrations per unit total volume (including matrix) of valve ($\gamma C$). In particular, to generate each figure, we calculated the LDL concentration as a function of r, z and t. We then choose the t value corresponding to the experiment. As noted a final fitting still needs to be done with regard to the implicit experimental spatial averaging. That is, Tompkins *et al.* cut the valve into $1\mu$ thick sections by slicing normal to the endothelia (i.e., in the z direction) They then report autoradiographic spot counts as a function of the depth z into the valve. Clearly the have averaged over the thickness ($1\mu$) of the slice- that is , in the x - direction - as well as in the transverse or y-direction. They do not , however, report the y distance over which they have averaged. Thus we take this parameter to be a fitting parameter, again to be fit once and then fixed for all subsequent curves. We do this in Fig. 38a. We consider curve 6 of Tompkins *et al.*'s Figure 4 and compare it with the case of a single aortic face leak and no ventricular faces leak. The value of y that we have determined, mainly scales the curves in question, as well as slightly affecting the steepness of the concentration in the thin layers. Finally, we have averaged over a $\Delta z$ of 10% of the value thickness in the measurement in question in Tompkins *et al*'s experiment.

Let us examine Figure 38a, the situation of one leak on the top and no leaks on the bottom faces. In this situation, a high LDL concentration appears near the top surface region and a much lower LDL concentration appears near the bottom surface region. Filled circles represent the experiments performed by Tompkins *et al.* [43], and the dotted curve represents our new theoretical model's results. The shapes are similar and with future parameter adjustments ($k_1$, $k_2$, D from adjustment of fit in Fig. 35) and is anticipated to be much better, including a slight turn-up in the profile near the ventricular face. This should result from the LDL that crosses the aortic valve having been swept downstream to the ventricular face and not being able to exit by convection and from the (reverse) tracer permeability of the ventricular face. See Fig. 38 for such a shape.

Figure 38b is for one leak on the top surface and one leak on the bottom surface. The data are from Tompkins *et al.'s* Fig 2, curve 10. This profile is similar to that in figure 38a, but the model, with the improved parameters, should show no pronounced turn-up near the ventricular face. In contrast to Fig. 38a, tracer entering through the aortic face can simply be swept out of the valve by the flow that converges to the ventricular face's leak. Since near the leaks convection dominates over diffusion, the back-diffusion through the ventricular face's leak(s) is ineffective in producing significant LDL concentrations in the valve's interior adjacent to the ventricular face other than by quick diffusion after animal has been sacrificed and before the fixation is complete (circa 20 minutes).

Let us now examine figures 38c and d. We begin with their characteristics. In Fig. 38d, the concentration of LDL in the valves is significantly smaller than in the previous two figures. Moreover, the concentration is much higher at the downstream than on the upstream leaflet face. Curve #1 in Fig. 37, on the other hand, has an LDL concentration that is more than a factor of two larger than those in Figs. 38 a and b. It also has higher concentrations near the ventricular face than near the aortic face, but the width of the high concentration region near this face is noticeably wider in curve #1, Fig. 37 than in 38d. The simplest way of trying to explain these shapes (ignoring for the moment the magnitudes) of these curves is to consider the case of no leaks on the aortic face and one or more on the ventricular face. A similar theoretical curve for Curve #1 figure 37 for one ventricular leak (not shown) shows, however, that this scenario would indeed lead to a concentration maximum at the ventricular face, but it would be much thinner than that observed in these figures. As such, it does not seem capable of explaining them.

Another possibility is the situation where at the beginning of the experiment, one or more leaks are open on the aortic face, but close during the course of the experiment. This possibility is not as far fetched as it may sound. Recall the mean lifetime of a leak is on the order of one hour, and the experiment lasts 30 minutes. So the potential exists for the experiment to have caught one or more leaks open for only part of the experiment. In order to test this possibility, at least qualitatively, to see if it generates the correct shapes, we performed the calculation in Figure 38c. It considers no ventricular leak and a single aortic leak that has been open for 10 minutes and then closes. The figure plots the concentration profiles across the valve for various times after the aortic leak closes. Notice how the shape of the profile changes with time. At first, it resembles the data in Fig. 38a, with a maximum near the aortic faces and a uniformly convex shape that rises at the ventricular face. However, after the leak closes, the aortic supply of tracer is almost cutoff and convection sweeps the pre-existing tracer downstream. This quickly decreases the concentration near the aortic face and increases it downstream, leading to a rising profile. The peak near the ventricular face grows with time. The theoretical curve in Figure 38d (one leak on the aortic faces closing during the experiment and no leaks on the ventricle face) show the result of this type of model as compared with the experimental curves. It is worth noting that this scenario would lead to a valve that, when viewed *en face*, would display only a light, spot staining on the ventricular side of the valve leaflet and essentially none on the aortic face. This staining pattern would result despite the fact that the calculation is now both two-dimensional and time-dependent.

Note that the numbers of aortic leaks were chosen for this figure and for curve #1, Fig. 37 so as to control the magnitude of the concentrations in the valves, and thus would differ between these two figures. One can estimate the product of the number of aortic leaks and the amount of time that these leaks would have to have been open (total leak-open time) from figure 38a. One could simply integrate the total amount of LDL present in the leaflet at the time of the experiment and comparing it with the influx rate found in the calculation that generated the theoretical curve in figure 38a. This yields a lower bound on the total leak-open time, since it neglects efflux. The value we find is for this lower bound is 5 minutes and for the best fit of figure 38d with the data is 10 minutes. This would be consistent with about 50% of the LDL that entered the leaflet during the experiment also leaving it during that time. Note that the difficulty in matching the magnitudes may be the result of the LDL volume availability in the larger animal (the monkey) may be different than for the smaller animal (rabbit).

In summary Tompkins were unable to explain the wide variation in apparent valvular endothelial permeabilities in different regions and at different times. Their one dimension diffusion model is not able to account for their experiments without attributing the variation in results simply to a variation in endothelial permeability, without further insight into the reason for this variation. In contrast, our models suggest that different leak occurrences on the two leaflet faces and different open times of the leaks during the course of Tompkins' experiments may have been the source of the very different trans-valvular LDL concentration profiles that he observed. Our theoretical model shows that the localized leakage sites and transient leaks on different faces generate different concentration profiles. Thus, our new theoretical models (a two dimensional diffusion and convective model) can offer a good explanation for some their experiments. We plan on continuing with these calculation to show similar explanation for the remaining curves in Fig. 37, all with the same fixed values of $k_1$, $k_2$, D, and y. Clearly, an experimental test where one looked both at the existence and number of leaks on leach of the two faces and at the trans-leaflet tracer profiles would be able to test this hypothesis.

Before leaving the data in Fig. 37, we would like to reconsider the importance that we have placed on convection in this process. Over the cardiac cycle, The valve is completely closed, and thus the leaflet expressions a large pressure drop across it, for 60-70% of the cycle [96,97]. One might argue that since during 30-40% of the cycle, the leaflet suffers no pressure drop, that the only process that could be important is diffusion. However, as we have shown the HRP spot size in the valve is almost as large as that in the artery. If there were only diffusion and no convection, even with the existence of isolated leaks, and the three layer interposed region and with the use of the diffusivity that we calculated from fiber matrix theory for the thin layer. The calculated spot size can not match the experimental value --See Fig. 33c. This stands in contrast to the situation with convection. In adding diffusion alone, through a localized leaks could not account for the total mass of tracer swept into the valve by convection, which the data display that the flux rate through leakage junction by convection is about 4 order larger than that through the normal junctions. Thirdly, shapes such as curve 1, Fig. 37, seen to only by achievable by virtue of convection. Note the diffusion only fit of Tompkins *et al.* nisses the shape completely. Finally, our studies show that convection occurs. Its importance simply arises by virtue of comparing its calculated effect relative to that of diffusion.

We have found that HRP and LDL concentration profiles in valves, structures that do not contain continuous IELs as do the artery walls of large arteries. Nevertheless, the tracer leakage spots calculated from our theoretical two dimensional models are surprisingly similar to those generated for arteries having this IEL barrier. This suggests that it is the mismatch in transport parameter, present in both the artery wall and in valves, that plays the dominant role in creating spot sizes and directing the convective-diffusive flows. Interestingly then, the IEL in the artery appears only to play a subsidiary role.

changing the spot size quantitatively by on the order of 20%, and not the controlling role. This may have important consequences for the transport of lipid into the walls of other vessels and their associated potential for and susceptibility to atherosclerosis.

## IX. Combination with of lipid transport and liposome formation and growth models

*Method:* After having obtained the LDL concentration profiles in the valve leaflets, we must now combine these results with the liposome formation and growth model used in arteries in order to attempt to explain liposome formation and growth in valves. The premise, again, is that the liposome formation and growth processes should be tissue-independent, since they reflect local lipid/matrix interactions, whereas the vessel transport is clearly dependent on both the architecture of the vessel in question as well as on the conditions to which it is exposed.

Since there are at least four possibilities for leak occurrence (leak on upstream or downstream face, leak or no leak on both faces), there are four different LDL concentration profiles in valves for short times. We generated a random function for leakage occurrence on each of the two faces and then obtained the corresponding leak-dependent LDL concentration profiles. Then we extended the liposome formation and growth models for arteries to introduce spatial variation in the similar manner employed in arteries. In contrast to the two dimensional variation of the liposome formation in the arterial intima, macromolecular transport in valves is by nature three-dimensional. As such, we chose a cubic grid corresponding to an area of valve (say 40 cells x 40 cells x 5 effective endothelial cell diameters), which is large compared with the extent of a single leak.

We assumed that leaks occur at random locations (x,y,0) and (x,y,1) in these two surfaces according to a Poisson process (for occurrence time t and duration time w). We take the values for t and w to be one hour and one hour, just as in the artery wall. We do this because we do not have any direct measurements of these quantities for the valve. As it turned out in our simulation, the two faces had, on average, about one cell leaking together at any given time. We assumed that the leaks generated LDL profiles with either the edge of the calculation corresponding to the edge of the leaflet (zero or one leak per leaflet face) or with periodic boundary conditions in x and y (more than one leak on a face), in analogy to the artery wall periodicity in section IV. Figure 39 shows the numerical simulation's cubic grid. The top and bottom faces represent the two endothelial cells surfaces. The four faces perpendicular to these two surfaces represent the periodic boundaries or the edges of the leaflet.

As in the simulation for the arterial intima, we shall begin with liposome-free valve. For each leak, one can obtain corresponding transient three dimensional LDL concentration L(x,y,z) as a function of x , y and z from our new theoretical two dimensional (axisymmetric) convective-diffusion solutions in the valves. Using the simplest (nucleation and polymerization only) liposome model developed for arteries, we can input the local instantaneous LDL concentration and integrate it forward in time at each grid point. This leads to a localized liposome size and number distribution at each grid point at each time. At the end of a time corresponding to the time of Frank *et al*'s rabbit feeding experiment we halt the simulation and sum up the local distribution of liposome sizes at either all of the sites of the grid or just at those corresponding to the thin layers (since the crack planes of Frank's work probably only sampled those regions) to get the overall distributions. We then compare these results (figures 18, 19 and 40) with the cholesterol-fed rabbits data generously provided by Frank (Section VIIC), and attempt to explain the liposome histograms in valves.

*Results:* In this section, we discuss the new model's simulation for predicting the liposome size distribution in the valve leaflets of rabbits subjected to the short time feedings corresponding to Frank's experiments. Frank *et al.* (personal communication) performed their feeding experiments for 29 days before sacrificing their rabbits and examining the rabbits' aortic valves. The resulting liposome histogram is shown in figure 40 by the solid curve. This figure shows that a histogram that is similar to that obtained from the rabbit aorta after a 10-16 day high cholesterol feeding experiment; that is, there exists a large amount of small size of liposome and a small, but non-negligible amount of large sized liposomes. Unlike in arteries though, Frank's experiments shows that in valves there are liposomes with diameters larger than 170nm. The amount of these liposomes is only 0.30% of the total liposome numbers in valves, but it is still novel. Our model's simulation is also show in the figure as the large size bar in figure 40 with the dashed curve. The model-generated amount of large sized liposomes is the far right bar, which accounts for only 0.49% of the total liposome number. However, otherwise the figure shows that the model does quite well. Note that there are no new adjustable parameters used in this fit. The uniform seepage invoked earlier is now taken into account by the values of $k_1$ and $k_2$ from the convection-diffusion equation discussion. Thus, our two-dimensional axisymmetric theoretical diffusion and convection model, combined with even the simplest liposome formation and growth model taken from the artery work, can explain Frank's ultra-freeze etching experimental valvular data for short time high cholesterol fed rabbits.

## Part four Outlook and future work

### X. Conclusions and outlook

*Conclusions:* Our experiments have shown that macromolecular transport across the valves endothelium is localized, which is similar to the situation in arteries. Secondly, our tracer spot size experiments indicate that there exists a mismatch in transport parameter in the valves, which seems to play the role, formerly ascribed to the IEL in arteries, of directing the convective-diffusive transport into the tissue to form a large spot from a small leak. Third, our new macromolecular transport model in valves can successfully explain the trans-valvular LDL concentration distributions measured by Tompkins *et al.*'s experiments on squirrel-monkey valves. Finally, the new transport model, combined with even the simplest of the liposome formation and growth models developed in the artery work, can successfully explain liposome formation and growth in valves.

*Outlook for future work:* Experimental: Before we perform further research, we would like to carry out the experiments to directly test whether the thin layer of the valves actually exists. In order to do this, we might use perform the ultra-rapid freezing/ rotary shadow etching technique [8, 40] to visualize the three dimensional structure of the proteoglycan matrix in valves, while taking care to see how close the crack plane lies to the endothelial surfaces. We need to see if the matrix structures from different depths in the valves are different, especially for the areas close to and far away from the endothelial cell layers. Our hypothesis is that Frank's crack planes probably were in these region, because the sparseness of the matrix structure there made these planes the weak points in the valve's structure. As such, we would try to confirm this as well as try to get a crack plane well into the thick layer in order to directly show that its structure is much denser.

We might also use monoclonal antibodies technique [88] to perform immunolocalization studies to see if the proteoglycan structure near the endothelial cell layers is different from that far away from the endothelial cell layer.

Finally, we would like to try to perform experiments where we introduce tiny, i.e., 10 nm bubbles or microspheres and try to directly measure their diffusivities in the different layers. Unfortunately, the size needed for such microspheres is practically molecular, in which case it would be difficult to make such measurements under realistic conditions. Moreover, in order for these bubbles to freely diffuse, rather than be convected, the valve would have to be in an environment where it had no pressure drop across it. This, as we noted in earlier work on the effect of transmural pressures on transport in the artery wall, could significantly influence the structure of the thin layers.

Theoretical and Experimental: The results discussed above suggest that one can successfully describe the transport and accumulation of lipoprotein cholesterol from the lumen into the artery wall by transport and reaction equations. In addition, it appears that the reactions of lipoprotein cholesterol with extracellular matrix that lead to liposome formation and growth and thus to subendothelial lipid accumulation, at least carry over to the valve and may be tissue-independent. This begs the question, can we extend these treatments to learn that how LDL transports into other vessel (i.e., veins, pulmonary arteries, etc.) walls and structures? Can we then begin to understand why calcification and atherosclerosis occur only in big arteries and in valves and not in other vessels? One surprising result we have found in the valve work is that the arterial IEL doesn't seem to play as controlling a role as we had previously thought in terms of the flow pattern; rather, it seems to be the loose subendothelial matrix and the matrix mismatch between subendothelial layers that plays this role. Thus it is possible that the general flow patterns that we have encountered are not restricted to the artery wall and that they are actually similar to those found in other vessel walls. This would presuppose, however, that other vessels also had intima-like structures, as in the case of the valve, despite the absence of continuous IELs. We might guess that many types of vessels may have intima-like layers due to a sparse matrix layer laid down by endothelial cells that abuts against the deeper and denser internal matrix. This would, of course need to be experimentally tested. If this turns out to be the case, it is conceivable that despite the lack if IELs in other vessel walls, the convective-diffusive flow patterns in these vessel walls may still be similar to that in the artery, albeit at much lower driving forces, i.e., transmural pressures. Since Darcy's law satisfies Potential flow, its streamline pattern would be independent of the driving force. However, the pressure difference ($\Delta p$) controls how much lipid is delivered into the tissue wall. Therefore, such considerations, such as wall architecture and typical driving force to which it is exposed, may allow the construction of transport and accumulation theories that can distinguish the different likelihood of different vessels towards atherosclerosis. This could in principle lead to patient-specific choices of the vessel to be used in coronary bypass procedures in order to minimize the likelihood of rapid restenosis.

To begin testing this vision, one needs to begin by experimentally testing if indeed such matrix mismatches exist in a wide variety of vessels. One would then need to investigate the flow patterns and lipid accumulation in those vessels and, in particular, the endothelial permeabilities in these vessels and the lipid accumulation as a function of transmural pressure in these vessels. Such a purview can potentially be the basis of a multi-year, experimental and theoretical research program.

**Table legends:**

**Table:**

Table 1. The constants and parameters

| | | | | | |
|---|---|---|---|---|---|
| L(μm) | 100 | (43) | μ(g/cm/s) | 0.0072 | (32) |
| h(μm) | 0.15 | (a) | $D_m$x$10^8$ ($cm^2$/s) | 1.10(HRP)<br>0.78(LDL) | (43) |
| Δp (mmHg) | 30 | (97) | $D_i$x$10^7$,i =1,3 ($cm^2$/s) | 4.09(HRP)<br>1.02(LDL) | (c) |
| $R_1$(μm) | 11.7 | (b) | $(K_p)_i$ x$10^{12}$ ($cm^2$) | 1.1 | (c) |
| ΔR(nm) | 20 | (70) | $\gamma_m$ | 0.14 (HRP)<br>0.0925(LDL) | (43) |
| $(L_p)_{ci}\times10^8$ cm/(smmHg) i=1,3 | 15.76 | (72) | $\gamma_i$, i=1,3 | 0.92 (HRP)<br>0.60 (LDL) | (c) |
| $(L_p)_m\times10^{11}$ ($cm^2$s/g) | 7.9 | (57) | $D_f\times10^7$ ($cm^2$/s) | 6.8 (albumin)<br>2.06 (LDL) | (94)<br>(30) |
| Φ | .00035 | (b) | $(K_p)_m$ x$10^{14}$ ($cm^2$) | 1.0 | (57) |

(a) is the reference of A. Huang's experiment; (b) is the reference of Y. Yin's experiment; (c) is the reference of the fiber matrix model combined with Joy Frank's ultra-rapid freeze etching experiments [40].

**Figure legends:**

**Figure 17.** Valves of cholesterol-fed normal rabbits (M. Simionescu [41]), after three weeks of a high cholesterol diet. Monocyte-derived macrophage right underneath the endothelium shows its nucleus (n), peroxisomes (p), and small granules (g), bl, basal lamina. x18000.

**Figure 18.** The extracellular matrix in the aortic valve of cholesterol fed normal rabbits has been clearly imaged via electron micrograph of an ultra-rapid freezing / rotary shadow etching. After 29 days of feeding, extracellular liposomes in the aortic valves were observed by Frank *et al.*[40]. Final magnification is 88,560.

**Figure 19.** Freeze-etch micrograph shows collagen fibers within the aortic valves for the normal rabbits after 29 days of a high cholesterol diet. Such figures allow compilation of liposome number and size distribution [40]. Final magnification for this sample of the aortic valve is 51,840.

**Figure 20.** Aortic valve anatomy. The top figure is a circular structure, which is the view from aortic side. The cross section of the aortic valve displays its detailed microscopic anatomy. The aortic valve leaflet is comprised of the two opposing layers of endothelium and an interposed collagen matrix. The upper surface is called the aortic face and the lower surface is called ventricular face. Figure taken form Tompkins *et al.* [43].

**Figure 21.** Electron micrograph of rat aortic valve leaflet four minutes after HRP injection. Dark staining just below endothelium demonstrates that the density of the HRP is relatively high right underneath the endothelial cell layer and drops abruptly deeper into the leaflet although there is no IEL in the valve. This suggests that there is a mismatch in matrix structure in the valves.

**Figure 22.** A matrix model for calculating the transport parameter in the thin layer of the valve. In the top view, $\delta$ is the average of fiber spacing, $r_M$ is the monomer radius and $\xi$ is the radius of the cylindrical region. The other figures show the structure of proteoglycan aggregate. $\alpha$ is the length ratio of the monomers to the central filament. $\beta$ is the length ratio of the glycosaminoglycans (GAG) to the proteoglycan core protein (PCP).

**Figure 23.** *En face* experiments for the aortic valves. The figure is obtained by light microscopy after 30 seconds of HRP circulation time and 45 seconds of Harris' Hematoxylin staining. The primary findings are that HRP transport across the endothelial cell layer is localized as in the large arteries. The endothelial cell layer size and the leakage frequencies are similar to those in arteries. The small dark circles are the nuclei of the endothelial cell. The brown spot is the leakage spot size, which is comparable to that for arteries.

**Figure 24a.** Tompkins *et al.*'s experimental results [43]. Horizontal coordinate represents the depth into valve and vertical coordinate represents the non-dimensional LDL concentration.

**Figures 24b,c.** Our preliminary valve transport model for fluid filtration (b) and convective-diffusive tracer transport (c). Interposed larger in valve is considered as a uniform matrix (one layer model). These figures also show the detailed boundary conditions for fluid and convective-diffusion problem.

**Figure 24d.** The comparison of the pressure in valve between our preliminary model and our new model that containing a mismatch in matrix structure. The preliminary model considers only a uniform matrix in the valve is interposed region. Aortic valves are considered as all intima surrounded by upper and lower endothelial cells. There are two lumens, one above the aortic face at high pressure, the other below the ventricular face at lower pressure. The new model considers a matrix mismatch in interposed region (3-layer model) as described in the text.

**Figure 25a.** The new 3-layer model for transport in the aortic valve (fluid mechanics). There is one leak on the top surface and no leak on the bottom surface. Horizontal coordinate is r, and vertical coordinate is z., and the origin of the coordinates is the center of the leaking cell. Governing field equation is Laplace's equation. At the interface of the layers, the pressure and velocity are continuous.

**Figure 25b.** The new 3-layer model for transport in the aortic valve (diffusion and convection of tracer). There is one leak on the top surface and no leak on the bottom surface. Horizontal coordinate is r, and vertical coordinate is z, and the origin of the coordinates is the center of the leaking endothelial cell. Governing field equation is the two dimensional unsteady state convective-diffusive mass transport equation. Similarly, at the interface between the layers, the macromolecular concentration and mass flux across the interface are continuous.

**Figure 26.** Based on our fiber matrix model for the thin layer in the valves and the experimental figures provided by Frank, we calculate the Darcy permeability ($K_p$) as a function of the core protein spacing $\delta$, both with and without collagen, in the thin layer of valves.

**Figure 27.** Similar to figure 26, the diffusion coefficient $D_i$ as a function of the fiber spacing $\delta$, both with and without collagen, for the thin layer of valves. The figure shows the diffusion coefficients for the two different sized molecules LDL and HRP.

**Figure 28.** The pressure distribution in the thin layer of the valves. $z=0$ is for the position right underneath the top face of the endothelial cell layer, $z=0.5$ is for the position in the middle of the valves, and $z=1$ is for the position right above the bottom face of the endothelial cell layer. $z_{12}$ and $z_{23}$ are the two interface positions. The pressure here is normalized by the lumen pressure. Curves for $z_{12}$ and 0 are indistinguishable, as are those for $z_{23}$ and 1 on the scale of the figure.

**Figure 29a,c.** Non-dimensional (a) and dimensional (c) velocity distribution in the lateral direction in the thin layer of the valves for the case of a single leak on the aortic surface and no leaks on the ventricular surface. This shows the lateral velocity $U_1$ and $U_3$ in the thin layers at the $z=0$ (aortic) and $z=1$ (ventricular) faces. The velocities U are appropriately non-dimensionalized in local Peclet numbers in order to weigh the contribution of the convection relative to diffusion. The coordinate z is the normalized depth in the values. $z_{12}$ and $z_{23}$ represent the interface positions. Curves for $z_{12}$ and 0 are indistinguishable, as are those for $z_{23}$ and 1 on the scale of the figure. It also clearly shows a large lateral velocity in the thin layer near the aortic surface, which decays to almost zero in the subsequent layers.

**Figure 29b,d.** Non-dimensional (b) and dimensional (d) velocity distribution in the normal direction in the thin layer of the valves for the case of a single leak on the aortic surface and no leaks on the ventricular surface. Again, the velocity W appropriately non-dimensionalized in local Peclet numbers in order to weigh the contribution of the convection relative to diffusion. Figures 29a and b show that the radial velocity dominates in the thin layer in the vicinity of the leakage.

**Figures 30.** Similar to those in figures 28 and 29, figures 30 are for the case of no leak on the aortic side and one on the ventricular side. **a.** The pressure distribution in the thin layer of valves. **b., d.** Non-dimensional (b) and dimensonal (d) velocity distribution in the lateral direction in the thin layer of the valves. **c., e.** Non-dimensional (c) and dimensional (e) velocity distribution in the normal direction in the thin layer of the valves. These figures show that the velocity in the thin layer beneath the upstream, i.e., aortic, face are now predominantly vertical, whereas those on the downstream, i.e., ventricular, face are now predominantly horizontal.

**Figures 31.** Similar to those in figures 28 and 29, figures 31 show for the case of one leak on each of the two faces. **a.** Similar to figure 28, this is the pressure distribution in the thin layer of valves. **b., d.** Non-dimensional (b) and dimensional (d) velocity distribution in the lateral direction in the thin layer of the valves. **c., e.** Non-dimensional (c) and dimensional (e) velocity distribution in the normal direction in the thin layer of the valves. These figures show that there are large lateral velocities in each of the two thin layers, but the prevailing flow in the thick layer is still vertical.

**Figure 32.** The HRP concentration profiles after different circulation times in the thin layer of the valve leaflet. The HRP concentration is normalized by the tracer concentration in the lumen. The absissa represents the position in the thin layer normalized by the endothelial cell radius. The ordinate represents the normalized HRP concentration in the thin layer of the valve.

**Figures 33a, b, c.** The early time growth of the leakage spots. The filled symbols show the short time *en face* HRP spot growth after 30 seconds, 1 minutes, 2 minutes and 4 minutes circulation from the theory in the text (figure **a** for 30 seconds and figure **b** for 60 seconds as the times of reference) and our experimental measurements. The figure shows that the theory is consistent with the experiment data. Figure **c** shows the early time growth of the leakage spots for the theory only diffusion and no convection.

**Figure 34.** The theoretical LDL concentration for the Tompkins *et al.*'s model with no convection, i.e., diffusion only. Using Tompkins *et al.*'s values $k_1$, $k_2$ and D, we recover his fit. This servers to check our numerical code.

**Figure 35.** The new transport model and the same data as in Figure 34. We re-fit the Tompkins *et al.*'s experimental data using our new 3-layer model, including convection by adjusting $k_1$, $k_2$ and D.

**Figures 36 a.** LDL concentration profiles for an experiment similar to the one in Fig. 32 that substitutes LDL for HRP as the tracer molecule for the case of a single aortic face leak and no ventricular face leaks. The circulation times vary from 1 minute to 30 minutes and include the steady state. We made this choice in order to be able to compare the results with Tompkins' experiment [43]. **b.** The early time growth of the LDL leakage spots from Fig. 36a.

**Figures. 37.** Tompkins *et al.*'s [43] experiments and their theoretical fits using only diffusion and a single interposed layer for Monkey.

**Figures. 38.** The LDL concentration, including both Tompkins *et al.*'s measurements and our theoretical calculations for various combinations of leaks on the two endothelial layers. We chose a configuration of leaks, solved the model and compared with a data set that looked most similar. Experiments did not investigate presence and number of leaks. As throughout, the abscissas of these figures represent the normalized depth (z) into the valve leaflets from the top face inward. That is, position z=0 is at the aortic surface; position z=1 is at the ventricular face. The ordinates are the normalized local (in z, averaged over r) LDL concentrations per unit total volume (including matrix) of valve ($\gamma C$), **a.** for the case of a single aortic face leak and no ventricular face leaks, **b.** for the case of one leak on each of the two faces, **c.** for the case of no ventricular face leak and a single leak on the aortic face that closes part way (after 10 minutes) through the experiment. The figure plots the concentration profiles across the valve for various times after the aortic leak closes. **d.** the one curve from Fig. 38c that fit one of Tompkins *et al.*'s experiment.

**Figure 39.** Cubic grid for the computer simulation of the liposome formation and growth for the aortic valves using the new theoretical macromolecular transport model combined with the simplest liposome formation and growth model from the arteries. In contrast to the two dimensional variation of the liposome formation in the arterial intima, the macromolecular transport in the valves is by nature three-dimensional. As such, we chose a cubic grid corresponding to a volume of valve (say 40 cells x 40 cells x 5 effective endothelial cell diameters), which is large compared with the extent of a single leak. We assumed that leaks occur at random locations (x,y,0) and (x,y,1) on these two surfaces and that the leaks generate LDL profiles with periodic boundary conditions for the leaks around the three dimensional cubic volume (x,y,z). The top and bottom faces represent the two endothelial cells surfaces. The four faces perpendicular to these two surfaces represent the periodic boundaries or the edges of the leaflet.

**Figure 40.** The new model simulation (Fig. 39) for predicting the liposome size distribution in the valve leaflets of rabbits subjected to the short time feedings corresponding to Frank's

experiments. Frank *et al.* (personal communication) performed feeding experiments for 29 days before sacrificing the rabbits and examining the rabbits' aortic valve leaflet. The resulting liposome histogram is shown in figure 40 by the solid curve. Frank's experiments show that in valves, unlike in the aorta, there are liposomes with diameters larger than 170nm. The number of these liposomes are only 0.30% of the total liposome numbers in valves, but their existence is still novel. Our model's simulation (figure 40, the dotted curve) also shows the existence of these large liposomes. The model-generated amount of large-sized liposomes is the far right bar, which accounts for only 0.49% of the calculated total liposome number.

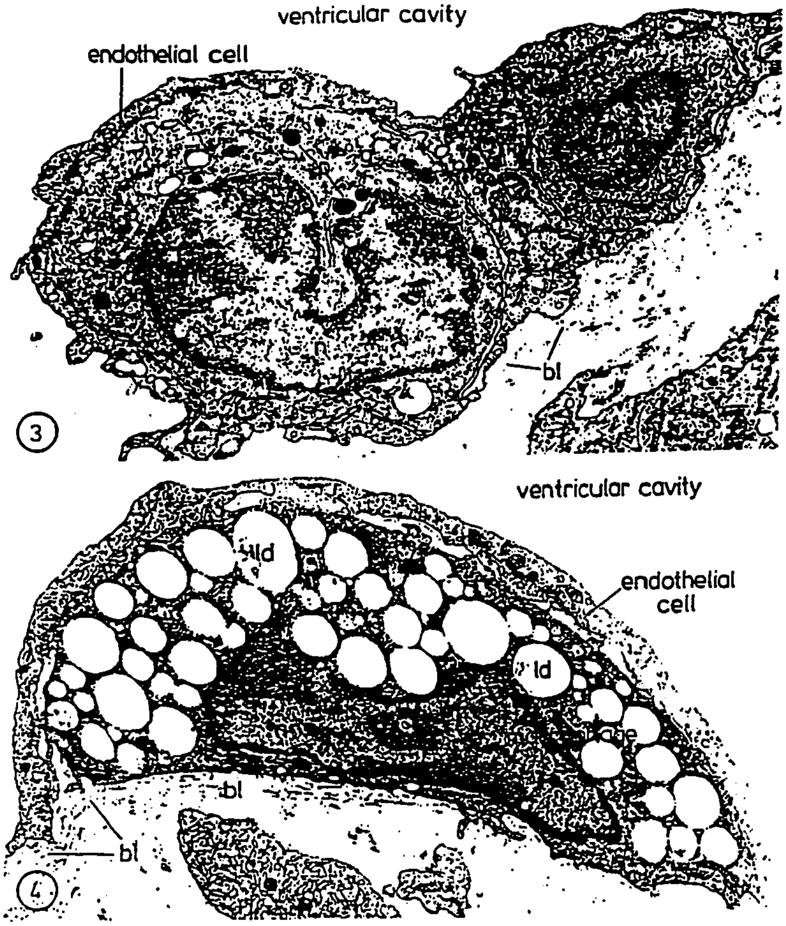
ventricular cavity
endothelial cell
bl
③
ventricular cavity
ld
endothelial cell
ld
bl
bl
④

Fig. 17

Fig. 18

Fig. 19

# AORTIC VALVE ANATOMY

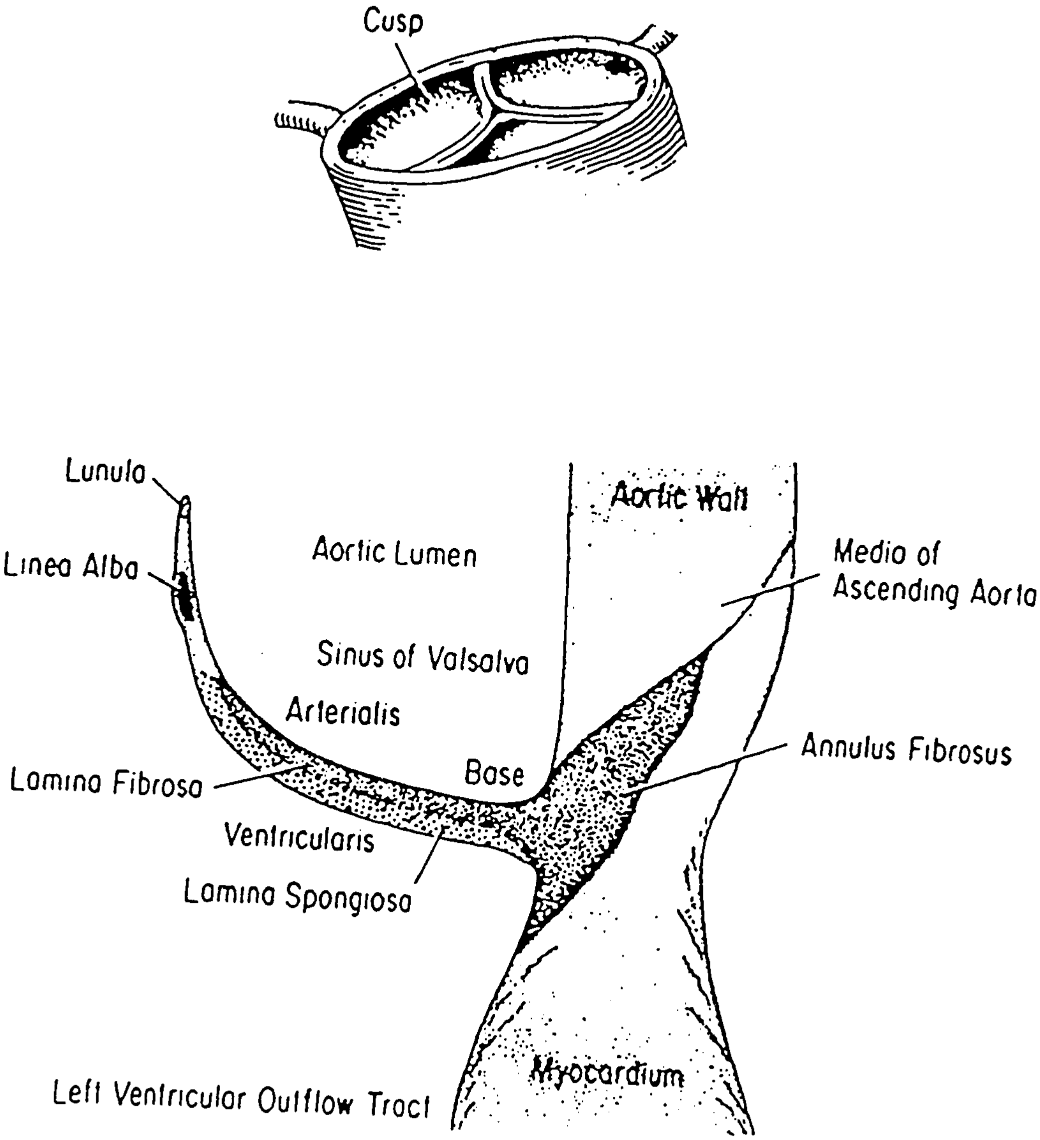

Fig. 20

Fig. 21

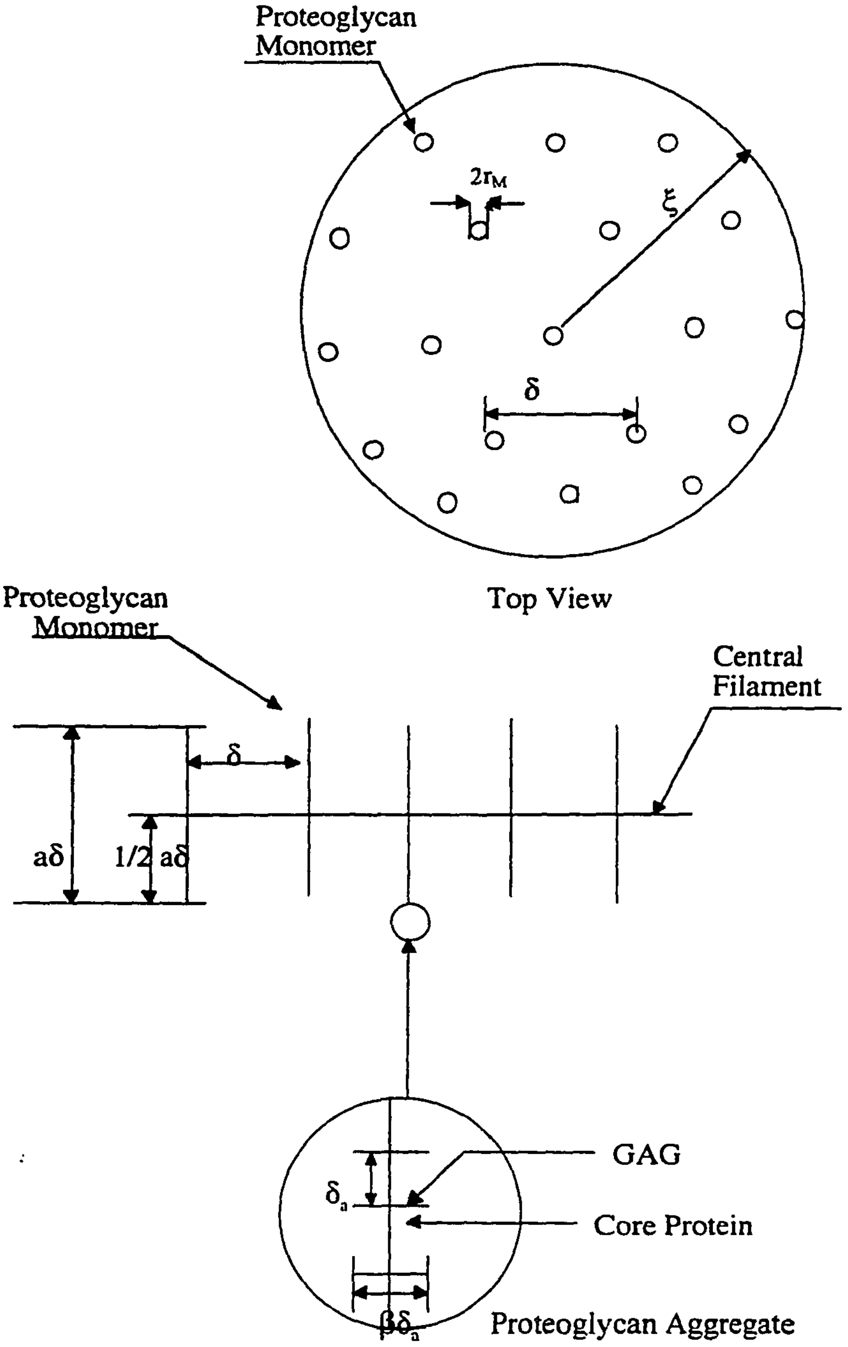
Proteoglycan Monomer
$2r_M$
$\xi$
$\delta$
Top View
Proteoglycan Monomer
Central Filament
$\delta$
$a\delta$
$1/2\ a\delta$
GAG
$\delta_a$
Core Protein
$\beta\delta_a$
Proteoglycan Aggregate

Fig. 22

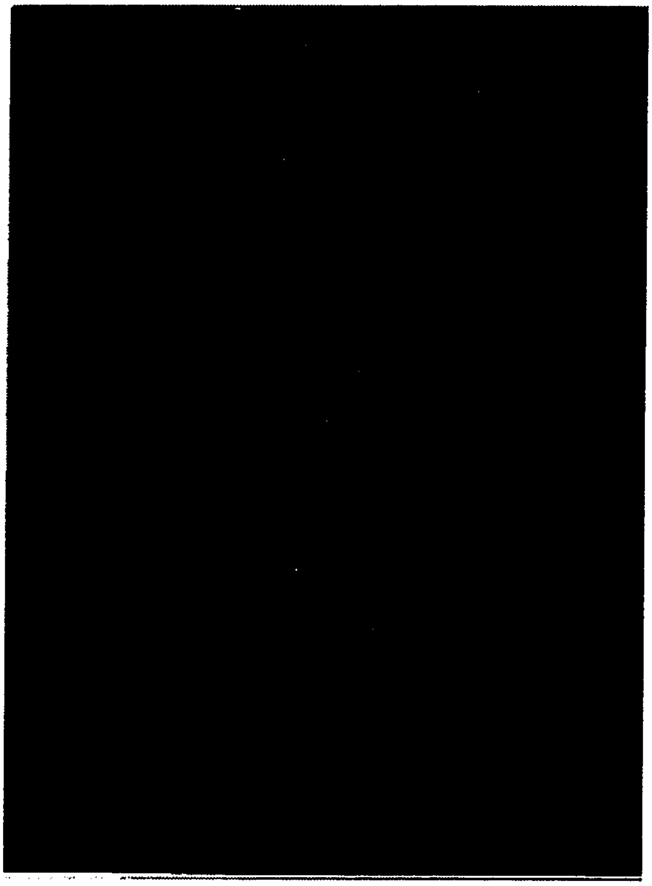

Fig. 23

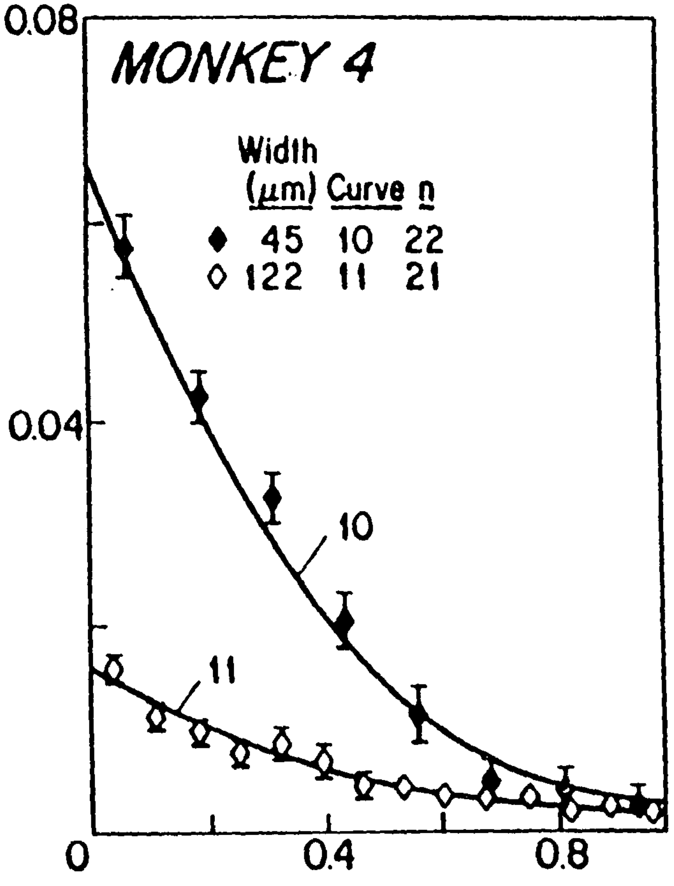

**Tompkins Model**

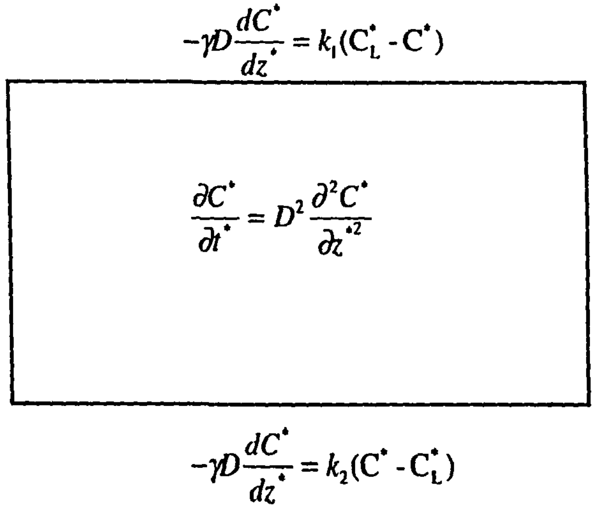

$$-\gamma D\frac{dC^*}{dz^*} = k_1(C_L^* - C^*)$$

$$\frac{\partial C^*}{\partial t^*} = D^2\frac{\partial^2 C^*}{\partial z^{*2}}$$

$$-\gamma D\frac{dC^*}{dz^*} = k_2(C^* - C_L^*)$$

Fig. 24a

# Preliminary Model for Transport in Aortic Valve Fluid Mechanics

*Governing Equation:* $\nabla^2 P = 0;$

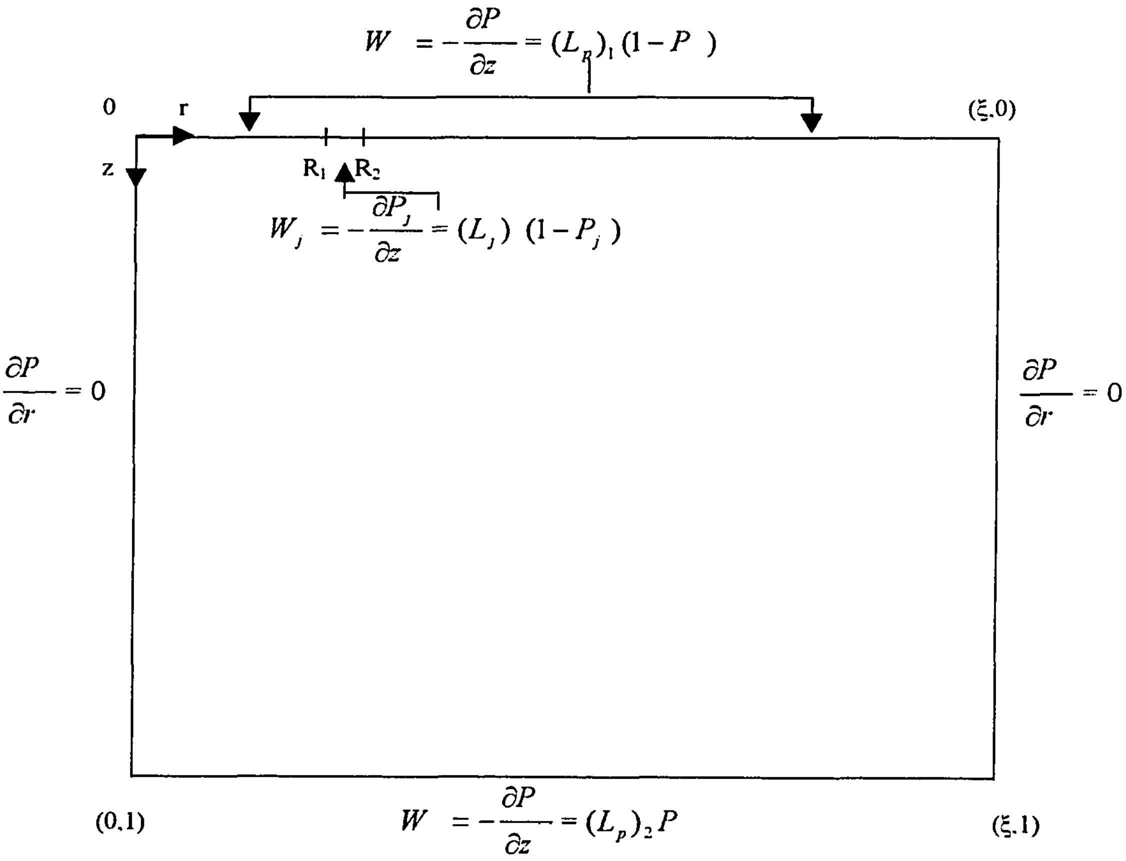

Fig. 24b

# Preliminary Model for Transport in Aortic Valve Diffusion and Convection

*Governing Equation:* $\gamma \dfrac{\partial C^*}{\partial t^*} + \underline{\nabla} \bullet \underline{q}^* = 0;$ $\qquad \underline{q}^* = -\gamma \; D \; \underline{\nabla} C^* + f \; \underline{V}^* C^*;$

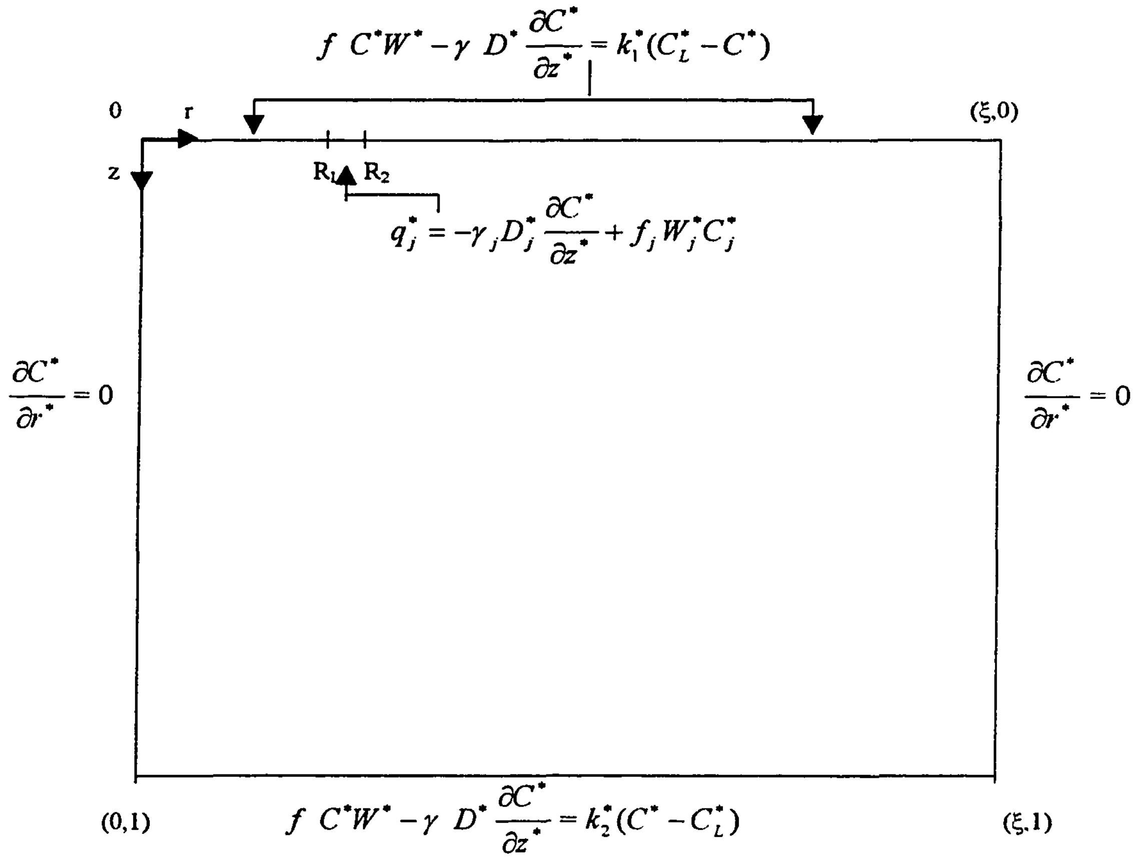

Fig. 24c

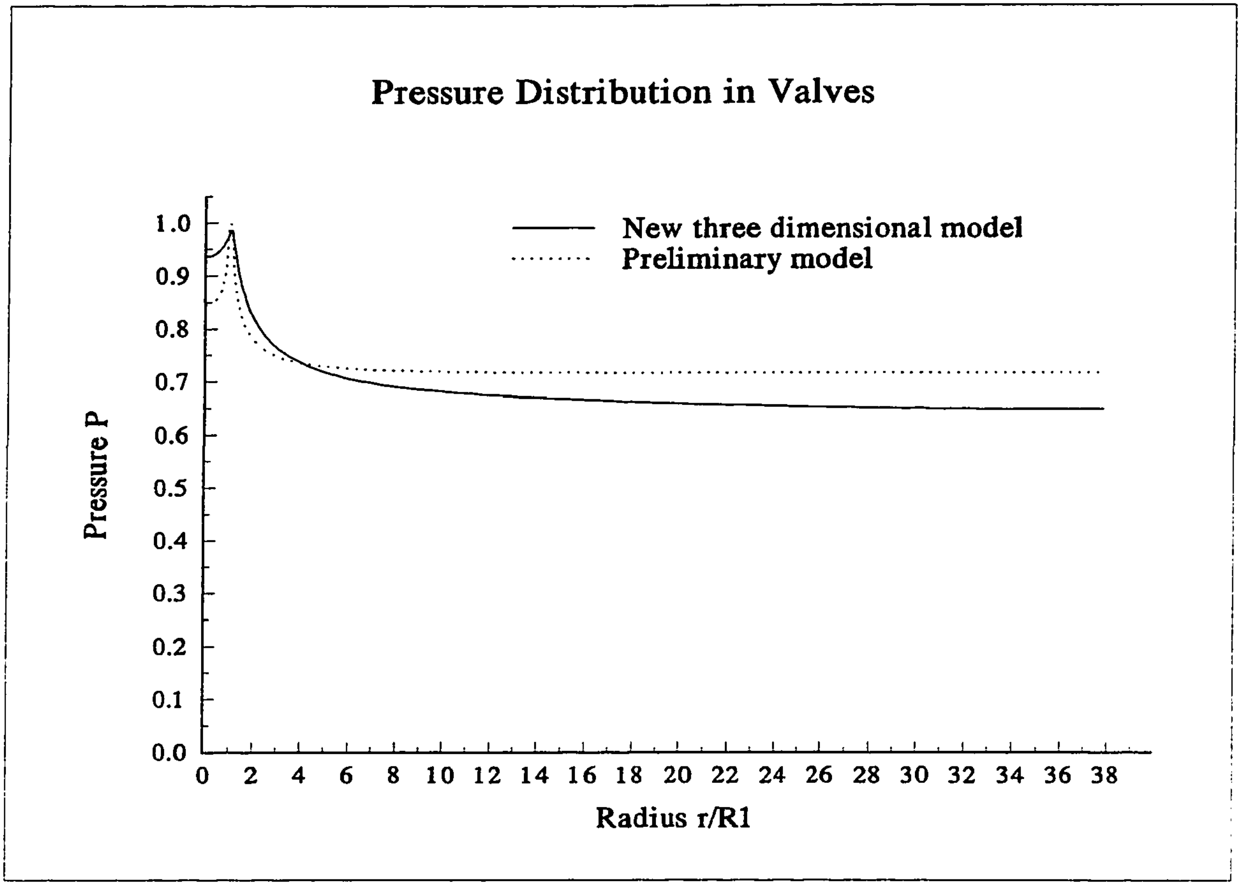
Pressure Distribution in Valves
New three dimensional model
Preliminary model
Pressure P
1.0
0.9
0.8
0.7
0.6
0.5
0.4
0.3
0.2
0.1
0.0
0 2 4 6 8 10 12 14 16 18 20 22 24 26 28 30 32 34 36 38
Radius r/R1

Fig. 24d

## New Model for Transport in Aortic Valve Fluid Mechanics

*Governing Equation:* $\nabla^2 P_i = 0; \quad i = 1,2,3$

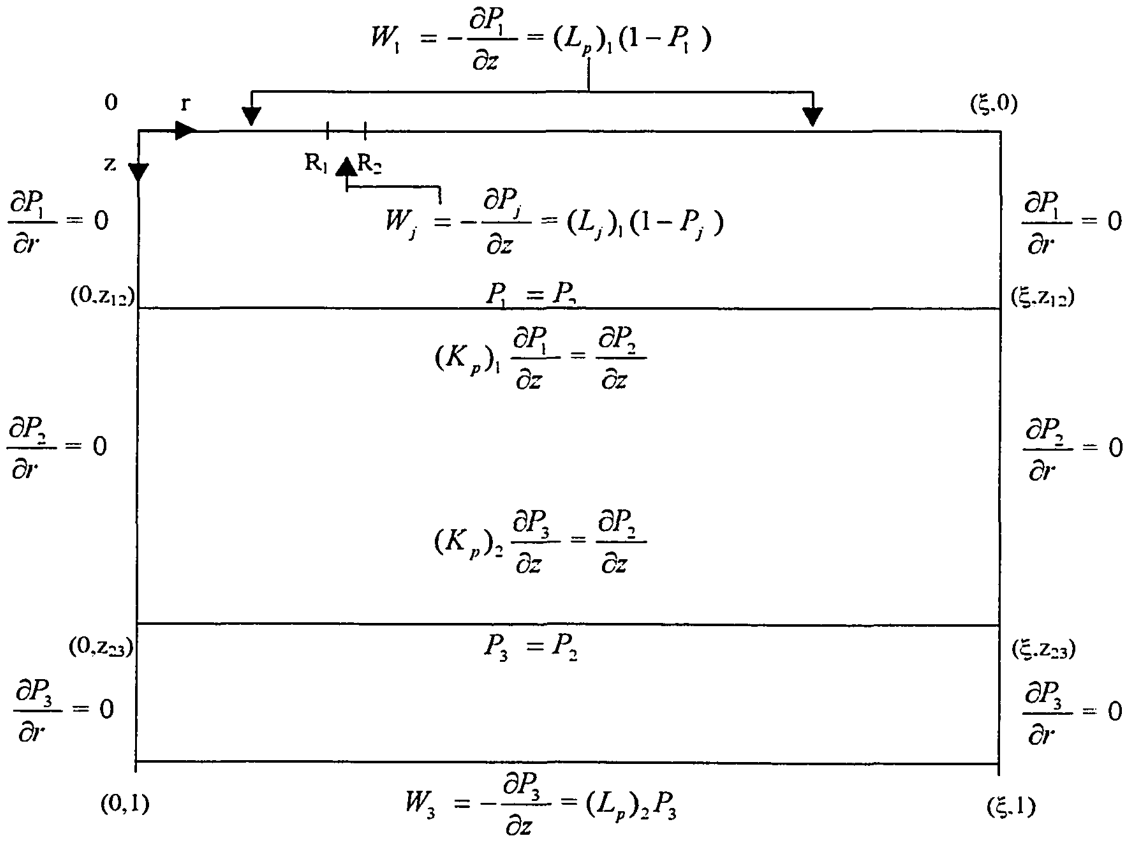

Fig. 25a

## New Model for Transport in Aortic Valve
## Diffusion and Convection

*Governing Equation:* $\gamma_i \frac{\partial C_i^*}{\partial t^*} + \underline{\nabla} \bullet \underline{q}^* = 0;$ $\underline{q}^* = -\gamma_i D_i \underline{\nabla} C_i^* + f_i \underline{V}^* C_i^*;$ $i = 1,2,3$

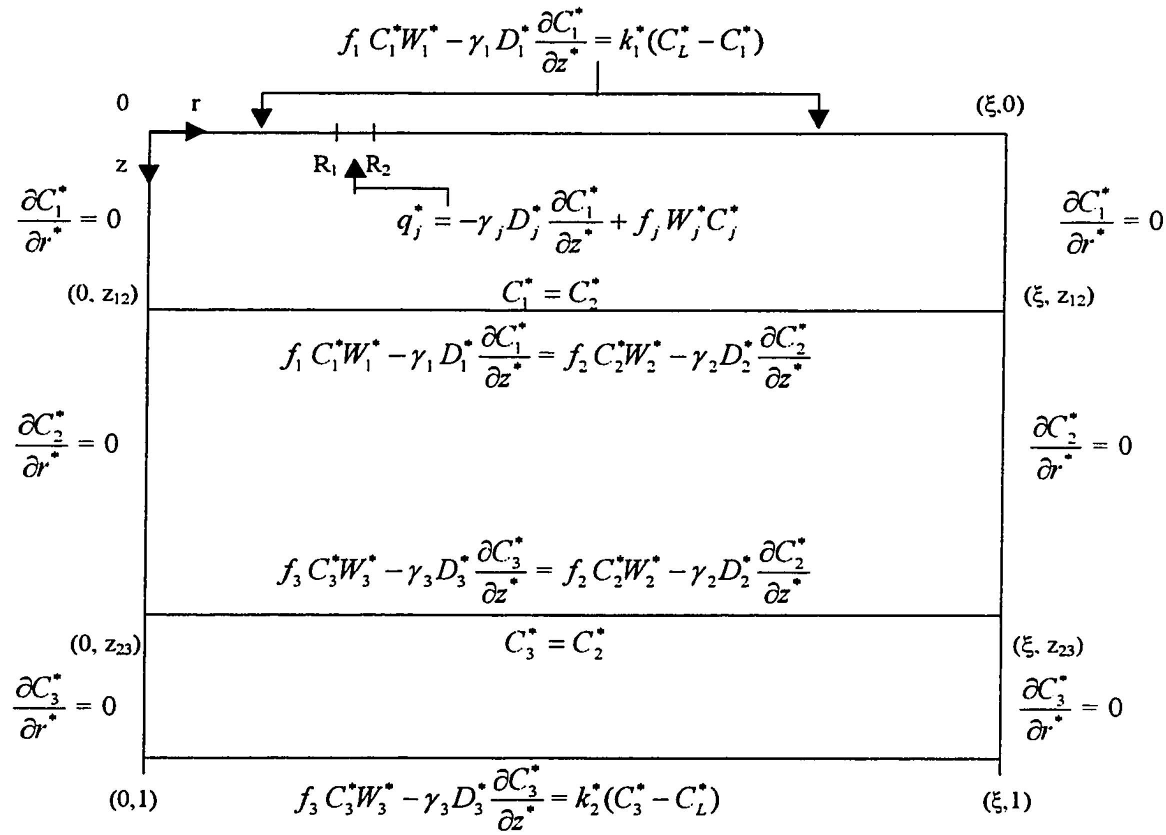

Fig. 25b

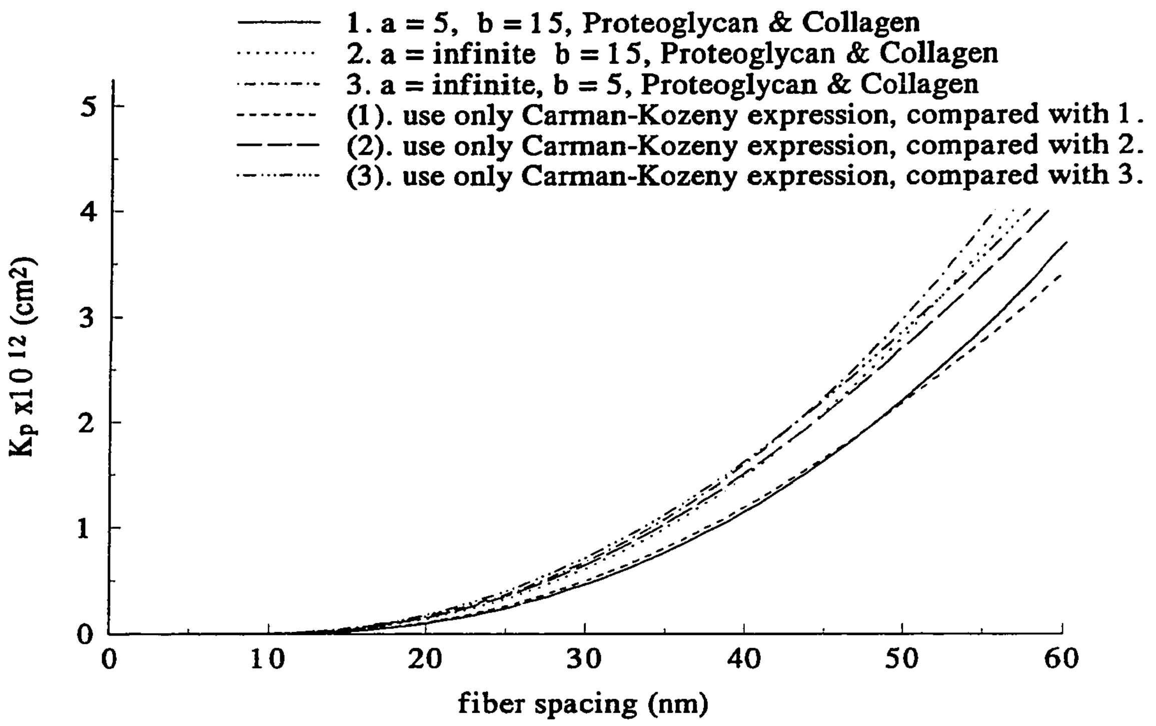
1. a = 5, b = 15, Proteoglycan & Collagen
2. a = infinite b = 15, Proteoglycan & Collagen
3. a = infinite, b = 5, Proteoglycan & Collagen
(1). use only Carman-Kozeny expression, compared with 1.
(2). use only Carman-Kozeny expression, compared with 2.
(3). use only Carman-Kozeny expression, compared with 3.
Kp x10 12 (cm2)
0
1
2
3
4
5
0
10
20
30
40
50
60
fiber spacing (nm)

Fig. 26

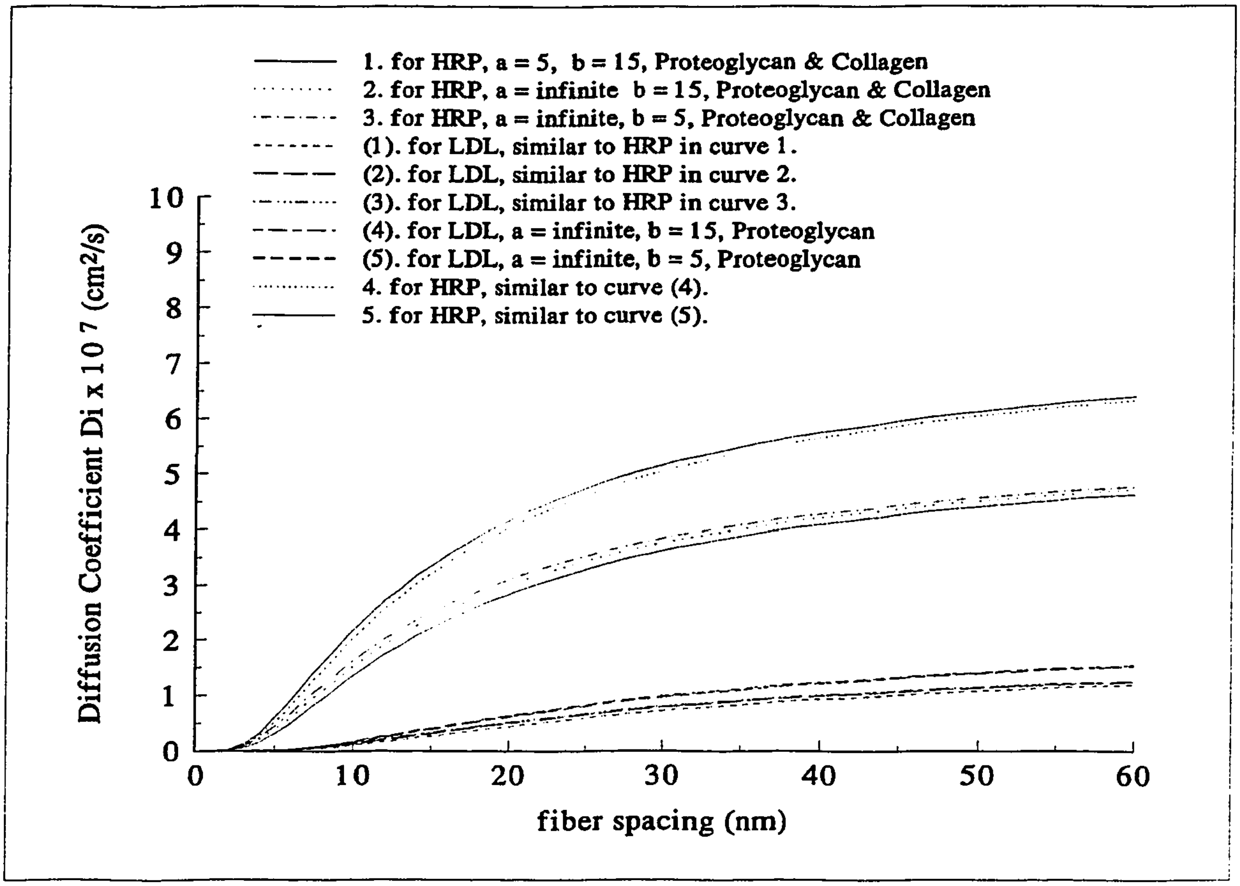
1. for HRP, a = 5, b = 15, Proteoglycan & Collagen
2. for HRP, a = infinite b = 15, Proteoglycan & Collagen
3. for HRP, a = infinite, b = 5, Proteoglycan & Collagen
(1). for LDL, similar to HRP in curve 1.
(2). for LDL, similar to HRP in curve 2.
(3). for LDL, similar to HRP in curve 3.
(4). for LDL, a = infinite, b = 15, Proteoglycan
(5). for LDL, a = infinite, b = 5, Proteoglycan
4. for HRP, similar to curve (4).
5. for HRP, similar to curve (5).
Diffusion Coefficient Di x 10 7 (cm2/s)
0
1
2
3
4
5
6
7
8
9
10
0
10
20
30
40
50
60
fiber spacing (nm)

Fig. 27

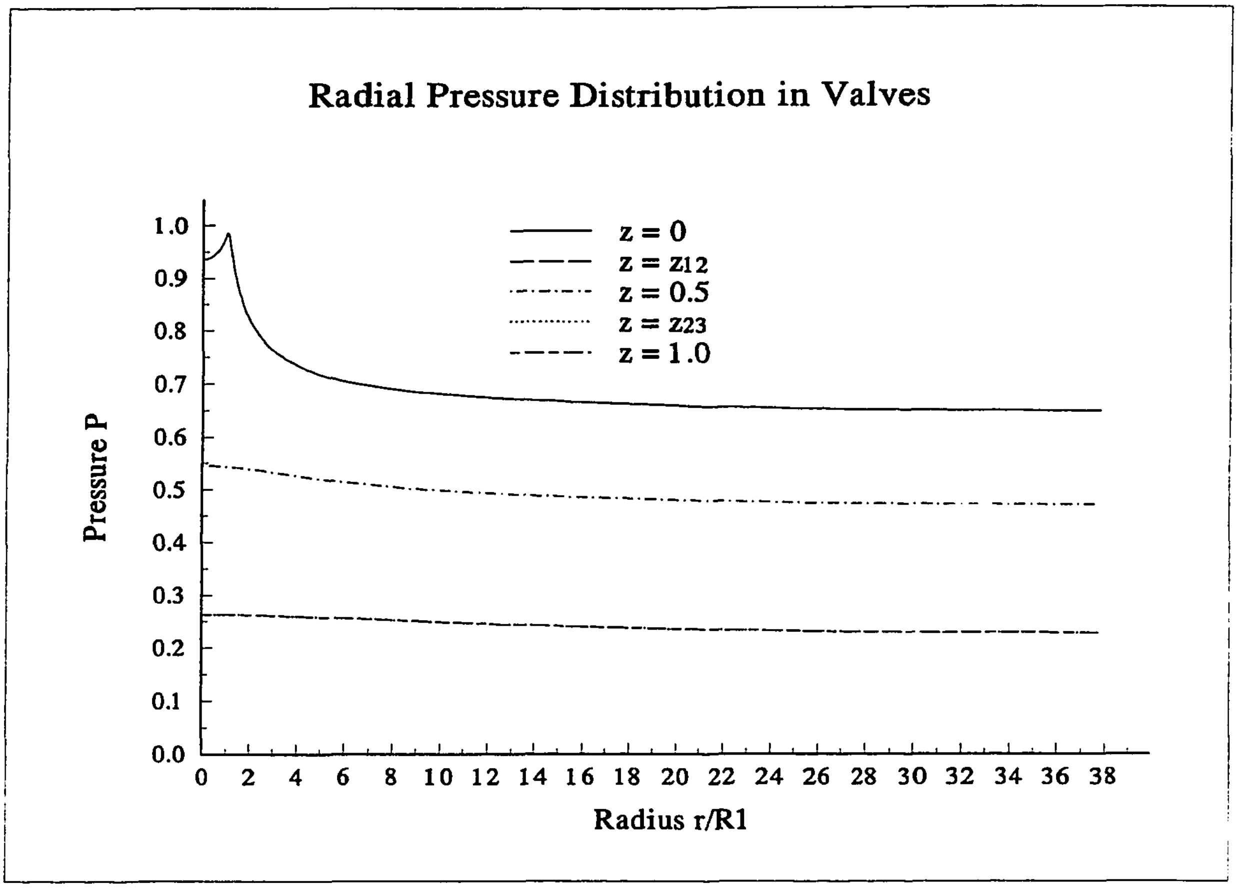
Radial Pressure Distribution in Valves
z = 0
z = z12
z = 0.5
z = z23
z = 1.0
Pressure P
1.0
0.9
0.8
0.7
0.6
0.5
0.4
0.3
0.2
0.1
0.0
0
2
4
6
8
10
12
14
16
18
20
22
24
26
28
30
32
34
36
38
Radius r/R1

Fig. 28

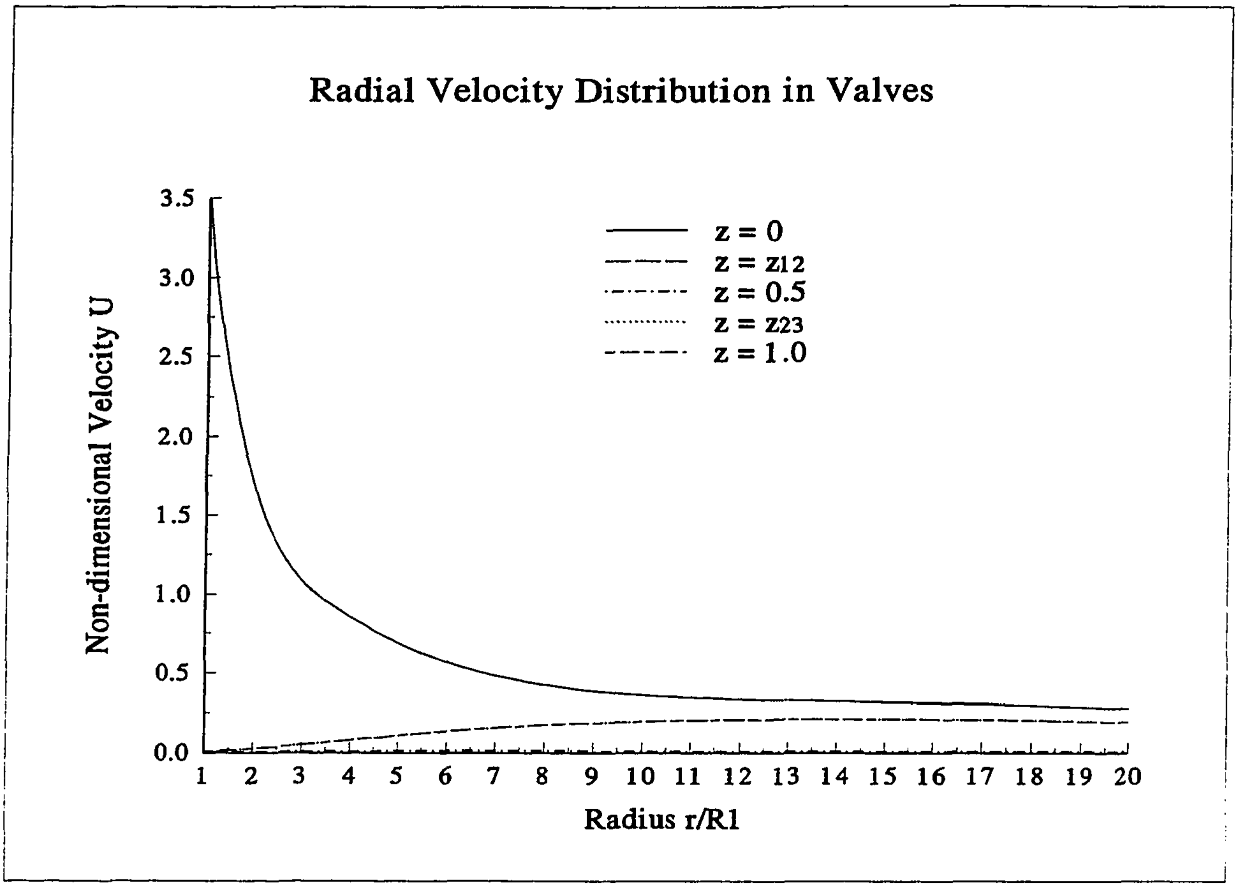
Radial Velocity Distribution in Valves
Non-dimensional Velocity U
3.5
3.0
2.5
2.0
1.5
1.0
0.5
0.0
z = 0
z = z12
z = 0.5
z = z23
z = 1.0
1
2
3
4
5
6
7
8
9
10
11
12
13
14
15
16
17
18
19
20
Radius r/R1

Fig. 29a

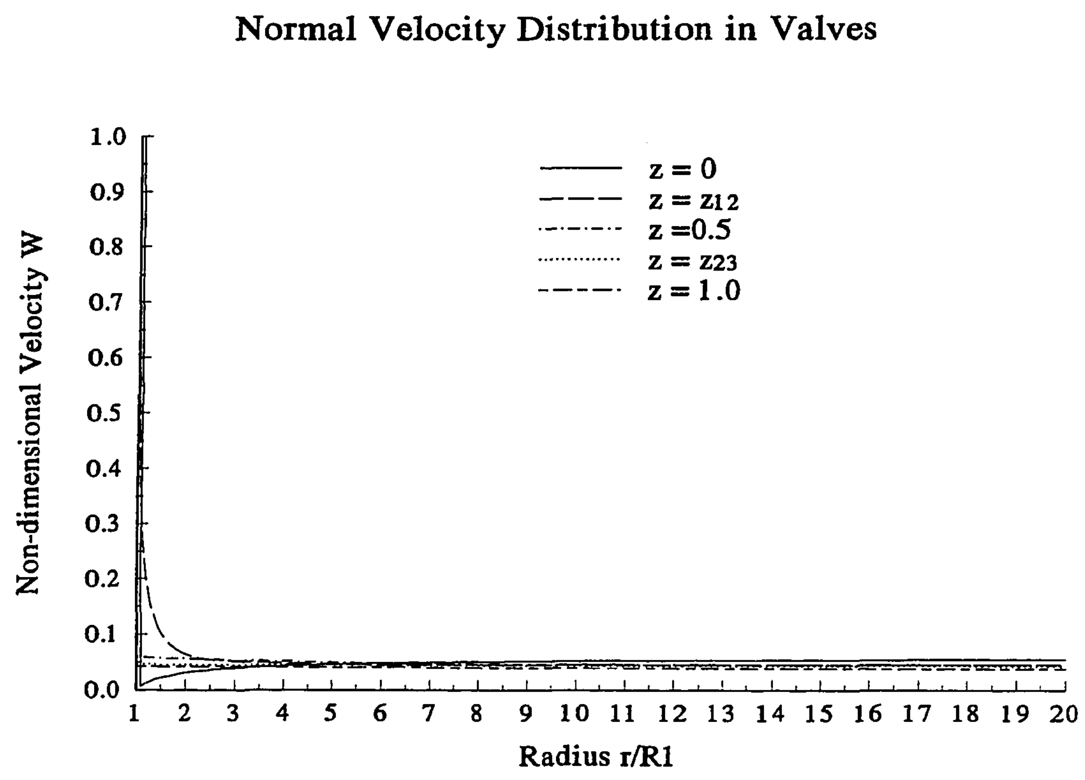
Normal Velocity Distribution in Valves
Non-dimensional Velocity W
1.0
0.9
0.8
0.7
0.6
0.5
0.4
0.3
0.2
0.1
0.0
1
2
3
4
5
6
7
8
9
10
11
12
13
14
15
16
17
18
19
20
Radius r/R1
z = 0
z = z12
z =0.5
z = z23
z = 1.0

Fig. 29b

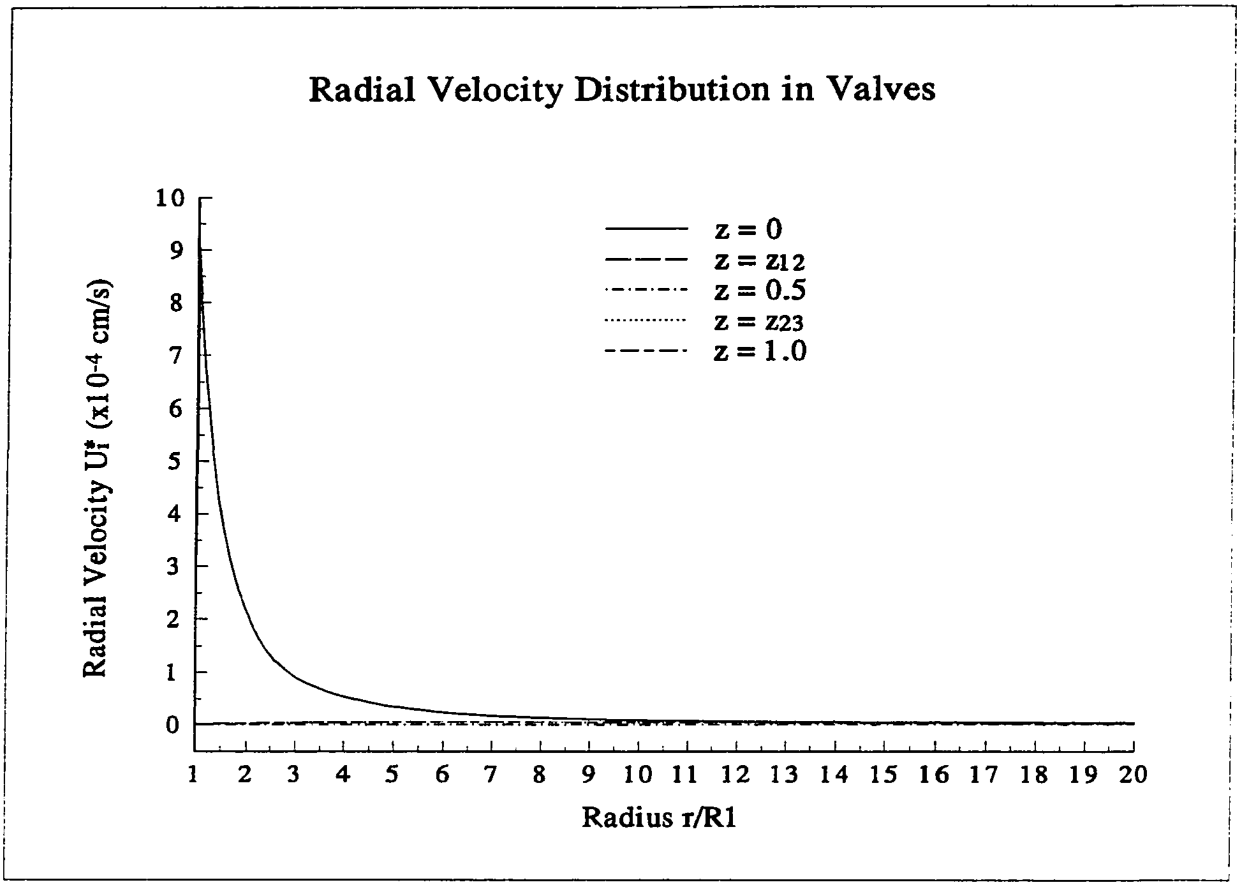
Radial Velocity Distribution in Valves
Radial Velocity $U_r^*$ (x10$^{-4}$ cm/s)
10
9
8
7
6
5
4
3
2
1
0
1
2
3
4
5
6
7
8
9
10
11
12
13
14
15
16
17
18
19
20
Radius r/R1
z = 0
z = z12
z = 0.5
z = z23
z = 1.0

Fig. 29c

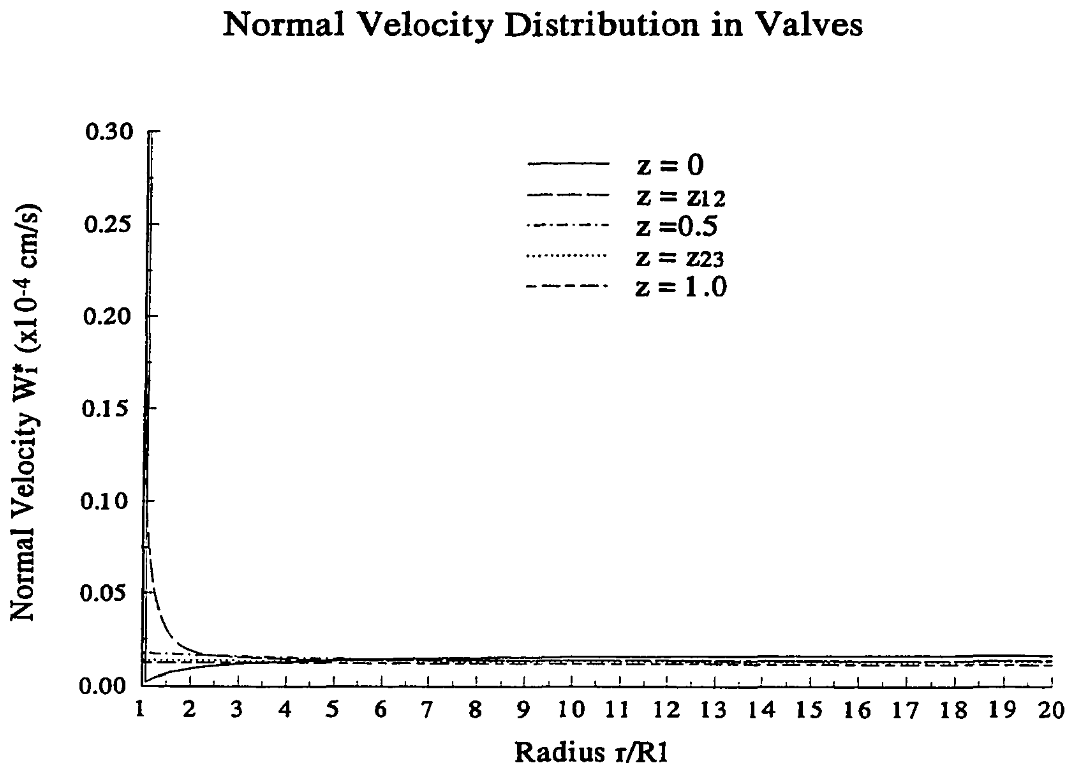
Normal Velocity Distribution in Valves
0.30
0.25
0.20
0.15
0.10
0.05
0.00
Normal Velocity Wi* (x10-4 cm/s)
z = 0
z = z12
z =0.5
z = z23
z = 1.0
1
2
3
4
5
6
7
8
9
10
11
12
13
14
15
16
17
18
19
20
Radius r/R1

Fig. 29d

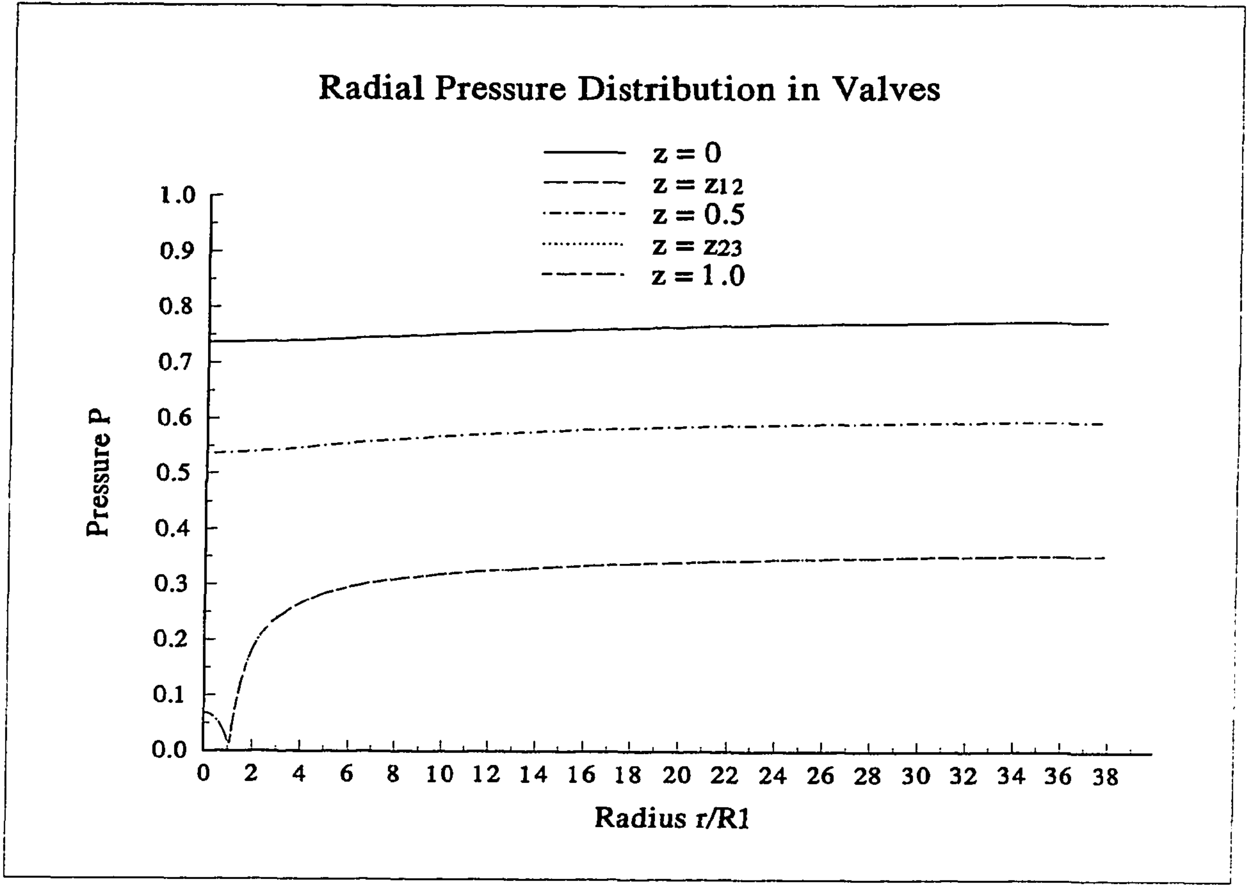
Radial Pressure Distribution in Valves
z = 0
z = z12
z = 0.5
z = z23
z = 1.0
Pressure P
1.0
0.9
0.8
0.7
0.6
0.5
0.4
0.3
0.2
0.1
0.0
0
2
4
6
8
10
12
14
16
18
20
22
24
26
28
30
32
34
36
38
Radius r/R1

Fig. 30a

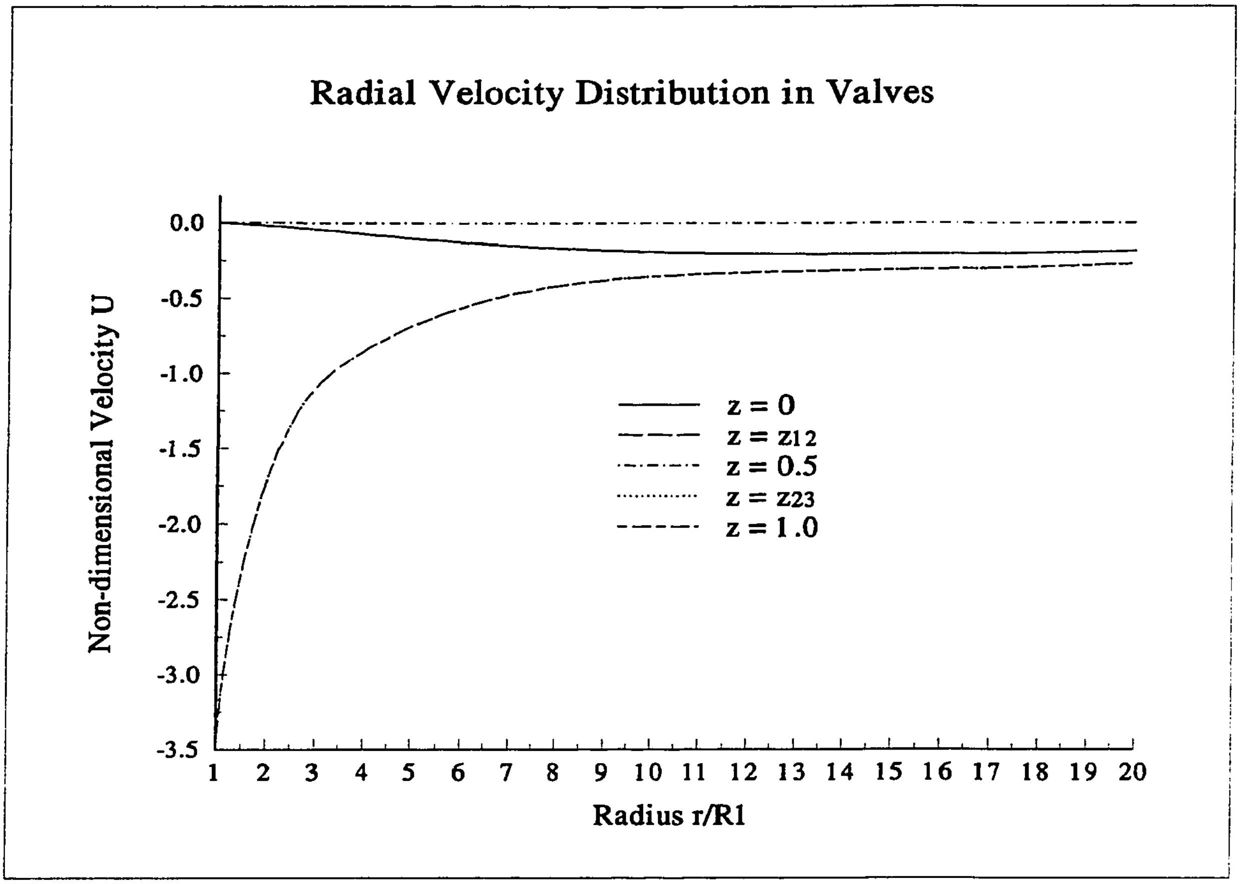
Radial Velocity Distribution in Valves
Non-dimensional Velocity U
0.0
-0.5
-1.0
-1.5
-2.0
-2.5
-3.0
-3.5
1
2
3
4
5
6
7
8
9
10
11
12
13
14
15
16
17
18
19
20
Radius r/R1
z = 0
z = z12
z = 0.5
z = z23
z = 1.0

Fig.30b

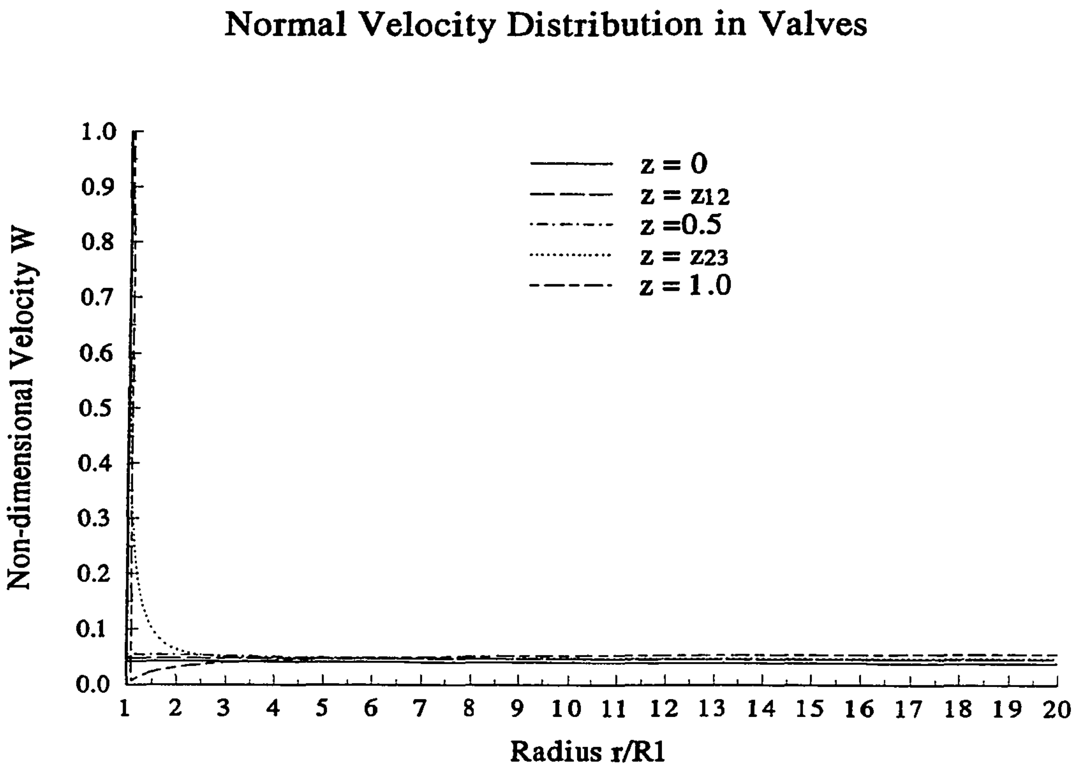
Normal Velocity Distribution in Valves
Non-dimensional Velocity W
1.0
0.9
0.8
0.7
0.6
0.5
0.4
0.3
0.2
0.1
0.0
z = 0
z = z12
z =0.5
z = z23
z = 1.0
1
2
3
4
5
6
7
8
9
10
11
12
13
14
15
16
17
18
19
20
Radius r/R1

Fig. 30c

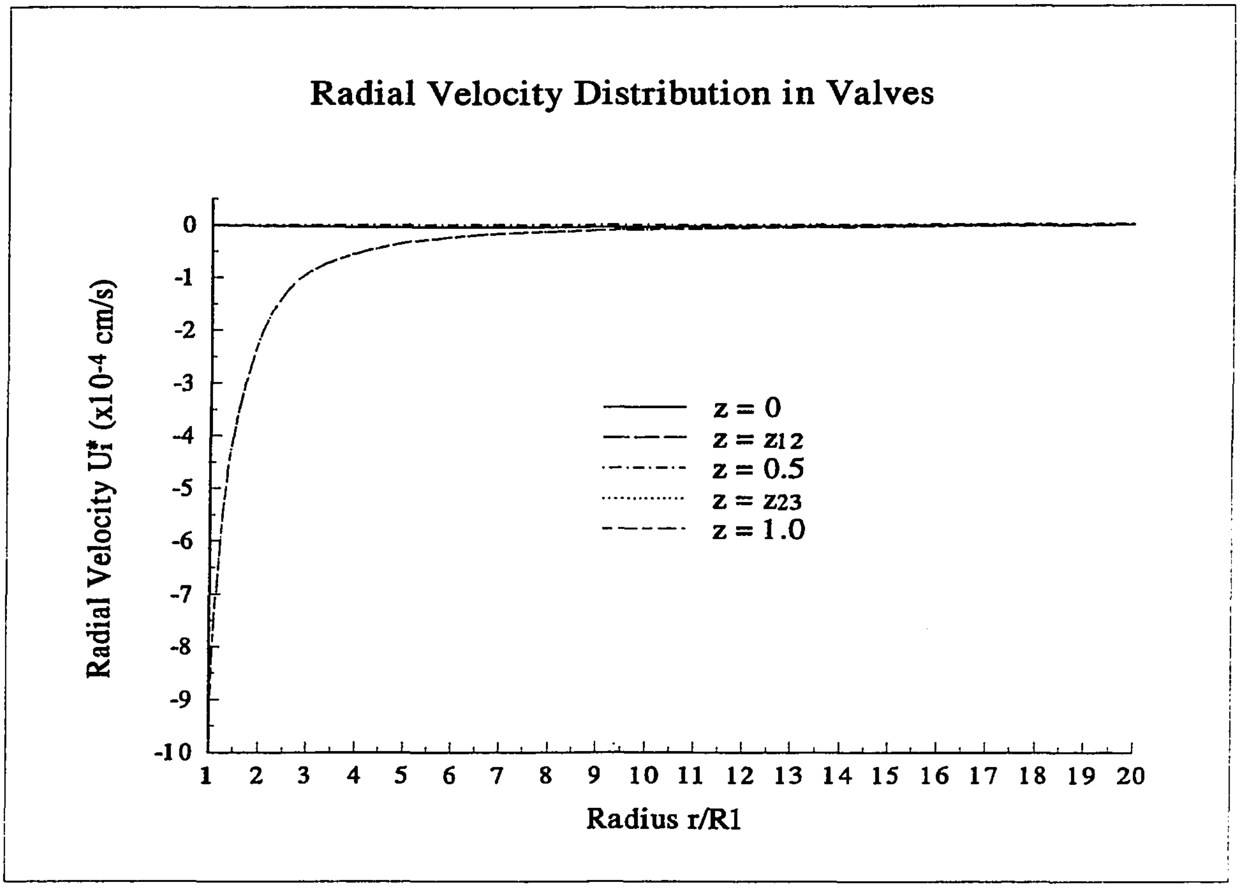
Radial Velocity Distribution in Valves
Radial Velocity $U_1^*$ (x10$^{-4}$ cm/s)
0
-1
-2
-3
-4
-5
-6
-7
-8
-9
-10
1
2
3
4
5
6
7
8
9
10
11
12
13
14
15
16
17
18
19
20
Radius r/R1
z = 0
z = z12
z = 0.5
z = z23
z = 1.0

Fig. 30d

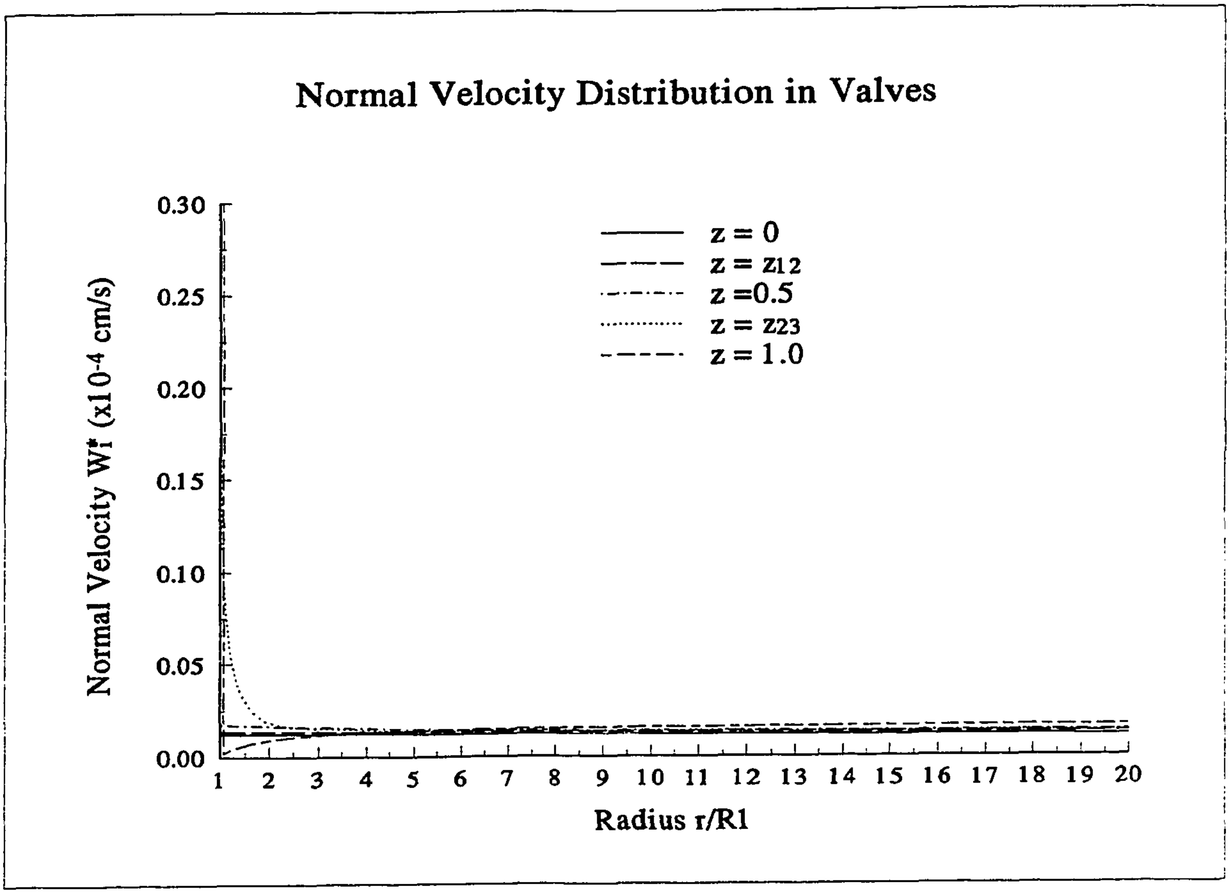
Normal Velocity Distribution in Valves
0.30
0.25
0.20
0.15
0.10
0.05
0.00
Normal Velocity Wi* (x10-4 cm/s)
z = 0
z = z12
z =0.5
z = z23
z = 1.0
1
2
3
4
5
6
7
8
9
10
11
12
13
14
15
16
17
18
19
20
Radius r/R1

Fig. 30e

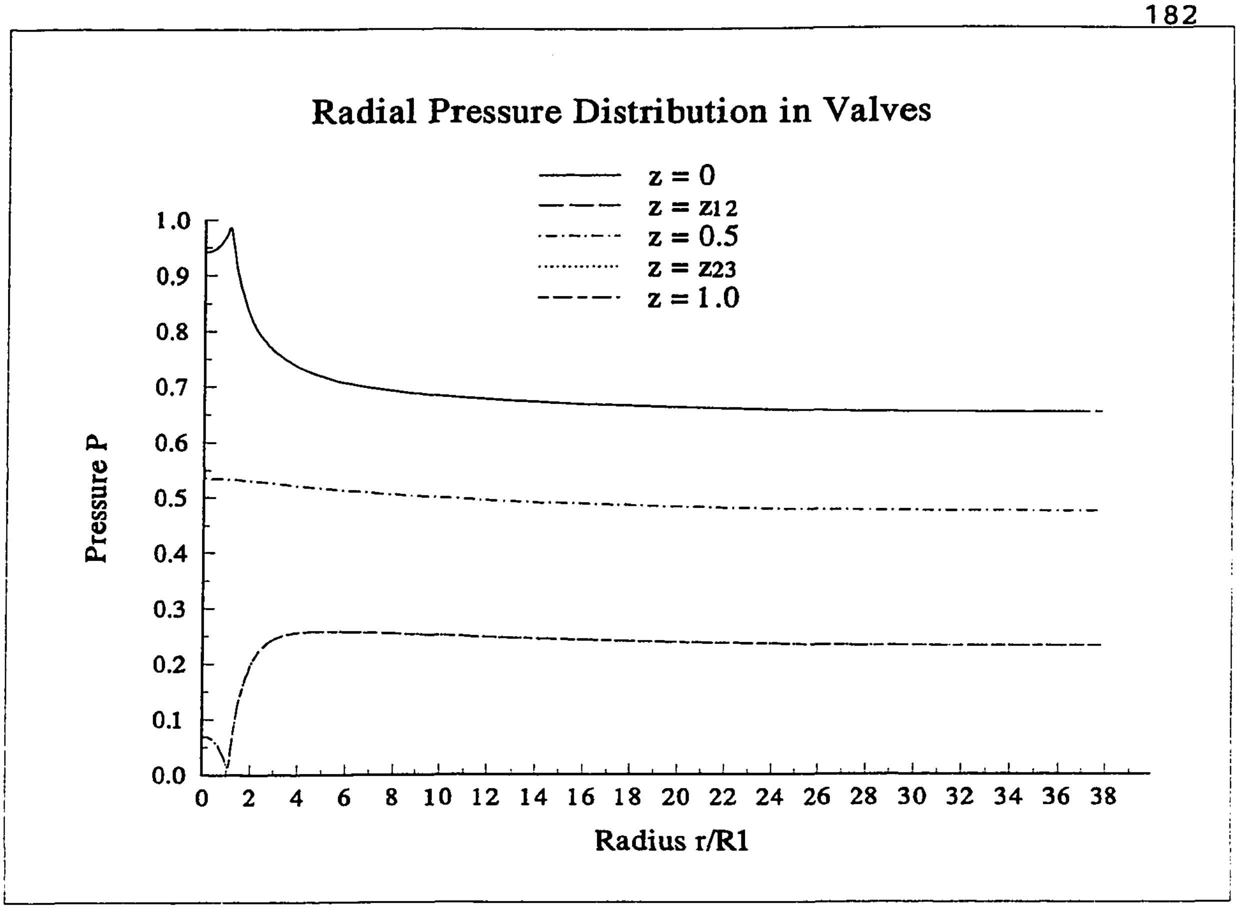
Radial Pressure Distribution in Valves
z = 0
z = z12
z = 0.5
z = z23
z = 1.0
Pressure P
1.0
0.9
0.8
0.7
0.6
0.5
0.4
0.3
0.2
0.1
0.0
0
2
4
6
8
10
12
14
16
18
20
22
24
26
28
30
32
34
36
38
Radius r/R1

Fig.31a

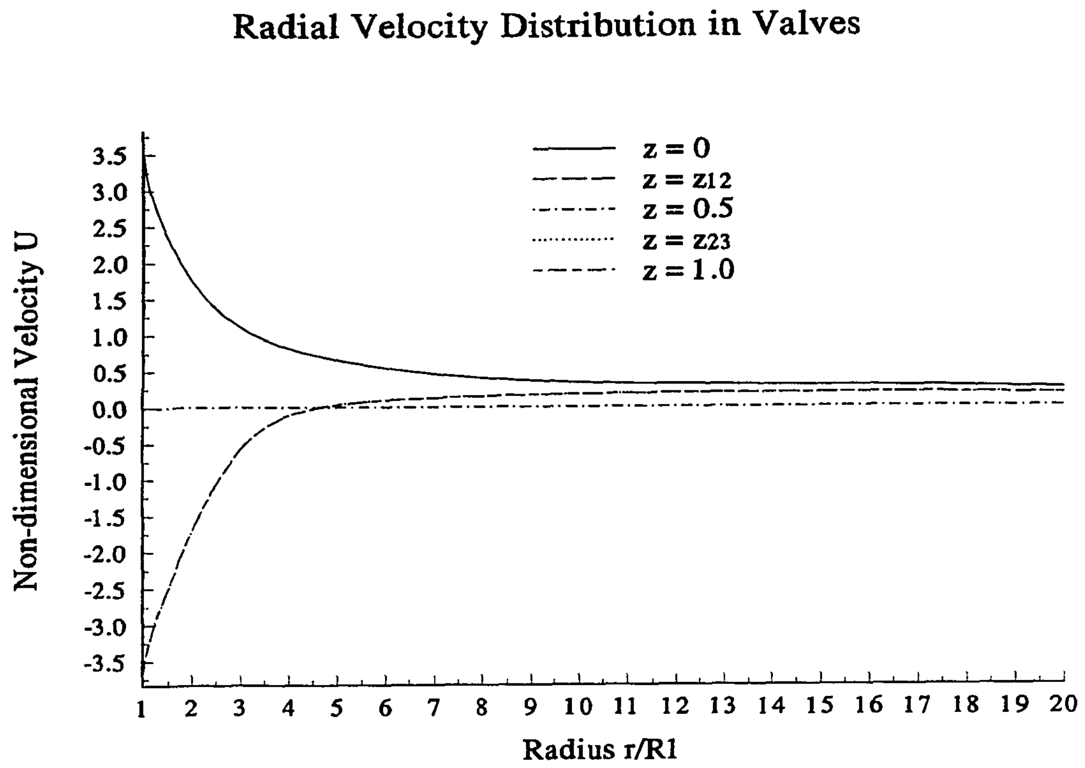
Radial Velocity Distribution in Valves
z = 0
z = z12
z = 0.5
z = z23
z = 1.0
Non-dimensional Velocity U
3.5
3.0
2.5
2.0
1.5
1.0
0.5
0.0
-0.5
-1.0
-1.5
-2.0
-2.5
-3.0
-3.5
1
2
3
4
5
6
7
8
9
10
11
12
13
14
15
16
17
18
19
20
Radius r/R1

Fig. 31b

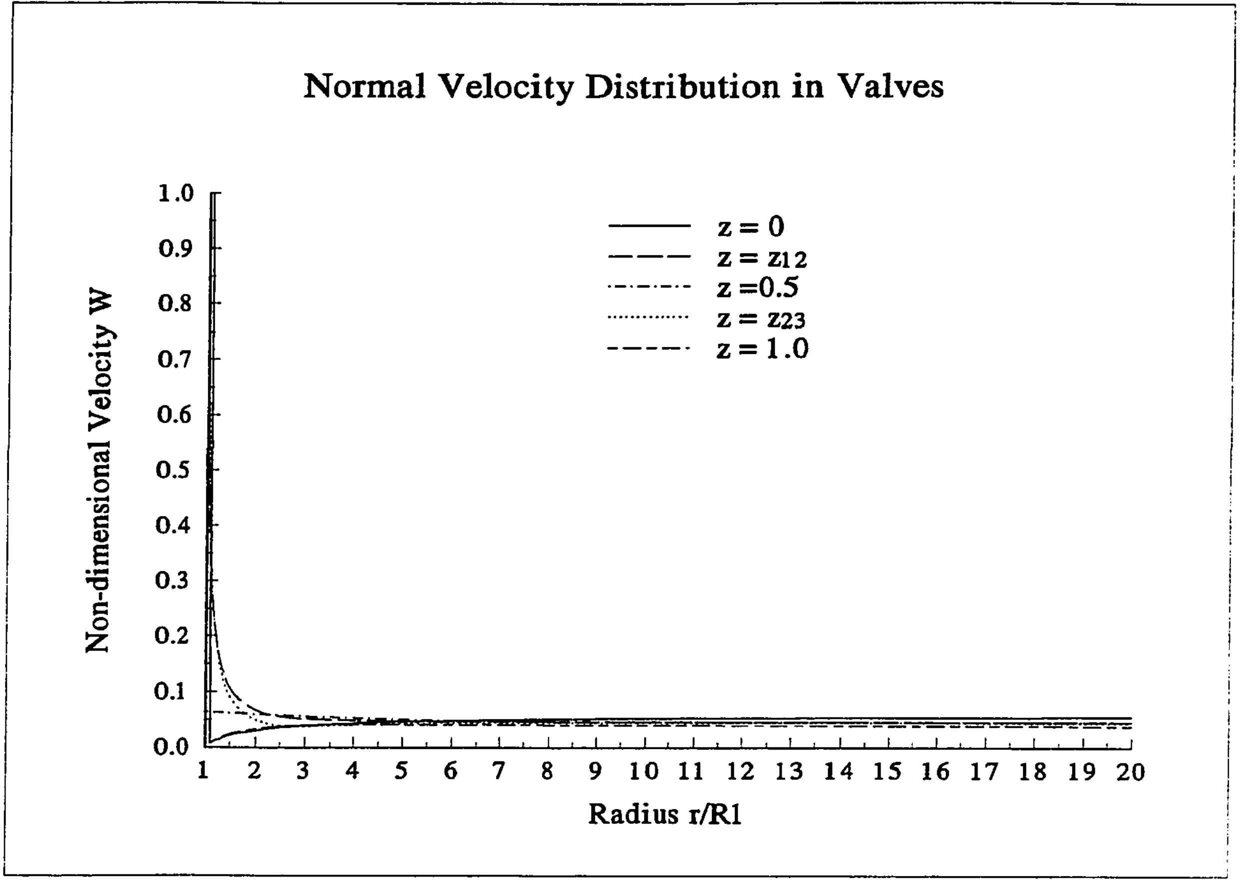
Normal Velocity Distribution in Valves
Non-dimensional Velocity W
1.0
0.9
0.8
0.7
0.6
0.5
0.4
0.3
0.2
0.1
0.0
1
2
3
4
5
6
7
8
9
10
11
12
13
14
15
16
17
18
19
20
Radius r/R1
z = 0
z = z12
z =0.5
z = z23
z = 1.0

Fig. 31c

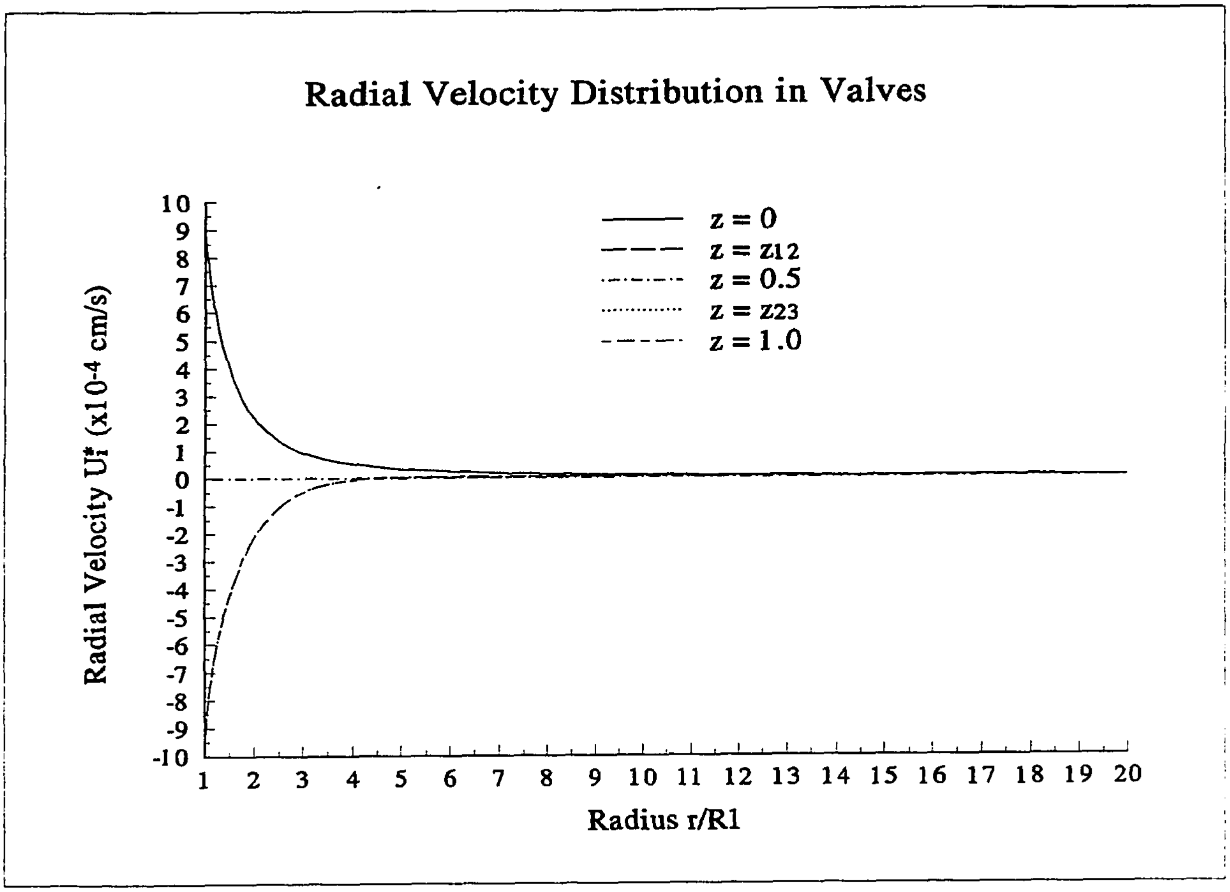
Radial Velocity Distribution in Valves
z = 0
z = z12
z = 0.5
z = z23
z = 1.0
Radial Velocity Ui* (x10-4 cm/s)
10
9
8
7
6
5
4
3
2
1
0
-1
-2
-3
-4
-5
-6
-7
-8
-9
-10
1 2 3 4 5 6 7 8 9 10 11 12 13 14 15 16 17 18 19 20
Radius r/R1

Fig. 31d

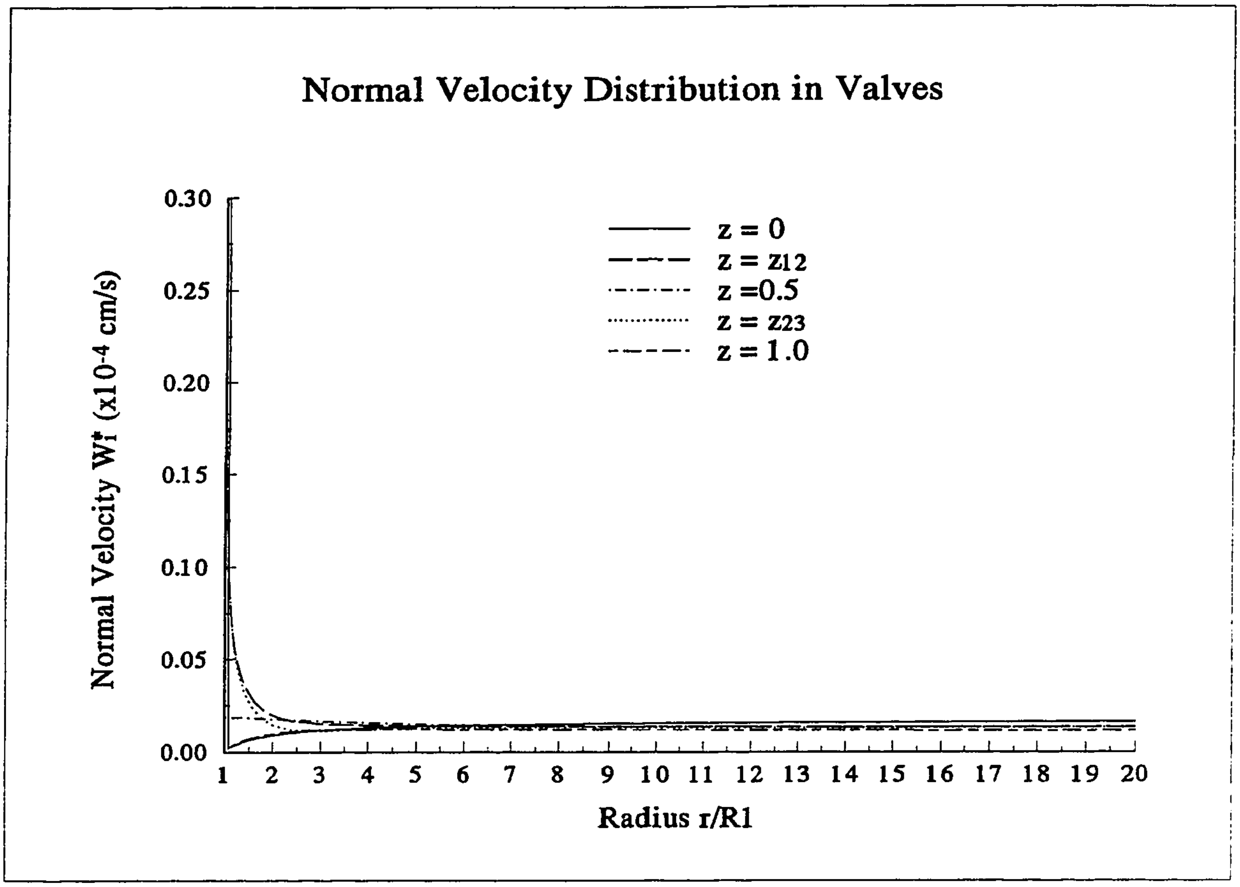
Normal Velocity Distribution in Valves
Normal Velocity $W_1^*$ ($\times 10^{-4}$ cm/s)
0.30
0.25
0.20
0.15
0.10
0.05
0.00
z = 0
z = z12
z =0.5
z = z23
z = 1.0
1
2
3
4
5
6
7
8
9
10
11
12
13
14
15
16
17
18
19
20
Radius r/R1

Fig. 31e

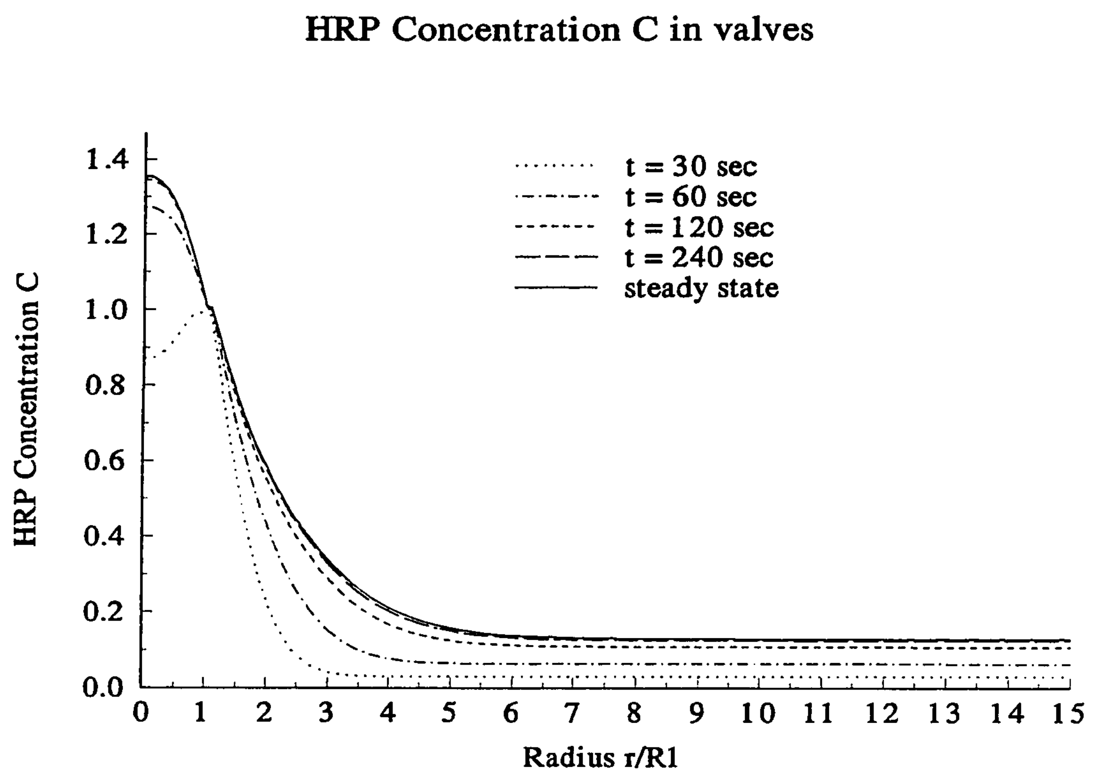
HRP Concentration C in valves
HRP Concentration C
1.4
1.2
1.0
0.8
0.6
0.4
0.2
0.0
0
1
2
3
4
5
6
7
8
9
10
11
12
13
14
15
Radius r/R1
t = 30 sec
t = 60 sec
t = 120 sec
t = 240 sec
steady state

Fig.32

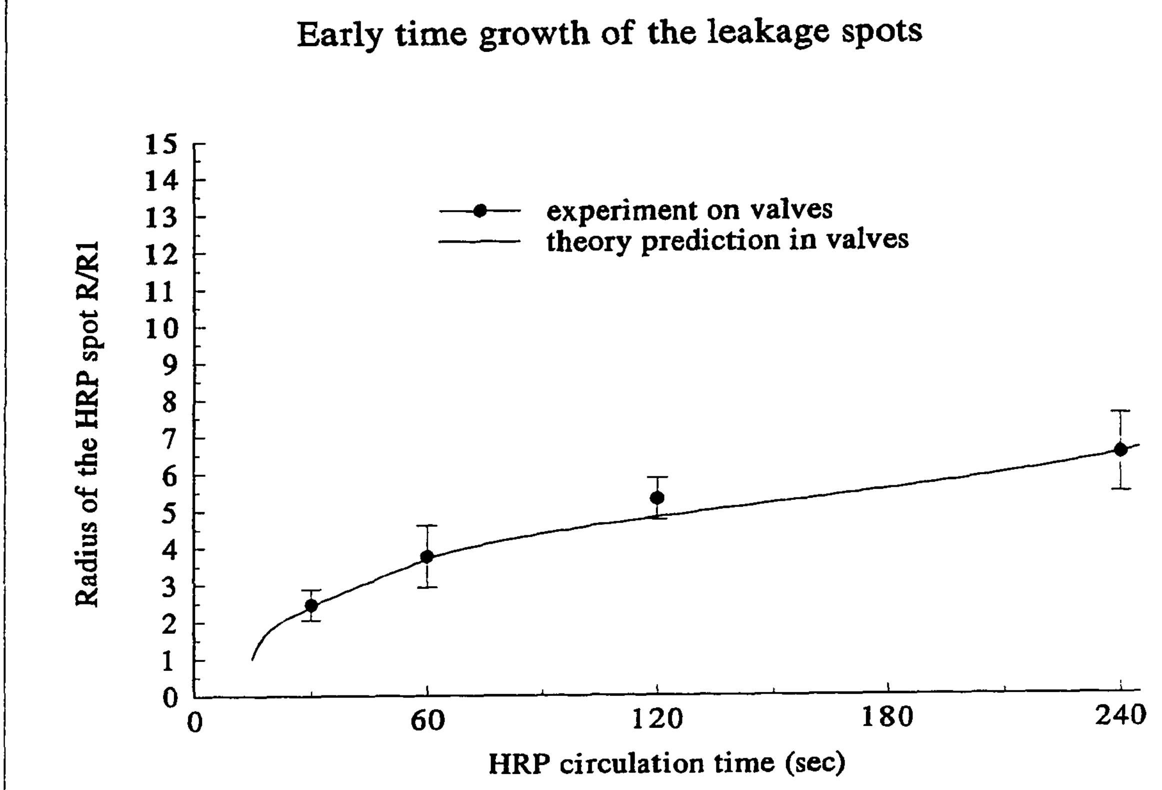
Early time growth of the leakage spots
Radius of the HRP spot R/R1
15
14
13
12
11
10
9
8
7
6
5
4
3
2
1
0
0
60
120
180
240
HRP circulation time (sec)
experiment on valves
theory prediction in valves

Fig. 33a

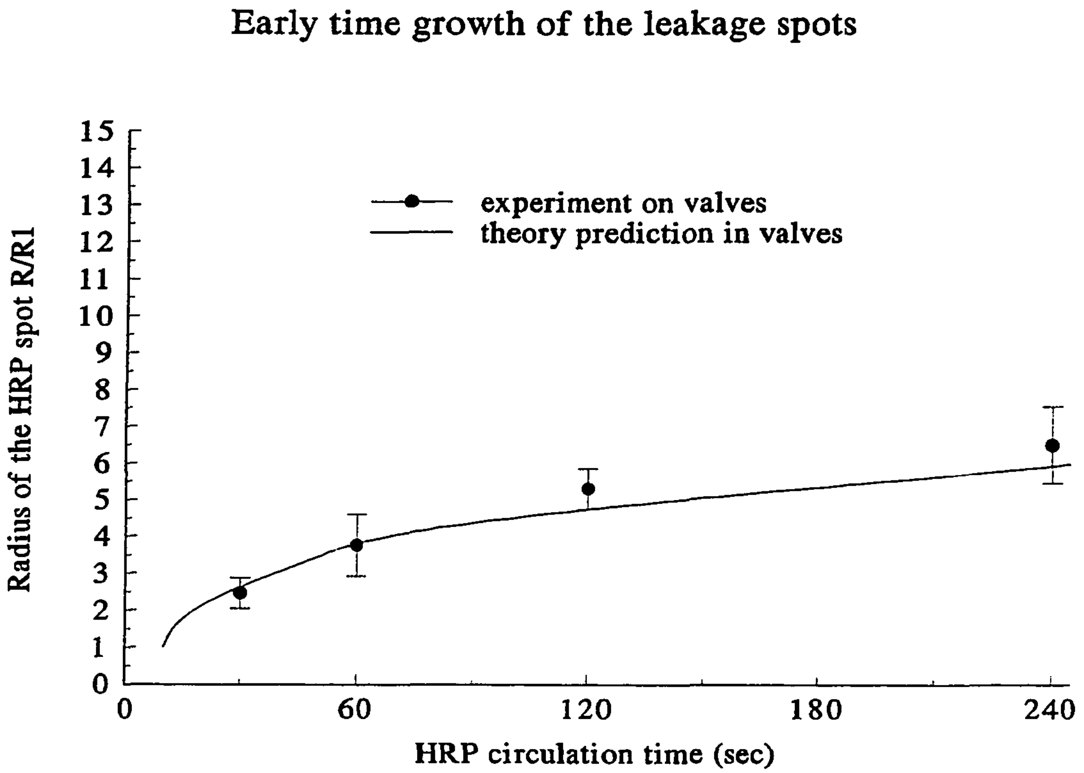

Early time growth of the leakage spots
experiment on valves
theory prediction in valves
Radius of the HRP spot R/R1
HRP circulation time (sec)
0
1
2
3
4
5
6
7
8
9
10
11
12
13
14
15
0
60
120
180
240

Fig.33b

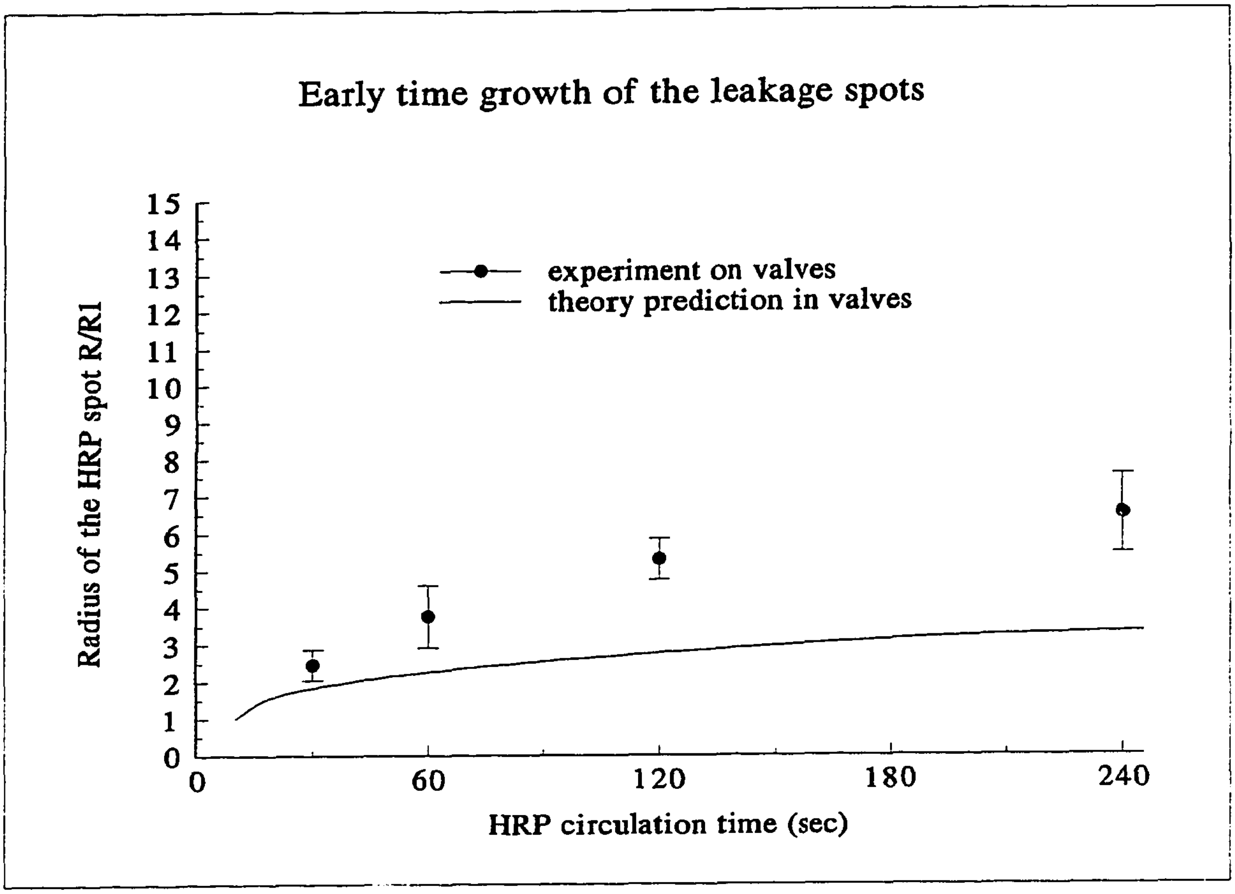
Early time growth of the leakage spots
Radius of the HRP spot R/R1
15
14
13
12
11
10
9
8
7
6
5
4
3
2
1
0
experiment on valves
theory prediction in valves
0
60
120
180
240
HRP circulation time (sec)

Fig.33c

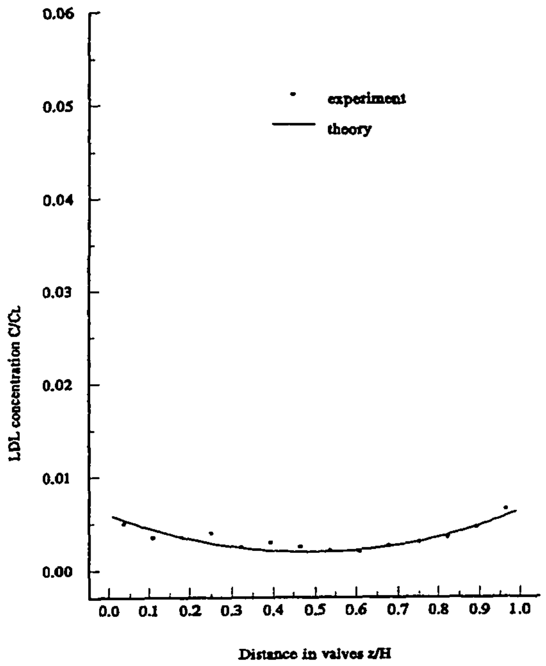
0.06
0.05
0.04
0.03
0.02
0.01
0.00
LDL concentration C/C₁
experiment
theory
0.0
0.1
0.2
0.3
0.4
0.5
0.6
0.7
0.8
0.9
1.0
Distance in valves z/H

Fig. 34

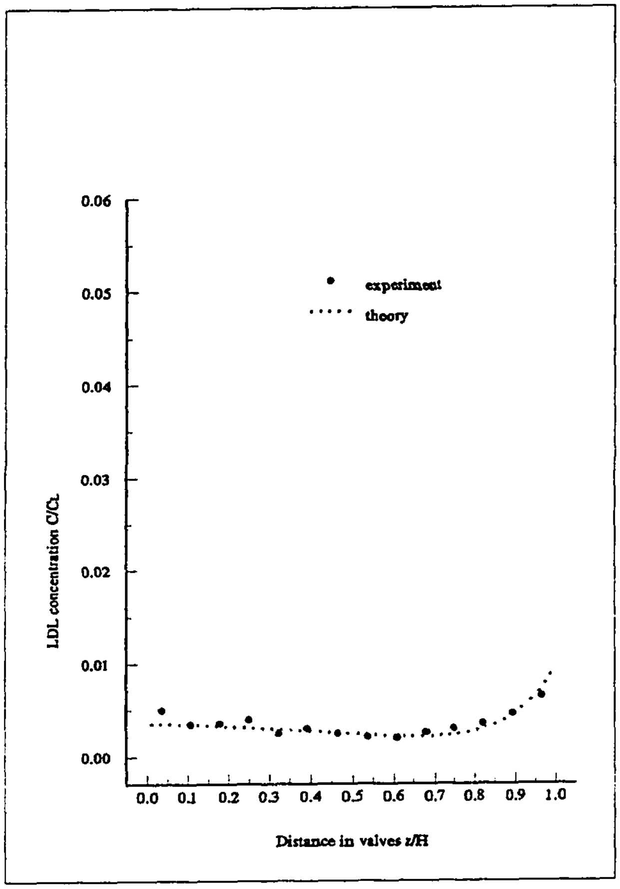
0.06
0.05
0.04
0.03
0.02
0.01
0.00
LDL concentration C/CL
● experiment
····· theory
0.0
0.1
0.2
0.3
0.4
0.5
0.6
0.7
0.8
0.9
1.0
Distance in valves z/H

Fig. 35

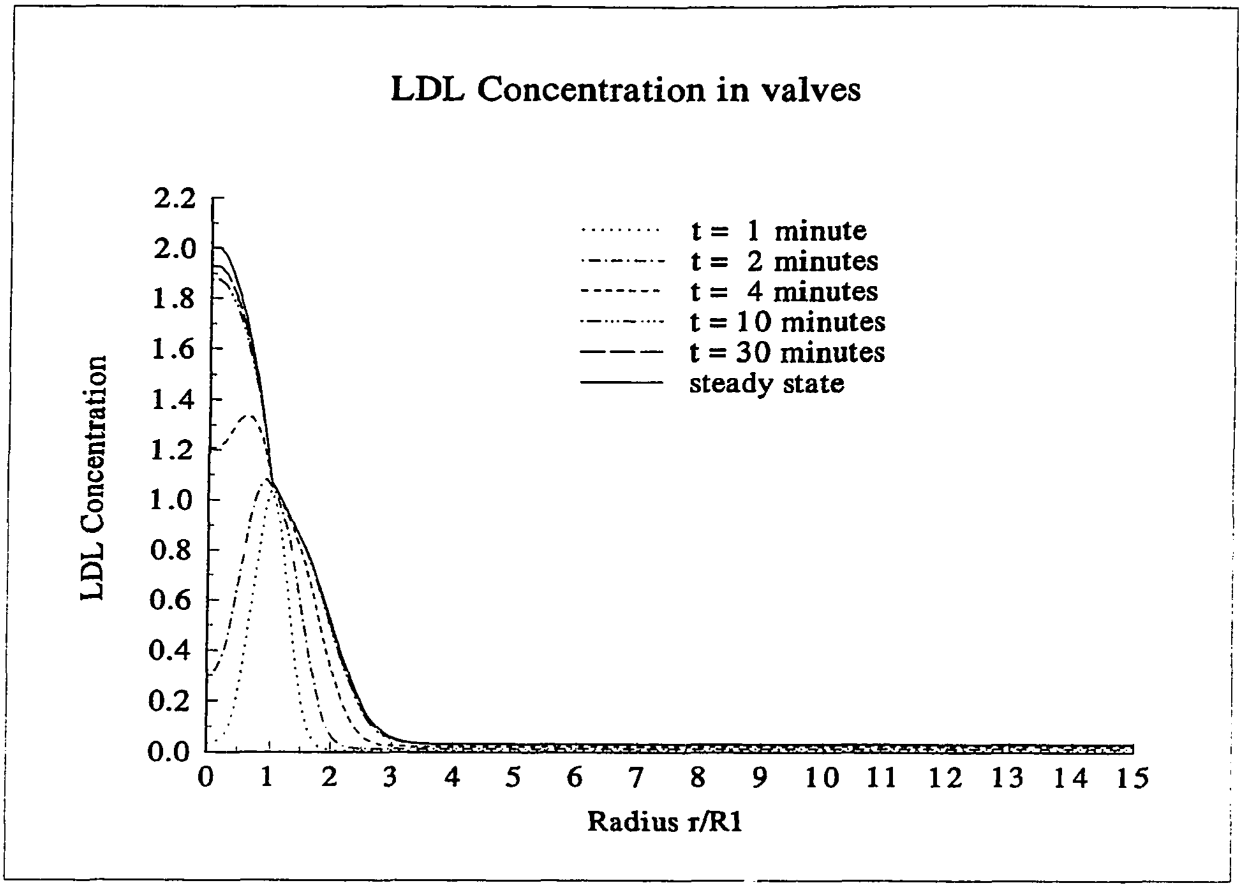
LDL Concentration in valves
LDL Concentration
2.2
2.0
1.8
1.6
1.4
1.2
1.0
0.8
0.6
0.4
0.2
0.0
0
1
2
3
4
5
6
7
8
9
10
11
12
13
14
15
Radius r/R1
t = 1 minute
t = 2 minutes
t = 4 minutes
t = 10 minutes
t = 30 minutes
steady state

Fig. 36a

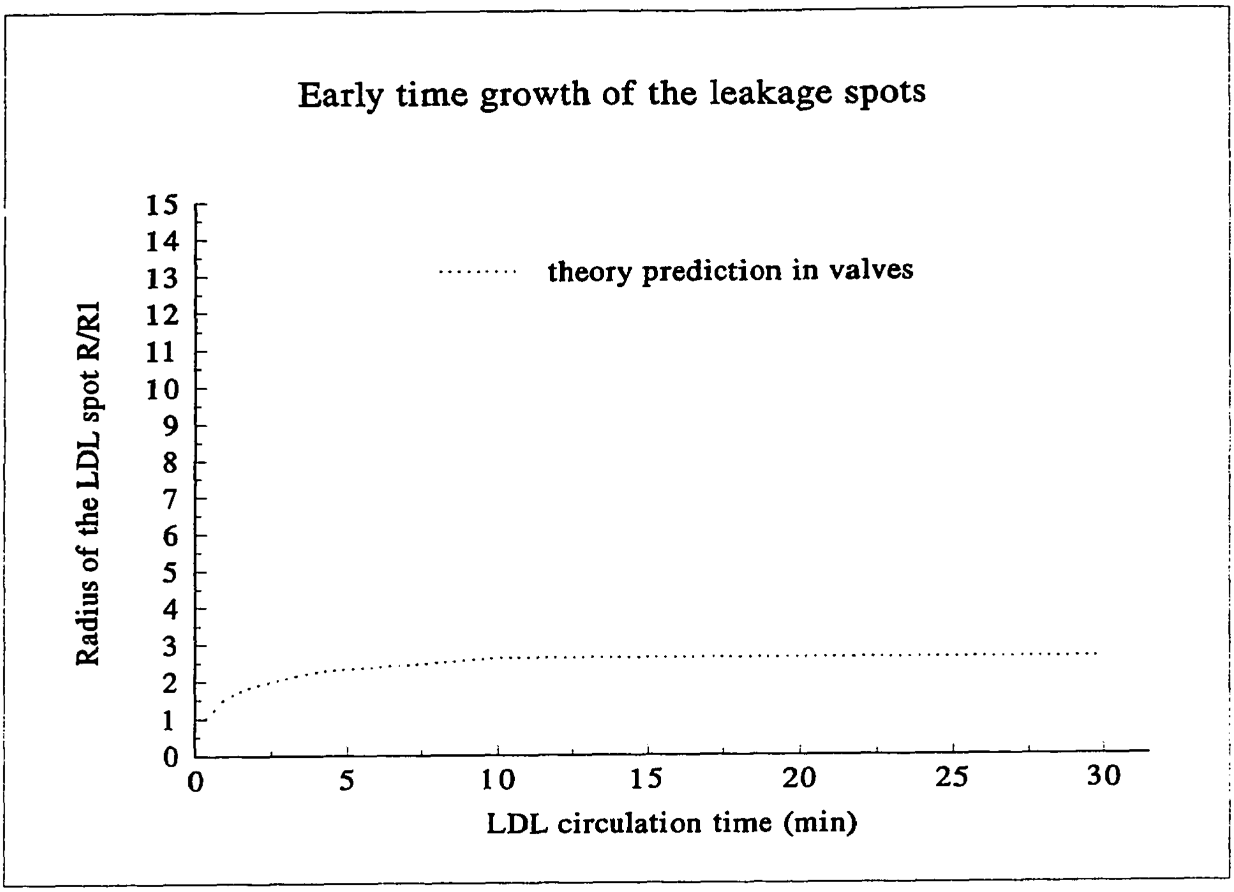
Early time growth of the leakage spots
theory prediction in valves
Radius of the LDL spot R/R1
15
14
13
12
11
10
9
8
7
6
5
4
3
2
1
0
0
5
10
15
20
25
30
LDL circulation time (min)

Fig. 36b

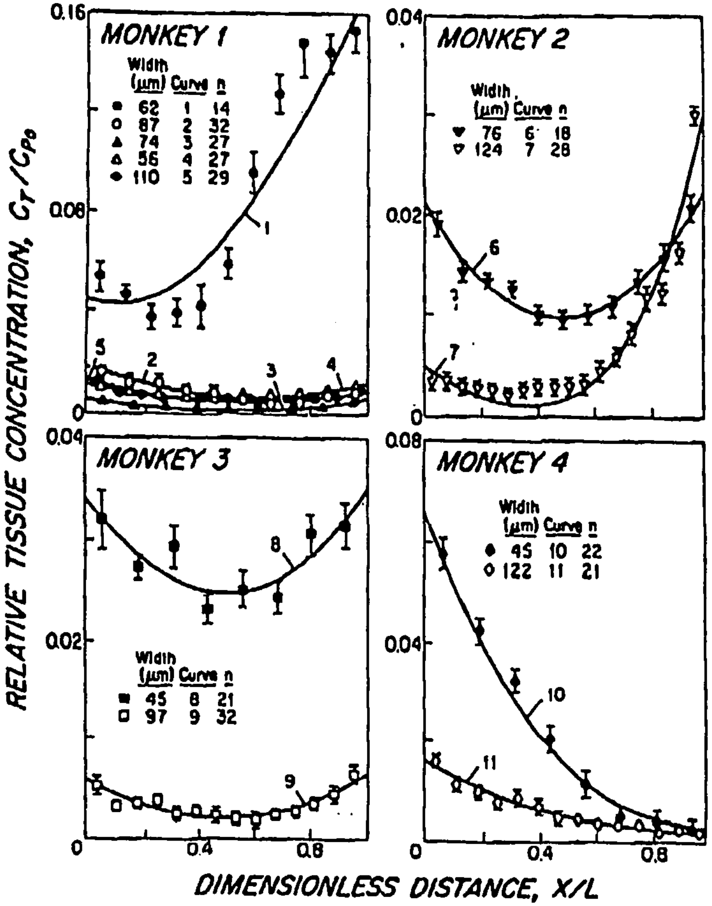
MONKEY 1
Width (μm) Curve n
● 62 1 14
○ 87 2 32
▲ 74 3 27
△ 56 4 27
◆ 110 5 29
MONKEY 2
Width (μm) Curve n
▼ 76 6 18
▽ 124 7 28
MONKEY 3
Width (μm) Curve n
■ 45 8 21
□ 97 9 32
MONKEY 4
Width (μm) Curve n
◆ 45 10 22
◇ 122 11 21
0.16
0.08
0
0.04
0.02
0.08
0.04
0.4
0.8
1
2
3
4
5
6
7
8
9
10
11
RELATIVE TISSUE CONCENTRATION, $C_T/C_{P0}$
DIMENSIONLESS DISTANCE, X/L

Fig. 37

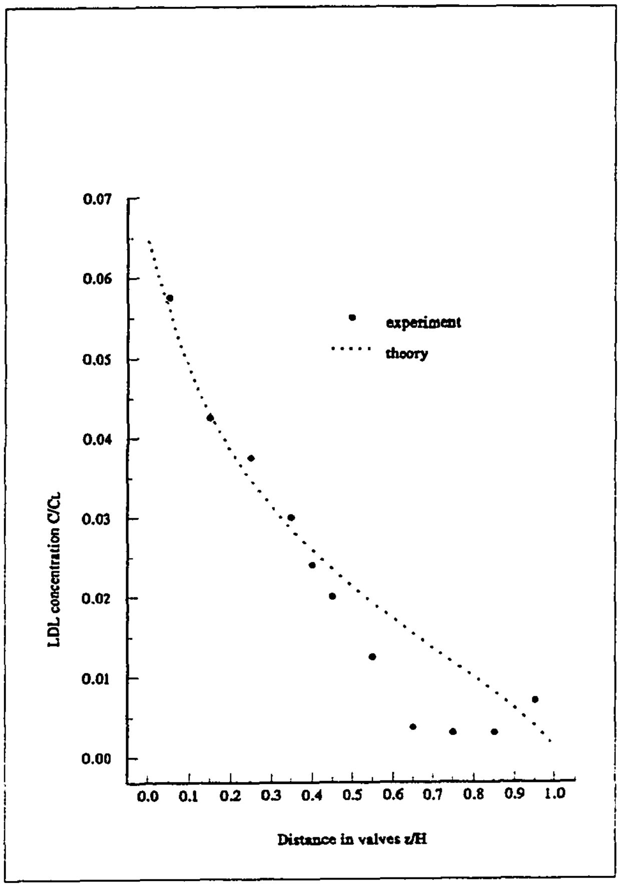

LDL concentration C/CL
0.07
0.06
0.05
0.04
0.03
0.02
0.01
0.00
0.0
0.1
0.2
0.3
0.4
0.5
0.6
0.7
0.8
0.9
1.0
Distance in valves z/H
● experiment
····· theory

Fig. 38a

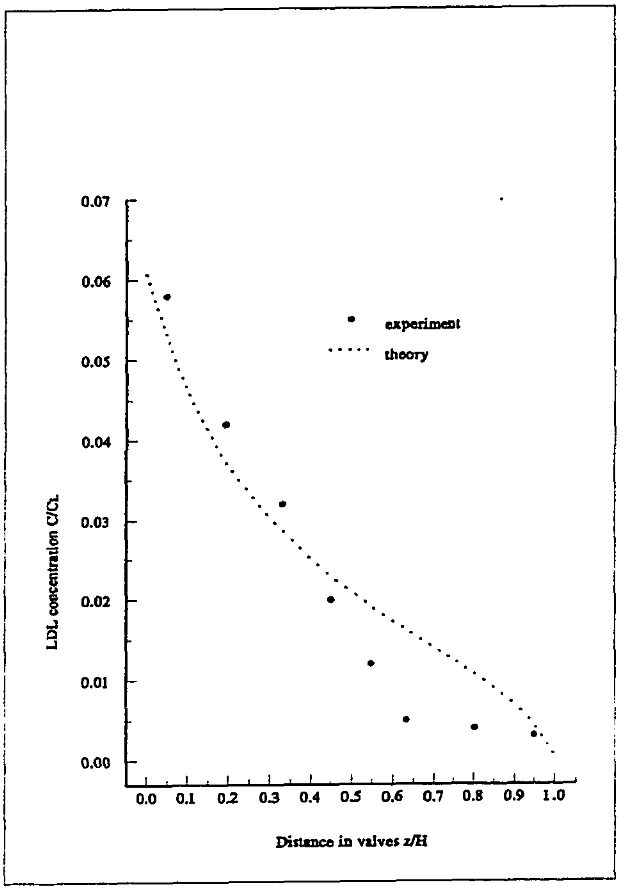
0.07
0.06
0.05
0.04
0.03
0.02
0.01
0.00
LDL concentration C/CL
● experiment
····· theory
0.0
0.1
0.2
0.3
0.4
0.5
0.6
0.7
0.8
0.9
1.0
Distance in valves z/H

Fig. 38b

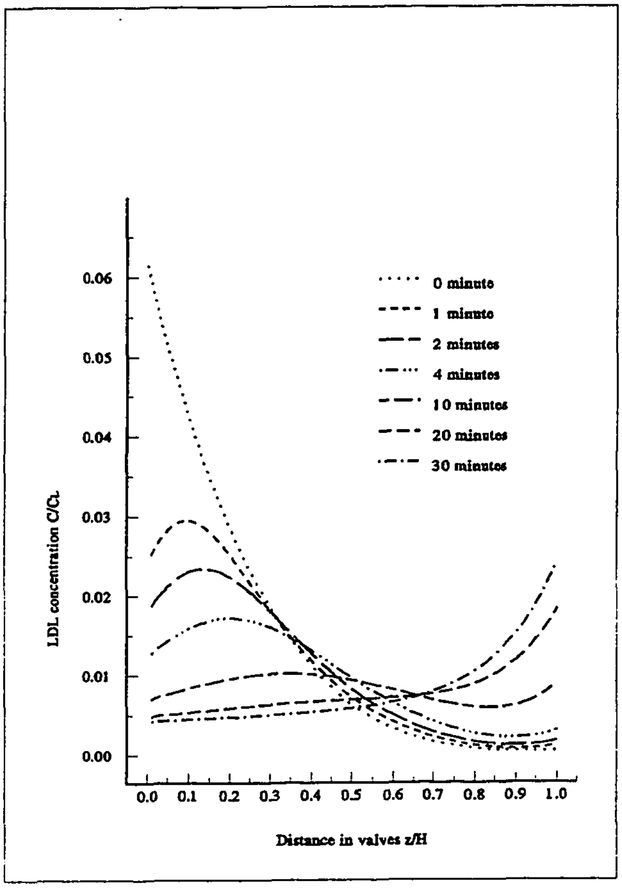
0 minute
1 minute
2 minutes
4 minutes
10 minutes
20 minutes
30 minutes
LDL concentration C/CL
0.06
0.05
0.04
0.03
0.02
0.01
0.00
0.0
0.1
0.2
0.3
0.4
0.5
0.6
0.7
0.8
0.9
1.0
Distance in valves z/H

Fig. 38c

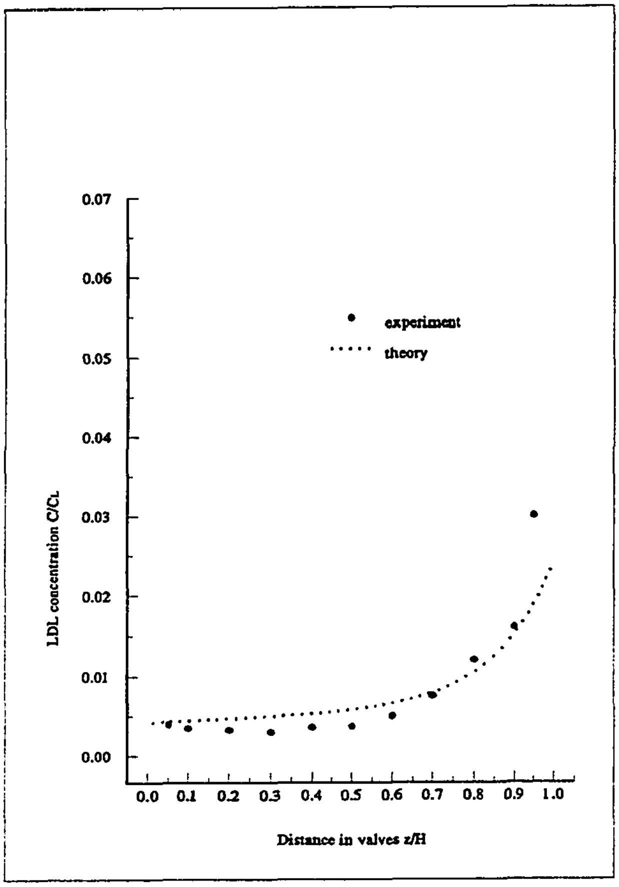
0.07
0.06
0.05
0.04
0.03
0.02
0.01
0.00
LDL concentration C/CL
● experiment
····· theory
0.0
0.1
0.2
0.3
0.4
0.5
0.6
0.7
0.8
0.9
1.0
Distance in valves z/H

Fig. 38d

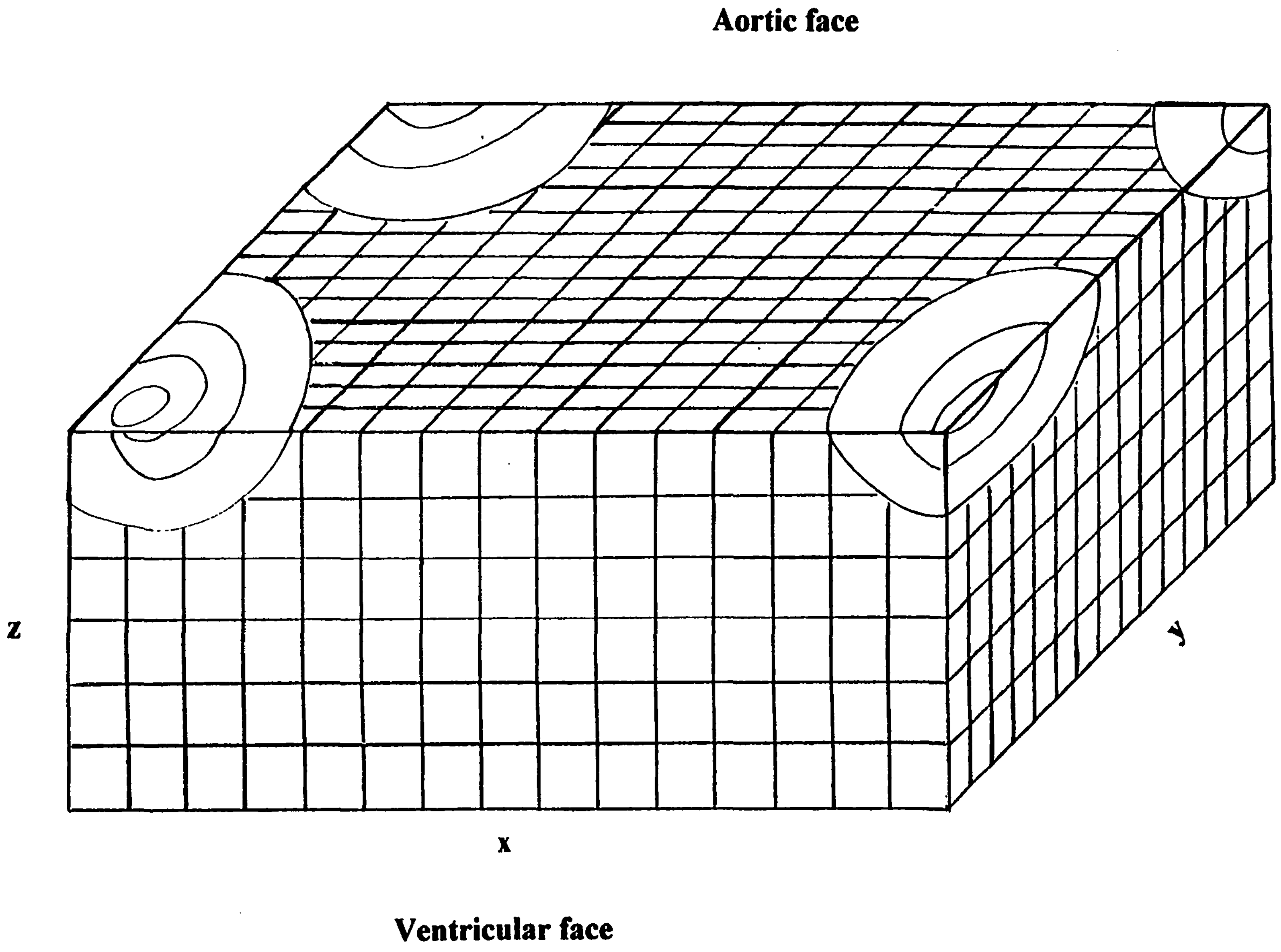

Fig. 39

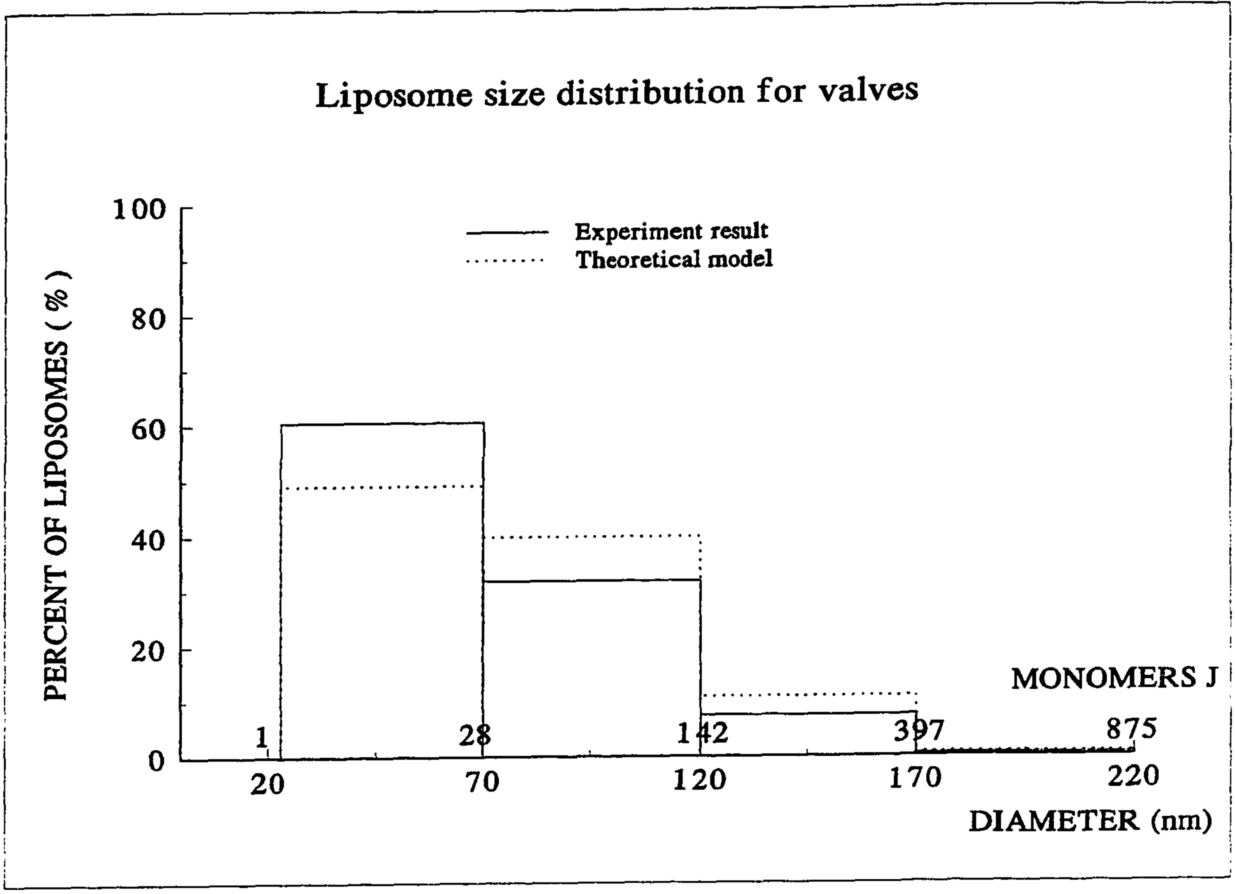
Liposome size distribution for valves
Experiment result
Theoretical model
PERCENT OF LIPOSOMES ( % )
100
80
60
40
20
0
MONOMERS J
1
28
142
397
875
20
70
120
170
220
DIAMETER (nm)

Fig. 40

**Bibliography:**

1. **Atkinson, J. B., Hoover, R. L., Berry, K. K., and Swift, L. L.** Cholesterol-fed heterozygous watanabe heritable hyperlipidemic rabbits: a new model for atherosclerosis. Atherosclerosis 78: 123-136, 1989.

2. **Barakat, A. I., Uhthoff, P. A. F., and Colton, C. K.** Topographical mapping of sites of enhanced HRP permeability in the normal rabbit aorta. ASME J. of Biomechanical Engineering 114: 283-292, 1992.

3. **Brown, M. S., and Goldstein, J. L.** Receptor-mediated control of cholesterol metabolism. Science 191:150-154, 1976.

4. **Camejo, G.** The interaction of lipids and lipoproteins with the intercellular matrix of arterial tissue: Its possible role in atherogenesis. Adv. Lipid Res. 19: 1-53, 1982.

5. **Camejo, G., Olofsson, S., Lopez, F., Carlsson, P., and Bondjers, G.** Identification of apo B-100 segments mediating the interaction of low density lipoproteins with arterial proteoglycans. Arteriosclerosis 8: 368-377, 1988.

6. **Carlson, T. L., and Kottke, B. A.** ApoA-I secretion by rabbit intestinal mucosa cell cultures. Lipids. 26: 684-688, 1991

7. **Chuang, P., Cheng, J., Lin, S., Jan, K., Wang, D., and Chien, S.** Macromolecular transport across arterial and venous endothelium in rats: studies with Evans blue-albumin and horseradish peroxidase. Arteriosclerosis 10: 188-197, 1990.

8. **Frank, J. S., and Fogelman, A. M.** Ultrastructure of the intima in WHHL and cholesterol-fed rabbit aortas prepared by ultra-rapid freezing and freeze-etching. J. of Lipid Research. 30: 967-978, 1989.

9. **Gerrity, R. G.** The role of the monocyte in atherogenesis: I. transition of blood-borne monocytes into foam cells in fatty lesions. Am. J. Path. 1103: 81-190, 1981.

10. **Guyton, J. R, and Klemp, K. F.** The lipid-rich core region of human atherosclerotic fibrous plaques. Am J Pathol 134: 705-717, 1989.

11. **Herrmann, R. A., Malinauskas, R. A., and Truskey, G. A.** Characterization of sites with elevated LDL permeability at intercostal, celiac, and iliac branches of the normal rabbit aorta. Arteriosclerosis and Thrombosis 14: 313-323, 1994.

12. **Huang, Y. Weinbaum, S., Rumschitzki, D., and Chien, S.** A fiber matrix model for the growth of macromolecular leakage spots in the arterial intima. J. of Biomechanical

Engineering. 116: 430-445, 1994.

13. **Iverius, P. H.** The interaction between human plasma lipoprotein and connective tissue glycosaminoglycans. J. Biol. Chem. 247: 2607-2613, 1972.

14. **Lin, S. J., Jan, K. M., Schuessler, G. B., Weinbaum, S., and Chien, S.** Enhanced macromolecular permeability of aortic endothelial cells in association with mitosis. Atherosclerosis 73: 223-232, 1988.

15. **Lin, S. J., Jan, K. M., Weinbaum, S., and Chien, S.** Transendothelial transport of low density lipoprotein in association with cell mitosis in rat aorta. Arteriosclerosis 9: 230-236, 1989.

16. **Malinauskas, R. A., Herrmann, R. A., and Truskey, G. A.** The distribution of intimal white blood cells in the normal rabbit aorta: Atherosclerosis 115: 147-163, 1995.

17. **Mitchison, M. J., Carpenter, K. L. M., and Ball, R. Y.** The role of macrophages in human atherosclerosis. In: Glagov S, Newman WP, Schaffer SA (eds.), Pathobiology of the Human Atherosclerotic Plaque, New York: Springer-Verlag, 121-128, 1990.

18. **Mora, R., Lupu, F., and Simionescu, N.** Prelesional events in atherogenesis. colocalization of apolipoprotein B, unesterified cholesterol and extracellular phospholipid liposomes in the aorta of hyperlipidemic rabbits. Atherosclerosis 67: 143-154, 1987.

19. **Nievelstein, P. F. E. M., Fogelman, A. M., Mottino, G., and Frank, J. S.** Lipid accumulation in rabbit aortic intima 2 hours after bolus infusion of low density lipoprotein: a deep-etch and immunolocalization study of ultrapidly frozen tissue. Arteriosclerosis and Thrombosis 11: 1795-1805, 1991.

20. **Schwenke, D. C., and Carew, T. E.** Initiation of atherosclerotic lesions in cholesterol-fed rabbits. II Selective retention of LDL vs. selective increases in LDL permeability in susceptible sites of arteries. Arteriosclerosis 9: 908-918, 1989.

21. **Simionescu, M., Ghitescu, L., Fixman, A., and Simionescu, N.** How plasma macromolecules cross the endothelium. News, Phys. and Sci. 2: 97-100, 1987.

22. **Simionescu, N., Mora, R., Vasile, E., Lupu, F., Filip, D. A., and Simionescu, M.** Prelesional modifications of the vessel wall in hyperlipidemic atherogenesis. Ann. N.Y. Acad. Sci. 598: 1-16, 1990.

23. **Simionescu, N., Vasile, E., Lupo, F., Popescu, G., and Simionescu, M.** Prelesional events in atherogenesis. Accumulation of extracellular cholesterol-rich liposomes in the arterial intima and cardiac valves of the hyperlipidemic rabbits. Am. J. Pathol. 123: 1109-

1125, 1986.

24. **Srinivasan, S. R., Dolan, P., Radhakrishnamurthy, B., Pargaonkar, P. S., and Berenson, G. S.** Lipoproteinacid mucopolysaccharide complexes of human atherosclerotic lesions. Biochem. Biophys. Acta 388: 58-70, 1975.

25. **Srinivasan, S. R., Vijayogopal, P., Dalferes, E. R., Abbate, B., Radhakrishnamurthy, B., and Berenson, G. S.** Dynamics of lipoprotein-glycosaminoglycan interactions in the arteriosclerotic rabbit aorta in vivo. Biochem. Biophys. Acta 793: 157-168, 1984.

26. **Stary, H. C.** Macrophage foam cells in coronary artery intima of human infants. Annals of the New York Academy of Sciences, Atherosclerosis 454: 4-8, 1985.

27. **Stary, H. C.** Macrophages, macrophage foam cells, and eccentric intimal thickening in the coronary arteries of young children. Atherosclerosis 964: 1-108, 1987.

28. **Stary, H. C.** Changes in the cells of atherosclerotic lesions as advanced lesions evolve in coronary arteries of children and young adults. In: Glagov S, Newman WP, Schaffer SA (Eds), and Pathobiology of the Human Atherosclerotic Plaque. New York: Springer-Verlag, 93-106, 1990.

29. **Steinberg, D., Parthasarathy, S., Carew, T. E., Khoo, J. C., and Witztum, J. L.** Beyond cholesterol: modifications of low-density lipoprotein that increase its atherogenicity. New England J. Med. 320: 915-924, 1989.

30. **Truskey, G. A., Robert, W. L., Herrmann, R. A., and Malinauskas, R. A.** Measurement of endothelial permeability to $^{125}$I-low density lipoproteins in rabbits arteries by use of En Face preparations. Circulation Research 71: 883-897, 1992.

31. **Weinbaum, S., Tzeghai, G., Ganatos, P., Pfeffer, R., and Chien, S.** Effect of cell turnover and leaky junctions on arterial macromolecular transport. Am. J. Physiol. 248: H945-H960, 1985.

32. **Yuan, F., Chien, S., and Weinbaum, S.** A new view of convective-diffusive transport processes in the arterial intima. J. Biomech. Engineering, 113: 314-329, 1991.

33. **Brown, M. S., and Goldstein, J. L.** How LDL Receptors Influence Cholesterol and Atherosclerosis" Scientific Amer. 251: 58-66, 1984.

34. **Angelo M. Scanu and Arthur A. Spector.** Biochemistry and Biology of Plasma Lipoproteins. Biochemistry of Disease, 11, 1986.

35. **Stary, H. C., Blankenhorn, D. H., Chandler, A. B., Glagov, S., Insull, W. Jr., Richardson, M., Rosenfeld, M. E., Schaffer, J. A., Schwartz, C. J., Wagner, W. D., and Wissler, R. W.** A Definition of the intima of human arteries and of atherosclerosis-prone regions. Arteriosclerosis and Thrombosis. 11: 120-134, 1992.

36. **Palade, G. E.** Transport in quanta across the endothelium of blood capillaries. Anat. Res. 136: 245-254, 1960.

37. **Casley-Smith, J. R.** The dimensions and numbers of small vesicles in cells, and the significance of these for endothelial permeability. J. Microscopy 90: 251-269, 1969.

38. **Stemerman, M. B., Morrel, E. M., Burke, K. R., Colton, C. K., Smith, K. A., and Lees, R. S.** Local variation in arterial wall permeability to low density lipoprotein in normal rabbit aorta. Arteriosclerosis 6: 64-69, 1986.

39. **Schwenke, D. C., and Carew, T. E.** Quantification in vivo of increased LDL content and rate of LDL degradation in normal rabbit aorta occurring at sites susceptible to early atherosclerotic lesions. Circ. Res. 62: 699-710, 1988.

40. **Nievelstein-Post, P., Mottino, G., Fogelman, A., and Frank, J.** An ultrastructural study of lipoprotein accumulation in cardiac valves of the rabbits Arteriosclerosis and Thrombosis. 14: 1151-1161, 1994.

41. **Filip, D. A., Nistor, A., Bulla, A., Radu, A., Lupu, F., and Simionescu, M.** Cellular events in the development of valvular atherosclerotic lesions induced by experimental hypercholesterolemia. Atherosclerosis, 67: 199-214, 1987.

42. **Zahor, Z. and Czabanova, V.** Experimental atherosclerosis of the heart valves in rat following a long-term atherogenic regimen. Atherosclerosis, 27: 49, 1977.

43. **Tompkins, R. G., Schnitzer, J. J., and Yarmush, M. L.** Macromolecular transport within heart valves. Cir. Res. 64: 1213-1223, 1989.

44. **Walton, K. W., Williamson, N., and Johnson, A. G.** The Pathogenesis of atherosclerosis of the mitral and aortic valves. The Journal of Pathology Vol. 101, No.3, 205-220, 1970.

45. **O'Brien, K. D., MD, and Chait, A., MD**. The biology of the artery wall in atherogenesis. Lipid disorders. 78:1 41-67, 1994.

46. The role of lipoprotein in atherogensis. Nutrition and biotechnology in heart disease and cancer. Plenum Press, New York. 29-38,1995.

47. **Davies, M. J, and Woolf, N.** What is it and why does it occur? British Heart Journal Atherosclerosis 69(1 suppl): S3-11, 1993.

48. **Ross, R.** The pathogenesis of atherosclerosis - an update. N. Engl. J. Md. 314: 488-500, 1986.

49. **Michael, C. C.** Capillary permeability and how it may change. J. Physiol. 404: 1-29, 1988.

50. **Brown, M. S. and Goldstein, J. L.** Lipoprotein metabolism in the macrophage: implications for cholesterol deposition in atherosclerosis. Ann. Rev. Biochem. 52: 223-261, 1983.

51. **Guyton, J. R., and Klemp, K. F.** Early extracellular and cellular lipid deposits in aorta of cholesterol-fed rabbits. Am. J. Pathol. 141:925, 1992.

52. **Guyton, J. R. and Klemp, K. F.** The lipid-rich core region of human atherosclerotic fibrous plaques: prevalence of small lipid droplets and vesicles by electron microscopy. Am. J. Pathol. 134: 705, 1989.

53. **Khoo, J. C., Miller, E., Mcloughlin, P. and Steinberg, D.** Enhanced macrophage update of low density lipoprotein after self-aggregation. Arterioscler. 8: 348, 1988.

54. **Hoff, H. F., Whitaker, T. E. and O'Neil, J.** Oxidation of low density lipoprotein leads to particle aggregation and altered macrophage recognition. J. Biol. Chem. 267:602, 1992.

55. **Weinbaum, S., Pfeffer, R., and Chien. S.** The Search for the Large Endothelial Pore and its Possible Link to the Localization of Atherosgenesis. PCH physicochemical Hydrodynamics. Vol. 10, 705-726,1988.

56. **Nerem, R. M., and Levesque, M. J.** The Case for Fluid Dynamics as a Localizing Factor in Atherogenesis. Fluid Dynamics as Localizing Factor for Atherosclerosis, Schettler. G. et al. eds. Springer-Verlag. Berlin. 26-37,1984.

57. **Vargas, C. B., Vargas, F. F., Pribyl, J. G., and Blackshear, P. L.** Mhydraulic Conductivity of the Endothelial and Outer Layers of the Rabbit Aorta. American Journal of Physiology. 236: H53-60, 1979

58. **Schwenke, D. C., and Carew, T. E.** Initiation of atherosclerotic lesions in cholesterol-fed rabbits. Selective retention of LDL vs. selective increases in LDL permeability in susceptible sites of arteries . Arteriosclerosis 9: 908-918, 1989.

59. **Schwenke, D. C., and Carew, T. E.** Initiation of atherosclerotic lesions in cholesterol-

fed rabbits. I. Focal increases in arterial LDL concentration precede development of fatty streak lesions. Arteriosclerosis 9: 895-907, 1989.

60. **Schwenke, D. C., and Carew, T. E.** Quantification in vivo of increased LDL content and rate of LDL degradation in normal rabbit aorta occurring at sites susceptible to early atherosclerotic lesions. Circ. Res.62: 699-710, 1988.

61. **Yin, Y., Lim, K. H., Weinbaum, S., Chien, S., and Rumschitzki, D. S.** A model for the initiation and growth of extracellular lipid liposomes in arterial intima. Am. J. Physiol. 272(Heart Circ. Physiol. 41): H1033-H1046,1997.

62. **Gross L, and Kugel, M. A.** Topographic anatomy and histology of the valves in the human heart. Am. J. Pathol; 7: 445-473, 1931.

63. **Rasche, R. F., and Kashi, J. P.** Diffusion in cardiac valves. Arch Pathol; 93: 325-329,1972.

64. **Chuang, P., Cheng, J., Lin, S., Jan, K., Wang, D., and Chien, S.** Macromolecular Transport Across Arterial Endothelium in Rats: Studies with Evans-Albumin and Horseradish Peroxidase. Arteriosclerosis. Vol. 10, 188-197. 1990.

65. **Ogston, A. G., Preston, B. N., and Wells, J. D.** On the Transport of Compact Particles Through Solutions of Chainpolymers. Proc. R. soc. London Ser. A 33, 297-316, 1973.

66. **Karnovsky, M. J.** Use of ferrocyanide-reduced osmium tetroxide in electron microscopy. Proceedings of the 11th Annual Meeting of the American Society for Cell Biology (abstr). 146,1971.

67. **Huang, A., Jan, K. M., and Chien, S.** Role of intercellular junctions in the passage of horseradish peroxidase across aortic endothelium. Laboratory Investigation; 67: 201-209,1992.

68. **Weinbaum, S., Wen, G., Ganatos, P., Pfeffer, R., Lee, M. M. L., and Chien, S.** On the time-dependent diffusion of macromolecules through transient open junctions and their subendothelial spread, I. Short-time model for cleft exit region. Journal of theoretical biology, Vol. 135, 1-30,1988.

69. **Gourlay, A. R.** Hopscotch: A fast second-order partial differential equation solver Journal of Institute Mathematics and Applications, Vol. 6,. 375-390,1970.

70.**Wen., G., Weinbaum, S, Ganatos, P., Pfeffer, R., and Chien, S**. On the time-Dependent Diffusion of Macromolecules Through Transient Open Junctions and Their Sunendothelial Spread. II. Long-Time Model for Interaction Between Leakage Sites. Journal of Theoretical Physiology, Vol. 135219-253. , 1988.

71.**Ganong, W. F.** Review of Medicine Physiology., 17th Edition 514-521,1989.

72. **Tedgui, A. and Lever, M. J.** Filtration through damaged and undamaged rabbit thoracic aorta. American Journal of Physiology 247: H784-791, 1984.

73. **Bundgarrd, M., Frokjaer-Jenson, J., and Crone, C**. Endothelial plasmalemmal vesicles as elements in a system of branching invaginations from the cell surface. Proc. Natn'l. Acad. Sci. 276: 6439, 1979.

74.**Chien, S., Laufer, L., and Handley, D. A**. Vesicle distribution in the arterial endothelium determined with ruthenium as an extracellular marker. J. Ultrastr. Res. 79: 198-206, 1982.

75. **Bundgaard, M., Hagman, P., and Crone, C.** The three-dimensional organization of plasmalemmal vesicular profiles in the endothelium of rat heart capillaries. Microvasc. Res. 25: 358-368, 1983.

76. **Baldwin, A. L., and Chien, S.** Effects of dextran 40 on endothelial binding and vesicle loading of ferritin in rabbit aorta. Arteriosclerosis 8: 140-146, 1988.

77. **Lin, S. J., Jan, K. M., and Chien, S.** The role of dying endothelial cells in transendothelial macromolecular transport. Arteriosclerosis 10: 730-709, 1990.

78. **Levick, J. R.** Flow through Interstitium and Other Fibrous Matrices. Quarterly Journal of Experimental Physiology. Vol. 72,409-438,1987.

79. **Curry, F. E. and Michel, C. C.** A Fiber Matrix Model of Capillary Permeability. Microvascular Research. Vol. 20,96-99,1980.

80. **Curry, F. E.** Mechanics and Thermodynamics of Transcapillary Exchange. Handbook of Physiology, Section 2. The Cardiovascular System. Vol. 4, Microcirculation. American Physiology Society. Bethesda, MD.309-374,1984.

81. **Curry, F. E.** Determinants of Capillary Permeability: A Review of Mechanism Based on Single Capillary Studies in the Frog. Circulation Research, Vol. 59, No. 4, 367-380, 1986.

82. **Happel, J., and Brenner, H.** Low Reynolds number hydrodynamics with special application to particulate media. Prentice-Hall. Englewood Cliffs. N. J., 392-404, 1965.

83. **Sangam, A. S., and Acrivos, A.** Slow flow past periodic arrays of cylinders with application to Heat transfer. Int. J. Multiphase Flow. Vol. 8, 193-206. 1982.

84. **Tsay, R., and Weinbaum, S.** Viscous flow in a channel with periodic cross-bridging fibers: exact solutions and Brinkman approximation. Journal of Fluid Mechanics. Vol. 125-148. 226,1991.

85. **Boerboom, L. E., Olinger, G. N., Bonchek, L. I., Gunay, I. I., Kisebah, A. H., Rodriguez, E. R., and Ferrans, V. J.** The relative influence of arterial pressure versus intraoperative distention on lipid accumulation in primate vein bypass grafts. J Thorac cardiovasc Surg, 90(5): 756-764, 1985.

86. **Van beusekom, H. M., Van der Giessen, W.J., Van Suylen, R., Bos, E., Bosman, J. F. T., and Serruys, P. W.** Histology after stenting of human saphenous vein bypass grafts: observations from surgically excised grafts 3 to 320 days after stent implantation. J Am Coll Cardiol 21(1):45-54,1993.

87. **Gotto, A. M. Jr**. Lipid lowering and coronary risk. Isr J Med Sci 32(6):355-359,1996.

88. **Lark, M. W., Yeo, T., Mar, H., Lara, S., Heilstrom, I., Heilstrom, K., and Wight, T. N.** Arterial Chondroitin Sulfate Proteoglycan: Localization with a Monoclonal Antibody. The journal of Histochemistry and Cytochemistry, Vol. 36: 1211-1221, 1988.

89. **Nir, A., and Pfeffer, R.** Transport of macromolecules across arterial wall in the presence endothelial injury. J. Theor. Biol. 81: 685-711, 1979

90. **Pfeffer, R., Ganatos, P., Nir, A., and Weinbaum, S.** Diffusion of macromolecules across the artery wall in the presence of multiple endothelial injuries. J. Biomech. Eng. 103: 197-203, 1981.

91. **Kay, M. J.** Pulmonary vascular lesions in chronic thromboembolic pulmonary hypertension. Chest 105(5):1619-1620, 1994

92. **Tedgui, A., and Lever, M. J.** Effect of pressure and intimal damage on $^{131}$I-Albumin and [$^{14}$C] Sucrose spaces in aorta. American Journal of Physiology. 253: H1530-H1539, 1987.

93. **Holman, J. P.** Heat Transfer, sixth edition, McGraw-Hill, New York, p647, 1986

94. **Wakeham, W. A., Salpadoru, N. H., and Cao, C. G.** Diffusion Coefficients for Protein Molecules in Blood Serum. Atherosclerosis. 25: 225-235, 1976

95. **Spencer, M. P.** Dynamics of Ventricular Ejection. Circ. Res. 10:274-279, 1962

96. **Little, R. C.** Physiology of the Heart Circulation 3rd Edition , Year Book Medical Publishers, Inc. 1985

97. **Braunwald, E.** Heart Disease: A textbook of Cardiovascular Medicine 5th Edition, W. B. Saunders Comp., 1997